

A Coupled Transport and Chemical Model for Durability Predictions of Cement Based Materials

Jensen, Mads Mønster; Johannesson, Björn ; Geiker, Mette Rica; Stang, Henrik; Poulsen, Søren Lundsted

Publication date:
2014

Document Version
Publisher's PDF, also known as Version of record

[Link back to DTU Orbit](#)

Citation (APA):
Jensen, M. M., Johannesson, B., Geiker, M. R., Stang, H., & Poulsen, S. L. (2014). A Coupled Transport and Chemical Model for Durability Predictions of Cement Based Materials. Technical University of Denmark, Department of Civil Engineering.

DTU Library Technical Information Center of Denmark

General rights

Copyright and moral rights for the publications made accessible in the public portal are retained by the authors and/or other copyright owners and it is a condition of accessing publications that users recognise and abide by the legal requirements associated with these rights.

- Users may download and print one copy of any publication from the public portal for the purpose of private study or research.
- You may not further distribute the material or use it for any profit-making activity or commercial gain
- You may freely distribute the URL identifying the publication in the public portal

If you believe that this document breaches copyright please contact us providing details, and we will remove access to the work immediately and investigate your claim.

A Coupled Transport and Chemical Model for Durability Predictions of Cement Based Materials

M. M. Jensen

Ph.D. Thesis

Department of Civil Engineering
Technical University of Denmark

2014

Supervisors:

Assoc. Professor Björn Johannesson, DTU-Byg

Professor Mette Rica Geiker, NTNU

Professor Henrik Stang, DTU-Byg

PhD. Søren Lundsted Poulsen, DTI

Assesment Committee:

Professor I. L. Fabricius, Technical University of Denmark

Professor L. Wadsö, Lund University, Sweden

Assoc. Professor L. S. Bennethum, University of Colorado Denver, United States

A Coupled Transport and Chemical Model for Durability Predictions of Cement Based Materials

Copyright © 2014 by M. M. Jensen

Department of Civil Engineering

Technical University of Denmark

Preface

The thesis is divided into three parts:

Part I The motivation for initiating the PhD project is described and the aims and scope are defined. A description of cement, from its production to its use in the end products is given in order to relate the origin of the physical properties to service life aspects. The continuum based reactive transport model is described in terms of mixture theory, the numerical scheme and the computer algorithm established. The overall research findings are evaluated by a summary of the scientific papers, together with a complete discussion and conclusion based on these.

Part II This part includes the scientific papers published and submitted to relevant journals. The papers treat individual subjects related to the project.

Part III This part is an appendix with supplementary description to Part I. An extensive review of the balance equations in mixture theory and hybrid mixture theory is given.

The PhD project is a part of different consortia, where the Danish Expert Center for Infrastructure Constructions (or Concrete Expert Center) is the primary. The Concrete Expert Center is a collaboration between the Civil Engineering Department at Technological University of Denmark and the Technological Institute in Denmark on improvement of knowledge within service life of concrete. Furthermore, the Concrete Expert Center includes a PhD project entitled “Numerical Modeling of Reinforcement Corrosion in Cracked Concrete”. The results from the PhD projects in the Concrete Expert Center have been presented to a group of stakeholders. The group were representatives from Danish engineering companies and government institutions, e.g., Rambøll, Cowi, the Danish Road Directorate, Bane Danmark and the cement producer Aalborg Portland.

The project is a part of the Nanocem consortium as the partner project for the Civil Engineering Department at Technological University of Denmark

in the Nanocem consortium. Nanocem is a global consortium of academic and industrial partners, with interest in fundamental research of cement and concrete. Annual project reports were delivered to the members with recent findings from the PhD project. The results from the PhD project was presented by posters and oral presentations at different workshops.

Knowledge from the PhD study was shared at the Denmark-USA Workshop Series on Innovation and Design of Next Generation Sustainable Transportation Infrastructure. Topics upon service life prediction and total life cycle analysis were debated with focus on the coupling of physical models and probabilistic modeling.

Kgs. Lyngby 30th June 2014

M. M. Jensen

Acknowledgements

I would like to thank my main supervisor Associated Professor Björn Johansson at the Technical University of Denmark. I was introduced and taught in a range of new subjects in a very helpful way. I have appreciated much the informal supervision on a daily basis and the fact that Björns office door was always open for help and discussions.

A great thanks to the co-supervisors Professor Mette Rica Geiker at the Norwegian University of Science and Technology and Professor Henrik Stang at the Technical University of Denmark. Thanks to Erik Pram Nielsen and Søren Lundsted Poulsen from the Technological Institute in Denmark.

A great thanks to Yoshifumi Hosokawa from the R&D center at Taiheiyo Cement in Japan for sharing essential modeling findings and results.

Thanks to Klaartje De Weerd from Norwegian University of Science and Technology for sharing experimental results and discussions upon the relation between modeling results and experimental results.

Thanks to Matti Ristinmaa and the group at the Solid Mechanics Department at Lund University for a great time during my external stay.

Thanks to my friends and family for their support and understanding during the project period. A special thanks to Maja Jeppesen for her endless forbearance and support in adversity and good fortune, especially in the finalizing part of the processes.

Abstract

The use of multi-physics numerical models to estimate different durability indicators and determine the service life of cement based materials is increasing. Service life documentation for concrete used in new infrastructure structures is required and the service life requirement for such structures is often in the range from 80-125 years. Numerical multi-physics models are valuable tools when long term predictions are of interest. The multi-physics models needs to be theoretical sound in order to account for all the essential coupled processes that occurs. The numerical approach and algorithm needs to be robust in order to meet the increasing requirements for the detail level for the simulations and increasing long term simulations.

A coupled reactive mass transport model for concrete is established and different simulations of concrete exposed to different service environments are conducted. The theoretical background for the model is to a large extent based on the hybrid mixture theory, which is a modern continuum approach. The hybrid mixture theory description considers the individual phases and species, building up the whole mixture, with individual differential equations. The differential equations includes exchange terms between the phases and species accounting for the exchange of physical quantities which are essential for a stringent physical description of concrete. Balance postulates for, mass, momentum and energy, together with an entropy inequality are studied within mixture theories. Special attention is paid to the criteria for the exchange terms in the studied balance postulates. A simple case of mixture theory is used to demonstrate how constitutive assumptions are used to obtain the governing equations for a specific model.

The governing equation system used for the multi-physics durability model, established in this work, is an extended version of the Poisson–Nernst–Planck system of equations. The extension of the Poisson–Nernst–Planck system includes a two phase description of the moisture transport as well as chemical interactions. The vapor and liquid contents are coupled by a sorption hysteresis function and the chemical equilibrium is solved in terms of mass actions laws using the geochemical code PHREEQC. The overall durability

model accounts for, ion diffusion, ion migration, two phase moisture transport including for hysteresis, ionic convection and chemical interactions in the pore solution and between the solid cement hydrates and the pore solution constituents. The mass transport equation system is solved using the finite element method. An operator splitting approach is utilized in order to solve the mass transport and chemical interactions sequentially. A detailed description of the continuum background of the governing equations and the numerical solution approaches used is given in this work.

The durability model is tested with different input parameters and boundary conditions in order to demonstrate the applicability of the model and robustness of the algorithm established. A calculated test example shows the model response to varying vapor content at the boundary, where saturated conditions occurs in periods and leaching of ions is only allowed in this period. The effect of the sorption hysteresis function is demonstrated in this test by a comparison to a more simple numerical approach.

The importance of the chemical interactions are demonstrated through different cases in terms of using different boundary conditions and chemical reaction calculation approaches. Sea-water compositions are used as multi-species boundary conditions to model natural exposure conditions of infrastructure constructions. Test examples shows that the simulation results are very sensitive to the choice of chemical reactions included in the model. It is concluded that the different numerical chemical equilibrium solution approaches used performs differently for the same initial and exposure conditions. Different numerical calcium silicate hydrate reaction approaches are studied and reactive transport modeling results using these are compared. Modeling results of ion ingress are compared with experimental results where mortar samples has been exposed to a NaCl solution or sea-water. Comparing the chloride ingress between the numerical model and the experiments at three different exposure times showed good agreement.

Resumé

Brugen af multi-fysiske modeller til estimering af forskellige holdbarhedsindikatorer til bestemmelse af levetiden for cement baserede materialer er stigende. Levetidsdokumentation kræves ofte for beton som anvendes i infrastruktur konstruktioner hvor levetidskravene for disse ofte er 80-125 år. Multi-fysiske numeriske modeller er yderst anvendelige værktøjer ved langtidsforudsigelser. De multi-fysiske modeller skal være teoretisk velfunderede for at inddrage alle essentielle koblede fysiske og kemiske processer. Den numeriske løsning og algoritme skal være robust for at imødekomme de øgede krav til detaljeniveauet i simuleringerne samt øget simuleret tid.

En koblet reaktiv masse transport model til beton er etableret og forskellige simuleringer af beton eksponeret imod forskellige eksponeringsmiljøer er udført. Den grundlæggende teoretiske baggrund for modellen er baseret på hybrid blandingsteori som er en moderne kontinuum metode. Den hybride blandingsteori beskriver de enkelte faser og de enkelte bestanddele med individuelle differentiale ligninger. Differentiale ligningerne inkluderer udbytningstermer som beskriver overførslen af fysiske mængder hvilket er essentielt for at opnå en stringent beskrivelse af beton. Studier af ligevægtspostulater for masse, momentum og energi, samt en entropi ulighed indenfor blandingsteorier er udført. I studierne er der er lagt specielt vægt udbytningstermerne i ligevægtspostulaterne. Et simpelt tilfælde fra blandingsteorien er brugt til at vise hvorledes de konstitutive antagelser bruges ved udledningen af de styrende ligninger for en specifik model.

Det styrende ligningssystem som anvendes i den multi-fysiske holdbarhedsmodel, etableret i dette projekt, er en udvidet version af Poisson–Nernst–Planck ligningssystemet. Udvidelsen af Poisson–Nernst–Planck systemet inkluderer en to fase beskrivelse af fugt transport, samt kemiske interaktioner. En sorptionshysterese funktion beskriver forholdet imellem damp og væskeindholdet og kemisk ligevægt er beregnet ved hjælp af 'mass action laws' i den geokemiske kode PHREEQC. Den overordnede holdbarhedsmodel beskriver, ion diffusion, ion migration, to faset fugttransport med sorption hysterese, ion konvektion og kemiske interaktioner i poreopløsningen og mellem pore-

opløsningen og de solide cement hydrater. Masse transport ligningsystemet er løst ved hjælp af finit element metoden. En operatorfordelings metode er anvendt for at løse masse transport og kemisk ligevægt sekventielt. En detaljeret gennemgang af kontinuum baggrunden for de styrende ligninger og fremgangsmåden for løsningen af disse er givet.

Holdbarhedsmodellen er testet med forskellige inputparametre og randbetingelser, for at demonstrere anvendeligheden af modellen og robustheden af algoritmen som er etableret. Et beregningseksempel viser modellens respons på varierende dampindhold ved randen, hvor vandmættede perioder forekommer og udludning af ioner er kun tilladt i denne periode. Effekten af sorptionshysterese funktionen vist ved en sammenligning med en simpel numerisk fremgangsmåde.

De vigtige kemiske interaktioner er vist igennem flere forskellige cases i form af forskellige påsatte randbetingelser og fremgangsmåder for kemisk reaktionsberegninger. Havvandskompositioner anvendes som multi-komponents randbetingelser til modellering af naturligt eksponerede infrastruktur konstruktioner. Test eksempler viser at simulerings resultaterne er yderst sensitive for valget af kemiske reaktioner inkluderet i modellen. Det konkluderes at forskellige numeriske fremgangsmåder for beregningen af kemisk ligevægt giver forskellige output for de samme initiale forudsætninger og eksponeringsbetingelser. Forskellige numeriske metoder for reaktionen med calcium silikat hydrater er undersøgt og disse er sammenholdt. Modelleringsresultater af ion indtrængning er sammenholdt med eksperimentelle resultater, hvor mørtel prøver har været eksponeret imod en NaCl opløsning eller havvand. Sammenligningen imellem den numeriske model og de eksperimentelle resultater vidste en god korrelation ved tre forskellige eksponeringstider.

Contents

I	Introduction and research findings	1
1	Introduction	3
1.1	Project background	3
1.1.1	Aim and scope	5
1.2	The use of concrete	6
1.3	Concrete as building material	8
1.3.1	Cement chemistry	8
1.3.2	Mass transport in concrete	12
1.3.3	Durability and service life of concrete	14
1.4	Concrete modeling tools	17
1.5	Concluding remarks	20
2	Numerical model description	23
2.1	Introduction of mixture theories	23
2.1.1	Balance equations and mixture theory results	25
2.1.2	Constitutive theory for reacting systems	28
2.1.3	Concluding remarks	32
2.2	Numerical methods	33
2.2.1	Mass transport	33
2.2.1.1	FEM development	34
2.2.2	Operator splitting method	35
2.2.3	Chemical equilibrium solvers	35
2.2.4	Implementation of computer code	37
2.2.5	Pseudo code of the framework algorithm	38
3	Research findings and conclusions	45
3.1	Summary of research	45
3.2	Long term durability simulations	47
3.3	Discussion and future work	49
3.4	Conclusions	52
3.5	References	55

II Scientific publications 63

Paper I

"A numerical comparison of ionic multi-species diffusion with and without sorption hysteresis for cement-based materials",

M. M. Jensen, B. Johannesson, M. R. Geiker.

Submitted: *Transport In Porous Media, Nov, 2013* 67

Paper II

"Framework for reactive mass transport: Phase change modeling of concrete by a coupled mass transport and chemical equilibrium model",

M. M. Jensen, B. Johannesson, M. R. Geiker.

Accepted: *Computational Material Science, May, 2014* 91

Paper III

"Comparison of solid phases in cement paste calculated by two different C-S-H models in a reactive mass transport model",

M. M. Jensen, Y. Hosokawa , B. Johannesson.

Submitted: *Modelling and Simulation in Materials Science and Engineering, Jul, 2014* 105

Paper IV

"Use of a multi-species reactive transport model to simulate chloride ingress in mortar exposed to NaCl solution or sea-water",

M. M. Jensen, K. De Weerd, M. R. Geiker, B. Johannesson.

Submitted: *Computers and structures, Jul, 2014* 121

III Appendix 135

A Mixture theories 137

A.1	Single phase mixture theory	139
A.1.1	Kinematics	139
A.1.2	Mass balance	143
A.1.3	Momentum balance	145
A.1.4	Balance of energy	151
A.1.5	Second axiom of thermodynamics	158
A.1.5.1	Entropy inequality for the whole system . . .	165
A.2	Multi-phase hybrid mixture theory	167
A.2.1	Mass balance	169
A.2.2	Momentum balance	172

A.2.3	Angular momentum	177
A.2.4	Energy balance	178
A.2.4.1	Definitions for energy balances	178
A.2.4.2	Energy balance for constituents	180
A.2.5	Entropy inequality	188
A.3	Multi-phase HMT with Maxwell's equations	195
A.3.1	Mass balance with massless interface.	195
A.3.2	Macroscopic form of Gauss' Law	196
A.3.3	Macroscopic form of Faraday's law	197
A.3.4	Macroscopic form of Ampère's law	197
A.3.5	Macroscopic form of conservation of electrical charge	198
A.3.6	Linear momentum with electromagnetic forces	199
A.3.7	Angular momentum with electromagnetic forces	200
A.3.8	Energy balance with electromagnetic forces	200
A.3.9	Entropy balance with electromagnetic forces	202
A.3.10	Constitutive theory with electroquasistatic effects	206

Abbreviations

Short notation	Chemical formula
C	CaO
S	SiO ₂
H	H ₂ O
A	Al ₂ O ₃
F	Fe ₂ O ₃
\bar{S}	SO ₃

Short notation	Clinker name
C ₃ S	Alite
C ₂ S	Belite
C ₃ A	Aluminate
C ₄ AF	Ferrite

Short notation	Phase name
C-S-H	Calcium Silicate Hydrate
CH	Portlandite
$\bar{C}\bar{S}\bar{H}_2$	Gypsum

OPC	Ordinary Portland Cement
PNP	Poisson–Nernst–Planck
FEM	Finite Element Method
FE	Finite Element
FVM	Finite Volume Method
LBM	Lattice Boltzmann Method
MAL	Mass Action Law
EDL	Electrical Double Layer
GEM	Gibbs Energy Minimization
HMT	Hybrid Mixture Theory

Part I

Introduction and research findings

Chapter 1

Introduction

A numerical framework for service life predictions in terms of durability indicators is established in this project. The background for establishing the project and the descriptions of the aims and scope for the project are presented in this chapter. Cement based materials, especially concrete, are of main interest in this project. Therefore, a general description of cement is given, in terms of cement production, the use of cement based materials and durability indicators. The description of the cement properties are related to service life aspects of concrete, where numerical service life modeling is an important tool for service life predictions. The service life concept as it is treated in this work is shortly described and a review of existing numerical service life models/tools for concrete is given.

The purpose of including a detailed description of cement as a material is twofold, firstly, to emphasize the importance of understanding that all physical and chemical processes from cement production have a significant influence on how cement based materials evolves over time and how they behave in their service environments. Secondly, further development of the numerical service life framework in terms of new models/tools requires a deep knowledge of the material in terms of physical and chemical behaviors.

1.1 Project background

Cement based materials are the most used building material in the world, where different types of concretes are the most used products. The total amount of cement requested world wide is extremely high, in 2013 the total global amount of cement produced was estimated to be 4.000[Mton] where the major parts were produced in China with 58%, 7% in India, 2% in the United States (U.S. Geological Survey, 2014). The enormous amount of

cement produced globally is in charge of 4-5% of the global CO₂ emission as the approximately energy consumption for the production is 1.4[GJ/ton] and due to the breakdown of the limestone in the cement kiln (NRMCA, 2012). Research has been devoted to reduce the energy consumption in the cement production, but it seems that practical limits have been reached, for developing this further. The research tends to focus on replacing the cement in the end products with other silicate based materials and in this way reduce the amount of cement needed in these. Examples of substitutes for cement are fly ash, ground granulated blast furnace slag and silica fume (Siddique and Khan, 2011).

Cement based materials are often very durable, so the total amount of CO₂ emitted from the production is often acceptable seen from a service life perspective. Service life requirements for large infrastructure constructions are often in the time frame of 80 - 125 years where only planned maintenance is accepted. The design phase of larger structures will often involve a long term service life estimation in order to ensure a sufficient service life which requires knowledge of the deterioration processes in the material caused by specific service environments. The physical and chemical deterioration processes involved are often very complex and interlinked, which makes a reliable service life estimate difficult to perform.

The overall durability of cement based materials is strongly dependent on the service environments they are placed in. A great majority of the overall durability aspects are related to mass transport mechanisms of different kinds in the porous network. The mass transport of ions, in the pore solution, change the equilibrium state between the solid and liquid phases in the system and thereby affects the durability. The ion transport affects the durability in two ways, with transport from the service environment into the pore solution and transport from the pore solution towards the service environment. The ingress of external ions from the service environment, may lead to formation of new solid phases or increase the amount of the existing ones. The formation of solid phases may result in volume expansions, that can cause cracking. The leaching of ions from the concrete pore solution to the service environment leads to dissolution of the initially formed solid phases.

Changes in the initial pore solution are especially critical for reinforced concrete structures as the pH-value may decrease due to the ion transport and rebar corrosion can initiate which is especially critical when chloride is present (Nielsen and Geiker, 2004; Geiker et al., 2007). Another important mass transport process to consider for the durability aspects of concrete is the moisture flow in non-saturated concrete. An external supply or loss of moisture will change the initial conditions of the pore solution and thereby change the ion concentrations. The moisture flow in concrete is rather com-

plex as it is heavily affected by sorption hysteresis. Examples of moisture level variations in service environments are typically from summer to winter periods or in tidal zones, in which parts of the structure are exposed to saturated conditions in periods.

The task of predicting the service life of a concrete structure as a function of durability indicators is challenging in different ways, the time frame considered (80 - 125 years), the number of coupled physical and chemical processes involved and variations in the service environment in both short and long time perspectives. The number of unknowns in the service life 'equation' for concrete is extensive and requires a robust and effective framework for its solution and equally important, the possibility to extend the framework in terms of coupling of additional physical and chemical processes. The computational power available today, enables rather large and complex coupled systems to be solved numerically within reasonable short time.

1.1.1 Aim and scope

The project is motivated by the increasing demands to service life predictions of concrete structures. Numerical service life frameworks based on sound theoretical descriptions in terms of numerical durability models, used as durability indicators, are relevant for this matter. Robust solving methods are also needed to meet the future demands. The overall aim of the project is:

- To identify and understand the main multi-physical and chemical processes in concrete through a sound continuum theory.
- To implement coupled moisture and ion transport equations into a tailor made finite element code.
- To implement a chemical equilibrium module into the mass transport equation scheme.
- To verify the multi-physics hypothesis in terms of mass transport and chemical interactions by comparing simulation results with experimental results.

The durability model established in this work will not account for all known physical and chemical processes related to durability. However, the structure of the model is such that future modifications and additions are straight forward. The theoretical mechanical background for the durability model established is based on continuum mixture theory (Bowen, 1976) and hybrid

continuum mixture theory (Bennethum and Cushman, 2002a,b). The transport of each ion and phase are considered individually in the mixture theories and the chemical interactions are taken into account. The mass transport part of the durability model is based on an extended version of the Poisson–Nernst–Planck system of equations derived from hybrid mixture theory, see e.g. Johannesson (2010a). The moisture transport part, of the durability model, which accounts for sorption hysteresis is included by the method described in Nyman et al. (2006); Johannesson and Nyman (2010). The finite element method is used as numerical solver for all included mass transport equations. The chemical interactions are described by equilibrium dissolution/precipitation reactions and the equilibrium state is determined in terms of the corresponding mass action laws. Special attention is paid to a robust chemical description which includes the state-of-art reaction schemes for the calcium silicate hydrate. The durability model is not validated against experiments in all parts but examples of its performance is checked by comparing simulation results with experimental data.

1.2 The use of concrete

Concrete is properly the most well known type of material based on cement. Concrete is used extensively as a building material, not only by professional craftsmen but also in simple do-it-yourself projects conducted by amateurs. Concrete is, therefore, available in different formats, from large trucks with 6-12 m² ready-mixed concrete to kinds of “shake’n-bake” mixtures in 5 kg bags where only water needs to be added. The placing of concrete is also varying, from a simple foundation under a single-family house to large constructions in terms of bridges, dams, tunnels, etc. The fluidity of fresh concrete is one of the reasons for the widespread use in the building industry. The properties of fresh concrete is also used by artists to form sculptures. Artists and architects may utilize the possibility of varying the color and surface treatments of concrete to create different visual expressions. A completely different application of cement paste is for dental repair, which is developed from commercial portland cement in combination with bismuth oxide powder (Torabinejad and Chivian, 1999). Durability is to some extent relevant for the applications listed above, but the requirements and service environment differs significantly for the application.

The most simple form of concrete is a mix of Ordinary Portland Cement (OPC), aggregates in variable sizes and water, where the properties of the hydrated concrete is highly depended on the proportions of the components in the mixture. The most important property for concrete as a building material

is the compressive strength. The compressive strength for ordinary concrete is around 30-50[MPa] and high-strength concrete has been developed with compressive strength >100[MPa]. High compressive strength is obtained by using high amounts of cement in relation to the amount of water used. The tensile strength is significant lower compared to the compressive strength, around a factor of 0.10.

Reinforced concrete is properly the most used type of concrete, where steel reinforcement is used to limit cracking of the concrete besides increasing the tensile strength. Different types of reinforcement methods have been developed for different purposes and different materials have been used in combination with concrete. Typical reinforcement for, e.g., bridge decks are a carefully designed net of steel rebars in which concrete is casted to cover the steel and add compressive strength to the structure. Another type is fiber reinforcement, where small fibers of different kind of shapes are mixed into the concrete. Fiber reinforcement increases the toughness of the concrete and therefore stresses can be transferred across local cracks. Fiber reinforcement is in some cases combined with the conventional steel rebars. A more advanced form of reinforcement is pre-stressed concrete, where the rebars are pre-stressed to increase the span for, e.g., concrete bridge decks. Common to most reinforced structures today, is the use of steel and the durability is therefore no longer only dependent on the concrete but also the durability of the steel embedded in the concrete.

Concrete is used in large scale for other purposes than the load bearing capacity. Common for the different types of concrete is that the cement paste glues together the aggregates. The amount of cement paste, density of the aggregates and the use of different add-mixtures are then varied in order to create different types of concrete. Lightweight concrete is often used for non-bearing walls, where it reduces the total dead load of a structure. Lightweight concrete has a comparable low bearing capacity but has improved thermal properties due to its high porosity. On the other hand, heavyweight concrete is for instances, used as radiation protection where the thickness of the construction required to obtain proper protection is reduced compared to conventional concrete. Another example is pre-stressed concrete which is used in pressure vessels for nuclear reactors (Mindess et al., 2003). Concrete is also used for storage and encapsulation of nuclear waste where the long term performance of concrete is very important, in the range of 1000 years (Fillmore, 2004; Acevedo and Serrato, 2010).

The review of the applications of concrete and the different types of concretes given here is not complete, but it gives an indication of the variety of its use and types of concretes available. A common issue for most of the applications considered here, is the durability. It is concluded that the dif-

ferent applications sets different requirements for the durability and gives significantly different service environments. Durability aspects of concrete are a factor in safety considerations for, e.g., bridge construction and nuclear power plants, but also a factor in the economical considerations for, e.g., larger infrastructure constructions.

1.3 Concrete as building material

Concrete is simply a mix of cement, water and aggregates, where cement and water forms the cement paste that binds together the aggregates to form a composite material. The chemistry involved, from production to cement paste in service environments is described in the following sections. Essential physical properties responsible for the mass transport in concrete are described. The coupled mass transport processes and chemical interactions in concrete are the main actions affecting the overall durability.

The experienced concrete researcher or civil engineer may find this section trivial, but it is included here to relate the basic cement properties, to durability problems where complex solution procedures are needed. Another purpose of this section is to describe concrete as a general material within the category of reactive porous media. The theoretical background for the modeling tool described and used in this work is valid for any porous medium, which facilitates that methods from other research fields may be transferred and utilized.

1.3.1 Cement chemistry

The cement chemistry is divided into three main processes in this work. The processes are related to the overall durability of the end products.

1. The manufacturing of cement from the raw materials
2. The hydration processes in which cement and water reacts
3. Cement paste degradation caused by a non-equilibrium condition between the paste and the pore solution.

The practical process of manufacturing cement is rather simple, the raw materials are heated in a kiln to approximately 1300 to 1400°C where different calcium silicates are formed (Taylor, 1997; Hewlett, 2003; Mindess et al., 2003; Boateng, 2008). The raw materials must be of a certain quality in order to control the chemical process in the kiln and get a uniform cement composition in a continuous production line. The typical raw materials for

Table 1.1: Clinker composition of a typically ordinary Portland cement according to Mindess et al. (2003).

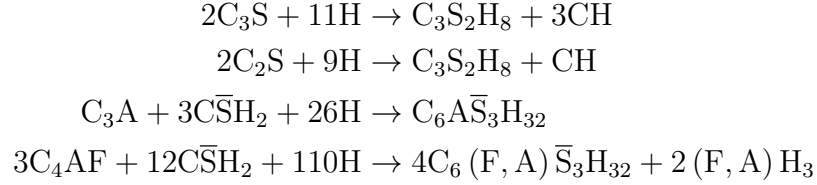
Clinker phase	Compound	Weight percent
Alite	C_3S	55
Belite	C_2S	18
Aluminate	C_3A	10
Ferrite	C_4AF	8
Gypsum	$C\bar{S}H_2$	6
Impurities		3

the calcium oxide supply are limestone, chalk and/or shell deposits. Iron-bearing aluminasilicates provides the silicate to the cement where clay and silts are the primary sources. One of the advantages of using clay and silts is that these minerals are often naturally finely divided. The raw materials are blended and grinded if necessary before they are heated in the kiln.

The chemical processes in the kiln starts in the calcination zone where carbon dioxide is released from the limestone at about 900°C and clinker components starts to form at a temperature of 1200°C . The first clinker component formed is typically belite (C_2S) which is produced by solid-state reactions, where the the present alumina and ferrite acts as fluxes. Increasing the kiln to the final temperature at 1300 to 1400°C will result in formation of the important alite (C_3S). The alumina and ferrite phases (C_3A and C_4AF) are formed in the cooling phase of the cement. A small amount of gypsum ($C\bar{S}H_2$) is added to the cement to control hydration of C_3A . A typically clinker composition of an OPC is shown in Tab. 1.1. The impurities or minor components in the cement are often found in the aluminate phases C_3A and C_4AF , where the oxides K_2O , Na_2O and MgO are the most common. The presence of magnesium oxide MgO in the cement may cause volume expansions in the cement paste after a hydration period, due to its relative slow reaction rate. The alkalis K_2O and Na_2O may cause alkali-silicate reactions with the aggregates in concrete which may lead to cracking. Crack formation is of course a significant durability issue and has significant influence, on e.g., the mass transport properties.

The hydration of cement is easy to initiate, as it involves only mixing water and cement. The chemical processes occurring during hydration are on the other hand very complex and these are not yet fully understood (Bullard et al., 2011; Mindess et al., 2003; Taylor, 1997). The reaction schemes for the hydration presented here are based on examination of the individual clinker minerals. A simple form of the hydration reactions of the clinker components

given in Tab. 1.1, are



The C_3S and C_2S reactions are similar, where both reactions forms calcium silicate hydrate (C-S-H or C-S-H gel) and calcium hydroxide (Portlandite or CH) in different amounts. C-S-H and CH are the two main components in cement paste and the two most important. The reaction schemes with the C-S-H are shown with a fixed stoichiometry, but the internal C/S ratio varies, which makes a sound and robust description of the C-S-H complicated. Some aspects regarding the structural description of the C-S-H are addressed in Paper III, where some of the recent chemical models for the C-S-H phase are shown and implemented in the durability model. The C_3A and C_4AF reacts with gypsum and water to form different types of ettringite phases. The aluminate reaction may also form monosulfoaluminate depending on the molar ratio between gypsum and aluminate, $\overline{\text{CS}}\text{H}_2/\text{C}_3\text{A}$, present. The simulated formations of ettringite and monosulfoaluminate are studied in Paper III and Paper IV where they are combined with formation of Friedel's salt, as a consequence of chloride ingress.

There exist no general agreement of the description of the chemical reactions involved in the hydration and therefore a detailed description and understanding of the kinetics is not yet achieved (Bullard et al., 2011). Some basic understanding of reaction rates for the clinker minerals, e.g. the order of the rates $k_{\text{C}_3\text{A}} > k_{\text{C}_3\text{S}} > k_{\text{C}_4\text{AF}} > k_{\text{C}_2\text{S}}$ and different stages of the hydration are determined from heat elaboration. The hydration kinetic is considered in this work in terms of the degree of hydration of each of the clinker minerals, which are functions of time. The total degree of hydration at a given time is of interest for this work, as all physical properties for the hardened cement paste are set and developed as a function of this, e.g. porosity, pore size distribution and connectivity of the pores.

The third cement chemistry topic discussed in this work is the chemical degradation of the cement paste (Le Bescop et al., 2013; Hewlett, 2003). Here it is assumed that the desired physical properties have been reached and that the solid phase composition is in a steady equilibrium with the pore solution. Chemical degradation of the initial cement paste composition occurs when a non-equilibrium state between the pore solution and the solid phases exist. The non-equilibrium state is caused by different exposures from the service environment. As described earlier, concrete and thereby cement paste are

used in a variety of applications which also gives a variety of service environments. Service environments for infrastructure structures are typically soil on concrete foundations and sea-water on, e.g., harbor, bridge or tunnel structures. Concrete placed in soil may suffer from sulfate attack whereas sea-water exposure is a combined exposure, where sulfate, magnesium and chloride in different concentrations are common. Leaching of ions from the pore solution causes dissolution of the solid phases. Sulfate attack from an external source may result in additional formation of gypsum, monosulfate and ettringite. This so-called delayed ettringite formation causes a volume expansion, which increase the internal tensile stresses in the cement paste and will lead to cracking if the tensile capacity is exceeded. Cracks accelerates the rate of ion ingress and thereby sulfate which in some cases causes spalling of the concrete cover. The major components in sea-water are typically sodium, chloride and magnesium which may react with the pore solution to form solid phases like, e.g., ettringite, brucite and Friedel's salt. Brucite is formed by the expense of CH and leads to decalcification of the C-S-H at a later stage as the pH-value of the pore solution drops. Formation of brucite and other magnesium phases may not always be a completely negative effect seen from a durability perspective as they may create a sealed area near the exposed surface which decreases the rate of mass transport. Chloride exposure on cement paste may form Friedel's salt and Kuzel's salt, which interacts chemically with other solid phases (Balonis et al., 2010). Chloride attack on cement paste is extensively studied as the chloride is one of the main reasons for initiation of reinforcement corrosion. The presence of chloride in the pore solution in combination with a low pH value will remove the corrosion protection of the steel rebar surfaces. The formation of solid phases containing chloride together with other binding mechanisms may work as retarders for the ingress rate. The chemical processes in steel corrosion is not considered in the durability model in this work, but calculated chloride concentrations may be used in, e.g., the Hausmann's free concentration criterion for initiation of steel corrosion, which is $[\text{Cl}^-]/[\text{OH}^-] > 0.6$ (Hausmann, 1967) or other similar criteria see, e.g., Alonso et al. (2000).

External ion ingress causes a range of changes to the initial cement paste. The changes described above are interlinked and some processes may preclude others. This fact complicates a formulation of a chemical model which is general and thereby usable for different cement compositions and service environments. It is also concluded that the solid phases are changed due to the mass transport and thereby change the mass transport properties, which complicates the formulation of a coupled durability model even more.

1.3.2 Mass transport in concrete

Mass transport in concrete plays a significant role for several durability considerations. The mass transport in the porous system is the main reason for establishing a chemical non-equilibrium state between the pore solution and the solid phases. The mass transport properties evolves during the hydration period which makes this process essential for the durability issues related to mass transport. The mass transport properties of concrete are also strongly dependent on the mix design of the specific concrete. The design criterion for concrete mix designs is often only specified in terms of the compressive strength and durability aspects may be considered as secondary.

The porous network in concrete is very complex at the micro and nano scale which makes the mass transport properties difficult to understand. The pores created are geometrically difficult to quantify due to the different shapes of the hydration products. The irregular shapes have an effect on, e.g., capillary condensation and water adsorption properties. The pore formation in concrete can be understood as a compaction of the reacted water, the density of water bound in the hydration products of OPC is approximately $\rho_{w,react} \approx 1333[\text{kg/m}^3]$.

The porous network is often quantified by the total porosity $p_{tot}(t)$, which is defined as

$$p_{tot}(t) = \frac{V_{pore}(t)}{V_{tot}} \quad (1.3.1)$$

where $V_{pore}(t)$ is the pore volume and V_{tot} is the total volume which is assumed constant. The pore volume is a function of time and evolves in the hydration period but may also change in the service period due to chemical interactions. The initial total porosity is dependent on the water to cement ratio (w/c) and the degree of hydration, where an increasing w/c ratio will increase the total porosity of the hydrated cement. The pores are divided into two main groups the capillary pores and the gel pores, depending on their size. The capillary pores are the water filled space in the unhydrated mix and gel pores are small pores in the C-S-H. The capillary pores are of great interest for many durability aspects as the mass transport occurs mainly in this part of the porous network. The capillary porosity $p_{cap}(t)$ is defined as

$$p_{cap}(t) = p_{tot}(t) - p_{gel}(t) \quad (1.3.2)$$

where $p_{gel}(t)$ is the gel porosity which is assumed to be 0.26 for a fully hydrated cement (Mindess et al., 2003). An important theoretically lower limit for the w/c ratio can be determined. A $w/c = 0.41$ will ensure that a sufficient amount of water is available for full hydration and a minimum of capillary porosity is created.

The porosity definitions do not include any informations of the geometrical configuration of the porous system, which is important in relations to the mass transport processes. A measure that is often used in concrete research to quantify the pore geometry is the pore size distribution determined by, e.g., mercury intrusion. The pore size distribution is, however, not a direct measure of the connectivity of the porous network. Another measure is the water permeability which is important, especially for non-saturated concretes, as the rate of attack from the service environment may be controlled by this factor. The flow of water in cement paste obeys the Darcy's law. An extended Darcy's law is studied through numerical examples in Paper I and II. A simple form of Darcy's law is

$$v = -K_p \frac{\Delta h}{\Delta x} \quad (1.3.3)$$

where v is the rate of flow, K_p is the permeability coefficient, Δh is the hydraulic pressure over the distance Δx . The permeability, in terms of the permeability coefficient K_p , is related to the capillary porosity and w/c ratio. An increase in w/c ratio and thereby the capillary porosity will increase the permeability coefficient for both cement paste and concrete. The water transport carries ions from the service environment and initiates a chemical attack. Another important permeability measure is the gas permeability which typically is higher than the water permeability. The gas phase transports water vapor and carbon dioxide which reacts with the pore solution. Modeling of vapor transport is studied in Paper I.

Moisture fixation in terms of adsorption and capillary condensation is related to the complex geometrical pore structure at the micro and nano scale. Concrete shows a significant sorption hysteresis effect on wetting and drying cycles which affects the chemical equilibrium of the pore solution. A fully theoretical understanding of the sorption hysteresis has not yet been reached, so phenomenological modeling approaches are sought in order to reproduce sorption hysteresis. A sorption hysteresis model which is included in the durability model is studied in Paper I.

The mass transport in concrete includes transport of ions in the pore solution which is a significant process, especially in saturated concrete. The ion transport is strongly affected by the moisture content in non-saturated pores and depends thereby on the sorption mechanisms. The ion transport in saturated pores is mainly diffusion and migration driven, which are dependent on the self diffusion constant for each ion $D_{0,i}$ and the migration coefficient $A_{0,i}$. The most simple case of ion transport is the diffusion of an uncharged

and non-reacting ion, which follows the simple form of Fick's second law

$$\frac{\partial c_i}{\partial t} = D_i \frac{\partial^2 c_i}{\partial x^2} \quad (1.3.4)$$

where c_i is the concentration of ion species i , t is time, D_i is the effective diffusion constant and x is distance. It is clear that the ions in the complex pore solution in concrete is affected by charged species and chemical reactions, this is described in more details in Paper I, II, III and IV. The complex geometrical structure of the porous network has an influence on the ion diffusion in terms of the diffusion coefficient. A tortuosity factor τ is often used to describe the relation between the self diffusion coefficient $D_{0,i}$ and the effective diffusion coefficient D_i of the pore system (Shen and Chen, 2007). The tortuosity factor can be defined as

$$\frac{1}{\tau^2} = \frac{D_{0,i}}{D_i} \quad (1.3.5)$$

Different authors may define the tortuosity factor differently (Latour et al., 1995), but the main concept is the same.

Common for all the mass transport mechanisms are that they are dependent on the geometrical configuration of the porous matrix. This means that changes in the geometrical configuration due to, e.g., cracking caused by volume expansion will change the effective diffusion coefficients.

The main concluding remarks on the limited review of cement chemistry and mass transport, Sec. 1.3.1 and 1.3.2, is that it is important to realize that all chemical and physical processes occurring are interlinked and influence each other. In other words, the quality of the raw materials has an influence on the concrete performance until it is taken out of service and maybe reused. All physical and chemical processes in this period may affect different durability aspects of the material. It should be the primary goal to incorporate as many general physical and chemical processes into a durability model in order to predict the behavior of any type concrete. Optimally, the clinker composition, the mix design and the load from the service environment should be the only input for a complete durability analysis of a concrete.

1.3.3 Durability and service life of concrete

The terms *durability* and *service life* are essential when the long term performance of concrete and concrete structures are predicted. A numerical service life framework based on numerical durability models is established in this work. But how are the terms defined and how are they linked?

Durability is a general term, so investigating concrete durability may be challenging as it covers a wide range of topics and it make no sense to study durability as a single measurable quantity. Durability is related to an event that causes fundamental changes to the exposed material. Some of the classical issues related to durability of concrete are

- Chemical attack
 - Sulfates, causing volume changes.
 - Carbonation, pore solution changes and formation of new phases.
 - Reinforcement corrosion, cracking and spalling due to volume changes.
 - Alkali-silica reaction, cracking.
 - Leaching, dissolution of solid species. Mass transport
 - Wetting and drying cycles
 - Moisture transport
 - Ion and gas transport
- Physical attacks
- Micro structure, including cracks and other defects

The list indicates that durability of concrete is used in many connections and the listed subjects are considered as individually problems in many cases. The use of the durability term for different purposes for concrete is highlighted by Mendoza-Rangel and Castro-Borges (2007) where it is concluded that there is no common agreement on how durability for concrete is defined. The term “ability” is highlighted by Mendoza-Rangel and Castro-Borges (2007) as an important term in a durability context. This term is adopted here to formulate a definition for durability of concrete for this work as “The ability to withstand any exposure that causes an equilibrium state that is different from a similar material in an isolated environment at the time t ”. There is no distinction made between pure concrete and reinforced concrete in the durability definition and it is defined solely for the material. The definition is constructed from a theoretical and modeling point of view. The time of concrete mixing corresponds to $t = 0$, so the definition covers, e.g., the hydration process, which is considered as being in equilibrium at all time but also reinforced structures as an equilibrium state is assumed between the concrete and the reinforcement material.

Service life of concrete or, maybe more relevant service life of concrete structures is also a general term, in the same way as the durability term.

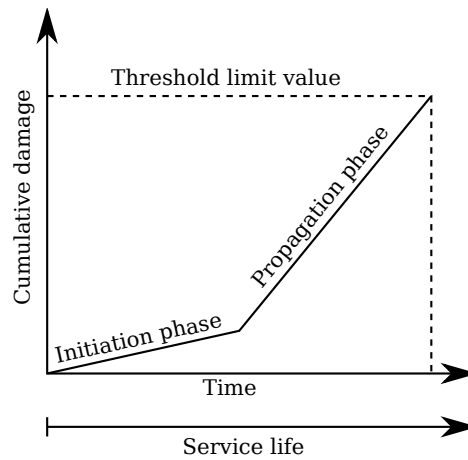


Figure 1.1: Schematic service life model, after Tuutti (1982).

Service life of concrete structures is often associated with the service life of reinforced concrete as many definitions and models relate the service life to corrosion of the reinforcement (Bazant, 1979; Tuutti, 1982). Most often when service life is considered, the actual concern is about the end of service life, at which state it occurs and the time until it occurs. One of the most known schematic service life models for reinforced concrete structures is proposed by Tuutti (1982) where the service life is described by an initiation phase and a propagation phase of reinforcement corrosion. At some time in the propagation phase, the structure will reach a limit state, e.g., in terms of failure, which then is defined as the end of service life. The schematic model by Tuutti (1982) has been extended in different versions and combined with probabilistic modeling of service life see, e.g., Li et al. (2007); Cusson et al. (2011); Pease et al. (2011); fib (2006). Recent topics within service life modeling includes further extensions where, e.g., monitoring, maintenance planning, future loading scenarios, life-cycle cost, etc., are considered, see Cusson et al. (2011); Kim et al. (2013).

A different service life modeling approach is given by the deterministic models. Some of these models are reviewed by Ahmad (2003); Mendoza-Rangel and Castro-Borges (2007). The deterministic models may also use the definitions of the initiation phase and the propagation phase of reinforcement corrosion and estimate the service life based on that. A model proposed by Bazant (1979) determines the time, to a defined volume expansion caused by rust formation on a rebar. A certain amount of rust will eventually lead to cracking or spalling which may be defined as the end of service life. A question that is not clearly answered with respect to service life of concrete structures is at which state the service life ends? The definitions of this is

often difficult to understand and to some degree very self-deciding, some of these concerns regarding the use of the service life term in standards are addressed by Helland (2013).

It should also be mentioned that the durability and service life terms may differ between applications of concrete, e.g., concrete used in nuclear energy production may have other definitions of durability and service life compared to infrastructure structures which are of main interest here. The numerical service life framework initiated in this work do not give the end of the service life as result, neither does it give the full picture of how durable a specific concrete is. However, the durability model established, which is the first module in the service life framework (see Fig. 1.2), will provide important information, that can be used to evaluate the service life of a concrete.

1.4 Concrete modeling tools

The research devoted to numerical modeling tools for concrete has been extended over the last 3-4 decades, where increasing computational power has enabled more complex problems to be solved within reasonable computational time. In general, the field of multi-physics modeling has gained currency and has become accepted as a reliable and useful tool in many industries. Modeling tools within concrete research are used for many different applications, e.g., a model by Svec et al. (2011) has been used to predict flow of fresh concrete with fiber reinforcement and a model for crack propagation in concrete is shown by Gasser and Holzapfel (2005). Modeling tools developed specific for concrete durability or/and service life predictions have been developed in terms of research models and more commercial models.

Modeling of the micro structural development during the hydration of concrete is not a direct indicator of durability or service life, but this has a significant influence on the physical processes involved in different durability aspects as described previously. For this reason, modeling of the cement paste micro structure is considered in different models. Examples of such models are HYMOSTRUCT, CEMHYD3D and μic proposed by van Breugel (1995), Bentz (1999) and Bishnoi and Scrivener (2009), respectively. The HYMOSTRUCT model assumes spherical cement particles and calculates the hydration of these to predict the cement paste micro structure. The model uses, i.a., the particle size distribution of the cement powder and the w/c ratio as input parameters and estimates the strength development and porosity as function of time (Van Breugel, 1995). The CEMHYD3D is a pixel based model where cellular automata is used to describe the micro structural development. The model uses information from digital scanning electron microscope (SEM)

images and particle size distributions of the cement. The model output is estimations of, i.a., strength development, percolation and diffusion properties. The `pic` model uses a spherical representation of the cement particles, with focus on computational speed and updated hydration rules compared to the `HYMOSTRUCT` model. The assumptions made in the above described models may be very rough, as for example the spherical representation and the hydration rules associated with these.

The most widely used engineering way to evaluate the concrete durability in aggressive environments is in terms of chloride ingress by using Fick's second law solved by the error function. The `ClinConc` model by Luping (2008) utilize the error function and extend the model by using a time-dependent diffusion coefficient (Luping and Gulikers, 2007) as well as a time dependent binding isotherm of chloride. This type of model is easy to solve numerically and this is properly the reason for the widespread use. The time dependent material properties used for, e.g., the diffusion coefficient and binding may not be strictly physical, seen from a mechanical and thermodynamic point of view. The time dependency is an attempt to invoke numerous of physical and chemical processes into one or more, reduction or accelerating functions.

The most commercialized service life prediction tool is properly `STADIUM` initiated by Samson et al. (1999a). `STADIUM` is one of the few service life modeling tools for concrete structures which has a graphical user interface, which makes it easy to use. The numerical model in the software package is based on solving differential equations which describes the mass transport in concrete coupled with chemical equilibrium. The model is capable of handling both saturated and non-saturated systems. The model uses the finite element method (FEM) as numerical solution method for the mass transport and the chemical equilibrium is calculated by the Newton's algorithm. The physical and chemical background of the model is described in different papers, e.g., Samson and Marchand (2007a, 1999); Samson et al. (1999a). The `STADIUM` software package offers to estimate the service life of a structure, both as a design tool for new structures but also for evaluation of the remaining service life of existing structures. Concrete cores from the existing structure are analyzed and the results are used as input values for the prediction of the remaining service life. The `STADIUM` software offers even further analysis of the structure than the service life prediction, such as, life-cycle costs analysis, based on different scenarios.

The `DuCom` (Durability CONcrete Model) code is a durability prediction tool for concrete structures that predicts the state of the concrete at a given time (Maekawa et al., 2008). The code has recently been extended to include features from the geochemical code `PHREEQC` and thereby solve coupled reactive transport problems, see Elakneswaran and Ishida (2013). The

mass transport is described by differential equations solved by the FEM. A DuCom durability calculation is initiated at the hydration of the cement and the output is given as, e.g., the degree of hydration, micro structure, distributions of moisture, pH in the pore water, corrosion rate, etc. The DuCom code includes mechanical actions in terms of, e.g., temperature and shrinkage effects, which introduces stress and strains. All the factors are included in an assembled durability calculation.

A reactive mass transport model for long term predictions of concrete is developed at Taiheiyo Cement in Japan and presented by Hosokawa et al. (2011). The model solves the mass transport differential equations by the FEM and utilize the features in PHREEQC as chemical equilibrium solver. The model uses the surface complexation equilibrium feature in PHREEQC to describe the C-S-H phase and determine the electrical double layer composition for this phase which enables, i.a., modeling of alkali binding. The model predicts the state of the concrete in terms of pore solution composition and amount of solid phases present.

A service life model for reinforced concrete structures is proposed by Baroghel-Bouny et al. (2009) where “durability indicators” are used as input in a service life estimation. The durability indicators are numerical durability models which offers different levels of detailing of ion ingress and moisture-ion transport. One level is a coupled reactive mass transport model solved by the Finite Volume Method (FVM). The model determines the service life of reinforced concrete from the chloride content determined by solving differential equations.

The models by Samson et al. (1999a), Elakneswaran and Ishida (2013), Hosokawa et al. (2011) and Baroghel-Bouny et al. (2009) are in the same category of multi-species reactive transport modeling of concrete. Different levels of calculations are offered by the models, from pure physical modeling showing the state of the material to life-cycle cost analysis. The models are seen as the state-of-art within multi-physics modeling of concrete although with different strengths and weaknesses in their current versions. The individual codes may focus on different parts, e.g., complete life cycle cost in STADIUM, hydration and structural considerations in DuCom, utilization of advanced chemical modeling in Hosokawa et al. (2011) and wetting and drying cycles in Baroghel-Bouny et al. (2009).

1.5 Concluding remarks

Concrete is widely used in different applications and a primary factor in the global CO₂ emission due to the extensive amount used per year. Infrastructure structures are responsible for a significant part of the amount of concrete used globally and it is therefore relevant to investigate optimal cement compositions in terms of increasing the service life of bridges, tunnels, etc. The service life in this work is investigated in terms of durability (or durability indicators adopting the terminology from Baroghel-Bouny et al. (2009)) where physical and chemical processes are described by modern continuum mechanic approaches. It is concluded that numerous of physical and chemical processes occurs over time and these are strongly coupled which results in non-linear numerical models. The concept for the numerical service life framework initiated in this work is shown in Fig. 1.2 where the reactive mass transport model established is the first durability indicator in the the service life framework. Different durability indicators may interact and the service life prediction becomes an iterative process between these. It is also concluded that the numerical service life framework is not complete in the sense that a limited number of physical and chemical processes are included.

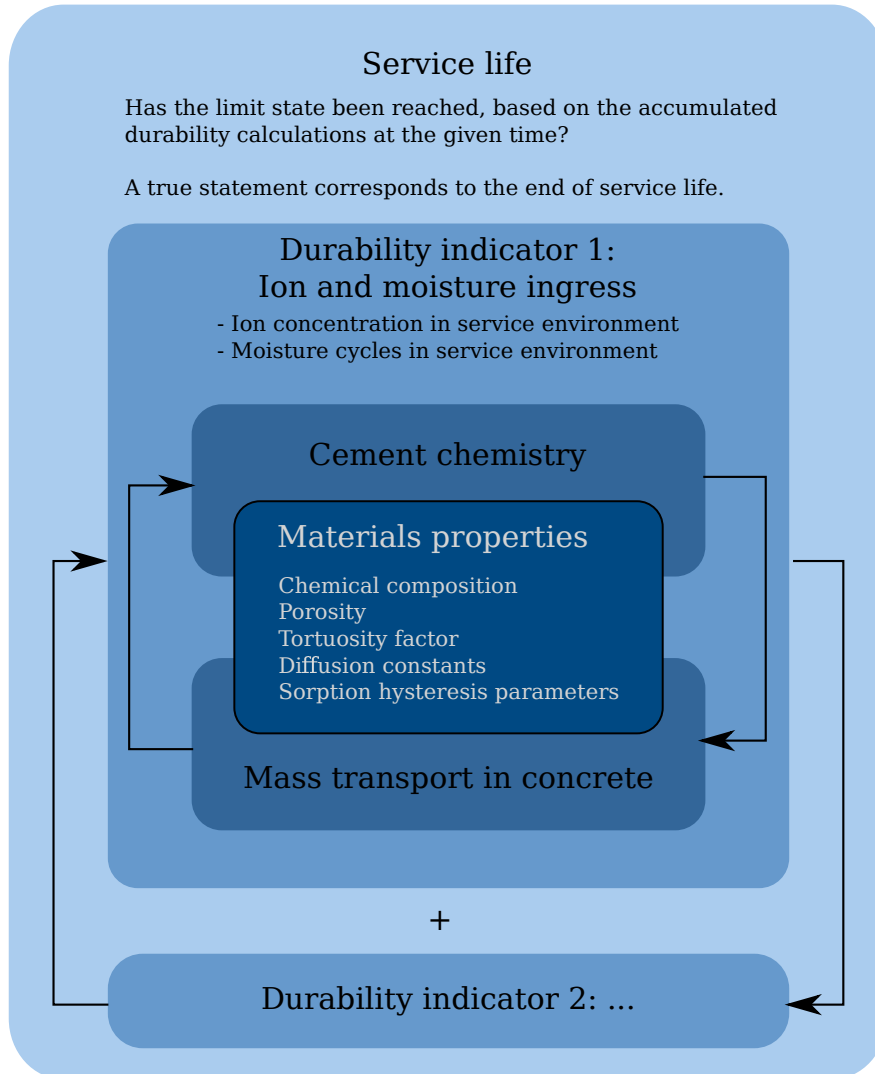


Figure 1.2: Schematic illustration of the connection between service life, durability and the modeling framework established in this project. The modeling framework includes the material properties, cement chemistry and mass transport which are coupled processes. The outcome of the framework is used to evaluate the durability for the specific problem, which may influence other durability aspects. The accumulated durability is used as basis for a service life estimation for the concrete in use.

Chapter 2

Numerical model description

2.1 Introduction of mixture theories

The complex durability aspects associated with concrete requires a sound theoretical background in order to incorporate all physical and chemical processes involved into a model. Modern continuum mixture theories are used in this work to define a set of balance laws, which together with appropriated constitutive assumptions yields the governing equation system. The different balance laws used are balance of mass, balance of momentum, balance of energy and an entropy inequality. The mixture theories are in general well suited for describing cement based materials as they are in the category of reacting porous media. The durability model established in this work compiles mass transport of ions, water and vapor and the chemical interactions into a non-linear coupled model. The solid phases are only accounted for in the chemical interactions with the liquid phase. It is important to note that the limited descriptions of the solid phases are a simplification as a description of stress and strains are not included. The term species used in this description corresponds to the term constituents used by other authors.

Two slightly different mixture theories are considered in this work, the classical single-phase mixture theory following the description of Bowen (1976) together with the review by Johannesson (1998) and the hybrid mixture theory (HMT) for multi-phase and multi-species mixtures following Bennethum and Cushman (2002b,a), the review by Johannesson (2010a) and lecture notes by Johannesson (2011b) from the course Introduction to Constitutive Theory and Continuum Physics with Numerical Applications using FEM at the Technical University of Denmark Department of Civil Engineering. Other related supplementary work used are Ristinmaa and Ottosen (2010); Tadmor et al. (2012); de Groot and Mazur (1984); Bear and Bachmat (1990);

Griffiths and College (1999).

The basic concept of mixture theory is shown schematically in Fig. 2.1 where the different levels, for which the balance laws are defined according to multi-phase and multi-species mixture theory. The whole mixture level, is in fact described by balance laws equivalent to classical continuum theories. The phase level, represents the different phases building up the whole mixture, typically consisting of solid, liquid and gaseous phases. The phases have a clear distinct boundary in the representative volume as illustrated on the dashed borderline between the whole mixture and the phase level in Fig. 2.1. The species level, is the species building up the individual phases. Contradictory to the phases the species are characterized by no distinct borders between the species. Conservations of the balance laws are obtained by a summation of all species for each phase and also a summation of all phases which yields the whole mixture. The summations of the balance laws on phase and species levels are used to obtain criteria for the exchange terms in the balance laws for the different levels. Exchanges of physical quantities are allowed to exist between phases on the phase level and between species on the species level. Exchange actions are also allowed among the species found in the different phases.

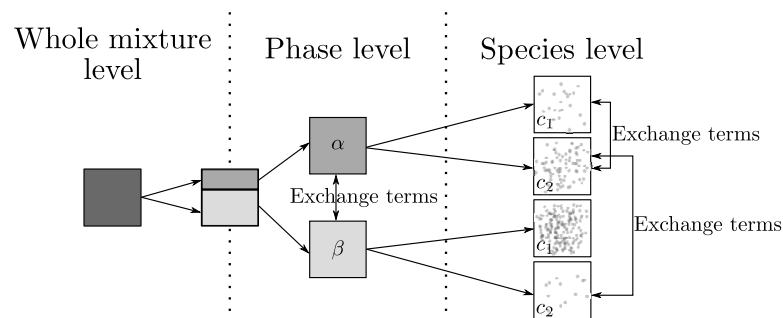


Figure 2.1: Multi-phase and multi-species mixture theory illustration. The different levels for which the balance equations are defined are shown and the exchange terms between these.

The multi-phase and multi-species mixture theory approach leads to a rather complex set of balance definitions which are shown in details in App. A.2 and A.3. The balance equations for the more simple single-phase mixture theory are shown in details in App. A.1. Detailed mathematical steps are shown in the appendixes for the relation between the balance laws at the different levels. The detailed study emphasizes criteria related to the exchange terms. The use of the balance laws and constitutive assumptions, to reach the governing equations for a reactive mass transport model are shown in the following sections using the single phase mixture theory. The derivation of

multi-phase and multi-species governing equations are in many parts similar but includes more mathematical steps which are briefly discussed in App. A.3.10.

2.1.1 Balance equations and mixture theory results

Essential mixture theory results in terms of restrictions on the exchange terms for a single-phase case are shown in the following section. A single-phase mixture, following Fig. 2.1 is to consider, e.g., the α phase as the whole mixture and only consider the exchange term on the species level. An extensive review showing all essential mathematical steps to obtain the results given here is shown in App. A.1.

The spatial position \mathbf{x} of a particle is described by the particle motion function χ_j which is defined as $\mathbf{x} = \chi_j(\mathbf{X}_j, t)$, where \mathbf{X}_j is the material coordinate and t is the time. In this case, the species are ions in the pore solution and it is therefore convenient to write the balance laws in terms of the ion concentration. The density of species j is defined as $\rho_j = \rho_j(\mathbf{x}, t)$, which leads to the species concentration $c_i = c_i(\mathbf{x}, t) = \rho_j/\rho$, where ρ is the density for the whole mixture.

Mass balance equations for the species and the whole mixture are defined where the mass balance for the species accounts for mass exchange between the species in terms of the property \hat{c}_j . The local form of the mass balance postulate for the species, is

$$\frac{\partial \rho_j}{\partial t} + \text{div}(\rho_j \mathbf{x}'_j) = \hat{c}_j \quad (2.1.1)$$

where \mathbf{x}'_j is the velocity of the j 'th species and t is time. The local form of the mass balance postulate for the whole mixture is

$$\frac{\partial \rho}{\partial t} + \text{div}(\rho \mathbf{x}') = 0 \quad (2.1.2)$$

where \mathbf{x}' is the velocity of the whole mixture which is defined as the mass weighted average of the species velocities. The balance equations (2.1.1) and (2.1.2) are rewritten into compatible versions, which yields a criteria for the mass exchange terms as

$$\sum_{j=1}^N \hat{c}_j = 0 \quad (2.1.3)$$

which is (A.1.43) repeated. The exchange term \hat{c}_j is in this case the chemical interactions in the reactive transport model where the criteria (2.1.3) must be fulfilled. An important rewriting, is the species mass balance law (2.1.1)

written in terms of the materials derivative for the mixture $\frac{D}{Dt}$ and the diffusion velocity \mathbf{u}_j which is defined as $\mathbf{u}_j(\mathbf{x}, t) = \mathbf{x}'_j(\mathbf{x}, t) - \mathbf{x}'(\mathbf{x}, t)$. The mass balance law for the species, using the material derivative, can be formulated as

$$\rho \frac{Dc_j}{Dt} = -\text{div}(\rho_j \mathbf{u}_j) + \hat{c}_j \quad (2.1.4)$$

which is (A.1.47) repeated.

The balance of momentum is described in terms of angular momentum and linear momentum. The angular momentum is conserved by assuming that the stress tensor \mathbf{T} for the whole mixture is symmetric. The symmetry condition is deduced from the postulate of angular momentum balance. The local form of the angular momentum postulate for the whole mixture is

$$\frac{\partial}{\partial t}(\mathbf{x} \times \rho \mathbf{x}') = -\text{div}(\rho(\mathbf{x} \times \mathbf{x}') \otimes \mathbf{x}') + \text{div}(\mathbf{x} \times \mathbf{T}) + \rho \mathbf{x} \times \mathbf{b} \quad (2.1.5)$$

where \mathbf{b} is the external body force density. The symmetry condition for the stress tensor is

$$\mathbf{T} = \mathbf{T}^T \quad (2.1.6)$$

which is (A.1.67) repeated.

The linear momentum balance is described in terms of compatible balance equations for the species and the whole mixture. The linear momentum balance of the species includes a momentum supply term $\hat{\mathbf{p}}_j$ accounting for interaction with other species and a supply involving the mass exchange term, that is $\hat{c}_j \mathbf{x}'_j$. The local form of the linear momentum postulate for the species is

$$\frac{\partial \rho_j \mathbf{x}'_j}{\partial t} = -\text{div}(\rho_j \mathbf{x}'_j \otimes \mathbf{x}'_j) + \text{div} \mathbf{T}_j + \rho_j \mathbf{b}_j + \hat{\mathbf{p}}_j + \hat{c}_j \mathbf{x}'_j \quad (2.1.7)$$

The local form of the postulate for the whole mixture is

$$\rho \frac{D\mathbf{x}'}{Dt} = \text{div} \mathbf{T} + \rho \mathbf{b} \quad (2.1.8)$$

In order to make the linear momentum balance postulate for the species compatible with the whole mixture, the following must hold

$$\sum_{j=1}^N (\hat{c}_j \mathbf{u}_j + \hat{\mathbf{p}}_j) = \mathbf{0} \quad (2.1.9)$$

which is (A.1.84) repeated. Note that the momentum contribution involving the mass supply $\hat{c}_j \mathbf{u}_j$ is written in terms of the diffusion velocity \mathbf{u}_j in order to be compatible with the mass balance (2.1.4).

The energy balance is described by a balance postulate for the species and a postulate for the whole mixture. The energy balance for the species level includes supply generated by the mass exchange term and the momentum supply from other species. Furthermore, the interaction energy \hat{e}_j from the species are included as a part of the energy balance. The local form of the energy balance postulate for j 'th species is

$$\begin{aligned} \frac{\partial}{\partial t} \rho_j \left(e_j + \frac{1}{2} (x'_j)^2 \right) \\ + \operatorname{div} \left(\rho_j \left(e_j + \frac{1}{2} (x'_j)^2 \right) \mathbf{x}'_j \right) = \operatorname{div} \left(\mathbf{T}_j^T \mathbf{x}'_j - \mathbf{q}_j \right) + \rho_j r_j \\ + \rho_j \mathbf{x}'_j \cdot \mathbf{b}_j + \mathbf{x}'_j + \mathbf{x}_j \cdot \hat{\mathbf{p}} + \hat{e}_j + \hat{c}_j \left(e_j + \frac{1}{2} (x'_j)^2 \right) \end{aligned} \quad (2.1.10)$$

The local energy balance postulate for the whole mixture is

$$\rho \frac{D}{Dt} \left(e + \frac{1}{2} \dot{x}^2 \right) = \operatorname{div} \left(\mathbf{T} \mathbf{x}' - \mathbf{q} \right) + \rho r + \sum_{j=1}^N \left(\rho_j \mathbf{x}'_j \cdot \mathbf{b}_j \right) \quad (2.1.11)$$

Comparison of the species postulate and the whole mixture postulate yields a criteria for the summation of the supply terms, as

$$\sum_{j=1}^N \left(\hat{c}_j \left(\frac{1}{2} u_j^2 + e_j \right) + \mathbf{u}_j \cdot \hat{\mathbf{p}}_j + \hat{e}_j \right) = 0 \quad (2.1.12)$$

which is (A.1.132) repeated.

The entropy inequality postulate is defined for the whole mixture. Different versions of the inequality can be derived as shown in App. A.1.5. The entropy inequality used here is written in terms of the inner Helmholtz internal free energy density $\psi_{\mathbf{I}}$ which is defined as $\psi_{\mathbf{I}} = e_{\mathbf{I}} - \eta\theta$, where $e_{\mathbf{I}}$ is the inner internal energy, η is the entropy and θ is the temperature which is assumed to be the same for all species for this case. The single temperature entropy inequality from which the governing equation is deduced is

$$\begin{aligned} 0 \leq \rho \left(-\eta \frac{D\theta}{Dt} - \frac{D\psi_{\mathbf{I}}}{Dt} + \sum_{j=1}^N \frac{Dc_j}{Dt} \mu_j \right) - \sum_{j=1}^N \rho_j \mathbf{u}_j \cdot \left[\theta \operatorname{grad} \left(\frac{1}{\theta} \left(\mu_j + \frac{1}{2} u_j^2 \right) \right) \right. \\ \left. - \mathbf{b}_j + \frac{D\mathbf{u}_j}{Dt} \right] - \sum_{j=1}^N \left(\mu_j + \frac{1}{2} u_j^2 \right) \hat{c}_j + \operatorname{tr}(\mathbf{T}\mathbf{L}) - \frac{\mathbf{q}}{\theta} \cdot \operatorname{grad}(\theta) \end{aligned} \quad (2.1.13)$$

which is (A.1.182) repeated.

2.1.2 Constitutive theory for reacting systems

The entropy inequality is used to derive the governing equation based on a specific choice of the inner Helmholtz energy. Reacting mixtures are considered in this case, where the inner Helmholtz energy is constituted as

$$\psi_{\mathbf{I}} = \psi_{\mathbf{I}}(\theta, \rho, c_1, \dots, c_N) \quad (2.1.14)$$

A differentiation of (2.1.14) is needed in order to evaluate each term in the entropy inequality (2.1.13). The differentiation is

$$\frac{D\psi_{\mathbf{I}}}{Dt} = \frac{\partial\psi_{\mathbf{I}}}{\partial\theta} \frac{D\theta}{Dt} + \frac{\partial\psi_{\mathbf{I}}}{\partial\rho} \frac{D\rho}{Dt} + \sum_{j=1}^N \frac{\partial\psi_{\mathbf{I}}}{\partial c_j} \frac{Dc_j}{Dt} \quad (2.1.15)$$

Each of the terms in (2.1.13) are evaluated separately with the inner Helmholtz energy in order to validate the inequality. The different parts are denoted with 'case' here, in a sense that all statements in the cases must be fulfilled.

Case 1:

The terms involving the material derivative of the temperature in (2.1.13) are considered together with (2.1.15), that is

$$0 \leq -\rho \frac{D\theta}{Dt} \left(\eta + \frac{\partial\psi_{\mathbf{I}}}{\partial\theta} \right) \quad (2.1.16)$$

where it is seen that the classical definition of the entropy η is obtained as $\eta = -\frac{\partial\psi_{\mathbf{I}}}{\partial\theta}$, for arbitrary temperature variations.

Case 2:

The terms involving the material derivative of the concentration is considered, that is

$$\rho \sum_{j=1}^N \frac{Dc_j}{Dt} \left(\mu_j - \frac{\partial\psi_{\mathbf{I}}}{\partial c_j} \right) \quad (2.1.17)$$

where the definition for the chemical potential μ_j is obtained as $\mu_j = \frac{\partial\psi_{\mathbf{I}}}{\partial c_j}$, for arbitrary concentration variations.

Case 3:

Consider the terms involving the density of the system ρ together with the term $\text{tr}(\mathbf{TL})$, that is

$$0 \leq -\rho \left(\frac{\partial \psi_{\mathbf{I}}}{\partial \rho} \frac{D\rho}{Dt} \right) + \text{tr}(\mathbf{TL}) \quad (2.1.18)$$

The total stress tensor is assumed to be equal to the hydrostatic pressure, $\mathbf{T} = -\pi \mathbf{I}$. The following relation will be used

$$\text{tr} \mathbf{L} = \text{div}(\mathbf{x}') = \frac{D\rho}{Dt} \frac{1}{\rho} \quad (2.1.19)$$

where the mass balance for the whole mixture (A.1.42) was used. Using (2.1.19) and the stress tensor assumption in (2.1.18), yields the condition involving the time derivative of the density of the mixture, as

$$0 \leq \frac{D\rho}{Dt} \left(-\rho^2 \frac{\partial \psi_{\mathbf{I}}}{\partial \rho} + \pi \right)$$

where it is concluded that the total hydrostatic pressure needs to be defined as: $\pi = \rho^2 \frac{\partial \psi_{\mathbf{I}}}{\partial \rho}$, for cases when the mixture density is allowed to change arbitrarily.

Case 4:

The last term on the right hand side of (2.1.13) is considered in order to obtain Fourier's Law. The term considered is

$$0 \leq -\frac{\mathbf{q}}{\theta} \cdot \text{grad}(\theta) \quad (2.1.20)$$

This part of the inequality is valid, using a specific choice of \mathbf{q} , which is Fourier's Law, given as

$$\mathbf{q} = -\lambda \text{grad}(\theta) \quad (2.1.21)$$

This specific constitutive relation will assure that the quadratic terms in 2.1.20 fulfill the inequality dissipation.

Case 5:

In order to obtain a generalized Fick's law, the following part of (2.1.13) is considered

$$0 \leq -\rho_j \mathbf{u}_j \cdot \left[\theta \text{grad} \left(\frac{1}{\theta} \left(\mu_j + \frac{1}{2} u_j^2 \right) \right) - \mathbf{b}_j + \frac{D\mathbf{u}_j}{Dt} \right] \quad (2.1.22)$$

It is assumed that the terms u_j^2 , \mathbf{b}_j and $\frac{D\mathbf{u}_j}{Dt}$ are negligible so the inequality 2.1.22 reduces to

$$0 \leq -\rho_j \mathbf{u}_j \cdot \theta \text{grad} \left(\frac{1}{\theta} \mu_j \right) \quad (2.1.23)$$

in which the choice of the diffusion velocity $\mathbf{u}_j = -D_j \text{grad}(\mu_j)$ will fulfill the inequality. In order to obtain a generalized version of Fick's law consider the potential defined as $\mu_j = \mu_j^0 + R\theta \ln(\rho_j \gamma)$ where μ_j^0 is the reference potential, R is the universal gas constant, γ is the activity coefficient and the product $\rho_j \gamma$ can be interpreted as the activity a_j of the species. The activity is often used in chemical equilibrium calculations. Using the constituted chemical potential for the choice of diffusion velocity \mathbf{u}_j and assuming constant temperature θ , yields

$$\rho_j \mathbf{u}_j = -D_j R \theta \left(\text{grad}(\rho_j) + \frac{\rho_j}{\gamma} \text{grad}(\gamma) \right) \quad (2.1.24)$$

If the density for the whole mixture ρ is assumed constant and the relation $\rho_j = \rho c_j$ is used on the right hand side of (2.1.22), and consequently the following is obtained

$$\rho_j \mathbf{u}_j = -D_j R \theta \rho \left(\text{grad}(c_j) + \frac{c_j}{\gamma} \text{grad}(\gamma) \right) \quad (2.1.25)$$

Combining (2.1.25) with the mass balance (A.1.47) yields

$$\begin{aligned} \rho \frac{\partial c_j}{\partial t} + \rho \dot{\mathbf{x}} \cdot \text{grad}(c_j) = \\ - \text{div} \left(-D_j R \theta \rho \left(\text{grad}(c_j) + \frac{c_j}{\gamma} \text{grad}(\gamma) \right) \right) + \hat{c}_j \end{aligned} \quad (2.1.26)$$

It is convenient to rewrite (2.1.26) in terms of molar concentration \tilde{c}_j by the relation $\tilde{c}_j = c_j \rho / M_j$ where M_j is the molar mass. Furthermore, the diffusion coefficient D_j^* is defined as $D_j^* = D_j R \theta$, hence, one obtain

$$\frac{\partial \tilde{c}_j}{\partial t} = -\text{div} \left(-D_j^* \left(\text{grad}(\tilde{c}_j) + \frac{\tilde{c}_j}{\gamma} \text{grad}(\gamma) \right) \right) - \dot{\mathbf{x}} \cdot \text{grad}(\tilde{c}_j) + \hat{\tilde{c}}_j \quad (2.1.27)$$

It is very important to note that any charge, generated when considering charged species such as ions, is not considered in the formulation (2.1.27). The derivation of the diffusion equation (2.1.27) in terms of the the classical chemical potential was shown to emphasize the close relation between the diffusion and chemistry as this definition for chemical activity lead to the

classical definition of the mass action law for solving chemical equilibrium. In order to introduce a term accounting for charge balance in the concept of mixtures, comprehensive derivations and assumptions are needed, e.g., see Bennethum and Cushman (2002a,b); Johannesson (2010a). The Nernst-Planck equation, accounting for diffusing charged species, is obtained by defining the electrochemical potential as $\mu_j = \mu_j^0 + R\theta \ln(\rho_j\gamma) + Fz_j\Phi$ where F is Faraday's constant, z_i is the valence state of a charged species and Φ is the electrical potential (or streaming potential). This invoke an additional term in (2.1.27) as

$$\frac{\partial \tilde{c}_j}{\partial t} = -\text{div} \left(-D_j^* \left(\text{grad}(\tilde{c}_j) + \frac{\tilde{c}_j}{\gamma} \text{grad}(\gamma) + \frac{F}{R\theta} z_j \tilde{c}_j \text{grad}(\Phi) \right) \right) - \dot{\mathbf{x}} \cdot \text{grad}(\tilde{c}_j) + \hat{\tilde{c}}_j \quad (2.1.28)$$

It should be carefully noted that the derivations made here is based on the specific choice of the Helmholtz free energy (2.1.14) which does not include the electric potential Φ . Of this reason the theory used here cannot define the electrical potential in terms of the inner Helmholtz free energy. More importantly, in the format used here, it is not possible to check that the Nernst-Planck equation fulfill the entropy inequality.

Case 6:

The terms involving the chemical interactions \hat{c}_j in the adopted inequality (2.1.13) is considered next. As in Case 5 it is assumed that u_j^2 is negligible and the part examined is reduced to

$$0 \leq - \sum_{j=1}^N \hat{c}_j \mu_j \quad (2.1.29)$$

In order to facilitate a direct relation to chemical reaction schemes, the condition described in (2.1.29) is reformulated into a matrix notation $\sum_{j=1}^N \hat{c}_j \mu_j = \hat{\mathbf{c}}^* \cdot \boldsymbol{\mu}^*$. The j species considered in the mass exchange term \hat{c}_j are related to r chemical reactions of the system with a stoichiometric matrix \mathbf{V}^* and a reaction rate vector \mathbf{j}^* . The mass exchanges is described as

$$\hat{\mathbf{c}}^* = \mathbf{V}^* \mathbf{j}^* \quad (2.1.30)$$

The stoichiometric matrix \mathbf{V}^* is constructed so that $\sum_{j=1}^N V_{ji} = 0$, that is, a stoichiometric normalization. The constitutive equation for the reaction rates \mathbf{j}^* leading to the classical equilibrium chemistry approach, is

$$\mathbf{j}^* = \mathbf{L}^* \mathbf{V}^{*\text{T}} \boldsymbol{\mu}^* \quad (2.1.31)$$

where the diagonal terms of \mathbf{L}^* are rate constants for each reaction considered. Setting all \mathbf{j}^* values to zero corresponds to chemical equilibrium which is the condition used in chemical equilibrium codes such as PHREEQC and GEM-Selektor. The solution to this is basically a minimization problem. Combining (2.1.30) and (2.1.31) yields kinetic constitutive relations for the mass gain/loss of the species of the system, as

$$\hat{\mathbf{c}}^* = \mathbf{V}^* \mathbf{L}^* \mathbf{V}^{*\text{T}} \boldsymbol{\mu}^* \quad (2.1.32)$$

By inserting (2.1.32) in the inequality (2.1.29), will assure fulfillment of the inequality by noting that the dot product of $\boldsymbol{\mu}^*$ is always positive and making sure that $\mathbf{V}^* \mathbf{L}^* \mathbf{V}^{*\text{T}}$ is positive definite by using a proper choice of \mathbf{L} , that is

$$0 \leq (\mathbf{V}^* \mathbf{L}^* \mathbf{V}^{*\text{T}} \boldsymbol{\mu}^*) \cdot \boldsymbol{\mu}^* \quad (2.1.33)$$

It is important to realize that (2.1.32) is not uniquely defined in the sense of determining the chemical potential from the known values of the chemical reaction rates and stoichiometric relations of the reactions.

2.1.3 Concluding remarks

The derivations shown in Secs. 2.1.1 and 2.1.2 and App. A do not contribute with further development of the mixture theory, the HMT or the governing equations compared to the indicated reference papers. The derivations shows the concept of the mixture theory and the HMT which are non-standard approaches within concrete durability modeling. The further development of the service life framework should follow these or similar concepts in order to ensure a sound thermodynamic description, which motivates the detailed description of the balance laws for both the mixture theory and the HMT. Studying the mixture theories in App. A helps to understand the complexity of a material like concrete. It is generally accepted that concrete is a complex material and the physical and chemical interactions are strongly coupled, but studying these couplings in terms of mathematical equations underlines this complexity.

The governing equation system for the coupled reactive mass transport model used in this work is described in Paper I. The derived Nernst-Planck equation (2.1.28) is extended further by a Poisson equation enforcing charge balance in the pore solution and a two phase liquid and vapor transport model accounting for sorption hysteresis.

2.2 Numerical methods

The numerical solution of the coupled reactive mass transport system considered in this work, involves different approaches. The differential equations for the mass transport part of the durability model are solved by FEM, but other approaches like the finite volume approach, different iterative methods, the lattice Boltzmann method, etc. are suggestions of other available numerical methods. The mass transport and the chemical equilibrium is decoupled for the numerical solution in this work, facilitated by an operator splitting approach, which is often used for solving reactive transport models. Chemical equilibrium is often formulated as a minimization problem, where the most used approaches are the mass action law (MAL) and the Gibbs energy minimization (GEM).

2.2.1 Mass transport

The governing mass transport equations employed in the durability model are solved by the FEM. A detailed formulation of the discrete system is shown in Paper I and therefore not repeated in details here. The FEM is widely used for solving mass transport systems and in general multi-physics problems due to its general robustness. Other durability models for concrete that are solved by the FEM are for instance Samson et al. (1999b) and Hosokawa et al. (2011).

The FE formulation presented in Paper I shows the governing equations in a strong form, which are derived from the HMT. The equations presented in strong form are rewritten into a weak form, primarily by multiplying two arbitrary weight functions and use the Green-Gauss method to rewrite the surface integrals. The state variables in the weak form are discretized by a linear expansion and the spatial weight function is discretized according to the Galerkin's method. The global mass matrix, stiffness matrix and load vector are constructed and the discrete system is solved as an initial value problem by a one-dimensional single parameter time stepping scheme.

Other numerical methods for solving differential equation systems are available such as the classical finite volume method (FVM) and the finite difference method. More recently the lattice Boltzmann method (LBM) has proven to be a valuable method in terms of its computational speed. The FVM is employed in different numerical models for ion and moisture transport in concrete. The method is used by Mainguy and Ulm (2001) for coupled diffusion-dissolution processes in reactive porous media, separated by a fracture channel and by Mainguy and Coussy (2000) for solving a more simple concrete degradation model. The FVM is chosen by Mainguy and

Ulm (2001) due to its ability to handle a sharp dissolution front. The FVM is also employed by Nguyen et al. (2006, 2008) where coupled ion and moisture transport is modeled. The module based reactive mass transport model HYTEC by Van Der Lee et al. (2003) has a transport module using the FVM for solving mass transport equations where it is emphasized that the FVM is useful for problems with variable porosity.

The use of the LBM as a numerical solver has increased over the last decade, especially within the field of fluid dynamics see, e.g., Svec et al. (2011). The fundamental idea of the LBM is to construct simplified kinetic models that incorporates the essential physics of microscopic and mesoscopic processes so that macroscopic averaged properties obeys the desired macroscopic equations (Chen and Doolen, 1998). The LBM is also used in, e.g., advection-diffusion problems which is related to concrete durability see Mohamad (2011) and for solving electro-diffusion problems described by the Nernst-Planck equation as in Minussi et al. (2013). Recently the LBM has been used by Patel et al. (2014) to solve the mass transport of a multi-species system in a reactive mass transport model. The chemical reactions in Patel et al. (2014) are solved by the geochemical code PHREEQC, which is a similar approach to the reactive mass transport models solved by the FEM together with an operator splitting approach. One of the main reasons for using the LBM is the computational efficiency and ease of parallelization, which also is emphasized as an advantage by Patel et al. (2014).

The numerical methods highlighted here have advantages that could be utilized in the durability model in this work, e.g. the FVM with its ability to handle variable porosity and the computational speed by LBM. The computational speed is of great interest for durability simulations of concrete due to the requirements of long term reactive multi-species simulations.

2.2.1.1 FEM development

The FE scheme, established in this work, is based on simple linear discretization in both the spatial domain and the time domain. The FEM offers a range of extensions of the computational scheme in order to minimize numerical errors and optimize computational speed, see e.g., Larson and Bengzon (2010). The suggestions for further development of the FE scheme given here is based on the experience obtained during development and testing of the model.

The current version of the FEM may be referred to as the h -version of the FEM where the only way to minimize the numerical error, introduced by the discretization, is by increasing the number of spatial elements. A fine mesh is needed in the current version of the durability model when a non-saturated system is exposed to a fully saturated boundary condition as shown

in Paper I. The mesh refining increases the computational time significantly when chemical equilibrium is included, as chemical equilibrium is calculated at each node. It is often a limited part of the spatial domain which needs the fine discretization in this type of problems and for that reason the adaptive mesh refinement method could be valuable in terms of optimizing the mesh. Another FEM extension is the p -version of the FEM, which can be combined with the h -versions. In the p -version, the order of the element polynomial is increased to obtain convergence. Higher order elements could be useful when the operator splitting method is used between the mass transport and chemical equilibrium. The calculated chemical equilibrium concentrations are used as initial values in the next time step and the concentrations may have steep gradients over single elements in the spatial domain. Higher order polynomials may describe these transition zones in a more smooth manner.

2.2.2 Operator splitting method

The reactive mass transport model is decoupled in the numerical scheme by an operator splitting method in order to solve the chemical equilibrium separately. For this matter instantaneous chemical reactions are assumed. Split operator approaches are widely used in reactive mass transport modeling, see an extensive list of papers in Simpson and Landman (2007). Different approaches for using the split operator has been proposed, a review of some of these is given by Carrayrou et al. (2004). The two most common approaches used in reactive mass transport modeling are the iterative and non-iterative method. The iterative method iterates between the mass transport and chemical equilibrium until convergence for a given time step. The non-iterative approach uses the result from the mass transport step as input values and calculates a new equilibrium state which is the overall result for the time step. The non-iterative method is used in two ways, either by a mass transport calculation followed by chemical equilibrium calculation or a chemical equilibrium calculation followed by a mass transport calculation. The non-iterative split operator approach introduces numerical errors at the boundary and in the spatial domain which is analyzed by Simpson and Landman (2007). The time step length in the numerical scheme should be sufficiently small in order to reduce the error. Errors introduced by the operator splitting is not explicitly evaluated and corrected for in this work.

2.2.3 Chemical equilibrium solvers

Chemical equilibrium in reactive mass transport models for cement based materials is often solved by geochemical equilibrium codes together with an

thermodynamic database valid for cement chemistry. Chemical equilibrium is calculated by the MAL approach in the durability model. A review of the MAL approach is given in Paper II and III, based on the PHREEQC manual by Parkhurst et al. (1999) and the more general description by Bethke (1996). The review in Paper II describes the MAL equations for aqueous reactions, pure phase reactions and solid solution reactions. The review in Paper II is extended in Paper III by a description of the surface complexation reactions and an estimation of the electrical double layer (EDL) ion composition. The ability to handle surface complexations and estimate the EDL on surfaces is one of the main reasons for using PHREEQC in this work.

The FE discretization and the operator splitting approach enables the use of different chemical equilibrium solvers, where the chemical composition is given as input and return a new chemical equilibrium state in terms of concentrations of the ions in the pore solution. A chemical equilibrium solver method which is widely used in cement chemistry is the GEM approach, which is implemented in the GEM-Selektor software, Kulik et al. (2003). The GEM algorithm (GEMS3K) in GEM-Selektor has recently been improved and a review of the numerical scheme is given by Kulik et al. (2013). The GEMS3K is now available in a version for coupling to mass transport codes which is of great interest for the future development of this service life framework.

The thermodynamic theoretical background for calculating chemical equilibrium, using either the MAL or GEM is in general the same so two identical systems solved by the two methods should in theory give the same result. The deviations between the two methods are found in the numerical schemes and algorithms, some of these deviations are highlighted by Kulik et al. (2013). One of the advantages of the GEM approach is the stability in finding assemblages by minimizing the total Gibbs energy while maintaining a detailed mass balance (Kulik et al., 2013), whereas a stable composition must be known using the MAL approach by, e.g., PHREEQC. The GEM approach is on the other hand, according to Kulik et al. (2013), 2-10 times slower than the MAL approach. Stability and computational speed are some of the most important considerations in reactive mass transport modeling and pros and cons for the two methods discussed here needs to be continuously evaluated in relation to the overall service life framework.

The chemical equilibrium solution is strongly dependent on the thermodynamic database used in the calculation. The current version of the durability model uses the standard databases *preeqc.dat* and *wateq4f.dat* from PHREEQC for the aqueous reactions, with additional solid phase dissolution reactions found mainly in the Cemdata07 database (Möschner et al., 2009; Schmidt et al., 2008; Möschner et al., 2008; Lothenbach et al., 2008; Lothenbach and

Winnefeld, 2006; Jacques, 2008) and from the work by Balonis et al. (2010). The solid phases reactions used in the numerical examples in the Papers II, III and VI are shown in their respective appendix sections. Some of the published thermodynamic databases like the Cemdata07 are continuously updated in terms of dissolution reactions and their corresponding equilibrium constants. It is therefore important that the durability model established is adaptable for these updates and not fixed to a single chemical model.

2.2.4 Implementation of computer code

The FE scheme for the durability model described in Paper I is implemented in a computer based algorithm. The algorithm is coded from scratch which have advantages and disadvantages. All the details in the algorithm is known and will ease a debugging process. It is relatively time consuming to code all parts of such algorithm, like simple meshing algorithms but on the other hand to acquaint oneself in larger existing software packages is also time consuming.

The scientific programming language Matlab is used due to its ease of use in matrix computations and it was found sufficiently fast for the one-dimensional FEM used in this work. The computational speed is an important factor when solving multi-physics problems, especially when long term non-linear problems are considered and 2D/3D simulations are of interest. The matrices in the algorithm is constructed as sparse matrices. The algorithm has continuously been evaluated, during the development, using the build-in profiling tool in Matlab in order to optimize the speed of the established functions.

Other high-level scripting languages like C++ can be considered in future versions for computational speed and utilization of existing FEM software packages that are available like FreeFem++, Elmer, MOOSE, OOFEM, etc. Commercial programs like Comsol and ANSYS could also be considered as numerical solver software in future versions. Some of the advantages of using existing software packages are that for instance basic meshing algorithms are established and special features like adaptive mesh refinement are implemented in some of these and the effect of these features can easily be tested with a given problem.

Chemical equilibrium is solved by using the geochemical code PHREEQC where the interface version IPHREEQC (Charlton and Parkhurst, 2011) is utilized. This part of the algorithm is based on the IPHREEQC version 3.1.2 and compiled with the GNU gcc/g++ 4.4 compiler for Linux. The C++ library of IPHREEQC is called from Matlab where the input statements for the chemical equilibrium calculation are generated. The advantage of using

the IPHREEQC interface is the direct call to the input and output functions in the library, whereas the use of the batch version of PHREEQC requires file exchanging. Solving the chemical equilibrium is by far the most computationally costly as 90-95% of the total computational time is consumed by this part. Chemical equilibrium is solved for each spatial node by a simple loop routine, which facilitates that this function could run in parallel.

A parallel version of the Matlab calls to IPHREEQC has been studied and the computational time was reduced in a constructed beta version. The actual parallel loop in Matlab was stable but some problems with the library calculations were detected. The primary issue with the parallel version was that some FE nodes did not converge in the IPHREEQC calculation, even though the non-parallel version was able to find a solution for the same FE node. The beta version was not developed further and not used for the simulations performed. The latest versions of the IPHREEQC library have special “modify” commands which should facilitate the coupling to, e.g., mass transport algorithms and these should be considered in future versions of the durability model.

2.2.5 Pseudo code of the framework algorithm

The main parts of the algorithm are presented in pseudo format in Alg. 1 to 4. The parts concerning the mathematical operations are shown in the pseudo code. The algorithm is constructed so that all input parameters are defined in an input file in order to easily examine different numerical settings and material configurations. All kinds of input data validation are left out, mesh generation procedures and details regarding the assembling of local FE matrices in the global FE system are left out.

Algorithm 1

An essential part of the algorithm is shown in Alg. 1, where the finite element time stepping scheme is implemented in the for-loop at line 5. The input parameters have been validated and the initial global matrices have been established prior to the entry of the for-loop. The linear matrix system is solved for the current time step, with the applied boundary conditions at line 9 and the result vector \mathbf{a}_{n+1} is updated with the new solution. The non-linear parts of the matrix system are updated to the current state by calling the function *matrix_assemble* at line 10. The Newton–Raphson optimization function *improve_solution* is called at line 13, if the variable ‘NewtonRaphson’ is true and the time stepping parameter is one, tested at line 12. The output of the *improve_solution* is an updated result vector \mathbf{a}_{n+1} .

Algorithm 1 Main multi-physics solver

```

1  def: (int)TimeSteps  $\Delta t/t_{total}$ ;
2  def: (bool)NewtonRaphson;
3  def: (bool)ChemicalEquilibrium;
4
5  for k = 1:TimeSteps
6       $\mathbf{K}^* = \mathbf{C}/\Delta t + \mathbf{K}\theta$ 
7       $\mathbf{F}^* = (\mathbf{C}/\Delta t - \mathbf{K} + \mathbf{K}\theta) \mathbf{a}_n$ 
8
9       $[\mathbf{a}_{n+1}, \mathbf{f}] = solve(\mathbf{F}^*, \mathbf{K}^*, \mathbf{f}_b)$ ;
10     matrix_assemble( $\mathbf{K}, \mathbf{C}$ );
11
12     if NewtonRaphson and  $\theta == 1$ 
13         improve_solution( $\mathbf{K}, \mathbf{C}, \mathbf{a}_n, \mathbf{a}_{n+1}$ );
14     end
15
16     if ChemicalEquilibrium
17         solve_chemical_equilibrium( $\mathbf{a}_{n+1}$ );
18     end
19
20      $\mathbf{a}_n = \mathbf{a}_{n+1}$ 
21 end

```

The variable `NewtonRaphson` is a setting that enables/disables the Newton-Raphson optimization routine. Chemical equilibrium is calculated by calling the function `solve_chemical_equilibrium` at line 17 and the result vector \mathbf{a}_{n+1} is updated to the new equilibrium state. The variable `ChemicalEquilibrium` is a setting that enables/disables the chemical equilibrium function by the if-statement at line 16. The statement at line 20 updates the initial solution vector \mathbf{a}_n for the continuing FE time stepping.

Algorithm 2

The Newton-Raphson iteration scheme is shown in Alg. 2. The user defined variables `IterationPrecision`, `IterationNumLimit` and `' δ_{acc} '` are the residual criterion, a maximum number of iterations if the criterion is unreachable and a convergence acceleration factor, respectively. The initial residual is determined at line 6 and evaluated in the if-statement at line 8 against the defined criterion, where a true statement will return to Alg. 1 and false will

start the Newton–Raphson iteration at line 14. The iteration is controlled by a while-statement, terminating when the residual criterion is met or by the if statement on line 17 evaluating the number of iteration compared to the defined maximum. The new global matrices are calculated at line 20 and 21 and the new system is solved at line 23. The matrix assemble function *matrix_assemble* is called at line 25 to update the global matrices and a new residual is determined at line 28. The new residual is compared with the residual from the previous iteration step at line 30. The iteration is stopped if the residual from the previous iterations is smaller than the current and the iteration number is larger than 50. In this case, the result vector from the previous time step is given as output result.

Algorithm 3

The non-linear matrix assembling function, shown in Alg. 3 updates the non-linear parts of the local stiffness and damping matrices and place the local matrices in their respective global systems. The initial call to *matrix_assemble* generates the local to global matrix coordinates $[i, j]$ at line 4 which are used in the following update calls to the function. The sorption hysteresis function *sorption_hysteresis* at line 6 is explained in more details in Alg. 4. The lines 7 and 8 assembles the local FE matrices and place these in their respective global matrices in the lines 9 and 10.

Algorithm 4

The sorption hysteresis function shown in Alg. 4 is a sub-function of the matrix assembling, Alg. 3. The function calculates the non-linear parameters for the sorption hysteresis model. It is presented separately here as it is non-standard method and the most complex part of the algorithm. The outer if-statements, the lines 3 and 15, determines whether any of the discrete nodes have changed the sorption direction¹ from the previous time step to the current. The if-statements at the lines 4 and 16 determines if the value of any of the changed nodes are larger than the tangent humidity point on the boundary sorption isotherm which was determined at the last change in sorption direction. The nodes, for which the statement is true, is saved and the boundary polynomial coefficients are applied for these nodes. The new tangent humidity point, according to the boundary isotherms, is set at the lines 6 and 18. The if-statements at the lines 8 and 20 determines the set of nodes for which a new scanning curve polynomial needs to be established. The new polynomial coefficients and the new boundary tangent

¹From absorption to desorption or vice versa.

Algorithm 2 Newton–Raphson iteration scheme

```

1  def: var (double) IterationPrecision
2  def:     (int) NeRaCounter
3  def: var (int) IterationNumLimit
4  def: var (double)  $\delta_{acc}$  % Acceleration factor
5
6   $\psi = \mathbf{C}^0 \frac{1}{\Delta t} (\mathbf{a}_{n+1}^0 - \mathbf{a}_n) + \mathbf{K}^{i-1} \mathbf{a}_{n+1}^{i-1} - \mathbf{f}$ 
7
8  if  $\psi \bullet \psi < \text{IterationPrecision}$ 
9      return
10 else
11 NeRaCounter = 0;
12  $\psi_{test} = \psi \bullet \psi$ ;
13  $i = 1$ 
14 while  $\psi \bullet \psi > \text{IterationPrecision}$ 
15     NeRaCounter++;
16
17     if NeRaCounter == IterationNumLimit
18         break
19     end
20      $\mathbf{K}_{NR} = \mathbf{C}/\Delta t + \mathbf{K}$ ;
21      $\mathbf{F}_{NR} = (\mathbf{C}/\Delta t + \mathbf{K}) \mathbf{a}_{n+1}^{i-1} - \psi \delta_{acc}$ ;
22
23      $[\mathbf{a}_{n+1}^i, \mathbf{f}^i] = \text{solve}(\mathbf{F}_{NR}, \mathbf{K}_{NR}, \mathbf{f}_b)$ ;
24
25     matrix_assemble( $\mathbf{K}, \mathbf{C}$ );
26      $\mathbf{f} = \mathbf{f} - \mathbf{f}^i$ 
27
28      $\psi = \mathbf{C} \frac{1}{\Delta t} (\mathbf{a}_{n+1}^i - \mathbf{a}_n) + \mathbf{K} \mathbf{a}_{n+1}^i - \mathbf{f}$ 
29
30     if  $\psi \bullet \psi > \psi_{test}$  and NeRaCounter > 50
31          $\mathbf{a}_{n+1}^i = \mathbf{a}_{n+1}^{i-1}$ ;
32         break
33     end
34      $\psi_{test} = \psi \bullet \psi$ ;
35      $i++$ 
36 end
37 end

```

Algorithm 3 Non-linear matrix assembler

```

1 def: var non_linear_vars ← {  $\tilde{c}_{l_i}, \tilde{\varepsilon}_l, v_{l,s}, \tilde{\phi}_v, \tilde{\varepsilon}^{l,eq}(\tilde{\phi}_v, h_1^*, h_2^*, h_3^*)$  }
2 if 'initial' or 'update'
3   if 'initial'
4      $[i, j] = \text{local2global\_matrix\_coordinate}();$ 
5   end
6    $[h_1^*, h_2^*, h_3^*] = \text{sorption\_hysteresis}(\phi_v^t, \phi_v^{t-\Delta t});$ 
7    $\mathbf{K}_{local} = \text{assemble\_local\_stiffness\_matrices}(\text{non\_linear\_vars});$ 
8    $\mathbf{C}_{local} = \text{assemble\_local\_damping\_matrices}(\text{non\_linear\_vars});$ 
9    $\mathbf{K}_{global} = \text{local2global}(\mathbf{K}_{local}, i, j)$ 
10   $\mathbf{C}_{global} = \text{local2global}(\mathbf{C}_{local}, i, j)$ 
11 end

```

point is calculated at the lines 9 and 21. Polynomials coefficients which are out of range are sorted out at the lines 10 and 22 by a tolerance factor set by the user. The polynomials that fulfill the statement are reset to the previous polynomials at the lines 11 and 23. The mathematical formulation and figures explaining the whole procedure are discussed in Paper I.

Algorithm 5

The chemical equilibrium function is shown in Alg. 5. The function calculates the chemical equilibrium state in each FE node by the for-loop statement at line 7. The input parameters for the IPHREEQC calculation are stored in the object *accumulate_phreeqc_string* as the concentration of the ions, the amount of water, pure phases, solid solutions and surface complexes at the lines 8 to 12. The concentrations of the ions and the amount of water are results from the mass transport calculation, whereas the amounts of solid phases are from the previous time step and thereby only updated in this function. The new chemical equilibrium state is calculated by the *iphreeqc_run* at line 14. The total result vector is distribute at line 16 where the \mathbf{a}_{n+1} is returned to the FE calculation in Alg. 1 as initial values for the next time step. All lines stored in the IPHREEQC buffer are cleared in every loop at line 18.

Algorithm 4 Sorption hysteresis function

```

1  def: var (double) tolerance
2
3  if  $\phi_{change}^t \leftarrow any(\phi_v^t > \phi_v^{t-\Delta t})$ 
4    if  $\mathbf{x} \leftarrow any(\phi_{change}^t \geq \phi_{v,tang}^t)$ 
5       $[\mathbf{h}_1^*(\mathbf{x}), \mathbf{h}_2^*(\mathbf{x}), \mathbf{h}_3^*(\mathbf{x})] \leftarrow absorption\_boundary\_isotherm(\mathbf{x})$ 
6       $\phi_{v,tang}^t(\mathbf{x}) \leftarrow 1$ 
7    end
8    if  $\mathbf{z} \leftarrow any(\phi_{change}^t \neq \mathbf{x})$ 
9       $[\mathbf{h}_1^*(\mathbf{z}), \mathbf{h}_2^*(\mathbf{z}), \mathbf{h}_3^*(\mathbf{z}), \phi_{v,tang}^t(\mathbf{z})] \leftarrow create\_scanning\_curve(\mathbf{z})$ 
10     if  $any(\mathbf{h}_1^*(\mathbf{z}), \mathbf{h}_2^*(\mathbf{z}), \mathbf{h}_3^*(\mathbf{z})) > tolerance$ 
11        $reset((\mathbf{h}_1^*(\mathbf{z}), \mathbf{h}_2^*(\mathbf{z}), \mathbf{h}_3^*(\mathbf{z}))$ 
12     end
13   end
14 end
15 if  $\phi_{change}^t \leftarrow any(\phi_v^t < \phi_v^{t-\Delta t})$ 
16   if  $\mathbf{x} \leftarrow any(\phi_{change}^t \leq \phi_{v,tang}^t)$ 
17      $[\mathbf{h}_1^*(\mathbf{x}), \mathbf{h}_2^*(\mathbf{x}), \mathbf{h}_3^*(\mathbf{x})] \leftarrow desorption\_boundary\_isotherm(\mathbf{x})$ 
18      $\phi_{v,tang}^t(\mathbf{x}) \leftarrow 0$ 
19   end
20   if  $\mathbf{z} \leftarrow any(\phi_{change}^t \neq \mathbf{x})$ 
21      $[\mathbf{h}_1^*(\mathbf{z}), \mathbf{h}_2^*(\mathbf{z}), \mathbf{h}_3^*(\mathbf{z}), \phi_{v,tang}^t(\mathbf{z})] \leftarrow create\_scanning\_curve(\mathbf{z})$ 
22     if  $any(\mathbf{h}_1^*(\mathbf{z}), \mathbf{h}_2^*(\mathbf{z}), \mathbf{h}_3^*(\mathbf{z})) > tolerance$ 
23        $reset((\mathbf{h}_1^*(\mathbf{z}), \mathbf{h}_2^*(\mathbf{z}), \mathbf{h}_3^*(\mathbf{z}))$ 
24     end
25   end
26 end

```

Algorithm 5 Chemical equilibrium solver

```

1 def: var (int) NumOfNodes
2 def: (object) accumulate_phreeqc_string % Assemble iphreeqc
3                                     % input file
4 def: (vector) s % Amount of solid species
5 def: (vector) d % New chemical equilibrium system
6
7 for 1:NumOfNodes
8   accumulate_phreeqc_string ← add_water_amount(ai)
9   accumulate_phreeqc_string ← add_ion_concentration(ai)
10  accumulate_phreeqc_string ← add_pure_phase_amount(sp)
11  accumulate_phreeqc_string ← add_solid_solution_amount(sss)
12  accumulate_phreeqc_string ← add_surface_compl_amount(ssc)
13
14  d ← iphreeqc_run(accumulate_phreeqc_string)
15
16  [a, s] ← distribute_result(d)
17
18  clear_accumulated_lines(accumulate_phreeqc_string)
19 end

```

Chapter 3

Research findings and conclusions

The research findings presented in the scientific papers in Part II of this thesis are summarized and related to the overall aim of the PhD project. An example of a 100 years durability simulation is presented showing the potential of the model in relation to long term simulations. A general discussion of the research findings together with suggestions for the future development of the suggested durability model and the service life framework are given. A conclusion of the project is presented based on the research findings.

3.1 Summary of research

A durability indicator in terms of a reactive mass transport model for the numerical service life framework is studied and presented in the scientific papers in Part II. The papers describes the first version of the reactive mass transport model by the numerical documentation and show different test simulations. The individual scientific paper in Part II treats parts of the aims defined for the overall project.

Paper I describes the governing equation system behind the reactive mass transport model and shows the mathematical steps for establishing a discrete FE system for the specific equation system. The governing equation system combines two existing mass transport models, an ion transport model which includes chemical interactions and a two phase, moisture transport model, which accounts for sorption hysteresis. The numerical coupling of the two mass transport models is new which encourage the detailed FE discretization description, shown in Paper I. The sorption hysteresis loop, which couples the liquid and vapor flow, is described by a phenomenological part in the mois-

ture transport. The reactive mass transport model described in Paper I is the complete durability model established, from which it is possible to use separate parts, depending on the physical problem considered. It is concluded, based on the simulations performed in Paper I, that the coupled differential equation system, neglecting the chemical interactions, is successfully solved by the suggested FEM. Paper I shows the effect of shifting between a saturated and an non-saturated boundary condition for the liquid phase. The phenomenological sorption hysteresis simulation is compared with a more simple approach which do not account for the hysteresis loop effect. It is concluded that including the sorption hysteresis loop in the durability model has an important effect on the pore solution concentrations. The shifting boundary conditions are important in service life modeling of concrete infrastructure constructions, for instance, the boundary humidity varies over the year or exposures in tidal zones.

Simulations using the complete durability model are shown in Paper II. A review of the MAL approach, as used by PHREEQC to determine chemical equilibrium is given in Paper II for the aqueous reactions, pure phase reactions and solid solution reactions. The numerical implementation of the degree of hydration for the clinker, in the initial chemical equilibrium calculation is shown. Typical exposure conditions of concrete are used in two simulations, a pure leaching simulation where the solid phases are dissolved and a combined ion ingress and leaching simulation where penetrating aggressive external ions change the chemical equilibrium state. The results from the simulations are shown in terms of pore solution composition and solid phase composition which can be used as durability indicators in a service life evaluation. It is concluded that the numerical scheme in terms of the FE scheme, the operator splitting approach and the PHREEQC code is fairly robust. The simulations shows the flexibility of the model in terms of different boundary conditions relevant for service life modeling of concrete.

A comparison between two different state-of-art C-S-H chemical descriptions incorporated in the reactive transport model is given in Paper III. The comparison involves a C-S-H description by a four end-member solid solution model and a surface complexation model where the EDL is taken into account. The paper extends the review of the MAL given in Paper II, to include a review of the surface complexation and EDL theory used in PHREEQC. Calculations of a multi-species ion ingress in concrete using a boundary solution corresponding to an averaged sea-water composition. The amount of solid phases after 2 and 10 years simulated exposure are given as result. The calculated solid phase compositions by means of the two C-S-H descriptions are compared after 2 years and 10 years simulated exposure. The simulation results shows a clear difference in the amount of ettringite, brucite, calcite and

hem carbonate formed after 10 years exposure simulations but only minor differences after 2 years exposure simulations.

Paper IV shows the current status of the suggested durability model in terms of numerical simulations compared with laboratory controlled experiments. Ion ingress experiments on a mortar with OPC with two different exposure solutions are used. The total chloride content at different depths from the exposed surface after 21, 90 and 180 days of exposure are studied. The actual cement oxide composition and the boundary solution compositions are used as input parameters for the numerical simulations of the experiment. The tortuosity factor τ , in the numerical durability model is used as fitting parameter in order to obtain the best fit for the three exposure times used in the experiment. The simulation results showed fairly good agreement with the experimental results for both exposure solutions studied. Some deviations are seen between the simulations results and the experimental results but the overall fit is shown to be good. Suggestions for the further development of the model are discussed in order to improve and extend the durability model.

3.2 Long term durability simulations

As described in the introduction, the service life requirement for concrete used in infrastructure structures is in the range of 80-125 years. The capability of the durability model to handle this relatively long period is shown in this section by extending simulation period in the simulations from Paper III. The results are presented in terms of simple durability indicators related to reinforced concrete. The computational time is recorded in order to evaluate the model in relation to the applicability as an engineering service life tool. The detail level of the durability model and the simulation must be sufficiently high in order not to lose valuable information in numerical errors. Increasing the numerical detail level in the durability model as it is constructed in this work will increase computational time. Hence, a reasonable combination between details and computational time is needed in order to use the model as an engineering tool.

A direct estimation of the end of service life is out of the scope of this work, instead the Hausmann's free concentration criterion is evaluated at a distance of 0.1[m] from the exposed surface over a 100 years simulated exposure period. The 0.1[m] is assumed to represent a reinforced concrete cover. The simulations are based on the model parameters and the sea water service environment as described in Paper III. The total simulation time is extended to 100 years and the total spatial length is extended to 0.1[m]

discretized with 350 elements, compared to the simulation in Paper III. The oxide composition for the cement simulated is shown in Tab. 3.1 and other important adjustable simulation parameters are given in Tab. 3.2. Chemical equilibrium is determined for every second mass transport step in order to save computational time and obtain a stable solution for the whole spatial domain.

Table 3.1: Oxide composition for the cement material used in the simulation.

	CaO	SiO ₂	Al ₂ O ₃	Fe ₂ O ₃	SO ₃	K ₂ O	Na ₂ O	MgO
mass%	64.00	22.00	5.00	4.00	3.00	0.78	0.15	1.00

Table 3.2: Conditions for the numerical calculation and material parameters.

Simulation parameters	
w/c	0.45
Spatial elements	350
Total spatial distance [m]	0.1
Total Time t_{total} [years]	100
Time step mass transport, Δt_{trans} [h]	24
Time step chemical equilibrium, Δt_{chem} [h]	48
Tortuosity factor, τ	0.0039

The results from the two simulations are shown in Figs. 3.1a and 3.1b where it is seen that the Hausmann criterion is exceeded between 34 and 35 years using this specific C-S-H solid solution model and between 35 and 36 years using this specific C-S-H surface complexation model. The pH starts to decrease significantly at the same points which are the main reason for the Hausmann criterion is exceeded. The simulated pore solution changes have an affect on the corrosion initiation and corrosion rate. It is, however, beyond the scope of this work to study the exact conditions for corrosion initiation and propagation. The predicted pH is lower after 100 years simulated exposure using the surface complexation model (Fig. 3.1b), compared to the solid solution model (Fig. 3.1a). The reactions used to describe the C-S-H phase have a significant influence on the final results when these are used in a reactive transport model, which is also one of the important conclusions of Paper III.

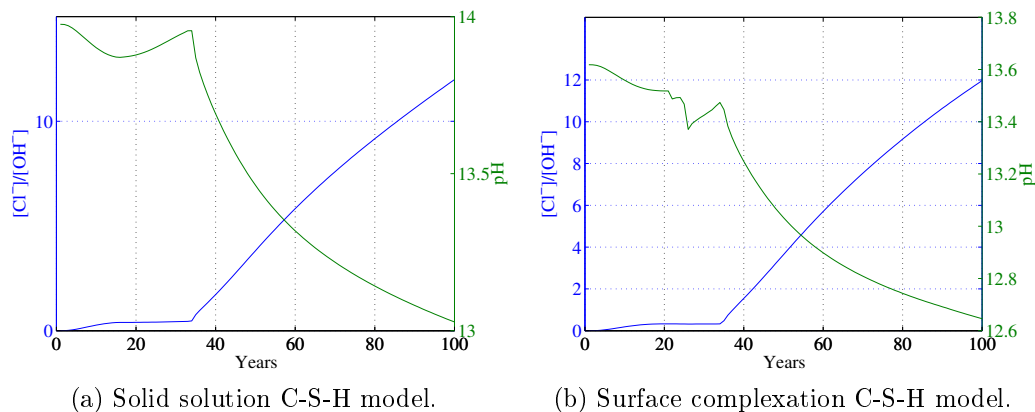


Figure 3.1: Hausmanns criterion for reinforcement corrosion and the pH-value 0.1[m] from the exposed boundary.

The computational times for the two models are shown in Tab. 3.3. The simulation is performed on a HP ProLiant SL2x170z G6 with the non-graphical and r-mode settings in Matlab for Linux. The computational times are reasonable, seen in the perspective of the actual simulation time of 100 years and the level of detail. It is also reasonable compared to many experimental investigations where accelerated experimental setup are much more time consuming in comparison. It is concluded that the current version of the durability model is applicable as engineering tool with respect to the computational time.

Table 3.3: Computational time for the 100 years simulations presented in Fig. 3.1.

	Surface complexation	Solid solution
CPU time[days]	8.56	6.13

3.3 Discussion and future work

The durability model presented is only one, of the needed durability indicators in the service life framework. The simulation tool is, therefore, not complete as a tool for calculating the end of service life for any given concrete. Some issues in the model needs to be improved in future versions in order to facilitate simulations used in the design of concrete structures.

A general issue, for which similar reactive mass transport models may suffer from as well, is related to the FE boundary node and the chemical equilibrium calculated at this node. The ion concentrations at the boundary node are prescribed in each FE time step, which eliminates the time dependency for this node. The implicit dissolution rates of the solid phases at the boundary node are only dependent on the number of time steps. The ultimate future goal should be a complete kinetic description of the dissolution reactions involved which would solve the above discussed problem. Other different solution methods may be relevant in this context, e.g., identification of the primary solid phases and their dissolution rate description or the assignment of multiple nodes in the FE system for the description of the boundary solution itself.

The current version of the durability model is sensitive to the chemical reactions used as input. The model requires that a single stable chemical model is defined for the whole spatial and transient domains. Prior knowledge of which chemical reactions occurs in specific environments is needed in order to get a valid result. This is not optimal in the sense of using the service life framework as an engineering tool. The durability model would be strengthened if stable validated chemical models are predefined. On the other hand, the model should continue the development in an open format where it also is possible to define custom chemical models for research purposes.

It is important that the model is continuously updated with the recent thermodynamic databases which also includes descriptions of supplementary cementitious materials. Supplementary cementitious materials are essential in modern concretes and especially in the the development of new more environmentally friendly concretes.

The durability model includes a description of water and vapor diffusion in order to simulate non-saturated concrete. Diffusion of ions in the gas phase is not accounted for in the current version of the model. The gaseous species establish an equilibrium condition primarily with the pore solution and thereby affects the whole chemical equilibrium. The diffusion of gaseous carbonates are of interest in this context due to the effects of carbonation of the concrete. A set of multi-species gaseous diffusion equations should be added to the existing differential equations in a future version. The chemical model needs to be extended along with the gaseous diffusion extension to account for the gas-liquid equilibrium.

The mass transport rate of ions is sensitive to the different reduction factors on the diffusion coefficient as shown in Paper IV. The tortuosity is assumed constant over time in the current version of the durability model even though the amount of solid phases are changed by ingress and leaching and thereby change the geometrical configuration of the pore structure.

The model should account for the pore structure evolution in terms of a tortuosity factor which is dependent on the actual solid phase composition at a given time and spatial position. The porosity could be calculated by the solid phase composition and then relate the porosity and tortuosity. The changed geometrical configuration may also create stresses and strains in the solid structure due to volume expansions. The mixture theory includes the theoretical description of mechanical impacts, but it may be extremely complicated to solve numerically, i.a. due to the strong non-linearities introduced and fracture mechanical considerations needs to be taken into account as well.

The service environment temperature and the variation of this is of great importance for the physical and chemical properties. The mass transport is therefore affected by temperature in the diffusion and convection process. The sorption isotherms, are changed with temperature and thereby also the sorption hysteresis described by the phenomenological model. The chemical reactions are individually temperature dependent and the overall chemical equilibrium state is affected. The temperature should be included as an additional state variable into the established durability model. Coupling of the temperature to the diffusion and chemical equilibrium calculations is pretty much straight forward whereas the coupling to the sorption hysteresis model may be more complex.

Computational speed is important in the further development of durability models but also for the complete service life framework calculation. Parallelization should be investigated even though a simple parallel version in some parts failed to succeed in this work. Computational speed is also an issue for extending the current one-dimensional FE model to two- or three-dimensions. Two- and three-dimensions are of interest for the durability modeling when for instances cracks are taken into account or in systems where different types of materials are combined, like in a brick wall or foundations with concrete combined with light weight blocks.

How should a coupled non-linear model be validated? The mass transport models, coupled in this work are validated individually and the reactions in the chemical models are validated by different separated experiments. Assembling these models and compare them with assembled experimental tests may not always give compatible results and a complex problem arises due to this. Validation of coupled models are difficult as it is difficult to experimentally separate the individual physical and chemical processes in order to detect the reasons for inconsistency between simulation results and experimental results. It is therefore difficult to know where to improve the numerical model.

3.4 Conclusions

A numerical service life framework for concrete is initiated in this project. The first durability model in the framework is established in terms of a reactive mass transport model. The reactive mass transport model is a durability indicator in the service life framework, which is extensible. The reactive mass transport model is based on a modern mixture theory approach which is suitable for describing porous media. The mixture theory approach is valuable for the further development of the service life framework as it includes a general physical description on the different phases and species needed to describe concrete in a sound theoretically way. The mixture theory can help to understand and constitute the coupling of the physical processes between the phases which are essential in the understanding of the deterioration processes of concrete.

A coupled numerical reactive mass transport model is established and a FE solution scheme for this is suggested and tested. The reactive mass transport model is a coupling of existing numerical models, describing physical processes in concrete in terms of partial differential equations under exposure of a given service environment. The physical processes treated involves, ion diffusion, ion migration, liquid transport, vapor transport, sorption hysteresis and chemical interactions. The finite element method is suggested for solving the mass transport part of the model and the chemical equilibrium is calculated by the geochemical code PHREEQC. The numerical scheme is implemented as a computer based algorithm, constructed in a format where the parameter space easily can be investigated and the thermodynamic databases are easily updated to adapt future extensions and modifications. The durability model is tested with different parameters in terms of varying liquid and vapor content at the boundary, simple leaching exposure, multi-species ingress exposure and the use of different chemical models. The numerical method and algorithm are concluded to be stable for the parameters tested in the project.

The current development status of the reactive transport model is evaluated by comparing numerical simulations with experimental tests. The model showed fairly good agreement between simulation results and experimental measurements, on the total chloride content using multi-species exposure solutions and multi-species simulations. It is concluded that the durability model still needs to be updated in order to remove crude assumptions and thereby make the model more general but it performs well at the current development state.

It is shown that the model and the algorithm are capable of meeting the requirements for multi-species long term simulations. Durability indicators

for service life predictions over 100 years simulated exposure is performed within reasonable computational time.

3.5 References

- C. E. Acevedo and M. G. Serrato. Determining the effects of radiation on aging concrete structures of nuclear reactors—10243. In *WM2010 Conference, Phoenix, USA*, 2010.
- S. Ahmad. Reinforcement corrosion in concrete structures, its monitoring and service life prediction—a review. *Cement and Concrete Composites*, 25(4):459–471, 2003.
- C. Alonso, C. Andrade, M. Castellote, and P. Castro. Chloride threshold values to depassivate reinforcing bars embedded in a standardized opc mortar. *Cement and Concrete research*, 30(7):1047–1055, 2000.
- M. Balonis, B. Lothenbach, G. Le Saout, and F. Glasser. Impact of chloride on the mineralogy of hydrated portland cement systems. *Cement and Concrete Research*, 40(7):1009–1022, 2010.
- V. Baroghel-Bouny, T. Nguyen, and P. Dangla. Assessment and prediction of rc structure service life by means of durability indicators and physical/chemical models. *Cement and Concrete Composites*, 31(8):522–534, 2009.
- Z. P. Bazant. Physical model for steel corrosion in concrete sea structures—application. *Journal of the structural division*, 105(ASCE 14652 Proceeding), 1979.
- J. Bear and Y. Bachmat. *Introduction to modeling of transport phenomena in porous media*, volume 4. Springer, 1990.
- L. Bennethum and J. Cushman. Multicomponent, multiphase thermodynamics of swelling porous media with electroquasistatics: I. macroscale field equations. *Transport in Porous Media*, 47(3):309–336, 2002a.
- L. Bennethum and J. Cushman. Multicomponent, multiphase thermodynamics of swelling porous media with electroquasistatics: II. constitutive theory. *Transport in Porous Media*, 47(3):337–362, 2002b.
- D. P. Bentz. Modelling cement microstructure: pixels, particles, and property prediction. *Materials and Structures*, 32(3):187–195, 1999.
- C. Bethke. *Geochemical reaction modeling: Concepts and applications*. Oxford University Press New York, 1996.

- S. Bishnoi and K. L. Scrivener. μic : A new platform for modelling the hydration of cements. *Cement and Concrete Research*, 39(4):266–274, 2009.
- A. A. Boateng. *Rotary kilns: transport phenomena and transport processes* /. Elsevier/Butterworth-Heinemann,, 2008. ISBN 0750678771, 9780750678773. [electronic resource].
- R. M. Bowen. Theory of mixtures. *Continuum physics*, 3(Pt I), 1976.
- J. W. Bullard, H. M. Jennings, R. A. Livingston, A. Nonat, G. W. Scherer, J. S. Schweitzer, K. L. Scrivener, and J. J. Thomas. Mechanisms of cement hydration. *Cement and Concrete Research*, 41(12):1208–1223, 2011.
- J. Carrayrou, R. Mosé, and P. Behra. Operator-splitting procedures for reactive transport and comparison of mass balance errors. *Journal of Contaminant Hydrology*, 68(3):239–268, 2004.
- S. R. Charlton and D. L. Parkhurst. Modules based on the geochemical model {PHREEQC} for use in scripting and programming languages. *Computers & Geosciences*, 37(10):1653 – 1663, 2011. ISSN 0098-3004. doi: <http://dx.doi.org/10.1016/j.cageo.2011.02.005>. URL <http://www.sciencedirect.com/science/article/pii/S0098300411000653>.
- S. Chen and G. D. Doolen. Lattice boltzmann method for fluid flows. *Annual review of fluid mechanics*, 30(1):329–364, 1998.
- D. Cusson, Z. Lounis, and L. Daigle. Durability monitoring for improved service life predictions of concrete bridge decks in corrosive environments. *Computer-Aided Civil and Infrastructure Engineering*, 26(7):524–541, 2011.
- S. R. de Groot and P. Mazur. *Non-equilibrium Thermodynamics*. Courier Dover Publications, 1984.
- Y. Elakneswaran and T. Ishida. Integrating physicochemical and geochemical aspects for development of a multi-scale modelling framework to performance assessment of cementitious materials. In *Multi-Scale Modeling and Characterization of Infrastructure Materials*, pages 63–78. Springer, 2013.
- fib. Model code for service life design, bulletin no. 34. 2006.
- D. Fillmore. *Literature Review of the Effects of Radiation and Temperature on the Aging of Concrete*. United States. Department of Energy, 2004.

- T. C. Gasser and G. A. Holzapfel. Modeling 3d crack propagation in unreinforced concrete using pufem. *Computer Methods in Applied Mechanics and Engineering*, 194(25):2859–2896, 2005.
- M. Geiker, E. P. Nielsen, and D. Herfort. Prediction of chloride ingress and binding in cement paste. *Materials and structures*, 40(4):405–417, 2007.
- D. J. Griffiths and R. College. *Introduction to electrodynamics*, volume 3. prentice Hall Upper Saddle River, NJ, 1999.
- D. Hausmann. Steel corrosion in concrete—how does it occur? *Materials protection*, 1967.
- S. Helland. Service life design of concrete structures: the limit state and reliability-based approach given in fib mc sld and iso 16204. *International Journal of Structural Engineering*, 4(1):14–23, 2013.
- P. Hewlett. *Lea’s chemistry of cement and concrete*. Butterworth-Heinemann, 2003.
- Y. Hosokawa, K. Yamada, B. Johannesson, and L.-O. Nilsson. Development of a multi-species mass transport model for concrete with account to thermodynamic phase equilibriums. *Materials and Structures*, pages 1–16, 2011. ISSN 1359-5997. URL <http://dx.doi.org/10.1617/s11527-011-9720-2>. 10.1617/s11527-011-9720-2.
- D. Jacques. Benchmarking of the cement model and detrimental chemical reactions including temperature dependent parameters. Technical report, ONDRAF/NIRAS, 2008.
- B. Johannesson. *Modelling of transport processes involved in service life prediction of concrete: important principles*, volume Licentiate thesis, 3083. Div of Building Materials LTH, Lund university, 1998.
- B. Johannesson. Development of a generalized version of the poisson-nernst-planck equations using the hybrid mixture theory: Presentation of 2d numerical examples. *Transport in Porous Media*, 85:565–592, 2010a. ISSN 0169-3913. URL <http://dx.doi.org/10.1007/s11242-010-9578-8>. 10.1007/s11242-010-9578-8.
- B. Johannesson. *Introduction to Engineering Continuum Mixture Theory with Numerical Application using FEM*. 2011b. Lecture notes.

- B. Johannesson and U. Nyman. A numerical approach for non-linear moisture flow in porous materials with account to sorption hysteresis. *Transport in porous media*, 84(3):735–754, 2010.
- S. Kim, D. M. Frangopol, and M. Soliman. Generalized probabilistic framework for optimum inspection and maintenance planning. *Journal of Structural Engineering*, 139(3):435–447, 2013.
- D. Kulik, U. Berner, and E. Curti. Modelling chemical equilibrium partitioning with the gems-psi code. Technical report, Paul Scherrer Institut, Villigen (2004), 2003.
- D. A. Kulik, T. Wagner, S. V. Dmytrieva, G. Kosakowski, F. F. Hingerl, K. V. Chudnenko, and U. R. Berner. Gem-selector geochemical modeling package: revised algorithm and gems3k numerical kernel for coupled simulation codes. *Computational Geosciences*, 17(1):1–24, 2013.
- M. G. Larson and F. Bengzon. The finite element method: Theory, implementation, and practice, 2010.
- L. Latour, R. L. Kleinberg, P. P. Mitra, and C. H. Sotak. Pore-size distributions and tortuosity in heterogeneous porous media. *Journal of Magnetic Resonance, Series A*, 112(1):83–91, 1995.
- P. Le Bescop, B. Lothenbach, E. Samson, and K. A. Snyder. Modeling degradation of cementitious materials in aggressive aqueous environments. In *Performance of Cement-Based Materials in Aggressive Aqueous Environments*, pages 177–218. Springer, 2013.
- C.-Q. Li, R. I. Mackie, and W. Lawanwisut. A risk-cost optimized maintenance strategy for corrosion-affected concrete structures. *COMPUTER-AIDED CIVIL AND INFRASTRUCTURE ENGINEERING*, 22(5):335–346, 2007. ISSN 10939687, 14678667.
- B. Lothenbach and F. Winnefeld. Thermodynamic modelling of the hydration of portland cement. *Cement and Concrete Research*, 36(2):209–226, 2006. ISSN 00088846, 18733948. doi: 10.1016/j.cemconres.2005.03.001.
- B. Lothenbach, T. Matschei, G. Möschner, and F. P. Glasser. Thermodynamic modelling of the effect of temperature on the hydration and porosity of portland cement. *Cement and Concrete Research*, 38(1):1–18, 2008.
- T. Luping. Engineering expression of the clinconc model for prediction of free and total chloride ingress in submerged marine concrete. *Cement and Concrete Research*, 38(8):1092–1097, 2008.

- T. Luping and J. Gulikers. On the mathematics of time-dependent apparent chloride diffusion coefficient in concrete. *Cement and Concrete Research*, 37(4):589–595, 2007.
- K. Maekawa, T. Ishida, and T. Kishi. *Multi-scale modeling of structural concrete*. Taylor & Francis, 2008. ISBN 0203927206, 0415465540, 9780415465540, 9780203927205.
- M. Mainguy and O. Coussy. Propagation fronts during calcium leaching and chloride penetration. *Journal of engineering mechanics*, 126(3):250–257, 2000.
- M. Mainguy and F.-J. Ulm. Coupled diffusion-dissolution around a fracture channel: the solute congestion phenomenon. *Transport in porous media*, 45(3):479–495, 2001.
- J. M. Mendoza-Rangel and P. Castro-Borges. Critical review of service life concepts of reinforced concrete structures. *ECS Transactions*, 3(13):3–8, 2007.
- S. Mindess, J. F. Young, and D. Darwin. *Concrete*. Prentice-Hall, 2003.
- R. B. Minussi, P. C. Philippi, A. A. M. Oliveira, and L. O. E. Santos. A second order lattice boltzmann equation to simulate electro-diffusion problems. 2013.
- A. A. Mohamad. *Lattice Boltzmann method : fundamentals and engineering applications with computer codes*. Springer, 2011. ISBN 0857294555, 9780857294555, 9780857294548.
- G. Möschner, B. Lothenbach, J. Rose, A. Ulrich, R. Figi, and R. Kretzschmar. Solubility of fe-ettringite ($\text{Ca}_6[\text{Fe}(\text{OH})_6]_2(\text{SO}_4)_3 \cdot 26\text{H}_2\text{O}$). *Geochimica et Cosmochimica Acta*, 72(1):1–18, 2008.
- G. Möschner, B. Lothenbach, F. Winnefeld, A. Ulrich, R. Figi, and R. Kretzschmar. Solid solution between al-ettringite and fe-ettringite (ca 6 [al 1- x fe x (oh) 6] 2 (so 4) 3 · 26h 2 o). *Cement and Concrete Research*, 39(6):482–489, 2009.
- T. Q. Nguyen, V. Baroghel-Bouny, and P. Dangla. Prediction of chloride ingress into saturated concrete on the basis of a multi-species model by numerical calculations. *COMPUTERS AND CONCRETE*, 3(6):401–421, 2006. ISSN 15988198, 1598818x.

- T. Q. Nguyen, J. Petković, P. Dangla, and V. Baroghel-Bouny. Modelling of coupled ion and moisture transport in porous building materials. *Construction and building materials*, 22(11):2185–2195, 2008.
- E. P. Nielsen and M. R. Geiker. *The durability of white Portland cement to chemical attack*. PhD thesis, Technical University of Denmark, Department of Structural Engineering and Materials, 2004.
- NRMCA. Concrete CO₂ fact sheet. Technical report, National Ready Mixed Concrete Association, 2012.
- U. Nyman, P. Gustafsson, B. Johannesson, and R. Häggglund. A numerical method for the evaluation of non-linear transient moisture flow in cellulosic materials. *International journal for numerical methods in engineering*, 66(12):1859–1883, 2006.
- D. L. Parkhurst, C. Appelo, et al. User’s guide to phreeqc (version 2): A computer program for speciation, batch-reaction, one-dimensional transport, and inverse geochemical calculations. *Water-Resources Investigations Report 99-4259, U.S. DEPARTMENT OF THE INTERIOR*, 1999.
- R. A. Patel, J. Perko, D. Jacques, G. D. Schutter, K. V. Breugel, and G. Ye. A versatile pore-scale multicomponent reactive transport approach based on lattice boltzmann method: Application to portlandite dissolution. *Physics and Chemistry of the Earth*, In press, 2014.
- B. J. Pease, A. Michel, M. R. Geiker, and H. Stang. Modeling moisture ingress through simplified concrete crack geometries. *Modeling Moisture Ingress Through Simplified Concrete Crack Geometries*, 2011.
- M. Ristinmaa and N. S. Ottosen. *Mixture theory - A Framework for Paper Mechanics*. 2010.
- E. Samson and J. Marchand. Numerical solution of the extended nernst-planck model. *Journal of Colloid and Interface Science*, 215(1):1 – 8, 1999. ISSN 0021-9797. doi: DOI:10.1006/jcis.1999.6145. URL <http://www.sciencedirect.com/science/article/pii/S0021979799961453>.
- E. Samson and J. Marchand. Modeling the transport of ions in unsaturated cement-based materials. *Computers & Structures*, 85(23):1740–1756, 2007a.
- E. Samson, J. Marchand, and J. Beaudoin. Describing ion diffusion mechanisms in cement-based materials using the homogenization technique. *Cement and Concrete Research*, 29(8):1341–1345, 1999a.

- E. Samson, J. Marchand, J. Robert, and J. Bournazel. Modelling ion diffusion mechanisms in porous media. *International Journal for Numerical Methods in Engineering*, 46(12):2043–2060, 1999b.
- T. Schmidt, B. Lothenbach, M. Romer, K. Scrivener, D. Rentsch, and R. Figi. A thermodynamic and experimental study of the conditions of thaumasite formation. *Cement and Concrete Research*, 38(3):337–349, 2008.
- L. Shen and Z. Chen. Critical review of the impact of tortuosity on diffusion. *Chemical Engineering Science*, 62(14):3748–3755, 2007.
- R. Siddique and M. I. Khan. *Supplementary cementing materials*. Springer, 2011. ISBN 3642178669, 3642178650, 9783642178665, 9783642178658.
- M. J. Simpson and K. A. Landman. Analysis of split operator methods applied to reactive transport with monod kinetics. *Advances in water resources*, 30(9):2026–2033, 2007.
- O. Svec, J. Skocek, H. Stang, J. F. Olesen, and P. N. Poulsen. Fully coupled lattice boltzmann simulation of fiber reinforced self compacting concrete. 2011.
- E. B. Tadmor, R. E. Miller, and R. S. Elliott. *Continuum mechanics and thermodynamics: from fundamental concepts to governing equations*. Cambridge University Press, 2012.
- H. F. Taylor. *Cement chemistry*. Thomas Telford, 1997.
- M. Torabinejad and N. Chivian. Clinical applications of mineral trioxide aggregate. *Journal of endodontics*, 25(3):197–205, 1999.
- K. Tuutti. Corrosion of steel in concrete. Technical report, 1982.
- M. C. S. U.S. Geological Survey. Cement, Feb. 2014. URL <http://minerals.usgs.gov/minerals/pubs/commodity/cement/mcs-2014-cemen.pdf>.
- K. van Breugel. Numerical simulation of hydration and microstructural development in hardening cement-based materials (i) theory. *Cement and Concrete Research*, 25(2):319 – 331, 1995. ISSN 0008-8846. doi: [http://dx.doi.org/10.1016/0008-8846\(95\)00017-8](http://dx.doi.org/10.1016/0008-8846(95)00017-8). URL <http://www.sciencedirect.com/science/article/pii/0008884695000178>.
- K. Van Breugel. Numerical simulation of hydration and microstructural development in hardening cement-based materials:(ii) applications. *Cement and Concrete Research*, 25(3):522–530, 1995.

- J. Van Der Lee, L. De Windt, V. Lagneau, and P. Goblet. Module-oriented modeling of reactive transport with hYTEC. *Computers & Geosciences*, 29 (3):265–275, 2003.

Part II

Scientific publications

The scientific publications produced in this PhD work is attached in this part. The papers presents the background of the proposed coupled reactive transport model for cement based materials and show the current state in terms of the theoretical background of the model and the ability to reproduce experimental data. The description of the model is to some extent repeated in the papers and some descriptions may be trivial, but it is important that the reader is able to reproduce the results.

A pre-study, which is not a part of this PhD thesis, of the mass transport model was published and presented at the Eighth International Conference on Engineering Computational Technology. The paper is entitled *A Coupled Chemical and Mass Transport Model for Concrete Durability*, by M. M. Jensen, B. Johannesson and M. R. Geiker, in Proceedings of the Eighth International Conference on Engineering Computational Technology. Civil-Comp Press, 2012. (Civil-Comp Proceedings).

Paper I

"A numerical comparison of ionic multi-species diffusion with and without sorption hysteresis for cement-based materials"

M. M. Jensen, B. Johannesson, M. R. Geiker

Submitted: *Transport In Porous Media*, Nov, 2013

A numerical comparison of ionic multi-species diffusion with and without sorption hysteresis for cement-based materials

M.M. Jensen · B. Johannesson · M. R. Geiker

Received: date / Accepted: date

Abstract A finite element solution for a mass transport model for porous materials accounting for sorption hysteresis is presented in this paper. The model is prepared for modeling of concrete durability, but the general presentation makes it suitable for other porous materials like soil and tissues. The model is an extended version of the Poisson–Nernst–Planck (PNP) system of equations. The PNP extension includes a two-phase vapor and liquid model coupled by a sorption hysteresis function and a chemical equilibrium term. The strong and weak solutions for the equation system are shown and a finite element formulation is established by Galerkin’s method. A single-parameter implicit time integration scheme is used for solving the transient response, and the out-of-balance solution is minimized by using a modified Newton–Raphson scheme in which the tangential stiffness is not computed exactly. The sorption hysteresis is added to the solution procedure by a rate function. The hysteresis effect is described by scanning curves defined between two boundary sorption isotherms. A numerical example was constructed to show the applicability and compare a simple approach and an extended approach within the sorption hysteresis model. The examples illustrate the impact of changing relative humidity at the mass transport boundary on the adsorption and desorption stages of a cement-based material. Changes in the pore solution ion concentrations are a result of the changing moisture content, which is shown by the example. Comparing the two approaches showed significant deviations in the liquid content and ion concentrations, in parts of the domain considered.

Keywords Mass transport, Sorption hysteresis, Finite element method, Cement-based materials

Nomenclature

	a	State variables vector
	C	Mass matrix
\hat{m}_l	f	Force vector
\hat{m}_v	j [⊕]	Electrical displacement

Mads Mønster Jensen
Department of Civil Engineering, Technical University of Denmark
Brovej b.118, 2800 Kgs. Lyngby, Denmark
Tel.: +45-27353614
E-mail: mmoj@byg.dtu.dk

Björn Johannesson
Department of Civil Engineering, Technical University of Denmark

Mette Rica Geiker
Department of Structural Engineering, Norwegian University of Science and Technology

\mathbf{j}^ϕ	Boundary flux of vapor	ξ_d	Relative dielectricity coefficient - [V/m]
\mathbf{j}^l	Boundary flux of liquid	A_i^l	Ion mobility - [m ² /(s V)]
\mathbf{j}_i^l	Boundary flux of species i	c_i^l	Ionic concentration of species i in liquid phase l - [mol/l]
\mathbf{K}	Stiffness matrix	D_ϕ	Diffusion coefficient for the vapor phase - [m ² /s]
\mathbf{N}	Global shape function	D_{ε^l}	Diffusion coefficient for the liquid phase - [m ² /s]
\mathbf{n}	Normal vector	D_i^l	Diffusion coefficient for constituent i - [m ² /s]
$\mathbf{v}^{l,s}$	Liquid phase l velocity with respect to the solid s - [m/s]	F	Faraday's constant - [C/mol]
Φ	Electrical potential - [V]	q_i	Chemical interactions - [1/s]
ϕ_v	Relative humidity - [-]	R	Rate constant for mass exchange between liquid and vapor - [1/s]
ρ_i^l	Density of species i in the liquid phase l - [kg/m ³]	R_g	Universal gas constant - [V C/(K mol)]
ρ_{vs}	Vapor saturation density - [kg/m ³]	S	Surface - [m ²]
ρ_w	Water density - [kg/m ³]	t	Time - [h]
$\tilde{\square}$	Non-linear variable notation	V	Volume - [m ³]
$\varepsilon^{l,eq}$	Sorption hysteresis function	W	Weight function time domain $W(t)$
ε^l	Liquid phase volume fraction - [m ³ /m ³]	w	Weight function spatial domain $w(x, y, z)$
ε_p	Porosity - [m ³ /m ³]	z_i	Valence - [-]
ε_v	Vapor phase volume fraction - [m ³ /m ³]		
ξ_0	Dielectricity coefficient of vacuum - [V/m]		

1 Introduction

Coupled mass transport modeling, based on continuum theories, is widely used and generally accepted as a valuable tool within different research fields, e.g. materials science, chemical engineering, soil mechanics and bio mechanics. The numerical solution described in this paper is aimed at describing durability-related changes in the porous system of concrete. Changes in concentration of the initial pore solution species lead to precipitation/dissolution reactions. To evaluate the durability of concrete, which often is in a time frame of more than 100 years, detailed and well-founded models for description of mass transport and chemical equilibrium are essential. The Poisson-Nernst-Planck (PNP) equations are often used for describing the flux of ionic components in the pore solution of concrete. The PNP system of equations is found in different extended/modified versions and is based on different assumptions. The extended PNP version presented by Johannesson (2010) includes convection of the liquid phase using the saturation degree of the porous system as driving potential. Chemical reactions are shown in the formulation of the model by Johannesson (2010), but are omitted in the numerical solution. A PNP version presented by Samson and Marchand (2007) takes into account ionic activity potential of the species and chemical reactions between a limited number of species and solid-liquid interactions. The extended PNP version used by Hosokawa et al. (2011) emphasizes the chemical reactions, by introducing a coupling between the geochemical code PHREEQC and the PNP solution. The models in (Johannesson, 2010; Samson and Marchand, 2007; Hosokawa et al., 2011) all include a solution of the Poisson equation for the electrical field, compared to the zero-current approach, e.g. presented by (Truc et al., 2000; Yuan et al., 2010). Different solution methods are proposed for the PNP system, where the finite element method has been used in (Samson and Marchand, 1999; Johannesson, 2010), a finite different algorithm is used in (Rudolph, 1994; Truc et al., 2000; Yuan et al., 2010) and a meshless solution approach is presented in La Rocca and Power (2005).

A well-known effect from wetting and drying cycles of porous materials such as concrete is the sorption hysteresis phenomenon, where the vapor-liquid ratio is dependent on the sorption history. The mechanisms causing the sorption hysteresis in concrete are not sufficiently understood to construct a thermodynamical continuum-based model. Therefore treatment of hysteresis is to a large extent limited to numerical approaches, see Ristinmaa et al. (2011). Different numerical approaches to model the sorption hysteresis are found for concrete, e.g. in Derluyn et al. (2012) which adopts the independent domain theory, where the pressure and temperature are used as driving potential for the moisture flow. The independent domain theory was originally described by Everett (1955). Another approach based on the pore connectivity is presented in Ranaivomanana et al. (2011), which was developed by Ishida et al. (2007). An approach suggested by Johannesson and Nyman (2010) is a direct method for describing the hysteresis effect by a mass exchange term. This model is based on a two-phase flow model, where the saturation degree and the relative humidity are used as driving potentials for the liquid and vapor phases, respectively.

In this paper a numerical finite element solution for an extended version of the PNP system of equations is given. The extended PNP system presented assembles the PNP system described in Johannesson (2010) with the two-phase vapor and liquid convection model described in Johannesson and Nyman (2010). The present paper focuses on the derivation of the numerical finite element (FE) solution and discusses the influence of the two-phase model on the pore solution. Chemical interactions are omitted in the numerical solution, which is a significant simplification of the physical system. The global responses from two different approaches within the sorption hysteresis model are compared in order to see deviations between a simple approach and a complex approach. The applicability and the simulation outcome are illustrated by a numerical example of cement-based material exposed to external relative humidity variations.

2 Numerical model

The governing system of equations, describing the mass transport in the porous network, is presented in terms of a strong form and a weak form, where the Dirichlet boundary conditions are utilized. The weak form leads to a transient finite element solution by a single-parameter time stepping scheme. The FE formulation is written out in details, in order to facilitate the reproducibility of the results presented in Sec. 3.

2.1 Governing system of equations (strong formulation)

The extended PNP equations are adopted from (Bennethum and Cushman, 2002a,b; Johannesson, 2010), where combined hybrid mixture theory and averaging are utilized to obtain macroscopic field equations for reactive mass transport problems. The complete set of field equations for swelling porous materials, including general assumptions and the averaging procedure used, is found in Bennethum and Cushman (2002a). Details for the appertaining constitutive theory is found in Bennethum and Cushman (2002b) and a review of the two papers is given by Johannesson (2010) together with a numerical solution procedure.

Definitions following the hybrid mixture theory as described in Johannesson (2010); Bennethum and Cushman (2002a) are introduced. The particle motion function χ_j is defined as $\mathbf{x} = \chi_j(\mathbf{X}_j, t)$, where \mathbf{x} is the spatial position, \mathbf{X}_j is the material coordinate and t is the time. The constituent i density in the liquid phase l is defined as $\rho_i^l = \rho_i^l(\mathbf{x}, t)$, leading to the constituent concentration $c_i^l = c_i^l(\mathbf{x}, t) = \rho_i^l/\rho^l$. The volume fraction of the liquid phase ε^l is defined as $\varepsilon^l = \varepsilon^l(\mathbf{x}, t) = V^l/V$, where V^l is representative volume of the liquid phase and V is the total volume. The conservation of charge is described by Gauss' law, by the assumption that the total

electrical field intensity \mathbf{E} is the gradient of the total electric intensity potential Φ , so $\mathbf{E} = \nabla\Phi$, hence the electrical field is assumed to be curl free. Chemical interactions are introduced as q_i , as a mass exchange term in the mass balance equation. It follows from hybrid mixture theory that $\sum_i q_i = 0$ must be satisfied. The general PNP equation in (Bennethum and Cushman, 2002b; Johannesson, 2010) is obtained by the Coleman-Noll procedure assuming the Helmholtz free energy A for the whole mixture is expressed by $A = A(\varepsilon^l, \varepsilon^l \rho_i^l, T)$, where T is the temperature. The PNP system adopted here is derived in (Bennethum and Cushman, 2002b; Johannesson, 2010) and takes the form

$$\varepsilon^l \frac{\partial c_i^l}{\partial t} + c_i^l \frac{\partial \varepsilon^l}{\partial t} = \nabla \cdot (D_i^l \varepsilon^l \nabla c_i^l + D_i^l c_i^l \nabla \varepsilon^l - A_i^l z_i \varepsilon^l c_i^l \nabla \Phi) + \mathbf{v}^{l,s} \cdot \varepsilon^l \nabla c_i^l + \mathbf{v}^{l,s} \cdot c_i^l \nabla \varepsilon^l + q_i; \quad i = 1, 2, \dots, m \quad (1)$$

where D_i^l is the diffusion coefficient for constituent i and A_i^l is the ionic mobility. The relation $A_i^l = D_i^l F / (R_g T)$ is used, see e.g. Johannesson (2010), where F is Faraday's constant and R_g is the universal gas constant. z_i is the valence state of constituent i and $\mathbf{v}^{l,s}$ is the liquid velocity with respect to the solid s . The liquid velocity is assumed by $\mathbf{v}^{l,s} = -D_{\varepsilon^l} \nabla \varepsilon^l$, see Johannesson (2010), and will be determined as a lumped value in the numerical scheme.

The chemical equilibrium term q_i is omitted in the further discretization towards the FE formulation and in the numerical example. A common assumption in reactive transport modeling is that the chemical reactions are in equilibrium and occur instantaneously upon changes in ionic concentrations, see e.g. Hosokawa et al. (2011). These assumptions motivate an operator splitting approach for the numerical solution method. The operator splitting approach completely decouples the chemistry and transport equations on a differential equation level. Solution methods to chemical equilibrium are not given in this paper, see e.g. Parkhurst et al. (1999) for a mass action law solution or Wagner et al. (2012) for Gibbs energy minimization.

The electrical potential of the problem considered is determined by Gauss' law together with appropriate constitutive relations, see Johannesson (2010), which leads to the Poisson part of the PNP equation system. The Poisson equation is coupled to the diffusion equation (1) by the electrical potential Φ . The Poisson equation is given as

$$\xi_d \xi_0 \nabla^2 \Phi = F \sum_{i=1}^m c_i^l z_i \quad (2)$$

where ξ_d is the relative dielectricity coefficient and ξ_0 is the dielectricity coefficient of vacuum.

A generalized version of Darcy's law is derived in Bennethum and Cushman (2002b) and it is shown in (Bennethum and Cushman, 2002b; Johannesson, 2010) how the volume fraction of an incompressible liquid in a porous material can be used as driving potential for the liquid flow. It is also shown how the liquid-phase diffusion constant D_{ε^l} is related to the unjacketed compressibility K' , the permeability K^l and the liquid viscosity μ^l . The liquid-flow equation from Bennethum and Cushman (2002b) is employed in (Nyman et al., 2006; Johannesson and Nyman, 2010) and further modified to account for vapor flow in terms of the sorption hysteresis coupling.

The mass balance equation for the liquid flow in Johannesson (2010) is extended by a mass exchange term \hat{m}_l in (Nyman et al., 2006; Johannesson and Nyman, 2010) and the same type of mass balance equation is employed to the vapor flow. The exchange terms for the liquid and vapor phases are related as $\hat{m}_l = -\hat{m}_v$, which is a result from the mixture theory. It is assumed in (Nyman et al., 2006; Johannesson and Nyman, 2010) that the solid skeleton of the porous material is restricted by $\partial \rho_s / \partial t = \partial \varepsilon_s / \partial t = 0$. The volume fractions are restricted by $\varepsilon_s + \varepsilon_p = 1$

and $\varepsilon_l + \varepsilon_v = \varepsilon_p$, where the indices s , p and v are the solid phase, the porosity and the vapor phase, respectively. The liquid phase is assumed incompressible and the diffusion coefficient is a function of the liquid volume fraction $D_{\varepsilon^l} = D_{\varepsilon^l}(\varepsilon^l)$. The derived equation for the volume fraction of liquid in (Nyman et al., 2006; Johannesson and Nyman, 2010) is

$$\rho_w \frac{\partial \varepsilon^l}{\partial t} = \nabla \cdot (D_{\varepsilon^l} \nabla \varepsilon^l) + \hat{m}_l \quad (3)$$

where ρ_w is the water density. Using the volume fraction restrictions and also assuming constant porosity, together with the mass balance postulate, yields the vapor flow expression, as presented in (Nyman et al., 2006; Johannesson and Nyman, 2010), as

$$\rho_{vs} (\varepsilon_p - \varepsilon^l) \frac{\partial \phi_v}{\partial t} - \rho_{vs} \phi_v \frac{\partial \varepsilon^l}{\partial t} = \nabla \cdot (D_\phi \nabla \phi_v) - \hat{m}_v \quad (4)$$

where ρ_{vs} is the vapor saturation density and ϕ_v is the relative humidity, defined as $\phi_v = \rho_v / \rho_{vs}$, where ρ_v is the actual mass density of the vapor in the pores of the material. In order to represent experimental results, using the suggested model, the diffusion coefficient D_ϕ needs to be strongly dependent on the volume fraction of water in the pores of the material, that is, $D_\phi = D_\phi(\varepsilon^l)$.

The mass exchange term is a kinetic term involving the effect of the sorption hysteresis. The proposed function in (Nyman et al., 2006; Johannesson and Nyman, 2010) is

$$\hat{m}_l = \hat{m}_v = R (\varepsilon^{l,eq}(\phi_v) - \varepsilon^l) \quad (5)$$

where R is a rate constant for the mass exchange and $\varepsilon^{l,eq}(\phi_v)$ is the function describing the equilibrium state between the liquid and vapor phases. The numerical establishment of $\varepsilon^{l,eq}(\phi_v)$ is explained in Section 2.3.

2.2 Finite element formulation (weak formulation)

A weak formulation of the governing system of equations (1)-(4) is established in order to obtain a finite element formulation of the complete equation system. The weighted residual method using Galerkin's approximation is adopted, together with a direct single time stepping scheme for the transient solution, see (Ottosen and Petersson, 1992; Zienkiewicz et al., 2005). The governing equation system is non-linear in different state variables and the FE solution from the single time stepping scheme is improved by a modified Newton-Raphson iteration scheme, see Ottosen and Ristinmaa (2005). The modified Newton-Raphson iteration scheme is employed as it reduces computational time compared to the complete scheme and still effectively minimizes the residual of the problem.

Two arbitrary weight functions are introduced, $w(x, y, z)$ in the spatial domain and $W(t)$ in the time domain. The notation $\tilde{\square}$ is introduced to emphasize the non-linear state variables, e.g. $\tilde{\varepsilon}^l$. Multiplying the weight functions, using matrix notation, with (1), and using the Green-Gauss

theorem yields the weak form, as

$$\begin{aligned}
& \int_{t_1}^{t_2} W \int_V w \tilde{\varepsilon}^l \frac{\partial c_i^l}{\partial t} dV dt + \\
& \int_{t_1}^{t_2} W \int_V w \tilde{c}_i^l \frac{\partial \varepsilon^l}{\partial t} dV dt = - \int_{t_1}^{t_2} W \int_V (\nabla w)^T (D_i^l \tilde{\varepsilon}^l \nabla c_i^l + D_i^l \tilde{c}_i^l \nabla \varepsilon^l - A_i^l \tilde{c}_i^l z_i \tilde{\varepsilon}^l \nabla \Phi) dV dt + \\
& \int_{t_1}^{t_2} W \oint_S w \mathbf{j}_i^l \mathbf{n} dS dt + \int_{t_1}^{t_2} W \int_V w \mathbf{v}^{l,s} \tilde{\varepsilon}^l \nabla c_i^l dV dt + \\
& \int_{t_1}^{t_2} W \int_V w \mathbf{v}^{l,s} \tilde{c}_i^l \nabla \varepsilon^l dV dt
\end{aligned} \tag{6}$$

where \mathbf{j}_i^l is the boundary flux at the surface S , of the i constituent, \mathbf{n} is the outward pointing normal to the surface and V is the volume considered.

The weak form of the Poisson equation (2) is obtained in the same fashion, multiplying the arbitrary weight functions and using the Green-Gauss theorem. The weak form is given as

$$\int_V (\nabla w)^T \xi_d \xi_0 \nabla \Phi dV = \int_V w F \sum_{i=1}^n \tilde{c}_i z_i dV - \oint_S w \mathbf{j}^\Phi \mathbf{n} dS \tag{7}$$

where \mathbf{j}^Φ is the electrical displacement at the surface.

The weak form of the liquid-phase equation (3) is given as

$$\begin{aligned}
& \int_{t_1}^{t_2} W \int_V w \rho_w \frac{\partial \varepsilon^l}{\partial t} dV dt = - \int_{t_1}^{t_2} W \int_V (\nabla w)^T (D_{\varepsilon^l} \nabla \varepsilon^l) dV dt + \\
& \int_{t_1}^{t_2} W \oint_S w \mathbf{j}^l \mathbf{n} dS dt + \int_{t_1}^{t_2} W \int_V w R (\varepsilon^{l,eq}(\tilde{\phi}_v) - \varepsilon^l) dV dt
\end{aligned} \tag{8}$$

where \mathbf{j}^l is the liquid-phase flux at the surface.

The weak form of the vapor-phase equation (4) is given as

$$\begin{aligned}
& \int_{t_1}^{t_2} W \int_V w \rho_{vs} (\varepsilon_p - \tilde{\varepsilon}^l) \frac{\partial \phi_v}{\partial t} dV dt - \\
& \int_{t_1}^{t_2} W \int_V w \rho_{vs} \tilde{\phi}_v \frac{\partial \varepsilon^l}{\partial t} dV dt = - \int_{t_1}^{t_2} W \int_V (\nabla w)^T (D_\phi \nabla \phi_v) dV dt + \\
& \int_{t_1}^{t_2} W \oint_S w \mathbf{j}^\phi \mathbf{n} dS dt - \int_{t_1}^{t_2} W \int_V w R (\varepsilon^{l,eq}(\tilde{\phi}_v) - \varepsilon^l) dV dt
\end{aligned} \tag{9}$$

where \mathbf{j}^ϕ is the vapor-phase flux at the surface.

The state variables in the weak formulations are approximated by the general expansion \mathbf{Na} , where \mathbf{N} is the global shape function and \mathbf{a} contains the state variables. In the one dimensional case, the local linear shape function is given as $\mathbf{N} = [1 - x/l_e, x/l_e]$, where l_e is the element length. The arbitrary spatial weight function w is approximated with the same general expansion following Galerkin's method. The notation $\hat{\square}$ is introduced to indicate an approximated variable. The approximated variables are

$$\hat{c}_i^l = \mathbf{Na}^i(a); \quad \hat{\Phi} = \mathbf{Na}^\Phi(b) \quad \hat{\varepsilon}^l = \mathbf{Na}^l(c); \quad \hat{\phi}_v = \mathbf{Na}^\phi(d); \quad \hat{w} = \mathbf{c}^T \mathbf{N}^T(e) \quad (10)$$

where the index j is the number of spatial elements. The arbitrary property of the spatial weight function and the fact that \mathbf{c} contains scalars according to Galerkin's approximation, yields $\mathbf{c} = \mathbf{c}^T$, so that $\mathbf{Nc} = \mathbf{c}^T \mathbf{N}^T$. The spatial discretization of spatial gradients are approximated by the general expansion \mathbf{Ba} , where $\mathbf{B} = \nabla \mathbf{N}$. The approximated derivatives are

$$\nabla \hat{c}_i^l = \mathbf{Ba}^i(a); \quad \nabla \hat{\varepsilon}^l = \mathbf{Ba}^l(b); \quad \nabla \hat{\Phi} = \mathbf{Ba}^\Phi(c); \quad \nabla \hat{\phi}_v = \mathbf{Ba}^\phi(d); \quad \nabla \hat{w} = \mathbf{Bc}(e) \quad (11)$$

Substituting the approximated variables (10)-(11), into the weak formulations (6)-(9) and use that the arbitrary property \mathbf{c} is independent of x, y, z and the fact that the expression should hold for any arbitrary \mathbf{c}^T -vector, yields the FE formulation $\int_{t_1}^{t_2} W [\mathbf{C}\dot{\mathbf{a}} + \mathbf{Ka} - \mathbf{f}] dt$. The sub-matrices for the global mass matrix \mathbf{C} , stiffness matrix \mathbf{K} and load vector \mathbf{f} are formulated in terms of the global matrix system. The time derivatives are defined as $\dot{\mathbf{a}} = \mathbf{da}/dt$. The sub-matrices of the mass matrix \mathbf{C} are determined as

$$\mathbf{C}^i = \int_V \mathbf{N}^T \hat{\varepsilon}^l \mathbf{N} dV(a); \quad \mathbf{W}^i = \int_V \mathbf{N}^T \hat{c}_i^l \mathbf{N} dV(b); \quad \mathbf{C}^\varepsilon = \int_V \mathbf{N}^T \rho_w \mathbf{N} dV(c) \quad (12)$$

$$\mathbf{C}^\phi = \int_V \mathbf{N}^T \rho_{vs} (\varepsilon_p - \hat{\varepsilon}^l) \mathbf{N} dV(a); \quad \mathbf{M} = - \int_V \mathbf{N}^T \rho_{vs} \hat{\phi}_v \mathbf{N} dV(b) \quad (13)$$

and the global mass matrix \mathbf{C} is constructed as

$$\mathbf{C}\dot{\mathbf{a}} = \begin{bmatrix} \mathbf{C}^1 & 0 & 0 & 0 & 0 & \mathbf{W}^1 & 0 \\ 0 & \mathbf{C}^2 & 0 & 0 & 0 & \mathbf{W}^2 & 0 \\ & & \ddots & & & \vdots & \\ 0 & 0 & 0 & \mathbf{C}^i & 0 & \mathbf{W}^i & 0 \\ 0 & 0 & 0 & 0 & 0 & 0 & 0 \\ 0 & 0 & 0 & 0 & 0 & \mathbf{C}^\varepsilon & 0 \\ 0 & 0 & 0 & 0 & 0 & \mathbf{M} & \mathbf{C}^\phi \end{bmatrix} \begin{bmatrix} \dot{\mathbf{a}}_1 \\ \dot{\mathbf{a}}_2 \\ \vdots \\ \dot{\mathbf{a}}_i \\ \dot{\mathbf{a}}_\Phi \\ \dot{\mathbf{a}}_\varepsilon \\ \dot{\mathbf{a}}_\phi \end{bmatrix} \quad (14)$$

The sub-matrices in the stiffness matrix \mathbf{K} are determined as

$$\mathbf{K}^i = \int_V \mathbf{B}^T D_i^l \hat{\varepsilon}^l \mathbf{B} dV(a); \quad \mathbf{P}^i = \int_V \mathbf{B}^T D_i^l \hat{c}_i^l \mathbf{B} dV(b); \quad \mathbf{V}^\varepsilon = \int_V \mathbf{B}^T A_i^l \hat{c}_i^l z_i \hat{\varepsilon}^l \mathbf{B} dV(c) \quad (15)$$

$$\mathbf{K}^\Phi = \int_V \mathbf{B}^T \xi_d \xi_0 \mathbf{B} dV(a); \quad \mathbf{E}^i = \int_V \mathbf{N}^T F z_i \mathbf{N} dV(b); \quad \tilde{\mathbf{K}}^i = \int_V \mathbf{N}^T v^{l,s} \hat{\varepsilon}^l \mathbf{B} dV(c) \quad (16)$$

$$\tilde{\mathbf{P}}^i = \int_V \mathbf{N}^T v^{l,s} \hat{c}_i^l \mathbf{B} dV(a); \quad \mathbf{K}^\varepsilon = \int_V \mathbf{B}^T D_\varepsilon^l \mathbf{B} dV(b); \quad \mathbf{R}^\varepsilon = \int_V \mathbf{B}^T \mathbf{R} \mathbf{B} dV(c) \quad (17)$$

$$\mathbf{R}_\varepsilon^{\text{eq}} = \int_V \mathbf{B}^T R \tilde{\varepsilon}^{l,\text{eq}}(\phi_v) \mathbf{B} dV \quad (a); \quad \mathbf{K}^\phi = \int_V \mathbf{B}^T D_\phi \mathbf{B} dV \quad (b) \quad (18)$$

and the sub-matrices are placed in the global system stiffness matrix \mathbf{K} , as

$$\mathbf{K}\mathbf{a} = \begin{bmatrix} \mathbf{K}^1 + \tilde{\mathbf{K}}^1 & 0 & 0 & 0 & \mathbf{V}^1 \mathbf{P}^1 + \tilde{\mathbf{P}}^1 & 0 \\ 0 & \mathbf{K}^2 + \tilde{\mathbf{K}}^2 & 0 & 0 & \mathbf{V}^2 \mathbf{P}^2 + \tilde{\mathbf{P}}^2 & 0 \\ & & \ddots & & \vdots & \vdots \\ 0 & 0 & 0 & \mathbf{K}^i + \tilde{\mathbf{K}}^i & \mathbf{V}^i \mathbf{P}^i + \tilde{\mathbf{P}}^i & 0 \\ \mathbf{E}^1 & \mathbf{E}^2 & \dots & \mathbf{E}^i & \mathbf{K}^\Phi & 0 \\ 0 & 0 & 0 & 0 & 0 & \mathbf{K}^\varepsilon + \mathbf{R}^\varepsilon \\ 0 & 0 & 0 & 0 & 0 & -\mathbf{R}_\varepsilon^{\text{eq}} \quad \mathbf{K}^\phi - \mathbf{R}^\varepsilon \end{bmatrix} \begin{bmatrix} \mathbf{a}_1 \\ \mathbf{a}_2 \\ \vdots \\ \mathbf{a}_i \\ \mathbf{a}_\Phi \\ \mathbf{a}_\varepsilon \\ \mathbf{a}_\phi \end{bmatrix} \quad (19)$$

The load vector \mathbf{f} is established as boundary loads only, as the load terms q_i from the chemical equilibrium are omitted:

$$\mathbf{f} = \begin{bmatrix} \oint_S \mathbf{N}^T \mathbf{j}_1^l \mathbf{n} dS \\ \oint_S \mathbf{N}^T \mathbf{j}_2^l \mathbf{n} dS \\ \vdots \\ \oint_S \mathbf{N}^T \mathbf{j}_i^l \mathbf{n} dS \\ \oint_S \mathbf{N}^T \mathbf{j}^\Phi \mathbf{n} dS \\ \oint_S \mathbf{N}^T \mathbf{j}^l \mathbf{n} dS \\ \oint_S \mathbf{N}^T \mathbf{j}^\phi \mathbf{n} dS \end{bmatrix} \quad (20)$$

The matrix system can be solved by different time discrete algorithms. A single parameter time stepping scheme is adopted for this solution, see e.g. Zienkiewicz et al. (2005). The time domain is discretized by

$$\mathbf{a}(t) \approx \hat{\mathbf{a}}(t) = \left(1 - \frac{\tau(t)}{\Delta t}\right) \mathbf{a}_n + \left(\frac{\tau(t)}{\Delta t}\right) \mathbf{a}_{n+1} \quad (21)$$

where $\tau = t - t_n$ and n is the discrete time step number and \mathbf{a}_{n+1} is the vector of the unknown state variables. A weighing parameter θ , with a value between $[0, 1]$ is introduced as

$$\theta = \frac{1}{\Delta t} \frac{\int_{t_1}^{t_2} W \tau d\tau}{\int_{t_1}^{t_2} W d\tau} \quad (22)$$

where $\theta = 0$ gives an explicit time integration scheme. Inserting (21) and (22) in the spatially discretized matrix formulation and solve for \mathbf{a}_{n+1} , yields

$$\mathbf{a}_{n+1} = (\mathbf{C}_n + \Delta t \theta \mathbf{K}_n)^{-1} [(\mathbf{C}_n - \Delta t (1 - \theta) \mathbf{K}_n) \mathbf{a}_n + \mathbf{f}_n + \theta (\mathbf{f}_{n+1} - \mathbf{f}_n)] \quad (23)$$

A modified version of the Newton-Raphson algorithm is used to improve the solution of the non-linear system, see e.g. Ottosen and Ristinmaa (2005) and Johannesson (2010). The modified Newton-Raphson algorithm does not consider the true tangential stiffness with the cost

of increasing the number of iterations before reaching a convergence criterion. Using $\theta = 1$ in eq. (23) and introducing a residual vector $\boldsymbol{\psi}^i$ yields

$$\boldsymbol{\psi}^{i-1} = \mathbf{C}_{n+1}^{i-1} \frac{1}{\Delta t} (\mathbf{a}_{n+1}^{i-1} - \mathbf{a}_n) + \mathbf{K}_{n+1}^{i-1} \mathbf{a}_{n+1}^{i-1} - \mathbf{f}_{n+1} \quad (24)$$

where i is the iteration number. Note that the non-linear parts of the mass and stiffness matrices are updated to $n + 1$ for the first Newton-Raphson iteration $i = 1$. Both the mass and stiffness matrices are updated in the following Newton-Raphson iterations. The iteration scheme is established between eq. (24) and a modified Taylor expansion of this, see Ottosen and Ristinmaa (2005) and Johannesson (2010) for a detailed derivation. The Taylor expansion, where the higher order terms are ignored, is

$$-\delta \boldsymbol{\psi}^{i-1} = \left[\mathbf{C}_{n+1}^{i-1} \frac{1}{\Delta t} + \mathbf{K}_{n+1}^{i-1} \right] (\mathbf{a}_{n+1}^i - \mathbf{a}_{n+1}^{i-1}) \quad (25)$$

where the improved result \mathbf{a}_{n+1}^i is determined and δ is a type of constant acceleration factor similar to that used in line search, see e.g. Ottosen and Ristinmaa (2005). The acceleration factor is added for this work in order to solve the numerical examples in Sec. 3. The eqs. (24) and (25) are solved sequentially until a sufficient convergence criterion is reached.

2.3 Sorption hysteresis

A recapitulation of the numerical procedure for establishment of $\varepsilon^{l,eq}(\phi_v)$ from the mass exchange term in eq. (5) is given in the following section. The procedure adopted is from (Nyman et al., 2006; Johannesson and Nyman, 2010) where the reader may find further details. The overall concept for this approach is to define two sorption boundary functions, an upper boundary for desorption and a lower boundary for absorption. The equilibrium function, denoted the ‘‘current’’ equilibrium function, that is, $\varepsilon^{l,eq}(\phi_v) = \varepsilon^{l,eq,cu}(\phi_v)$, is a function with values between or equal to the boundary function values. A sequence of values between the boundary functions is often referred to as a scanning curve or an inner sorption curve.

The liquid-equilibrium function $\varepsilon^{l,eq,cu}(\phi_v)$ and the boundary functions are defined as a simple third-order polynomial in (Nyman et al., 2006; Johannesson and Nyman, 2010), as

$$\varepsilon^{l,eq,*}(\phi_v) = h_1^* \phi_v + h_2^* \phi_v^2 + h_3^* \phi_v^3$$

where the * is either, *cu* for current equilibrium function, *lb* for lower boundary function or *ub* for upper boundary. The boundary functions $\varepsilon^{l,eq,lb}(\phi_v)$ and $\varepsilon^{l,eq,ub}(\phi_v)$ have constant polynomial coefficients $\{h_1^*, h_2^*, h_3^*\}$, whereas the current equilibrium function $\varepsilon^{l,eq,cu}(\phi_v)$ depends on the sorption history and the polynomial coefficients change accordingly. A re-establishment of $\varepsilon^{l,eq,cu}(\phi_v)$ is induced by a change in sorption ‘direction’ from absorption to desorption or desorption to absorption. The constructed function is in this case denoted $\varepsilon^{l,eq,in}(\phi_v)$. A sorption change is determined between time steps n and $n + 1$, so that the constructed function $\varepsilon^{l,eq,in}(\phi_v)$ becomes the current function $\varepsilon^{l,eq,cu}(\phi_v)$ in the following time step. The determination of the equilibrium function polynomial coefficients for $\varepsilon^{l,eq,in}(\phi_v)$ is determined from a set of relations given in (Nyman et al., 2006; Johannesson and Nyman, 2010) presented here in a general format, as

$$\left. \frac{d\varepsilon^{l,eq,in}}{d\phi_v} \right|_{\phi_v=(\phi_v)_{n+1}} = K_\beta \left. \frac{d\varepsilon^{l,eq,cu}}{d\phi_v} \right|_{\phi_v=(\phi_v)_{n+1}}; \quad 0 \leq K_\beta \leq 1 \quad (26)$$

$$\varepsilon^{l,eq,in}((\phi_v)_{n+1}) = \varepsilon^{l,eq,cu}((\phi_v)_{n+1}) \quad (27)$$

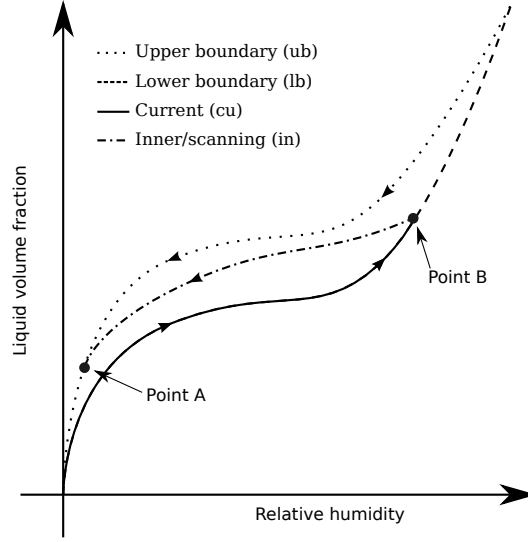


Figure 1: Illustration of a change from absorption to desorption according to the numerical restrictions shown in eq. (26) to (29). Point A corresponds to eq. (28) and (29), which is the tangent relative humidity ϕ_v^{tang} using that $\alpha = ub$. Point B corresponds to eq (26) to (27), in which the current equilibrium function cu equals the lower boundary function lb in this case.

$$\left. \frac{d\varepsilon^{l,eq,in}}{d\phi_v} \right|_{\phi_v=\phi_v^{tang}} = \left. \frac{d\varepsilon^{l,eq,\alpha}}{d\phi_v} \right|_{\phi_v=\phi_v^{tang}} \quad (28)$$

$$\varepsilon^{l,eq,in}(\phi_v^{tang}) = \varepsilon^{l,eq,(\alpha)}(\phi_v^{tang}); \quad [\varepsilon^{l,eq,in}(\phi_v^{tang}), \phi_v^{tang}] \in [0, 1] \quad (29)$$

where K_β is a material parameter related to the angle at a sorption change point from absorption to desorption or desorption to absorption, so $\beta = ab \rightarrow de$ or $\beta = de \rightarrow ab$, and may differ in its value for these two cases. The notation *tang* is the tangent determined in eq. (28) and α is either *lb* or *ub* depending on the change in sorption direction. The procedure from eqs. (26)-(29) is graphically illustrated in Fig 1.

3 Numerical example – effect of sequential boundary conditions

A numerical example was constructed to show the finite element solution of the extended PNP system and to compare two approaches within the sorption hysteresis model. The example is focused on the response of the porous material when subjected to a sequential boundary condition in terms of the vapor phase. The response of the ionic concentrations in the pore solution is of interest as this affects the chemical equilibrium. The sorption hysteresis model described in 2.3 is compared with a more simple approach that is dependent on an average sorption curve defined here as $\varepsilon^{l,eq,avg} = (\varepsilon^{l,eq,lb} + \varepsilon^{l,eq,ub})/2$. The simple approach is employed so that $\varepsilon^{l,eq,in} = \varepsilon^{l,eq,cu} = \varepsilon^{l,eq,avg}$ regardless of any change in sorption from absorption to desorption or desorption to absorption. In relation to cement-based materials, this example could for instance be a part of a concrete bridge structure placed in seawater, where the tide changes the boundary conditions for the vapor and liquid phases.

Table 1: Clinker composition of a cement

	CaO	SiO ₂	Al ₂ O ₃	Fe ₂ O ₃	SO ₃	K ₂ O	Na ₂ O
mass%	0.64	0.22	0.05	0.04	0.03	0.0078	0.0015

Table 2: Diffusion properties for ionic components used in this case study. The values are in line with Hosokawa et al. (2011).

	OH ⁻	H ⁺	Al(OH) ₄ ⁻	Al(OH) ₃	Al(OH) ₂ ⁺	Al ³⁺
$D_i^{l,0} \cdot 10^{-8}$	0.5300	0.9311	0.5040	0.1040	0.1040*	0.0541
$A_i^{l,0} \cdot 10^{-6}$	0.2253	0.3958	0.2142	-	0.0442*	0.0229
z_i	-1	1	-1	-	1	3
$c_{i,initial}^l$	$3.4018 \cdot 10^{-2}$	$4.4998 \cdot 10^{-13}$	$1.6096 \cdot 10^{-4}$	$2.5167 \cdot 10^{-11}$	$8.2259 \cdot 10^{-17}$	$7.8315 \cdot 10^{-24}$
	CaOH ⁺	CaSO ₄	CaHSO ₄ ⁺	SO ₄ ²⁻	HSO ₄ ²⁻	H ₂ SiO ₄ ²⁻
$D_i^l \cdot 10^{-8}$	0.0792	0.0471	0.0471*	0.1070	0.1385	0.1100
$A_i^l \cdot 10^{-6}$	0.0337	-	0.0200*	0.0455	0.0589	0.0468
z_i	1	-	1	-2	-2	-2
$c_{i,initial}^l$	$2.1678 \cdot 10^{-2}$	$5.0461 \cdot 10^{-3}$	$5.1576 \cdot 10^{-3}$	$1.4533 \cdot 10^{-14}$	$7.1111 \cdot 10^{-3}$	$1.3253 \cdot 10^{-13}$
	Al(SO ₄) ₂ ⁻	AlOH ²⁺	H ₄ SiO ₄	Ca ²⁺	AlSO ₄ ⁺	H ₃ SiO ₄ ⁻
$D_i^l \cdot 10^{-8}$	0.1040*	0.1040*	0.1100*	0.0792	0.1040*	0.1100*
$A_i^l \cdot 10^{-6}$	0.0442*	0.0442*	-	0.0337	0.0442*	0.0468*
z_i	-1	1	-	2	1	-1
$c_{i,initial}^l$	$1.3680 \cdot 10^{-30}$	$1.2480 \cdot 10^{-31}$	$7.3585 \cdot 10^{-7}$	$1.4688 \cdot 10^{-9}$	$5.9757 \cdot 10^{-31}$	$2.6351 \cdot 10^{-7}$

* is an estimated value.

3.1 Input data and databases

The initially defined ionic composition of the pore solution for the numerical example is determined by a chemical-equilibrium calculation in PHREEQC, see Tab. 2. The clinker composition used in the initial chemical-equilibrium calculation is shown in Tab. 1. A modified version of the Cemdata07 thermodynamic database was used for the calculation, see (Möschner et al., 2009; Schmidt et al., 2008; Möschner et al., 2008; Lothenbach et al., 2008; Lothenbach and Winnefeld, 2006) for references to original Cemdata07 database. The database is modified for this case by substituting the jennite-type and tobermorite-type of phases by the solid solution as described in Kulik (2011). The initial chemical-equilibrium calculation yields a total of 28 different ionic species, whereof 18 are included in this example. The reduced representation of the solution, see Tab. 2, is in line with the reactive transport modeling of cement paste in Hosokawa et al. (2011).

The material parameters used in the numerical example are valid for a typical cement-based material. The diffusion properties in liquids, denoted $D_i^{l,0}$, used in the example are given in Tab. 2. The diffusion coefficients D_i^l are modified by a tortuosity factor $\tau = 0.009$, so that $D_i^l = D_i^{l,0}\tau$, see e.g. Johannesson (2003) where $\tau = 0.009$ is determined for a cement paste with water/cement ratio 0.5. The physical constants in the Poisson equation (2), relative dielectricity, dielectricity in vacuum and Faraday's constant, are $\xi_d = 78.54$, $\xi_0 = 8.854 \cdot 10^{-12}$ and $F = 96490$, respectively.

The example is solved as a one-dimensional problem, with linear spatial elements. The spatial length of the system considered is 0.05[m], discretized with 1999 elements. The transient part is solved with a time step length of $\Delta t = 1$ [h] and the total time for the simulation is 1750[h]. The weighting parameter for the time domain is $\theta = 1$, which is required in order to utilize the adopted Newton–Raphson scheme. The convergence criterion for the Newton–Raphson scheme is $\psi \cdot \psi < 10^{-12}$ and a maximum of 50 iterations if the criterion was not reached. The introduced iteration limit was reached in few time steps in the numerical example. The minimization minimum of the residual is in this case coupled to the magnitude of the rate constant R , which is later described by a penalty number. For this case we prioritize keeping the residual criterion low and the penalty number high, at the expense of an upper iteration limit. The low residual criterion ensures that the residual is minimized for non-linear parts of the system that are not directly coupled to R . The acceleration factor is $\delta = 0.08$.

The material properties for the vapor and liquid transport are the diffusion coefficients for the individual vapor and liquid phases, two boundary sorption isotherms and the K_β values describing the characteristics of the sorption hysteresis. The diffusion coefficient for the vapor phase is assumed constant at $D_{\phi_v} = 2.6 \cdot 10^{-11}$. The vapor diffusion coefficient is dependent on the liquid saturation, the constant value used here is an average value from the observations presented in Johannesson and Nyman (2010), where it is found that the magnitude is more important than its relation to the liquid content, see Johannesson and Nyman (2010). The diffusion coefficient for the liquid phase is assumed non-linear in terms of the liquid-phase volume ratio ε^l . The diffusion coefficient D_{ε^l} is defined by $D_{\varepsilon^l} = D_0 + D_1 \varepsilon^n$ where $D_0 = 10^{-12}$, $D_1 = 5 \cdot 10^{-7}$ and $n = 50$. The magnitude of n is set by the authors in order to emphasize the increased liquid transport when $\varepsilon^l \rightarrow 1$. The vapor-diffusion coefficient and liquid-diffusion coefficient and their relations to the liquid-phase volume ratio are shown in Fig. 2c. The liquid-diffusion coefficients adopted here are in line with values determined by Johannesson and Nyman (2010). The vapor-saturation density at room temperature is $\rho_{vs} = 0.017$ and the liquid-water density is $\rho_w = 1000$.

The sorption boundary functions $\varepsilon^{l,eq,lb}(\phi_v)$ and $\varepsilon^{l,eq,ub}(\phi_v)$ are experimentally fitted functions. The functions used in this example correspond to the shape of the upper and lower sorption boundaries of a typical cement-based material. The functions are restricted to be described by polynomials of a third degree, which makes it possible to represent a wide range of different porous materials. In this case the coefficients for the polynomial $\varepsilon^{l,eq,lb}(\phi_v)$ and $\varepsilon^{l,eq,ub}(\phi_v)$ are $\{h_1^{lb}, h_2^{lb}, h_3^{lb}\} = \{13/8, -15/4, 25/8\}$ and $\{h_1^{ub}, h_2^{ub}, h_3^{ub}\} = \{7/4, -13/4, 5/2\}$. The polynomial for the average approach is $\{h_1^{avg}, h_2^{avg}, h_3^{avg}\} = \{27/16, -7/2, 45/16\}$. The functions are shown in Fig. 2a. Mass exchange rates between the vapor and liquid phases R are reported in Johannesson (2002). A penalty number R_p is introduced for this case, as in Nyman et al. (2006), $R \rightarrow R_p$. $R_p = 10^7$ is assumed sufficiently high to assure that the equilibrium sorption state is always followed. The material constant K_β , used at changes in sorption direction, is assumed here to be $K_\beta = 0.3$, both in the case of adsorption and desorption scanning. The value is in accordance with the values used in Johannesson and Nyman (2010). The initial vapor and liquid content in the material is assumed to be at the relative humidity $\phi_v = 0.6$, which yields the liquid volume ratio $\varepsilon^{l,eq,cu}(0.6) = \varepsilon^{l,eq,lb}(0.6) = 0.3$, assuming the initial current equilibrium function is equal to the lower boundary function. The initial vapor content using the average approach is set to be the same as the approach including the scanning, which yields the liquid-phase content, $\varepsilon^{l,eq,avg}(0.6) = 0.36$.

The example considered is established as a boundary value problem for the overall mass transport, where a sequential function describes the relative humidity at the boundary. The sequential boundary function $\phi_v(t)$ is shown in Fig. 2b. From the definitions of relative humidity and the volume fraction of the liquid, we get that $\varepsilon^l(\phi_v) = \varepsilon^l(1) = 1$ at saturation. Boundary fluxes for the ions in the pore solution are established only when saturated boundary conditions

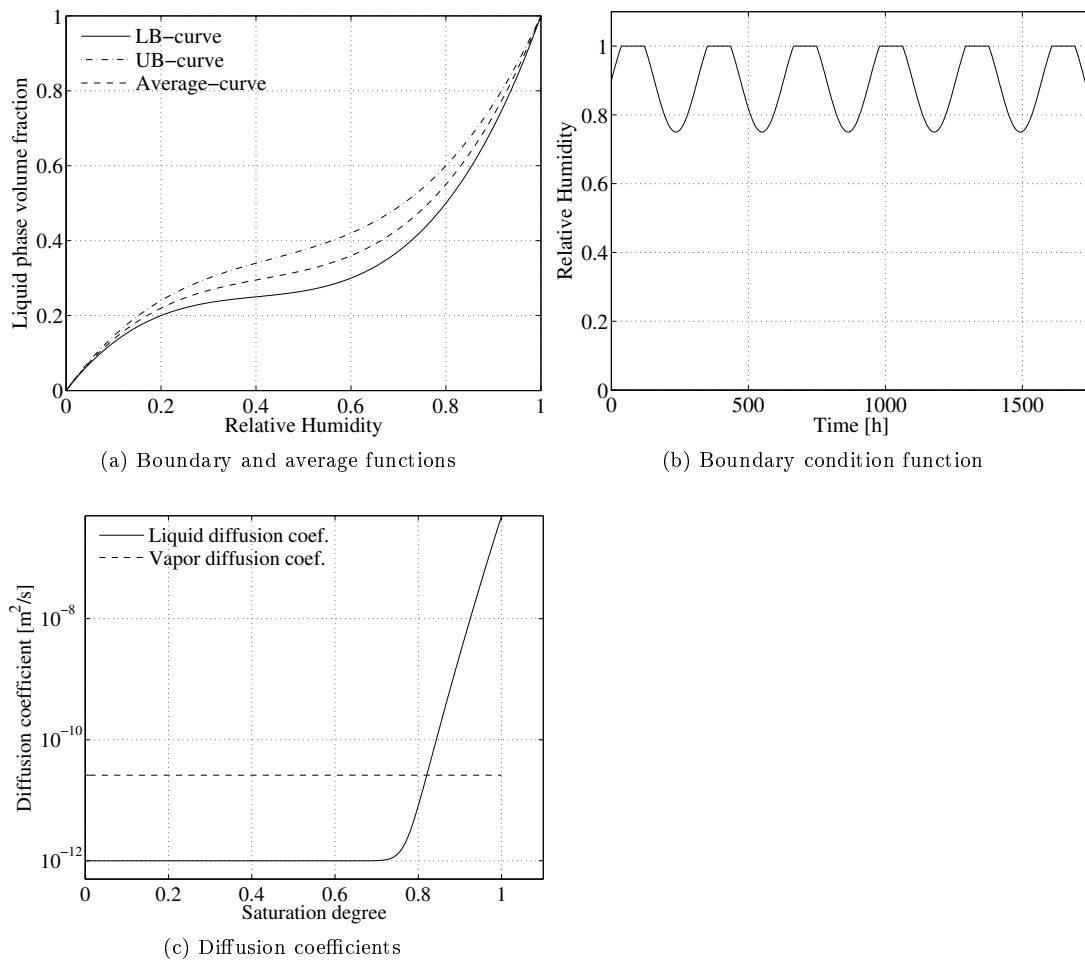


Figure 2: The sorption boundary functions, together with the average function of these, is shown in Fig. 2a. The sequential boundary condition for the vapor phase is shown in Fig. 2b. The relation between the vapor and liquid phase diffusion coefficients is shown in Fig. 2c.

occur, otherwise symmetric boundary conditions are applied. The boundary concentration for the ions when $\varepsilon^l(1) = 1$ is set to zero, except $[\text{OH}^-] = [\text{H}^+] = 10^{-7} [\text{mol/l}]$ which represents the pure water.

3.2 Results

The solution to the numerical example, determined by the hysteresis and the average approach is shown and compared. The results in Fig. 3 show the solution of equations (3) and (4), where 'Distance' on the x-axis refers to the distance from the exposed mass transport boundary. This yields that the exposed boundary (distance=0.0[m]) corresponds to the relative-humidity function given in Fig. 2b. The calculated liquid and vapor contents in the material are shown for three different time steps in Fig. 3. The Figs. (3a) and (3b) show the liquid and vapor content

at $t = 587[\text{h}]$ for both the hysteresis approach and the average approach considered. The vapor and liquid content shown at $t = 587[\text{h}]$ is shortly after a local minimum on the vapor boundary function was reached, see Fig. 2b. It is seen that the liquid content is slightly lower for the average approach in the first part of the spatial domain and higher from around $0.017[\text{m}]$ and further into the domain compared to the hysteresis approach. A significant deviation in liquid content between the two approaches is seen in the interval $[0.03[\text{m}], 0.05[\text{m}]]$. This is caused by the deviation in the determined initial liquid content and the fact that the effect of the boundary conditions have not reached this part of the domain yet. The Figs. 3c and 3d show the liquid and vapor content after $t = 1000[\text{h}]$. At this time in the simulation we have that the vapor boundary condition is $\phi_v = 1$ so that $\varepsilon^l = 1$, which results in that the liquid-phase diffusion becomes dominant in the first part of the spatial domain, according to the choice of diffusion coefficient relation shown in Fig. 2c. The average approach shows a larger or equal liquid content compared to the hysteresis approach. Figs. 3e and 3f show the final liquid and vapor content after $t = 1750[\text{h}]$. The liquid content determined from the average approach is slightly lower in the first part of the spatial domain and higher in the last part compared to the hysteresis approach.

Evaluating the solutions of the liquid and vapor content determined by the two approaches shows that the average approach differs slightly from the hysteresis approach in the spatial domain affected by the boundary conditions. This conclusion is only valid for the boundary condition and the boundary functions $\varepsilon^{l,eq,lb}(\phi_v)$ and $\varepsilon^{l,eq,ub}(\phi_v)$ studied here. The difference between the results from the two approaches decreases when the liquid content is $\varepsilon^l \rightarrow 1$, which is seen in Fig. 3c.

The history-dependent nodal sorption functions $\varepsilon^{l,eq,cu}(\phi_v, t)$ are shown for selected spatial elements in Fig. 4. Figs. 4a-4d show a projection of the history-dependent function. The initial liquid and vapor content for all elements are $(\varepsilon^l, \phi_v) = (0.3, 0.6)$ and $(\varepsilon^l, \phi_v) = (0.36, 0.6)$ for the hysteresis and average approach, respectively. Figs. 4a and 4b show the average approach and sorption hysteresis development at $0.0125[\text{m}]$ and $0.025[\text{m}]$ from the exposed boundary. The current equilibrium functions $\varepsilon^{l,eq,cu}(\phi_v)$ for the hysteresis approach are initially equal to the adsorption boundary isotherm $\varepsilon^{l,eq,lb}(\phi_v)$ and all spatial elements follow this towards saturated conditions, which is a result of the increased vapor content at the boundary. The hysteresis loops are clearly seen in the two figures and different scenarios handled by the numerical model are shown. Fig. 4a and its detailing in Fig. 4e clearly show the shift from a constructed current equilibrium function $\varepsilon^{l,eq,cu}(\phi_v, t)$ to the sorption boundary functions $\varepsilon^{l,eq,lb}(\phi_v)$ and $\varepsilon^{l,eq,ub}(\phi_v)$. Fig. 4b and its detailing in Fig. 4f show a shift between two inner scanning curves. The results shown in Figs. 4c and 4d are not affected by the hysteresis loop in the sense that the liquid content is monotonically increasing, which is also seen in Fig. 3. The time dependency of the average approach is difficult to show in the type of plot in Fig. 3, but it is shown here to emphasize some of the differences between the approaches shown in Fig. 3. The Figs. 4d and 4c show very well the difference in initial liquid content, which is seen at the end of the spatial domain in Fig. 3. Fig. 4c shows a significant difference between the two approaches in both the liquid and vapor contents.

A clear advantage of the two-phase sorption hysteresis model is also shown in Fig. 4, where it is seen that each of the spatial elements follow an individual sorption hysteresis function, which is only dependent on the sorption history in that element.

Some numerical issues were found for this particular numerical example, where the difference between $\varepsilon^{l,eq,lb}(\phi_v)$ and $\varepsilon^{l,eq,ub}(\phi_v)$ is decreasing when $\phi_v \rightarrow 1$. It was found necessary to introduce an upper limit on ϕ_v , for establishment of inner scanning curves, and restrict the magnitude of polynomial coefficient in $\varepsilon^{l,eq,in}(\phi_v)$. Tests showed that for this specific choice of $\varepsilon^{l,eq,lb}(\phi_v)$ and $\varepsilon^{l,eq,ub}(\phi_v)$, a sorption direction change at $\phi_v > 0.99$ should enforce a direct change from $\varepsilon^{l,eq,lb}(\phi_v) \rightarrow \varepsilon^{l,eq,ub}(\phi_v)$. For this purpose an upper limit for the polynomials coefficients was

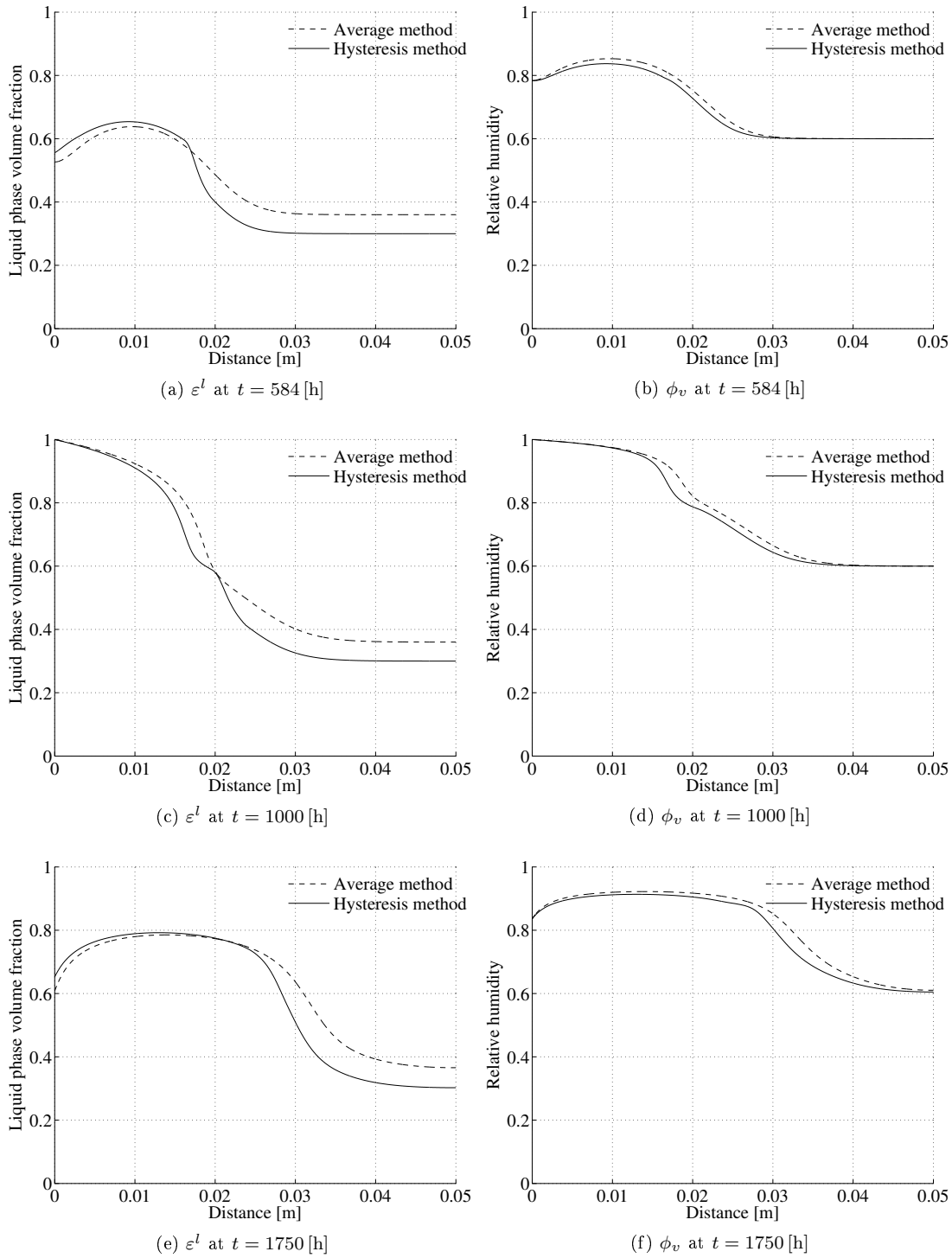


Figure 3: The liquid and vapor content at the times $t = 584$ [h], $t = 1000$ [h] and $t = 1750$ [h] calculated using the average sorption and hysteresis sorption approaches. The vapor boundary variations on the mass transport boundary are defined in Fig. 2b.

defined based on tests. It was found that $\{h_1^{in}, h_2^{in}, h_3^{in}\} < 10^5$ was sufficient to restrict the out-of-balance solution in the following time step. The constructed function $\varepsilon^{l,eq,in}(\phi_v)$ was rejected if the upper limit for the polynomial coefficients was met and the element would follow $\varepsilon^{l,eq,cu}(\phi_v)$ despite a sorption change. The numerical precision was reduced for the sorption change determination in order to save computational time. A change in sorption direction was only considered if $\Delta\phi_v > 9 \cdot 10^{-6}$.

The response of the ion concentrations, caused by the applied boundary condition in terms of the vapor phase is shown in Figs. 5 and 6. The concentration distributions after 1000 [h] are shown in Fig. 5, where the exposed boundary is saturated by the presence of the liquid phase, so that mass flow of ions through the exposed boundary is allowed. This is clearly seen on the concentration gradient near the exposed boundary, for most of the species. The applied boundary concentration of $[H^+]$ is seen in Fig. 5b and represents the only species with flow direction into the domain. The concentration distributions after 1750 [h] are shown in Fig. 6 where the vapor content at the boundary is $\phi_v < 1$ so that mass flow of pore solution ions through the boundary is not physically possible.

The average and hysteresis approaches are compared in terms of the ionic concentrations in Figs. 5 and 6, where it is seen that deviations, in the part of the domain where hysteresis loops are established, are relatively small. The spatial sub-domain affected by the hysteresis in Fig. 5 is $\approx [0 \text{ [m]}, 0.022 \text{ [m]}]$ and $\approx [0 \text{ [m]}, 0.028 \text{ [m]}]$ for Fig. 6. Both approaches show increased ion concentrations and a steep concentration gradient for H^+ . The spatial position of the steep gradient corresponds well to the position of increased liquid content, shown in Fig. 3 for the same instance of time. A significant difference between the two approaches is seen at the H^+ gradient, where the domain with high ionic concentrations determined by the average approach is wider compared with the results from the hysteresis approach. This is related to the difference in the calculated liquid content as shown in Fig. 3c, where the average approach determines a higher liquid content than the hysteresis approach. Comparing the two different exposure times in Figs. 5 and 6 show that the difference, in position of the steep H^+ gradient, increases with time for the initial values and boundary conditions employed in this example. Differences in ion concentration are also seen in the part of the domain where the liquid phase content is only changed slightly (the sub-domain considered is $\approx [0.026 \text{ [m]}, 0.05 \text{ [m]}]$ for Fig. 5 and $\approx [0.034 \text{ [m]}, 0.05 \text{ [m]}]$ for Fig. 6). This affect is due to the difference in initial liquid and vapor content, in which the liquid content for the average approach is higher compared with the hysteresis approach.

4 Discussion

The comparison between the two approaches studied in Sec.3.2 and the conclusion drawn from these are valid for this specific choice of $\varepsilon^{l,eq,lb}(\phi_v)$ and $\varepsilon^{l,eq,ub}(\phi_v)$ and the average function determined from these. Another scenario could be that e.g. $\varepsilon^{l,eq,lb}(\phi_v) = \varepsilon^{l,eq,avg}(\phi_v)$ and the conclusions may be different from what is presented in Sec.3.2. In many cases, only a single sorption curve is determined by experimental observations and where here it would be difficult to determine how far a measured curve is from the real average. It is also observed that in many instances it is difficult to find reasonable initial values of the vapor- and liquid-phase concentrations since they are dependent on the sorption history before the start of the actual simulation.

Numerical restrictions were introduced in order to handle elements close to the point around fully saturated condition and cases involving very small changes in the sorption direction. Small errors are introduced by these restrictions, but are not considered significant compared with,

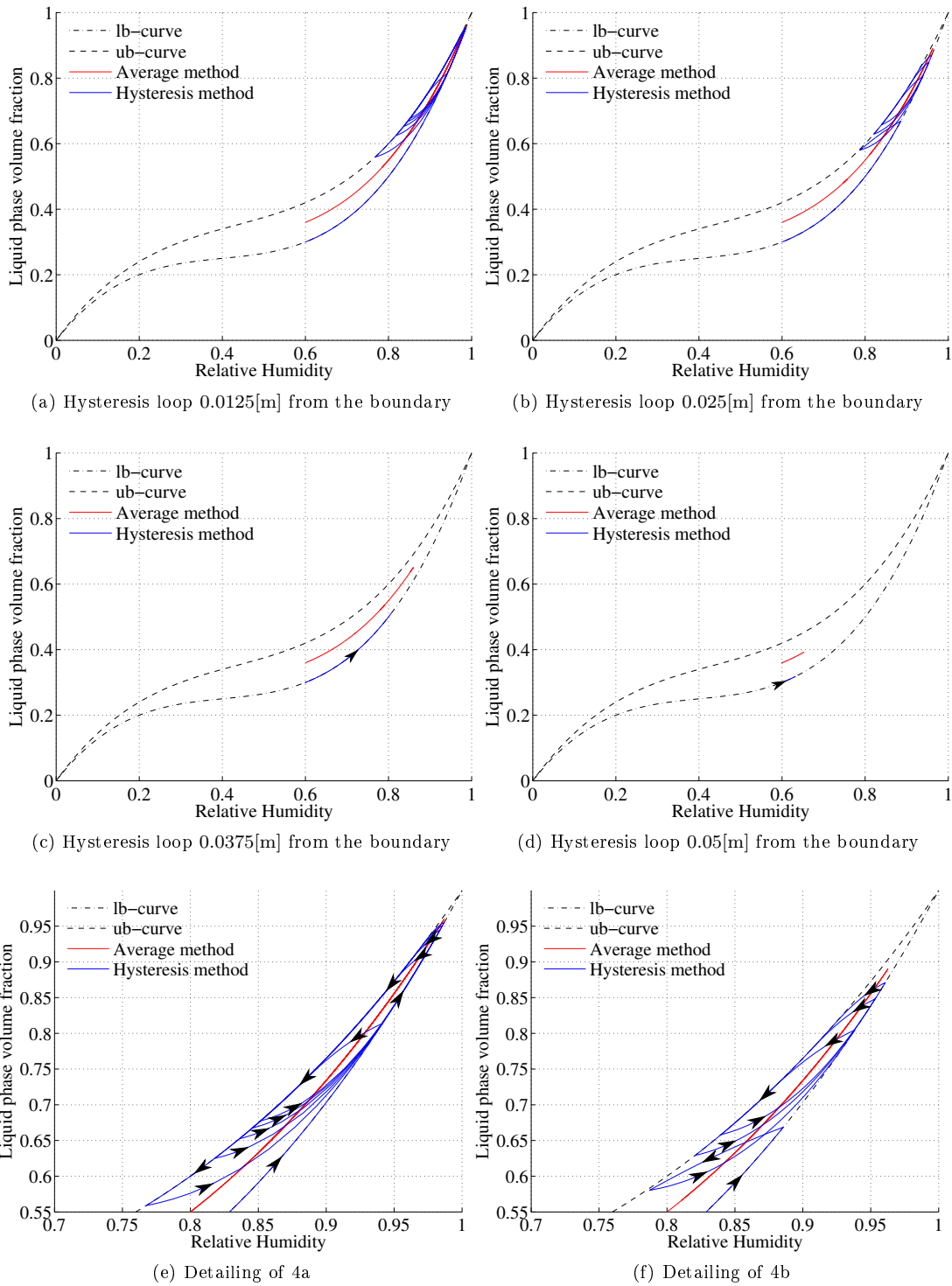


Figure 4: The current sorption function $\varepsilon^{l,eq,cu}(\phi_v, t)$ for selected elements in discretized system.

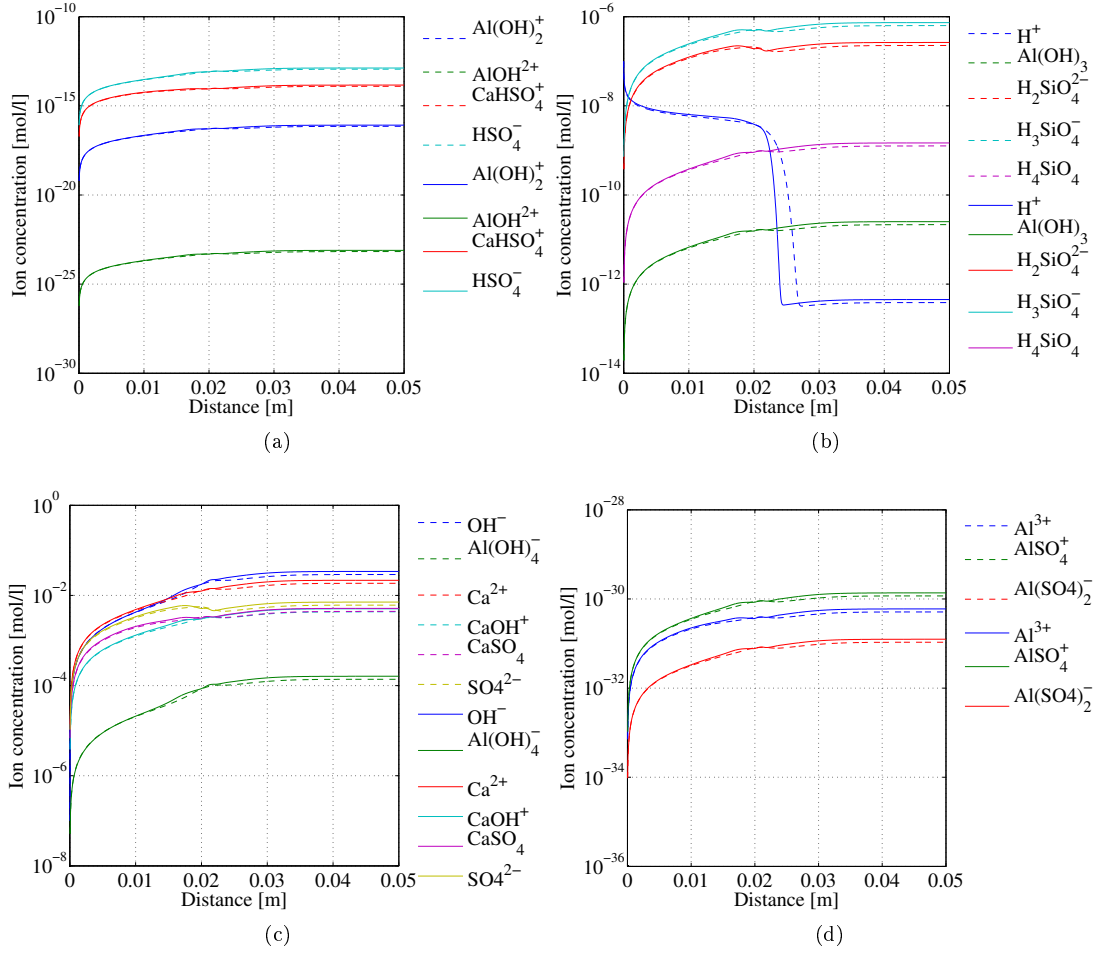


Figure 5: (- -) Average approach, (—) Hysteresis approach. Concentration of solution species after 1000[h] where the boundary function for the vapor phase is $\phi = 1$ and consequently mass flow of ions is allowed through the boundary.

e.g., the precision of experimentally determined sorption boundary functions at high relative humidities.

Chemical equilibrium, described by q_i , is omitted in the numerical treatment in this work as it would be difficult to evaluate the effect of the sorption hysteresis on the ionic concentration with chemical equilibrium included in the numerical solution. However, omitting chemical interactions limits direct comparison with experimental observations for cement-based materials. The precipitation/dissolution reaction model would feed the pore solution due to the assumption of instantaneously equilibrium. It is also noted that if chemistry were included in the model, the precipitation/dissolution would change the solid structure and thereby also the mass flow properties. These facts motivate that parts of the framework for reactive mass transport eqs. (1) - (5) are evaluated separately.

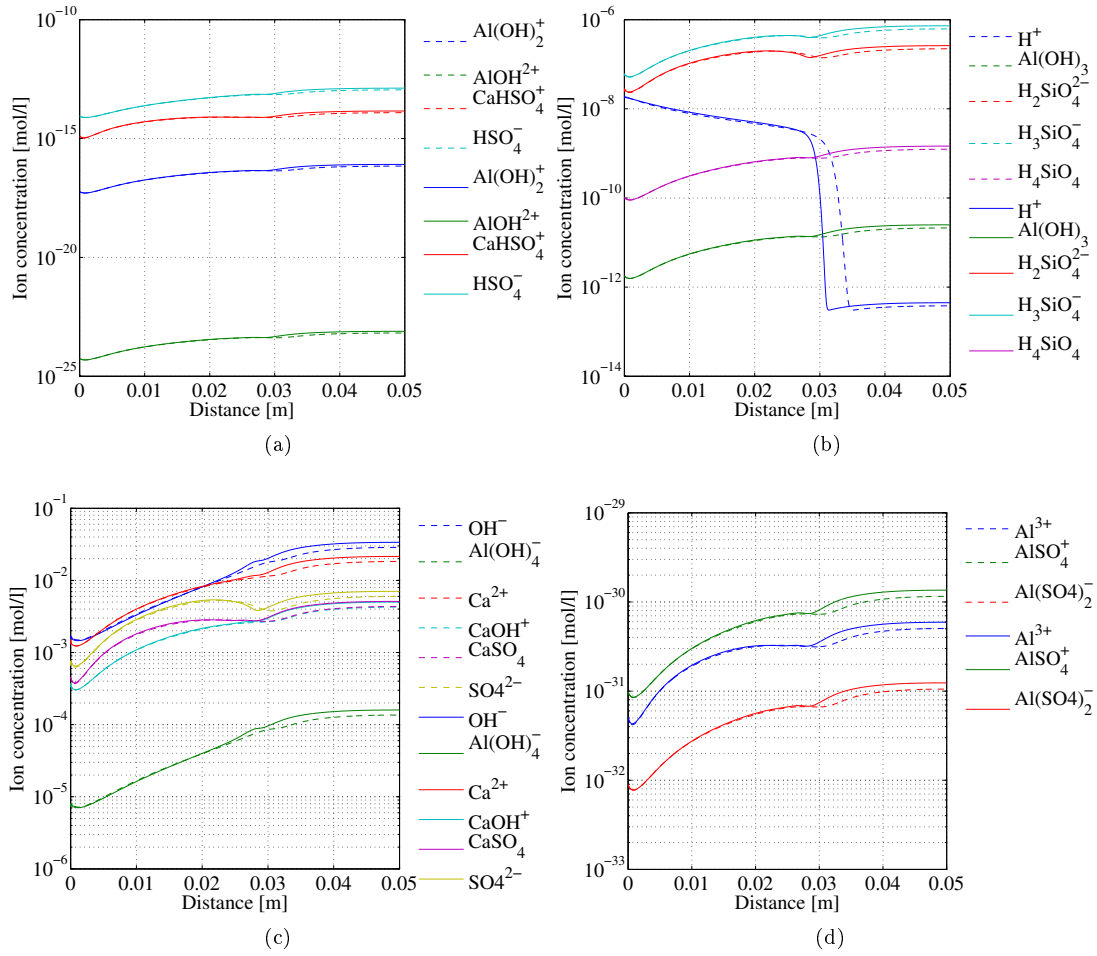


Figure 6: (- -) Average approach, (—) Hysteresis approach. Concentration of solution species after 1750[h] where the boundary function for the vapor phase is $\phi_v < 1$ and consequently the mass flow of ions at the boundary is set to zero.

5 Conclusion

A coupled model for ionic mass transport coupled to a moisture transport model including sorption hysteresis was presented and a finite element solution was derived. A strong form and a weak form of an extended version of the Poisson–Nernst–Planck system of equations were presented. The weak form of the system was derived together with a discretization of the spatial domain and the time domain. The general finite element matrix system was established and the local global stiffness and mass matrices were derived. The time domain was solved by a single-parameter implicit scheme and the solution was improved by a modified Newton–Raphson scheme. A review of the numerical implementation of the sorption hysteresis model was given, where the numerical criteria for modeling inner scanning curves were covered.

A numerical example was constructed in order to demonstrate the numerical approach and compare two approaches for describing the history-dependent sorption. One approach included

the sorption hysteresis and another utilized a more simple average approach. The simulation results showed the global transient and spatial response of the ionic concentrations in the pore solution, the liquid and vapor contents in the material, when a relative-humidity variation is applied at the boundary. The spatial variation in the liquid and vapor content showed that the model is capable of handling both non-saturated and saturated boundary conditions and simulating an increased liquid ingress with increasing saturation degree. The average approach, in which the sorption isotherm was described by a constant third-order polynomial, was compared with an approach in which the sorption isotherm polynomial was assumed history-dependent. The results of the two studied approaches deviated mostly for ionic species with flow direction into the domain from a saturated boundary condition. The average sorption approach showed comparably higher ionic concentrations than compared the results from the sorption hysteresis approach. Future work should focus on improving the strong non-linearity related to the liquid phase and implementation of chemical equilibrium into the framework.

References

- B. Johannesson, Development of a Generalized Version of the Poisson- Nernst-Planck Equations Using the Hybrid Mixture Theory: Presentation of 2D Numerical Examples, *Transport in Porous Media* 85 (2010) 565–592, ISSN 0169-3913, URL <http://dx.doi.org/10.1007/s11242-010-9578-8>, 10.1007/s11242-010-9578-8.
- E. Samson, J. Marchand, Modeling the effect of temperature on ionic transport in cementitious materials, *Cement and Concrete Research* 37 (3) (2007) 455–468.
- Y. Hosokawa, K. Yamada, B. Johannesson, L.-O. Nilsson, Development of a multi-species mass transport model for concrete with account to thermodynamic phase equilibriums, *Materials and Structures* (2011) 1–16ISSN 1359-5997, URL <http://dx.doi.org/10.1617/s11527-011-9720-2>, 10.1617/s11527-011-9720-2.
- O. Truc, J. Ollivier, L. Nilsson, Numerical simulation of multi-species diffusion, *Materials and Structures* 33 (9) (2000) 566–573.
- Q. Yuan, C. Shi, G. De Schutter, D. Deng, F. He, Numerical model for chloride penetration into saturated concrete, *Journal of Materials in Civil Engineering* 23 (3) (2010) 305–311.
- E. Samson, J. Marchand, Numerical Solution of the Extended Nernst-Planck Model, *Journal of Colloid and Interface Science* 215 (1) (1999) 1 – 8, ISSN 0021-9797, doi:\bibinfo{doi}{DOI:10.1006/jcis.1999.6145}, URL <http://www.sciencedirect.com/science/article/pii/S0021979799961453>.
- M. Rudolph, Digital simulations with the fast implicit finite-difference (FIFD) algorithm. part 4. Simulation of electrical migration and diffuse double-layer effects, *Journal of Electroanalytical Chemistry* 375 (1) (1994) 89–99.
- A. La Rocca, H. Power, Free mesh radial basis function collocation approach for the numerical solution of system of multi-ion electrolytes, *International journal for numerical methods in engineering* 64 (13) (2005) 1699–1734.
- M. Ristinmaa, N. Ottosen, B. Johannesson, Mixture theory for a thermoelasto-plastic porous solid considering fluid flow and internal mass exchange, *International Journal of Engineering Science* 49 (11) (2011) 1185–1203.
- H. Derluyn, D. Derome, J. Carmeliet, E. Stora, R. Barbarulo, Hysteretic moisture behavior of concrete: Modeling and analysis, *Cement and Concrete Research* .
- D. H. Everett, A general approach to hysteresis. Part 4. An alternative formulation of the domain model, *Transactions of the Faraday Society* 51 (1955) 1551–1557.

- H. Ranaivomanana, J. Verdier, A. Sellier, X. Bourbon, Toward a better comprehension and modeling of hysteresis cycles in the water sorption–desorption process for cement based materials, *Cement and Concrete Research* 41 (8) (2011) 817–827.
- T. Ishida, K. Maekawa, T. Kishi, Enhanced modeling of moisture equilibrium and transport in cementitious materials under arbitrary temperature and relative humidity history, *Cement and concrete research* 37 (4) (2007) 565–578.
- B. Johannesson, U. Nyman, A Numerical Approach for Non-Linear Moisture Flow in Porous Materials with Account to Sorption Hysteresis, *Transport in porous media* 84 (3) (2010) 735–754.
- L. Bennethum, J. Cushman, Multicomponent, multiphase thermodynamics of swelling porous media with electroquasistatics: I. Macroscale field equations, *Transport in Porous Media* 47 (3) (2002a) 309–336.
- L. Bennethum, J. Cushman, Multicomponent, multiphase thermodynamics of swelling porous media with electroquasistatics: II. Constitutive theory, *Transport in Porous Media* 47 (3) (2002b) 337–362.
- D. L. Parkhurst, C. Appelo, et al., User’s guide to PHREEQC (Version 2): A computer program for speciation, batch-reaction, one-dimensional transport, and inverse geochemical calculations, Water-Resources Investigations Report 99-4259, U.S. DEPARTMENT OF THE INTERIOR .
- T. Wagner, D. A. Kulik, F. F. Hingerl, S. V. Dmytrieva, GEM-Selektor geochemical modeling package: TSolMod library and data interface for multicomponent phase models, *The Canadian Mineralogist* 50 (5) (2012) 1173–1195.
- U. Nyman, P. Gustafsson, B. Johannesson, R. Hägglund, A numerical method for the evaluation of non-linear transient moisture flow in cellulosic materials, *International journal for numerical methods in engineering* 66 (12) (2006) 1859–1883.
- N. Ottosen, H. Petersson, Introduction to the finite element method, Prentice-Hall, 1992.
- O. Zienkiewicz, R. Taylor, J. Zhu, The finite element method: its basis and fundamentals, vol. 1, Butterworth-Heinemann, 2005.
- N. Ottosen, M. Ristinmaa, Mechanics of Constitutive Modeling, Elsevier, 2005.
- G. Möschner, B. Lothenbach, F. Winnefeld, A. Ulrich, R. Figi, R. Kretzschmar, Solid solution between Al-ettringite and Fe-ettringite ($\text{Ca}_6[\text{Al}_{1-x}\text{Fe}_x(\text{OH})_6]_2(\text{SO}_4)_3 \cdot 26\text{H}_2\text{O}$), *Cement and Concrete Research* 39 (6) (2009) 482–489.
- T. Schmidt, B. Lothenbach, M. Romer, K. Scrivener, D. Rentsch, R. Figi, A thermodynamic and experimental study of the conditions of thaumasite formation, *Cement and Concrete Research* 38 (3) (2008) 337–349.
- G. Möschner, B. Lothenbach, J. Rose, A. Ulrich, R. Figi, R. Kretzschmar, Solubility of Fe-ettringite ($\text{Ca}_6[\text{Fe}(\text{OH})_6]_2(\text{SO}_4)_3 \cdot 26\text{H}_2\text{O}$), *Geochimica et Cosmochimica Acta* 72 (1) (2008) 1–18.
- B. Lothenbach, T. Matschei, G. Möschner, F. P. Glasser, Thermodynamic modelling of the effect of temperature on the hydration and porosity of Portland cement, *Cement and Concrete Research* 38 (1) (2008) 1–18.
- B. Lothenbach, F. Winnefeld, Thermodynamic modelling of the hydration of Portland cement, *Cement and Concrete Research* 36 (2) (2006) 209–226, ISSN 00088846, 18733948, doi: [10.1016/j.cemconres.2005.03.001](https://doi.org/10.1016/j.cemconres.2005.03.001).
- D. A. Kulik, Improving the structural consistency of C-S-H solid solution thermodynamic models, *Cement and Concrete Research* 41 (5) (2011) 477–495, ISSN 00088846, 18733948, doi: [10.1016/j.cemconres.2011.01.012](https://doi.org/10.1016/j.cemconres.2011.01.012).
- B. Johannesson, A theoretical model describing diffusion of a mixture of different types of ions in pore solution of concrete coupled to moisture transport, *Cement and concrete research* 33 (4) (2003) 481–488.

-
- B. Johannesson, Prestudy on diffusion and transient condensation of water vapor in cement mortar, *Cement and concrete research* 32 (6) (2002) 955–962.

Paper II

"Framework for reactive mass transport: Phase change modeling of concrete by a coupled mass transport and chemical equilibrium model"

M. M. Jensen, B. Johannesson, M. R. Geiker

Accepted: *Computational Material Science, May, 2014*



Framework for reactive mass transport: Phase change modeling of concrete by a coupled mass transport and chemical equilibrium model



M.M. Jensen^{a,*}, B. Johannesson^a, M.R. Geiker^b

^a Technical University of Denmark, Department of Civil Engineering, Brovej 118, 2800 Kgs. Lyngby, Denmark

^b Department of Structural Engineering, Norwegian University of Science and Technology (NTNU), NO-7491 Trondheim, Norway

ARTICLE INFO

Article history:

Received 3 January 2014

Received in revised form 12 May 2014

Accepted 14 May 2014

Keywords:

Chemical equilibrium modeling

Mass transport modeling

Phase change

Cement

ABSTRACT

Reactive transport modeling is applicable for a range of porous materials. Here the modeling framework is focused on cement-based materials, where ion diffusion and migration are described by the Poisson–Nernst–Planck equation system. A two phase vapor/liquid flow model, with a sorption hysteresis description is coupled to the system. The mass transport is solved by using the finite element method where the chemical equilibrium is solved explicitly by an operator splitting method. The IPHREEQC library is used as chemical equilibrium solver. The equation system, solved by IPHREEQC, is explained for aqueous, pure phase and solid solution reactions. Numerical examples, with cement-based materials, are constructed to demonstrate transient phase change modeling. A simulation of pure multi-species leaching from the material, showing deterioration of the solid phases is described and calculated. A second simulation, showing multi-species ingress with formation of new solid phases in the domain is described and calculated. It is shown that the numerical solution method is capable of solving the reactive mass transport system for the examples considered.

© 2014 Elsevier B.V. All rights reserved.

1. Introduction

Chemical phase changes as a consequence of a reactive mass transport process in porous media are well known phenomena. For example, cement-based materials show phase changes when exposed to aggressive environments, both from liquid solutions and gases. The alterations of cement-based materials are strongly related to durability and service life. The phase changes in most cement-based materials are often very slow processes due to the complex matrix of the porous network. Modeling frameworks for describing phase changes over a long period of time are useful in the sense of evaluating the long term durability of the material and as indicator for service life estimation.

Reactive mass transport modeling of cement-based materials is in many cases focused on single ionic species transport, especially chloride ingress due to its influence on reinforcement corrosion. Single ionic ingress modeling is often related to a modified diffusion coefficient. Time-dependent diffusion coefficients are used in different engineering models see e.g. Thomas and Bamforth [1], Tang and Gulikers [2]. This approach compensates for all chemical and physical changes over time in a single parameter. Other suggested diffusion coefficient dependencies are, e.g., a function

of diffusion depth Yuan et al. [3], a function of concentration Bigas [4], Tang [5], Francy and François [6].

Over the last decade multi-species transport modeling has gained acceptance, where a constant species dependent intrinsic diffusion coefficient is considered in these types of models and the transient change of the diffusion properties is a consequence of the ionic composition development. Transport models of this type are found in, e.g., Nguyen et al. [7], Truc et al. [8]. Multi-species transport modeling within porous media is often described by the Nernst–Planck equation or the Poisson–Nernst–Planck (PNP) system of equations, see e.g. Samson et al. [9], Johannesson [10], and Johannesson [11]. The multi-species transport approaches enable establishment of extended reactive transport modeling, where each ionic species is considered in chemical reactions, both in aqueous reactions and solid/liquid reactions. It has been concluded that the flexibility of the multi-species approach is a great advantage in long term simulations of cement-based materials see e.g. Marchand and Samson [12], Baroghel-Bouny et al. [13] even though the models are often associated with a range of input parameters, which can be difficult to measure separately.

A coupled reactive mass transport model within cement-based materials was proposed by Hosokawa et al. [14] based on an extended version of the Poisson–Nernst–Planck equation system coupled to a chemical model. In their work a surface complexation

* Corresponding author. Tel.: +45 45 25 17 00.

E-mail address: mmej@byg.dtu.dk (M.M. Jensen).

model of the C–S–H phase was utilized, see Nonat and Lecoq [15], Hosokawa et al. [16]. The chemical equilibrium system of equations was solved by the PHREEQC code in which it is possible to estimate the electrical double layer composition on the C–S–H surface and thereby include binding of ionic species from the pore solution. Another model was proposed by Samson and Marchand [17], based on a Poisson–Nernst–Planck type of equation, coupled with a liquid diffusion equation in order to model non-saturated systems. A chemical model having a limited number of ions and solids was solved together with the mass transport system. Both models were solved under the assumption of instantaneous local equilibrium, which enables an operator splitting method (also known as staggered method).

The framework presented in this paper is mainly based on the work by Johannesson [10], Hosokawa et al. [14]. The model from these papers is extended with a two phase vapor/liquid model described in Johannesson and Nyman [18]. The mass transport model is coupled to the chemical equilibrium code IPHREEQC (see Parkhurst et al. [19], Charlton and Parkhurst [20]). The proposed model presented here differs from earlier work by coupling of the extended vapor/liquid transport model with the chemical equilibrium code, where all features and calculation methods are available.

The coupled model is solved numerically by the finite element method (FEM) and a brief overview of the chemical equilibrium calculation is given, based on Parkhurst et al. [19]. Precondition calculations and non-linear material parameters related to cement-based materials are shown. Numerical examples are constructed to show a numerical solution for a cement-based system, exposed to different boundary conditions. An important aspect in this framework is the capability of modifying and testing various chemical models together with a mass transport code. The constructed examples demonstrate this by combining a well known thermodynamic database CEMDATA07 (see Möschner et al. [21], Schmidt et al. [22], Möschner et al. [23], Lothenbach et al. [24], Lothenbach and Winnefeld [25]), with recent external phase descriptions, see Kulik [26].

2. Methods

2.1. Reactive mass transport

Mass transport in the porous system of a cement-based material is in this model described by an extended version of the PNP system of equations. The equation system describing the mass transport is based on the work of Johannesson [10] with the exception that chemical interactions are taken into account in the solution procedure as described in Hosokawa et al. [14]. The transport of the individual ionic species in the pore solution is described by individual transport equations. The governing mass transport equation in use is

$$\varepsilon^l \frac{\partial c_i^l}{\partial t} + c_i^l \frac{\partial \varepsilon^l}{\partial t} = \nabla \cdot \left(D_i^l(\varepsilon^l) \varepsilon^l \nabla c_i^l + D_i^l c_i^l \nabla \varepsilon^l - A_i^l c_i^l z_i \varepsilon^l \nabla \Phi \right) + v^{ls} \varepsilon^l \nabla c_i^l + v^{ls} c_i^l \nabla \varepsilon^l + q_i; \quad i = 1, 2, \dots, m \quad (1)$$

where c_i^l is the concentration of the i th ion in the liquid phase l , ε^l is the volume saturation of the liquid phase in the pore system, $D_i^l(\varepsilon^l)$ is the diffusion coefficient for the i th ion, A_i^l is the ionic mobility, z_i is the valence state of the i th ion, Φ is the total electrical potential of the liquid, v^{ls} is the liquid velocity with respect to the solid s and q_i is a source/sink term accounting for chemical equilibrium. The numerical solution of chemical equilibrium is introduced in the transport equation as an operator splitting approach, by assuming an instantaneous local chemical equilibrium state after each mass transport step performed. The operator

splitting approach for reactive transport models is simply to determine a transient solution for the mass transport part and use these results as input for the chemical equilibrium calculation. This solution is then used as a set of initial values for the next transport calculation. Through this approach chemical equilibrium is solved for each discrete element in the spatial domain at all considered time steps.

The electrical potential of the solution considered is determined by the Gauss law, see Johannesson [10], this is the Poisson part of the PNP equation system. The Poisson equation is coupled to the diffusion Eq. (1) by the electrical potential Φ . The Poisson equation is given as

$$\xi_d \xi_0 \nabla^2 \Phi = F \sum_{i=1}^m c_i z_i \quad (2)$$

where ξ_d is the relative dielectricity coefficient, ξ_0 is the dielectricity coefficient of vacuum and F is the Faraday's constant.

The liquid transport for non-saturated porous materials is described by a two phase model proposed by Nyman et al. [27], Johannesson and Nyman [18]. The proposed model uses the saturation degree as driving potential for moisture transport. The two phase model enables a detailed transient description of changing boundary conditions, e.g. tidal zone modeling. The governing equation for the liquid transport is given as

$$\rho_w \frac{\partial \varepsilon^l}{\partial t} = \nabla \cdot \left(D_{\varepsilon^l}(\varepsilon^l) \nabla \varepsilon^l \right) + R(\varepsilon^{l,eq}(\phi_v) - \varepsilon^l) \quad (3)$$

where ρ_w is the water density, $D_{\varepsilon^l}(\varepsilon^l)$ is the transport coefficient for the liquid phase, R is a penalty number and $\varepsilon^{l,eq}(\phi_v)$ is the liquid volume fraction equilibrium function. The function $\varepsilon^{l,eq}(\phi_v)$ is a history dependent function, describing the sorption hysteresis. An individual function is established for each spatial element in the numerical discretization, based on a third order polynomials. The function is established between a set of initially defined adsorption and desorption boundary isotherms, see Johannesson and Nyman [18], Nyman et al. [27] for details.

The governing equation for the vapor phase transport, which is coupled to (3) is given by

$$\rho_{vs}(\varepsilon_p - \varepsilon^l) \frac{\partial \phi_v}{\partial t} - \rho_{vs} \phi_v \frac{\partial \varepsilon^l}{\partial t} = \nabla \cdot \left(D_{\phi} \nabla \phi_v \right) - R(\varepsilon^{l,eq}(\phi_v) - \varepsilon^l) \quad (4)$$

where ρ_{vs} is the vapor saturation density, ε_p is the porosity of the system, ϕ_v is the relative humidity and D_{ϕ} is the diffusion coefficient for the vapor phase. It is seen that the penalty function in Eq. (4) has opposite sign compared to Eq. (3) in order to establish an equilibrium between the vapor and liquid phase, based on the volume fraction equilibrium function $\varepsilon^{l,eq}(\phi_v)$.

2.2. Numerical calculation method

The mass transport equations are solved by the FEM, where weak formulations of Eqs. (1)–(4) are established and discretized by Galerkins method, see Ottosen and Petersson [28]. The transient system is solved by a single parameter implicit time integration scheme, given as

$$\mathbf{a}_{n+1} = (\mathbf{C} + \Delta t \theta \mathbf{K})^{-1} [(\mathbf{C} + \Delta t(1 - \theta)\mathbf{K})\mathbf{a}_n + \mathbf{f}_n + \theta(\mathbf{f}_{n+1} - \mathbf{f}_n)] \quad (5)$$

where \mathbf{a}_{n+1} is the solution at the time step $n + 1$, \mathbf{C} is the global damping matrix, Δt is the time stepping length, θ is the time stepping parameter, \mathbf{K} is the global stiffness matrix, \mathbf{f} is the load vector and \mathbf{a}_n the initial values for the time step. The numerical solution is improved, due to the non-linearities introduced, by a modified version of the Newton–Raphson scheme, see Ottosen and Ristinmaa [29]. The residual ψ of the solution is given by

$$\psi^{i-1} = \mathbf{C}^{i-1} \frac{1}{\Delta t} (\mathbf{a}_{n+1}^{i-1} - \mathbf{a}_n) + \mathbf{K}^{i-1} \mathbf{a}_{n+1}^{i-1} - (\mathbf{f}_{n+1}^{i-1} - \mathbf{f}_n^i) \quad (6)$$

where i is the iteration number. The improved solution is determined from

$$\psi^{i-1} = \left[\mathbf{C}^{i-1} \frac{1}{\Delta t} + \mathbf{K}^{i-1} \right] (\mathbf{a}_{n+1}^i - \mathbf{a}_{n+1}^{i-1}) \quad (7)$$

by solving for \mathbf{a}_{n+1}^i . The Newton–Raphson iteration scheme is controlled by a convergence criterion on ψ .

The volume fraction equilibrium function $\varepsilon^{l,eq}(\phi_v)$ is a third order polynomial which enables a detailed description of sorption hysteresis. The polynomial coefficients change, with a change in sorption direction determined by $\Delta \mathbf{a} = \mathbf{a}_{n+1} - \mathbf{a}_n$. Third order polynomials are well suited for the description of inner scanning curves in cement-based materials. The adsorption and desorption boundary are also described by third order polynomials, see Johannesson and Nyman [18].

The mass transport equation system is an initial value problem, where the initial values at $t = 0$ are determined from different pre-conditioning models. A hydration model adopted from Hosokawa et al. [14] is used to determine the amount of oxides reacted at a given degree of hydration for the individual clinker minerals. The oxide content with respect to the degree of hydration of the different hydrates is determined by

$$\mathbf{u} = \mathbf{A} \text{diag}(\alpha_M) \mathbf{A}^{-1} \mathbf{b} \quad (8)$$

where \mathbf{u} is the reacted amount of oxides in mass%, with respect to the degree of hydrations, \mathbf{A} is a mass balance matrix between the clinker mineral, α_M is the degree of hydrations where M refers to the clinker considered and \mathbf{b} is initial oxide amount in mass%. The clinker minerals considered are $M = [\text{C}_3\text{S}, \text{C}_2\text{S}, \text{C}_3\text{A}, \text{C}_4\text{AF}, \text{CS}^*, \text{K}^*\text{S}^*, \text{K}_3\text{N}^*\text{S}_4^*]$, where the notation S^* , K^* and N^* refers to SO_4 , K_2O and Na_2O , respectively. The oxides considered are $N = [\text{CaO}, \text{SiO}_2, \text{Al}_2\text{O}_3, \text{Fe}_2\text{O}_3, \text{SO}_3, \text{K}_2\text{O}, \text{Na}_2\text{O}]$. The mass balance matrix shown here is in this case where $(\text{Al}_2\text{O}_3)/(\text{Fe}_2\text{O}_3) \geq 0.64$ given as

$$\mathbf{A} = \begin{bmatrix} 0.7368 & 0.6512 & 0.3420 & 0.4616 & 0.4119 & 0 & 0 \\ 0.2632 & 0.3488 & 0 & 0 & 0 & 0 & 0 \\ 0 & 0 & 0 & 0.2098 & 0 & 0 & 0 \\ 0 & 0 & 0.4870 & 0.3286 & 0 & 0 & 0 \\ 0 & 0 & 0 & 0 & 0.5881 & 0.4594 & 0.5060 \\ 0 & 0 & 0 & 0 & 0 & 0.5406 & 0.4466 \\ 0 & 0 & 0 & 0 & 0 & 0 & 0.0979 \end{bmatrix}$$

The mass balance matrix is an extended Bogue calculation see e.g. Taylor [30] for the standard Bogue calculation. The oxide content is used in the chemical equilibrium calculation in order to determine the composition and amount of the solid phases and pore solution. The water/cement ratio for the cement paste is given as input parameter and used as initial water in the chemical model.

Three types of diffusion mechanisms are considered in this model, each with their individual diffusion coefficient, D_i^l , $D_{i,l}$ and D_ϕ . It is assumed that these diffusion properties are dependent on the saturation degree of the porous network, see e.g. Shackelford and Daniel [31] and Hu and Wang [32]. The ion diffusion is depended on a tortuosity factor τ , a constrictivity factor δ_i and the saturation of the porous system. Different definitions of the tortuosity and constrictivity factors can be found in the literature, this work follows the method analogue to Hosokawa et al. [14]. A non-linear relation between D_i^l and ε^l is described in, e.g. Shackelford and Daniel [31]. For this model an exponential relation is defined, as

$$D_i^l = \varepsilon_i^m \left(\frac{\delta_i}{\tau} D_{0,i}^l \right) \quad (9)$$

where $D_{0,i}^l$ is a free ion diffusion coefficient. The diffusion coefficients for the liquid and vapor phase are assumed to depend on the saturation index, see e.g., Hu and Wang [32]. In a similar fashion an exponential development for the liquid phase diffusion coefficient, as a function of the liquid saturation degree, is adopted in this work. This is in line with, e.g., Johannesson and Nyman [18]. The liquid diffusion coefficient is determined from

$$D_{\varepsilon^l} = D_{0,\varepsilon^l} + D_{1,\varepsilon^l} \varepsilon_i^n \quad (10)$$

where D_{0,ε^l} and D_{1,ε^l} are diffusion coefficients determined from experimental observations and n is the exponential factor. With n sufficiently high and a constant vapor diffusion coefficient D_ϕ , one can model a fast ingress of liquid at high saturation degree using this model. D_ϕ is implicitly dependent on ε^l due to the vapor/liquid coupling of (3) and (4). This is an implicit way of simulating capillary suction, which is responsible for relatively fast transport of the boundary solution into the porous material, compared to a pure diffusion process.

2.3. Chemical equilibrium

Chemical equilibrium, defined as q_i in Eq. (1), is solved by the external geochemical code IPHREEQC, see Charlton and Parkhurst [20]. In order to illustrate the compatibility of the transport module and the chemical module adopted a brief review of the equation system solved by IPHREEQC to calculate chemical equilibrium state is presented, based on Parkhurst et al. [19]. The IPHREEQC code solves the mass action laws, derived from thermodynamics. The IPHREEQC library includes several methods to handle different chemical reactions, the equation system shown here is limited to aqueous species, pure phases and solid solutions.

The mass action equation for aqueous species can be written as

$$K_i = a_i \prod_j a_j^{-c_{j,i}} \quad (11)$$

where K_i is the temperature dependent solubility constant, a_i is the activity of the aqueous species i , a_j is the activity of the defined master species j , $c_{j,i}$ is the stoichiometric coefficient for master species j in aqueous species i . Master species are defined as pure elements and elements at different valence state, e.g., Ca^{+2} , Fe^{+2} and Fe^{+3} . All constituents in the chemical system are described in terms of the master species. Eq. (11) can be written in terms of

$$a_i = \gamma_i b_i \quad n_i = b_i m_{aq} \quad (12)$$

to yield

$$n_i = m_{aq} K_i \frac{\prod_j a_j^{-c_{j,i}}}{\gamma_i} \quad (13)$$

where n_i is moles of the aqueous species i in the solution, m_{aq} is the mass of solvent water and γ_i is the activity coefficient of the aqueous species i . b_i is the molality of species i , introduced in Eq. (12).

The activity coefficient γ_i is determined from either the Davies equation or by the extended WATEQ Debye–Hückel equation depending on the material data available. The Davies equation is defined as

$$\log \gamma_i = -Az_i^2 \left(\frac{\sqrt{\mu}}{1 + \sqrt{\mu}} - 0.3\mu \right) \quad (14)$$

where A is a temperature dependent constant, z_i is the ionic charge of the aqueous species i and μ is the ionic strength. The WATEQ Debye–Hückel equation is defined as

$$\log \gamma_i = -\frac{Az_i^2 \sqrt{\mu}}{1 + B\alpha_i} + \beta_i \mu \quad (15)$$

where B is a temperature dependent constant, α_i and β_i are constants for species i derived from mean salt activity coefficient data.

The activity of the water $a_{\text{H}_2\text{O}}$ is considered as a special case in IPHREEQC and approximated by

$$a_{\text{H}_2\text{O}} = 1 - 0.017 \sum_i \frac{n_i}{m_{\text{aq}}} \quad (16)$$

which formula is based on Raoult's law.

The ionic strength μ of the solution is determined by

$$\mu = \frac{1}{2} \sum_i z_i^2 \frac{n_i}{m_{\text{aq}}} \quad (17)$$

Note that the ionic strength is one of the unknowns for which the complete system is solved for.

2.3.1. Pure phase and solid solution equilibrium

Pure phase equilibrium is probably the simplest solid–liquid chemical equilibrium calculation to establish and solve. In theory the number of pure phases in the model is unlimited. Phases must be described by a valid dissolution reaction scheme and with its solubility constant in order to fit the solution algorithm in IPHREEQC. The mass-action equation for pure phases is given by the same type of formula as used for the aqueous reactions, that is

$$K_p = \prod_j a_j^{-c_{pj}} \quad (18)$$

where K_p is the solubility constant for the pure phase p described by a dissolution reaction and c_{pj} is the stoichiometric coefficient of the j th master species in the p th pure phase. For multiple phase assemblages, Gibbs' phase rule must be satisfied. The activity of the pure phase itself is assumed to equal 1.0. The saturation index, SI is introduced for the numerical solution procedure. The saturation index shows whether the phase is supersaturated, in equilibrium or undersaturated, by $SI > 0$, $SI = 0$ and $SI < 0$, respectively. The definition is given as

$$SI = \log \prod_j a_j^{c_{pj}} \quad (19)$$

Solid solution is a widely used method for describing an internal coupling between two or more solid phases and their dissolution reaction with respect to each other. Two main methods are included in the IPHREEQC code, non-ideal solid solution, limited to binary solid assemblages and ideal solid solution with two or more end-members in the solid assemblages. Only ideal solid solution is considered here, where the unknowns for solving the system are the moles of each end-member. The activity of the end-member is determined by $a_{\text{ss}p} = \lambda_{\text{ss}p} x_{\text{ss}p}$, where notation ss_p refers to the p pure phase in solid solution ss and $x_{\text{ss}p}$ is the mole fraction of the p th component in the solid solution. This differs from the pure phase assumption, where the activity of the solid phase is 1.0. For the ideal solid solution it is assumed that $\lambda_{\text{ss}p} = 1$ for all p , so the activity reduces to $a_{\text{ss}p} = x_{\text{ss}p}$ where the mole fraction is defined as

$$x_{\text{ss}p} = \frac{n_{\text{ss}p}}{\sum_p n_{\text{ss}p}} \quad (20)$$

where $n_{\text{ss}p}$ is the moles of the pure phase p in the solid solution ss . The general mass-action law for solid solution is given as

$$K_{\text{ss}p} = \frac{\prod_j a_j^{c_{\text{ss}p}j}}{a_{\text{ss}p}} = n_{\text{ss}p} \frac{\prod_j a_j^{c_{\text{ss}p}j}}{\sum_p n_{\text{ss}p}} \quad (21)$$

In a similar fashion to Eq. (19) a solubility quotient $Q_{\text{ss}p}$ is introduced as

$$Q_{\text{ss}p} = \frac{\prod_j a_j^{c_{\text{ss}p}j}}{K_{\text{ss}p} a_{\text{ss}p}} \quad (22)$$

where $Q_{\text{ss}p} = 1$ at solid solution equilibrium.

2.3.2. Mole balance and charge balance

The mole balance for the reacting system includes all the chemical elements present in the different phases. Mole balance for the reaction mechanisms aqueous reaction, pure phase reaction and solid solution reactions is shown. The mole balance is given as

$$0 = T_m - \sum_p C_{j,p} n_p - \sum_{\text{ss}} \sum_p C_{j,\text{ss}p} n_{\text{ss}p} - \sum_i C_{j,i} n_i \quad (23)$$

where T_m is the total moles of master species and C_j is the moles of element j per mole of each entity, in this case n_p , $n_{\text{ss}p}$ and n_i .

The charge balance in the aqueous solution is determined from the valence state and amount of each ionic species represented, the charge balance equation being defined as

$$T_z = \sum_i z_i n_i \quad (24)$$

where T_z is the residual charge of the calculations. Natural systems are always in charge balance, whereas numerical simulations may introduce small errors in terms of charge balances.

2.3.3. Numerical solution for chemical equilibrium

The IPHREEQC code for forward modeling of chemical equilibrium uses the Newton–Raphson iteration scheme to find the equilibrium solution based on the equations defined in the previous sub-sections. The system is solved for the unknowns $\ln a_j$, $\ln m_{\text{aq}}$, $\ln a_{\text{H}_2\text{O}}$, μ , n_{ss} and n_p , with an equal number of equations. For the Newton–Raphson scheme, Eqs. (16), (17), (19), (22), (23) and (24) are used and their derivative with respect to the unknowns. All equations involved are solved for zero residuals. Different numerical optimization techniques are applied to the solution procedure, e.g. to avoid singular matrices.

3. Numerical examples

Numerical examples were constructed to demonstrate the potential of this framework in reactive transport modeling for porous materials and particularly for cement-based materials. The examples will show that it is possible to solve the equations system numerically and also illustrate the open format of this framework. The term “open format” is used here for the ability to adjust all the material parameters, chemical reactions, boundary settings, etc. The key feature to emphasize in the open format is the ability to modify the chemical components considered, both in terms of the pore solution, solid matrix composition and the boundary conditions. The framework is not fixed to a single chemical composition, but it is possible to adjust with experimental findings or to test different thought scenarios, such as different exposure conditions.

The coupled model described in this work includes a range of input parameters, which should be determined or estimated directly from experiments. The material parameters were divided into two groups related to the mass transport part of the model and the chemical part, with reaction schemes and the parameter related to these. The ionic species considered in the mass transport calculation are shown in appendix A.3 together with the diffusion coefficients, electromigration coefficients, valences and tortuosity factors. The approach was to allow all solid phases and ion complexes in the database to be formed and then invoke the ionic species in the mass transport. The phreeqc.dat database and additional elements defined in Jacques [33] was used. The initial solid matrix

was described by the phases defined in appendix B.4, which is based on the CEMDATA07 Möschner et al. [21], Schmidt et al. [22], Möschner et al. [23], Lothenbach et al. [24], Lothenbach and Winnefeld [25], where the C–S–H model by Kulik [26] substitute the jennite and tobermorite C–S–H description. The IP_{HREEQC} formulation of the original CEMDATA07 database is from Jacques [33].

The examples are:

1. A cement-based material is considered. The material was exposed to pure water at the boundary, which yields that the concentration for $[OH^-] = 1.0 \cdot 10^{-7}$ and $[H^+] = 1.0 \cdot 10^{-7}$ mol/l was prescribed at the boundary and the rest of the ionic concentrations was set to be zero. The material is assumed to be fully water-saturated, so $\epsilon^l = 1$ and $\nu^{ls} = 0$.
2. The second numerical example was constructed to simulate a multi-species exposed cement-based material. A multi-species solution was defined at the boundary in order to determine the ingress and the chemical effect from their presences in the pore solution. The initial pore solution of the cement-based material was enabled to diffuse through the boundary. The boundary was assumed water-saturated in the whole time domain so vapor/liquid diffusion, with sorption hysteresis was taken into account.

3.1. Input parameters and databases

The oxide composition for the cement used in the simulations is given in Table 1. The cement composition is in line with values used in Hosokawa et al. [14]. The same degree of hydration was chosen for each element for simplicity and to increase stability in the chemical equilibrium calculation. The initial pore solution and solid matrix composition was modeled by IP_{HREEQC} , where the oxide amount from the extended Bogue was treated as solution species together with an amount of water corresponding to the water/cement ratio, see Table 2. The excess water from the hydration model was used to determine the initial water saturation degree and this was introduced as initial water for the numerical example 2.

The simulations were solved as 1-dimensional boundary value problems. The spatial and transient constants for the numerical calculation, together with some of the material constants are shown in short form in Table 2, the individual diffusion properties are given in Table A.3. The general tortuosity factor is in agreement with Johannesson [34]. The exponential factor, relating the saturation degree and diffusion is solely to facilitate a high diffusion rate at high saturation degree. The relatively high number of elements used is mainly a consequence of the liquid/vapor terms, which have been proven to be difficult to solve with sufficient accuracy, see Jensen et al. [35]. The time step length is relatively short, compared to the total time, and the time scale for the liquid/vapor diffusion combined with the chemical equilibrium behavior, in all essential parts determines an acceptable time step length. The pore solution composition changed relatively much when these two mechanism were solved in the coupled system and if Δt was too large, the initial value for the following time step, would not be sufficiently good. Chemical equilibrium was solved at every fifth time step for these examples in order to save computational time

Table 1
Oxide composition for the cement material used in the simulation

	CaO	SiO ₂	Al ₂ O ₃	Fe ₂ O ₃	SO ₃	K ₂ O	Na ₂ O	Minor oxides ^a
Mass%	0.64	0.22	0.05	0.04	0.03	0.0078	0.0015	0.0107

^a The minor oxides are not considered in the simulation.

Table 2
Constant material and model parameters for the numerical calculation.

	Simulation parameters
W/C	0.6
Spatial elements	2000
Total spatial distance (m)	0.06
Total time (year)	2.5
Time step, Δt (h)	10
Time parameter ¹ , θ	1
Tortuosity factor, τ	0.009
Exponential relation for ions, n	20
Liquid diffusion coef. D_{0,ϵ^l} m ² /s	$1 \cdot 10^{-12}$
Liquid diffusion coef. D_{1,ϵ^l} m ² /s	$2 \cdot 10^{-8}$
Liquid density ρ_w kg/m ³	1000
Porosity ϵ_p	0.2
Exponential relation for liquid phase, m	50
Liquid diffusion coef. D_ϕ m ² /s	$1 \cdot 10^{-12}$
Vapor saturation density, ρ_{vs} kg/m ³	0.017
Penalty number R	10^6
Relative dielectricity	78.54
Dielectricity in vacuum	$8.854 \cdot 10^{-12}$
Faraday's constant	96490

¹ $\theta = 1$ due to the Newton–Raphson scheme adopted.

and obtain a sufficiently change in the pore solution from the mass transport calculation in the spatial domain. The increased time step length for the split operator scheme will increase the truncated boundary error as a result, see e.g. Simpson and Landman [36]. The vapor and liquid diffusion properties are in agreement with values reported in literature, see Johannesson and Nyman [18]. The exponential relation for the liquid phase was chosen such that the liquid phase diffusion was dominant at $\phi \gtrsim 0.97$. The porosity ρ_p is considered constant for these examples despite the fact that precipitation/dissolution reactions would change the porosity over time.

3.2. Results from leaching simulation (example 1)

Results from the leaching simulation are shown in Figs. 1 and 2 as the spatial pore solution distribution and solid phase composition, respectively. The solid phase changes are only dependent on the change in the pore solution composition and thereby the mass flow in the porous system. The mass transport system was solved for 28 ionic species and it is seen from Fig. 1 that the concentrations of the different species have developed differently in the spatial domain over time, according to their individual boundary concentration and diffusion properties.

The effect from the boundary conditions, on the pore solution is clearly seen in Fig. 1. H^+ was the only ion resulting in a diffusion direction into the domain, which is seen in Fig. 1b. Local peak values are seen on some concentration profiles near the boundary, which is mainly due to the effect from the imposed charge balance of the system. Species with exact zero concentration were seen in the transient solution, e.g. $[Al^{3+}]$. Zero concentration is seldomly seen in numerical simulations of the kind studied here, where a gradient is almost always established towards the boundary. The

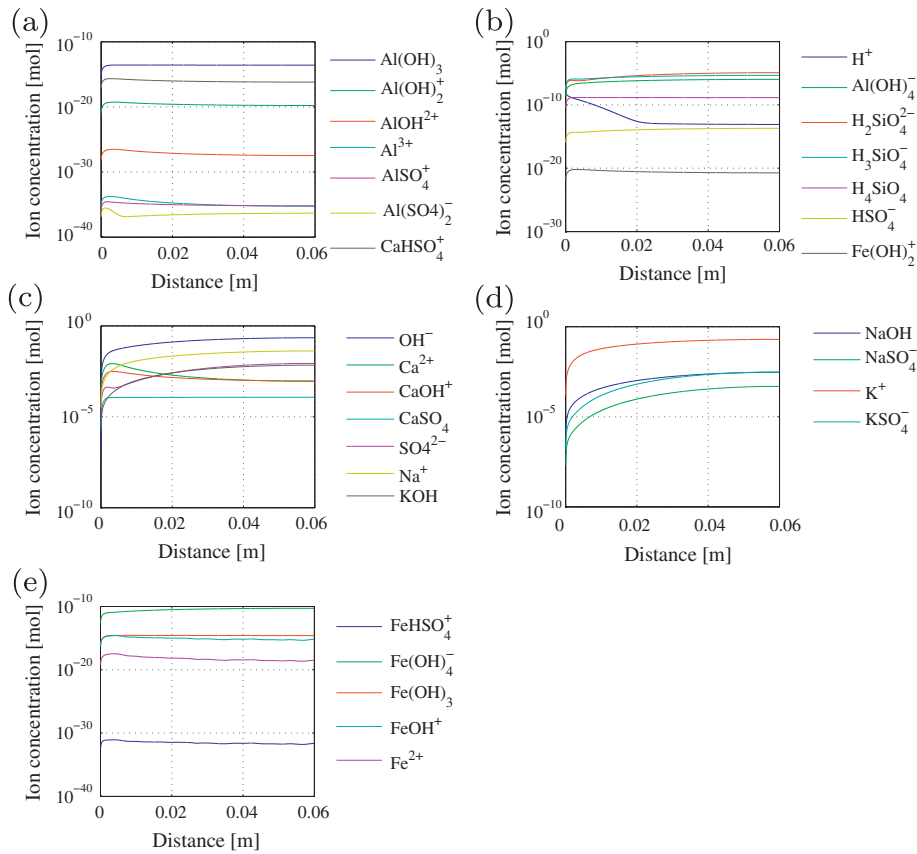


Fig. 1. Concentration profiles in the pore solution of a cement-based material, after a leaching simulation. The plots are from the chemical equilibrium calculation at the last time step considered.

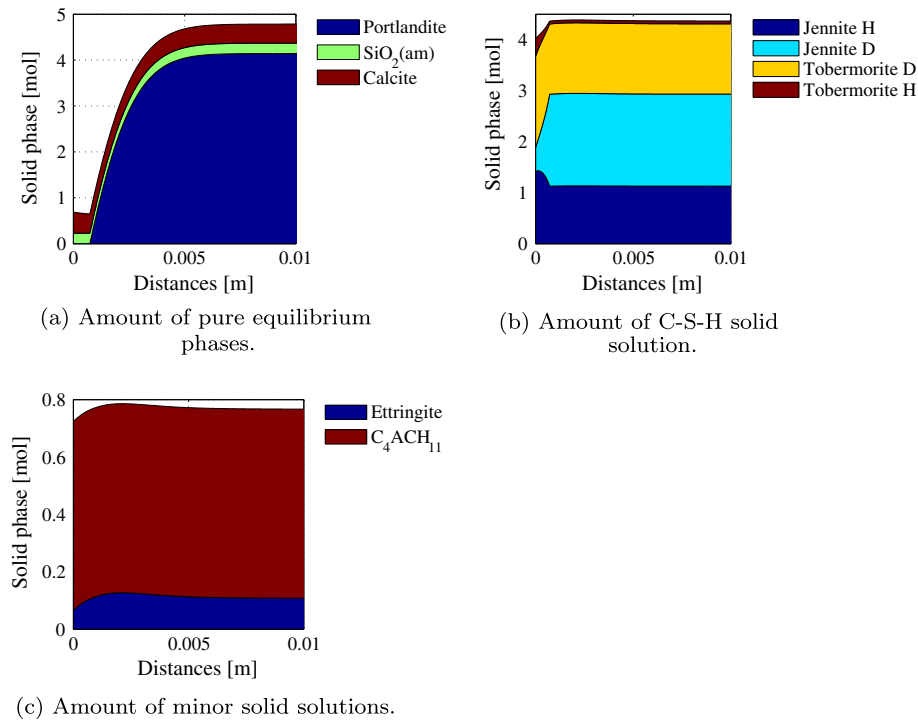


Fig. 2. Solid phases in a cement-based material after a leaching simulation. The plots are from the chemical equilibrium calculation at the last time step considered. Note that only 0.01 m of the domain is shown in order to emphasize the changes near the boundary.

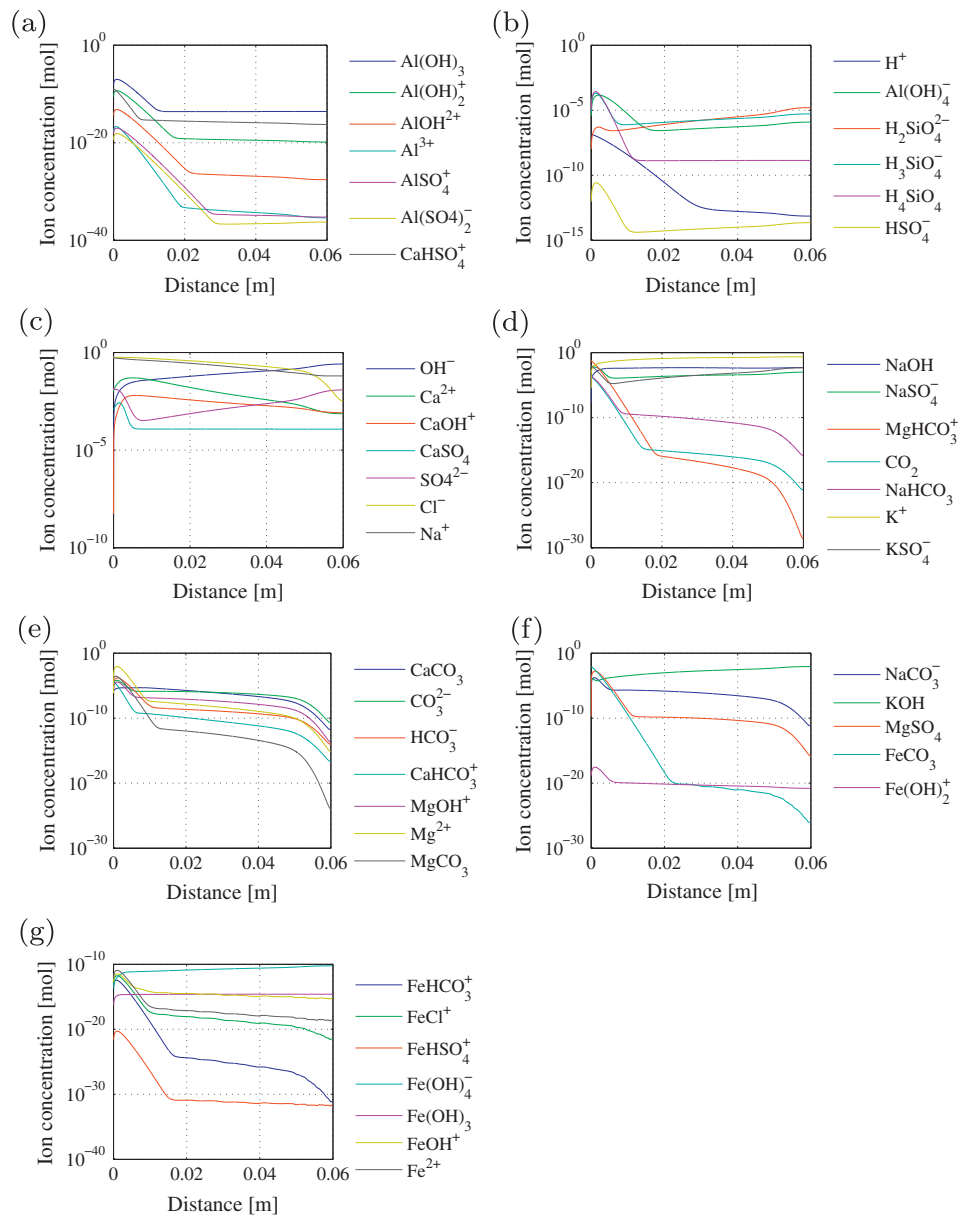


Fig. 3. Concentration profiles after ingress and chemical interaction of a multi-species solution into the pore solution of a cement-based material. The plots are just before the chemical equilibrium calculation at the last time step considered.

effect seen here, is from the chemical equilibrium part where elements can have zero concentration in the individual nodes, if the chemical conditions for their presences is not there. The following mass transport step for such case would re-establish a concentration gradient in the affected domain.

The solid phase dissolution is clearly seen in Fig. 2a for the pure equilibrium phase portlandite. This is in line with the simulation results of the C–S–H solid solution, by Kulik [26]. The C–S–H model used here is described by Kulik [26] as a four end-member solid solution, together with the pure equilibrium phases portlandite and amorphous silica. Portlandite is dissolved first, relative to the C–S–H end-members and as a function of decreasing $[\text{Ca}]/[\text{Si}]$ ratio in the solids. The internal ratio between the C–S–H end-members starts to evolve after complete dissolution of portlandite. The increase of jennite-H and decrease of jennite-D as seen in Fig. 2b is in line with the single solid-solution simulation in Kulik [26].

3.3. Results from ingress simulation (example 2)

The external species set on the boundary, of a non-saturated cement-based material, are typically ions found in sea-water. In total 46 ionic species were considered in the mass transport where 25 species had a boundary value >0 . The ionic species were solved together with 32 solid phases in the chemical equilibrium calculation. The boundary was assumed saturated in the whole time domain, so changes in sorption direction did not occur. The initial saturation degree was determined to be 0.87 (using the chemical module to initiate the calculations) and it was assumed that the adsorption would follow the adsorption isotherm, defined as $\epsilon^{l,eq}(\phi_v) = \frac{13}{8}\phi_v - \frac{15}{4}\phi_v^2 + \frac{25}{8}\phi_v^3$. The liquid equilibrium state was evaluated at each node in the spatial domain in each time step.

The example was solved for 49 unknowns in the mass transport and 78 unknowns in the chemical equilibrium calculation. The cause of the transient change in the individual calculated ionic

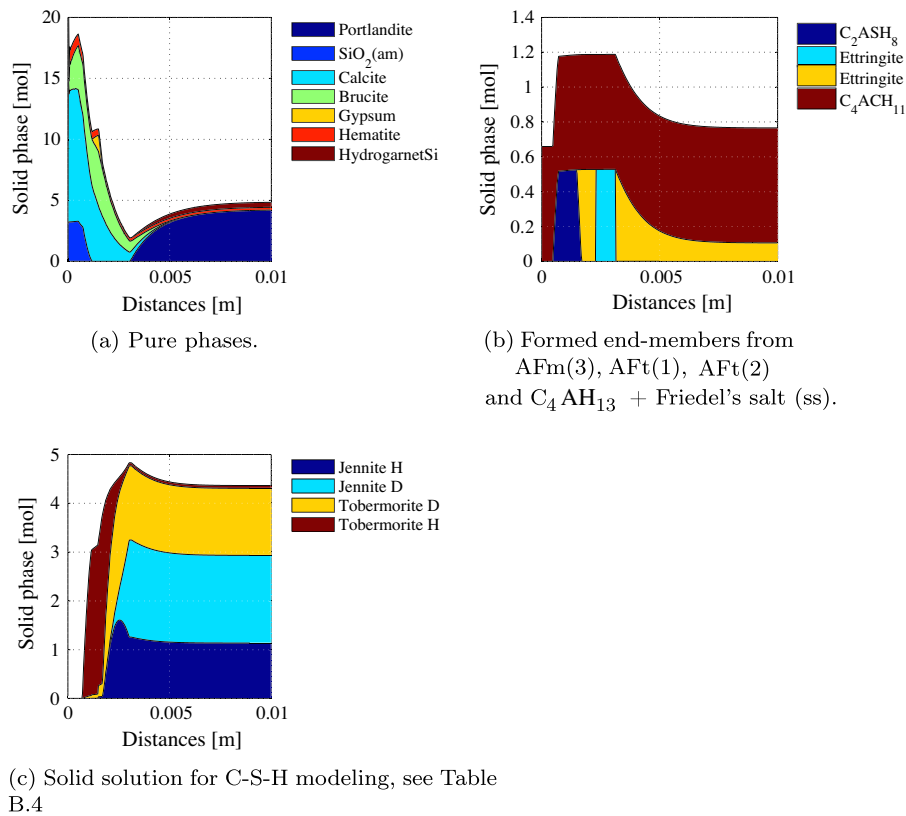


Fig. 4. Change in solid chemical composition, after/at an age of 2.5 years. Note that some end-members in Fig. 4b are shown twice, as they occur in more than one solid solution. Note that only 0.01 m of the domain is shown in order to emphasize the changes near the boundary.

concentration profiles is difficult to evaluate due to the size of the system considered and the number of physical phenomenon involved. General tendencies are seen by comparing Figs. 3 and 4, where the chemical interactions are a significant factor for the changes in the pore solution in the spatial domain at 0–0.02 m. Some concentration profiles in, e.g., Fig. 3e and d show a significant change in the concentration gradient near 0.05–0.06 m. This effect is related to the liquid diffusion gradient, where the liquid velocity increases the mass flow of ionic species.

For this simulation the strong non-linearity introduced by the liquid/vapor phase transport, caused numerical stability problems in the Newton–Raphson iteration scheme for this simulation. It was found that the criteria $\epsilon^i \leq 1$ were not satisfied after the Newton–Raphson improvement. A damping constant on the step size was introduced in the Newton–Raphson scheme. The method is analogue to line search, with the cost of increasing the number of iterations compared to more detailed search methods.

The solid phase changes due to the changing pore solution composition can be seen in Fig. 4. It is seen in Fig. 4a that, e.g. brucite formation is simulated near the left boundary, which contains magnesium. Magnesium is not a part of the initial oxide components, see Table 1 and indicates that magnesium diffusion into the domain is simulated by the model.

The relationship between the portlandite and the C–S–H solid solution as observed in example 1, is also seen in this example. The C–S–H end-members change in the time domain, is similar to what observed in the leaching example 1 and the reported results in Kulik [26]. Furthermore, it is seen that the amorphous silica (SiO_2) is formed near the exposed boundary, see Fig. 4a. This is formed, according to the model by Kulik [26], at low Ca/Si ratio in the solids and when tobermorite-H has reached its maximum

share in the C–S–H solid solution ratio. The dissolution of the C–S–H and the change to amorphous silica indicates that leaching processes were simulated by the model, parallel with the ingress.

The minor solid solutions are shown in Fig. 4b where, e.g., ettringite is formed. Note that ettringite occurs twice in Fig. 4b, which shows that it changes solid solution from AFt (1) to AFt (2). The ettringite is further changed to C_2ASH_8 close to the exposed boundary. The sharp interfaces between solid solutions increased the number of required iterations by the `IPHREEQC` library. Less than 0.1% of the total number of chemical calculations did not converge. A non-converged node n adopted the values from the $n - 1$. The error introduced by this operation was assumed to be small due to the relative small element length used.

4. Discussion

The number of input parameters is extensive in the presented framework, e.g. for all ions the free diffusion coefficient is needed for all ions and the number of assumed/estimated values in the example calculations are significant. One could argue whether all the minor relevant ions are needed in such calculations. The experience from this work has shown that it is very difficult to separate the effect from single elements or processes when working with such large coupled system, across different physics. When the numerical solution method allows for a large number of ions and the computational times are reasonable, one should include all the ions formed in this framework. Testing of the framework and especially the coupling to the chemical equilibrium library showed that including all ions increased the stability of the chemical equilibrium calculation.

Table A.3
Diffusion properties for ionic components in the numerical examples.

	$D_i^l \cdot 10^{-8}$	$A_i^l \cdot 10^{-6}$	z_i	δ_i	Boundary Ex. 2 mol/l
OH ⁻	0.5300 ^a	0.2253	-1	1.0 ^a	1.621e-07
H ⁺	0.9311 ^c	0.3958	1	1.0 ^b	1.327e-07
Al(OH) ₄ ⁻	0.5040 ^a	0.2142	-1	1.0 ^a	-
Al(OH) ₃	0.5040 ^f	-	-	1.0 ^b	-
Al(OH) ₂ ⁻	0.5040 ^f	0.2142	-1	1.0 ^b	-
Al ³⁺	0.0541 ^c	0.0229	3	1.0 ^b	-
AlSO ₄ ⁺	0.5040 ^f	0.0442	1	1.0 ^b	-
Al(SO ₄) ₂ ⁻	0.5040 ^f	0.0442	-1	1.0 ^b	-
AlOH ²⁺	0.5040 ^f	0.0442	1	1.0 ^b	-
CaOH ⁺	0.0792 ^a	0.0337	1	0.2 ^a	5.330e-09
CaSO ₄	0.0471 ^a	-	-	1.0 ^a	1.196e-03
CaHSO ₄ ⁺	0.0471 ^b	0.0200	1	1.0 ^b	1.099e-09
SO ₄ ²⁻	0.1070 ^a	0.0455	-2	1.0 ^a	1.609e-02
HSO ₄ ⁻	0.1385 ^c	0.0589	-2	1.0 ^b	-
H ₂ SiO ₄ ²⁻	0.1100 ^a	0.0468	-2	0.02 ^a	-
H ₃ SiO ₄ ⁻	0.107 ^e	0.0468	-1	1.0 ^b	-
H ₄ SiO ₄	0.107 ^e	-	-	1.0 ^b	-
Ca ²⁺	0.0792 ^a	0.0337	2	0.2 ^a	9.879e-03
CaHCO ₃ ⁺	0.107 ^e	0.0200	1	1.0 ^b	3.880e-05
CaCO ₃	0.0446 ^a	-	-	1.0 ^a	1.368e-06
Cl ⁻	0.203 ^a	0.0862	-1	1.0 ^a	6.183e-01
K ⁺	0.1957 ^a	0.0405	1	0.02 ^a	9.911e-03
KSO ₄ ⁻	0.1070 ^a	0.0454	-1	1.0 ^a	1.648e-04
KOH	0.196 ^a	-	-	1.0 ^a	1.771e-10
Mg ²⁺	0.0705 ^a	0.0299	2	1.0 ^a	4.861e-02
MgSO ₄	0.0705 ^b	0.0299	-	1.0 ^b	8.019e-03
MgHCO ₃ ⁺	0.0705 ^b	0.0299	1	1.0 ^b	1.819e-04
MgCO ₃	0.0705 ^b	-	-	1.0 ^b	4.436e-06
MgOH ⁺	0.0705 ^a	0.0299	1	1.0 ^a	6.656e-07
Na ⁺	0.133 ^a	0.0565	1	0.02 ^a	4.898e-01
NaSO ₄ ⁻	0.618 ^a	0.0262	-1	1.0 ^a	6.625e-03
NaHCO ₃	0.133 ^g	-	-	1.0 ^b	1.373e-04
NaCO ₃ ⁻	0.0585 ^a	0.0405	-1	1.0 ^a	3.345e-06
NaOH	0.133 ^g	-	-	1.0 ^b	1.902e-08
CO ₂	0.191 ^e	-	-	1.0 ^b	1.618e-04
CO ₃ ²⁻	0.0955 ^a	0.0405	-2	1.0 ^a	1.903e-06
HCO ₃ ⁻	0.118 ^a	0.0501	-1	1.0 ^a	-
FeCO ₃	0.0719 ^d	-	-	1.0 ^b	-
FeHCO ₃ ⁺	0.0719 ^d	0.0299	1	1.0 ^b	-
FeCl ⁺	0.0719 ^d	0.0299	1	1.0 ^b	-
FeSO ₄	0.0719 ^d	-	-	1.0 ^b	-
FeHSO ₄ ⁺	0.0719 ^d	0.0299	1	1.0 ^b	-
Fe(OH) ₄ ⁻	0.0719 ^d	0.0299	-1	1.0 ^b	-
Fe(OH) ₃	0.0719 ^d	-	-	1.0 ^b	-
Fe(OH) ₂ ⁺	0.0719 ^d	0.0299	1	1.0 ^b	-
FeOH ²⁺	0.0719 ^d	0.0299	2	1.0 ^b	-
FeOH ⁺	0.0719 ^d	0.0299	1	1.0 ^b	-
Fe ²⁺	0.0719 ^c	0.0299	2	1.0 ^b	-

^a Data from Hosokawa et al. [14].

^b Estimated value.

^c Data from Lide and Haynes [37].

^d Estimated from Fe²⁺.

^e Data from Shen et al. [38].

^f Estimates from Al(OH)₄⁻.

^g Estimated from Na⁺.

The local instantaneous chemical equilibrium assumption and the boundary value description chosen in this work, may not reflect the true solution in the boundary node. Chemical equilibrium is calculated on the boundary node, but the boundary values are forced on this node in the following mass transport step. All transient properties are eliminated for the boundary node by this operation. The chemical equilibrium assumption is thereby no longer diffusion and time dependent. Increasing the number of spatial elements and decrease the time step length would help to overcome the problem. A more sound solution would be to

introduce kinetic rate laws in the chemical reactions. The assumption is in some sense valid if the boundary is considered as an infinite buffer.

5. Conclusion

A coupled reactive mass transport model was presented based on an extended PNP system of equations, coupled with a two phase liquid/vapor model and chemical equilibrium determined by an operator splitting method. The FEM with Galerkins approximation was used as numerical solver for the non-linear problem, together with a modified Newton–Raphson iteration scheme. A brief review of the chemical equilibrium algorithm in *IPHREEQC* was given, with focus on the aqueous reactions, pure equilibrium phases and solid solutions. Methods for describing non-linear material constants related to cement-based materials where found in the literature and presented here in the context to the modeling framework. An extended Bogue model, for preconditioning of the input parameters was suggested, which also included minor chemical elements in cement oxide composition.

The numerical examples addressed leaching and ingress simulation of ions in a cement-based material and the impact on the solid composition. The numerical solutions indicated that the coupling of chemistry and mass transport was working for the examples examined. Comparing simulation results of the C–S–H solid-solution model used with the multi-species model of this work showed the same internal type of changes in the end-member composition of the C–S–H. Furthermore it was shown for the ion ingress simulation (example 2), that solid phases that were not initially present could be formed (in this example brucite).

The FEM approach adopted was shown to be robust for the numerical examples under consideration. The change in the initial values by the operator splitting method did not seem to cause any problems as long as the residual was sufficiently minimized in both the mass transport part and the chemical equilibrium part. It was found that a damping factor for the step size in the Newton–Raphson iteration was necessary in order to satisfy restrictions on the liquid saturation.

The two examples considered the general open format of the framework developed, further, the examples demonstrate that both simple and complex boundary conditions can be simulated by the suggested framework. In the same way, it was shown that the chemical model was flexible in the sense of changing the number of unknowns and combining models included in different thermodynamic databases.

It was indicated in the discussion, that future work should focus on implementing kinetic rate laws in the chemical part, although this is a complicated topic on its own. Furthermore, implementation of other chemical reaction types, like surface complexation and gas phase reactions into the framework would improve the generality and open format of the framework.

Appendix A. Diffusion properties

The diffusion properties for the pore solution are given in Table A.3.

Appendix B. Solid phase reaction database

Thermodynamic database based on CEMDATA07 [21–25] and rewritten for *PHREEQC* by Jacques [33]. The CSH solid solution model is changed from the original CEMDATA07 database, to the latest C–S–H model proposed by Kulik [26] (see Tables B.4 and B.5).

Table B.4
Thermodynamic database for the chemical equilibrium model.

Reactions		
Pure phases		log K
Portlandite	$\text{Ca(OH)}_2 + 2\text{H}^+ \leftrightarrow \text{Ca}^{2+} + 2\text{H}_2\text{O}$	22.799
Silica (am)	$\text{SiO}_2 + 2\text{H}_2\text{O} \leftrightarrow \text{H}_4\text{SiO}_4$	-2.714
Brucite	$\text{Mg(OH)}_2 + 2\text{H}^+ \leftrightarrow \text{Mg}^{2+} + \text{H}_2\text{O}$	16.839
Gypsum	$\text{CaSO}_4 : 2\text{H}_2\text{O} \leftrightarrow \text{Ca}^{2+} + \text{SO}_4^{2-} + 2\text{H}_2\text{O}$	-4.580
Calcite	$\text{CaCO}_3 \leftrightarrow \text{CO}_3^{2-} + \text{Ca}^{2+}$	1.849
Hematite	$\text{Fe}_2\text{O}_3 + 6\text{H}^+ \leftrightarrow 2\text{Fe}^{3+} + 3\text{H}_2\text{O}$	-4.008
HydrogarnetSi	$\text{Ca}_3\text{Al}_2(\text{SiO}_4)_{0.8}(\text{OH})_{8.8} + 2.4\text{H}_2\text{O} \leftrightarrow 3\text{Ca}^{2+} + 2\text{Al(OH)}_4^- + 0.8\text{H}_3\text{SiO}_4^- + 3.2\text{OH}^-$	-29.871
Fe-monosulfate	$\text{Ca}_4\text{Fe}_2(\text{SO}_4)(\text{OH})_{12} : 6\text{H}_2\text{O} \leftrightarrow 4\text{Ca}^{2+} + 2\text{Fe(OH)}_4^- + \text{SO}_4^{2-} + 4\text{OH}^- + 6\text{H}_2\text{O}$	-33.203
<i>Solid solution</i>		
	C-S-H (ss)	
TobH	$(\text{CaO})_{0.66}(\text{SiO}_2)(\text{H}_2\text{O})_{1.5} + 1.32\text{H}^+ \leftrightarrow 0.66\text{Ca}^{2+} + \text{H}_4\text{SiO}_4 + 0.16\text{H}_2\text{O}$	8.272
TobD	$(\text{CaO})_{0.83}(\text{SiO}_2)_{0.66}(\text{H}_2\text{O})_{1.83} + 1.66\text{H}^+ \leftrightarrow 0.83\text{Ca}^{2+} + 0.66\text{H}_4\text{SiO}_4 + 1.34\text{H}_2\text{O}$	13.624
JenH	$(\text{CaO})_{1.33}(\text{SiO}_2)(\text{H}_2\text{O})_{2.16} + 2.66\text{H}^+ \leftrightarrow 1.33\text{Ca}^{2+} + \text{H}_4\text{SiO}_4 + 1.49\text{H}_2\text{O}$	22.173
JenD	$(\text{CaO})_{1.5}(\text{SiO}_2)_{0.66}(\text{H}_2\text{O})_{2.5} + 3.00\text{H}^+ \leftrightarrow 0.66\text{Ca}^{2+} + \text{H}_4\text{SiO}_4 + 0.16\text{H}_2\text{O}$	28.713
	AFm (1) (ss)	
C ₂ AH ₈	$\text{Ca}_2\text{Al}_2(\text{OH})_{10} : 3\text{H}_2\text{O} \leftrightarrow 2\text{Ca}^{2+} + 2\text{Al(OH)}_4^- + 2\text{OH}^- + 3\text{H}_2\text{O}$	-13.562
C ₂ FH ₈	$\text{Ca}_2\text{Fe}_2(\text{OH})_{10} : 3\text{H}_2\text{O} \leftrightarrow 2\text{Ca}^{2+} + 2\text{Fe(OH)}_4^- + 2\text{OH}^- + 3\text{H}_2\text{O}$	-17.602
	AFm (2) (ss)	
C ₄ AH ₁₃	$\text{Ca}_4\text{Al}_2(\text{OH})_{14} : 6\text{H}_2\text{O} \leftrightarrow 4\text{Ca}^{2+} + 2\text{Al(OH)}_4^- + 6\text{OH}^- + 6\text{H}_2\text{O}$	-25.403
C ₄ FH ₁₃	$\text{Ca}_4\text{Fe}_2(\text{OH})_{14} : 6\text{H}_2\text{O} \leftrightarrow 4\text{Ca}^{2+} + 2\text{Fe(OH)}_4^- + 6\text{OH}^- + 6\text{H}_2\text{O}$	-29.403
	AFm (3) (ss)	
C ₂ ASH ₈	$(\text{CaO})_2\text{Al}_2\text{O}_3\text{SiO}_2 : 8\text{H}_2\text{O} \leftrightarrow 2\text{Ca}^{2+} + 2\text{Al(OH)}_4^- + \text{H}_3\text{SiO}_4^- + \text{OH}^- + 2\text{H}_2\text{O}$	-20.490
C ₂ FSH ₈	$(\text{CaO})_2\text{Fe}_2\text{O}_3\text{SiO}_2 : 8\text{H}_2\text{O} \leftrightarrow 2\text{Ca}^{2+} + 2\text{Fe(OH)}_4^- + \text{H}_3\text{SiO}_4^- + \text{OH}^- + 2\text{H}_2\text{O}$	-24.800
	AFm (4) (ss)	
C ₄ ASH ₁₂	$(\text{CaO})_3\text{Al}_2\text{O}_3(\text{CaSO}_4) : 12\text{H}_2\text{O} \leftrightarrow 4\text{Ca}^{2+} + 2\text{Al(OH)}_4^- + \text{SO}_4^{2-} + 4\text{OH}^- + 6\text{H}_2\text{O}$	-27.700
C ₄ FSH ₁₂	$(\text{CaO})_3\text{Fe}_2\text{O}_3(\text{CaSO}_4) : 12\text{H}_2\text{O} \leftrightarrow 4\text{Ca}^{2+} + 2\text{Fe(OH)}_4^- + \text{SO}_4^{2-} + 4\text{OH}^- + 6\text{H}_2\text{O}$	-32.020
	Hydrogarnets (ss)	
C ₃ AH ₆	$(\text{CaO})_3\text{Al}_2\text{O}_3 : 6\text{H}_2\text{O} \leftrightarrow 3\text{Ca}^{2+} + 2\text{Al(OH)}_4^- + 4\text{OH}^-$	-34.070
C ₃ FH ₆	$(\text{CaO})_3\text{Fe}_2\text{O}_3 : 6\text{H}_2\text{O} \leftrightarrow 3\text{Ca}^{2+} + 2\text{Fe(OH)}_4^- + 4\text{OH}^-$	-22.46
	Aft (1) (ss)	
Al-Ettringite	$\text{Ca}_6\text{Al}_2(\text{SO}_4)_3(\text{OH})_{12} : 26\text{H}_2\text{O} \leftrightarrow 6\text{Ca}^{2+} + 2\text{Al(OH)}_4^- + 3\text{SO}_4^{2-} + 4\text{OH}^- + 26\text{H}_2\text{O}$	-44.909
Fe-Ettringite	$\text{Ca}_6\text{Fe}_2(\text{SO}_4)_3(\text{OH})_{12} : 26\text{H}_2\text{O} \leftrightarrow 6\text{Ca}^{2+} + 2\text{Fe(OH)}_4^- + 3\text{SO}_4^{2-} + 4\text{OH}^- + 26\text{H}_2\text{O}$	-44.008
	Aft (2) (ss)	
Al-Ettringite	$\text{Ca}_6\text{Al}_2(\text{SO}_4)_3(\text{OH})_{12} : 26\text{H}_2\text{O} \leftrightarrow 6\text{Ca}^{2+} + 2\text{Al(OH)}_4^- + 3\text{SO}_4^{2-} + 4\text{OH}^- + 26\text{H}_2\text{O}$	-44.909
Tricarboaluminate	$\text{Ca}_6\text{Al}_2(\text{CO}_3)_3(\text{OH})_{12} : 26\text{H}_2\text{O} \leftrightarrow 6\text{Ca}^{2+} + 2\text{Al(OH)}_4^- + 3\text{CO}_3^{2-} + 4\text{OH}^- + 26\text{H}_2\text{O}$	-46.509

Table B.5
The reaction schemes for formation of chloride phases [39].

Reactions		
<i>Solid solution</i>		
	C ₄ AH ₁₃ + Friedel's salt (ss)	
Friedel's salt	$\text{Ca}_4\text{Al}_2\text{Cl}_2(\text{OH})_{12} : 4\text{H}_2\text{O} \leftrightarrow 4\text{Ca}^{2+} + 2\text{Al(OH)}_4^- + 4\text{OH}^- + 2\text{Cl}^- + 4\text{H}_2\text{O}$	-27.300
C ₄ AH ₁₃	$\text{Ca}_4\text{Al}_2(\text{OH})_{14} : 6\text{H}_2\text{O} \leftrightarrow 4\text{Ca}^{2+} + 2\text{Al(OH)}_4^- + 6\text{OH}^- + 6\text{H}_2\text{O}$	-25.403
	C ₄ A $\bar{\text{C}}\text{H}_{11}$ + Friedel's salt (ss)	
Friedel's salt	$\text{Ca}_4\text{Al}_2\text{Cl}_2(\text{OH})_{12} : 4\text{H}_2\text{O} \leftrightarrow 4\text{Ca}^{2+} + 2\text{Al(OH)}_4^- + 4\text{OH}^- + 2\text{Cl}^- + 4\text{H}_2\text{O}$	-27.300
C ₄ A $\bar{\text{C}}\text{H}_{11}$	$(\text{CaO})_3\text{Al}_2\text{O}_3(\text{CaCO}_3) : 11\text{H}_2\text{O} \leftrightarrow 4\text{Ca}^{2+} + 2\text{Al(OH)}_4^- + \text{CO}_3^{2-} + 4\text{OH}^- + 5\text{H}_2\text{O}$	-31.470

References

- [1] M.D. Thomas, P.B. Bamforth, *Cem. Concr. Res.* 29 (4) (1999) 487–495.
- [2] L. Tang, J. Gulikers, *Cem. Concr. Res.* 37 (4) (2007) 589–595.
- [3] Q. Yuan, C. Shi, G. De Schutter, D. Deng, F. He, J. Mater. Civ. Eng. 23 (3) (2010) 305–311.
- [4] J.-P. Bigas, La diffusion des ions chlore dans les mortiers, Ph.D. thesis, 1994.
- [5] L. Tang, *Cem. Concr. Res.* 29 (9) (1999) 1463–1468.
- [6] O. Francy, R. François, *Cem. Concr. Res.* 28 (7) (1998) 947–953.
- [7] T.Q. Nguyen, V. Baroghel-Bouny, P. Dangla, *Comput. Concr.* 3 (6) (2006) 401–421. ISSN 15988198, 1598818x.
- [8] O. Truc, J. Ollivier, L. Nilsson, *Mater. Struct.* 33 (9) (2000) 566–573.
- [9] E. Samson, J. Marchand, J. Beaudoin, *Cem. Concr. Res.* 29 (8) (1999) 1341–1345.
- [10] B. Johannesson, *Transp. Porous Media* 85 (2010) 565–592. ISSN 0169–3913, <http://dx.doi.org/10.1007/s11242-010-9578-8>.

- [11] B. Johannesson, *Comput. Geotech.* 37 (5) (2010) 667–677.
- [12] J. Marchand, E. Samson, *Cem. Concr. Compos.* 31 (8) (2009) 515–521.
- [13] V. Baroghel-Bouny, T. Nguyen, P. Dangla, *Cem. Concr. Compos.* 31 (8) (2009) 522–534.
- [14] Y. Hosokawa, K. Yamada, B. Johannesson, L.-O. Nilsson, *Mater. Struct.* (2011) 1–16. ISSN 1359-5997, <http://dx.doi.org/10.1617/s11527-011-9720-2>.
- [15] A. Nonat, X. Lecoq, *The structure, stoichiometry and properties of CSH prepared by C3S hydration under controlled conditions*, Nuclear Magnetic Resonance Spectroscopy of Cement-Based Materials, Springer, Berlin, 1998.
- [16] Y. Hosokawa, K. Yamada, A. Nonat, A thermodynamic model with the electrical double layer on the C-S-H particle surface to predict liquid-solid compositions of hardened cement paste, *J Res Taiheiyō Cem Corp* 157 (2009) 3–10.
- [17] E. Samson, J. Marchand, *Comput. Struct.* 85 (23) (2007) 1740–1756.
- [18] B. Johannesson, U. Nyman, *Transp. Porous Media* 84 (3) (2010) 735–754.
- [19] D.L. Parkhurst, C. Appelo, et al., User's guide to PHREEQC (version 2): a computer program for speciation, batch-reaction, one-dimensional transport, and inverse geochemical calculations, Water-Resources Investigations Report 99-4259, U.S. Department of the Interior.
- [20] S.R. Charlton, D.L. Parkhurst, *Comput. Geosci.* 37 (10) (2011) 1653–1663. ISSN 0098-3004, <http://dx.doi.org/10.1016/j.cageo.2011.02.005>. <<http://www.sciencedirect.com/science/article/pii/S0098300411000653>>.
- [21] G. Möschner, B. Lothenbach, F. Winnefeld, A. Ulrich, R. Figi, R. Kretzschmar, *Cem. Concr. Res.* 39 (6) (2009) 482–489.
- [22] T. Schmidt, B. Lothenbach, M. Romer, K. Scrivener, D. Rentsch, R. Figi, *Cem. Concr. Res.* 38 (3) (2008) 337–349.
- [23] G. Möschner, B. Lothenbach, J. Rose, A. Ulrich, R. Figi, R. Kretzschmar, *Geochim. Cosmochim. Acta* 72 (1) (2008) 1–18.
- [24] B. Lothenbach, T. Matschei, G. Möschner, F.P. Glasser, *Cem. Concr. Res.* 38 (1) (2008) 1–18.
- [25] B. Lothenbach, F. Winnefeld, *Cem. Concr. Res.* 36 (2) (2006) 209–226, <http://dx.doi.org/10.1016/j.cemconres.2005.03.001>. ISSN 00088846, 18733948.
- [26] D.A. Kulik, *Cem. Concr. Res.* 41 (5) (2011) 477–495, <http://dx.doi.org/10.1016/j.cemconres.2011.01.012>. ISSN 00088846, 18733948.
- [27] U. Nyman, P. Gustafsson, B. Johannesson, R. Häggglund, *Int. J. Numer. Methods Eng.* 66 (12) (2006) 1859–1883.
- [28] N. Ottosen, H. Petersson, *Introduction to the Finite Element Method*, Prentice-Hall, 1992.
- [29] N. Ottosen, M. Ristinmaa, *Mechanics of Constitutive Modeling*, Elsevier, 2005.
- [30] H.F. Taylor, *Cement Chemistry*, Thomas Telford, 1997.
- [31] C.D. Shackelford, D.E. Daniel, *J. Geotech. Eng.* 117 (3) (1991) 467–484.
- [32] Q. Hu, J.S. Wang, *Aqueous-phase diffusion in unsaturated geologic media: a review*, *Crit. Rev. Env. Sci. Tec.* 33 (3) (2003) 275–297.
- [33] D. Jacques, *Benchmarking of the cement model and detrimental chemical reactions including temperature dependent parameters*, Tech. Rep., ONDRAF/NIRAS, 2008.
- [34] B. Johannesson, *Cem. Concr. Res.* 33 (4) (2003) 481–488.
- [35] M.M. Jensen, B. Johannesson, M. Geiker, A numerical comparison of ionic multi-species diffusion with and without sorption hysteresis for cement-based materials, *Transp. Porous Media* (submitted for publication).
- [36] M.J. Simpson, K.A. Landman, *Adv. Water Resour.* 30 (9) (2007) 2026–2033.
- [37] D.R. Lide, W.M. Haynes, R. Lide, W.M. Haynes, *CRC Handbook of Chemistry and Physics: A Ready-Reference Book of Chemical and Physical Data*, 91 ed., CRC Press, 2010. ISBN 1439820775, 9781439820773.
- [38] J. Shen, P. Dangla, M. Thiery, *Geomech. CO Storage Facil.* (2013) 181–208.
- [39] M. Balonis, B. Lothenbach, G. Le Saout, F. Glasser, *Impact of chloride on the mineralogy of hydrated Portland cement systems*, *Cem. Concr. Res.* 40 (7) (2010) 1009–1022.

Paper III

"Comparison of solid phases in cement paste calculated by two different C-S-H models in a reactive mass transport model"

M. M. Jensen, Y. Hosokawa , B. Johannesson

Submitted: *Modelling and Simulation in Materials Science and Engineering, Jul, 2014*

Comparison of solid formation calculated by two different C-S-H models in a reactive mass transport model

M. M. Jensen^{a,*}, Y. Hosokawa^b, B. Johannesson^a

^aTechnical University of Denmark, Department of Civil Engineering, Brovej 118, 2800 Kgs. Lyngby
^bR & D Center, Taiheiyo Cement Corporation, Japan

Abstract

Reactive transport modeling of cement based materials are investigated in terms of a numerical comparison between two C-S-H descriptions. The governing equations for the reactive transport model is the Poisson–Nernst–Planck equations and the chemical equilibrium is solved by the geochemical code PHREEQC. A short review of the mass actions laws, used by phreeqc to determine the equilibrium state is given. The two C-S-H models used are a four end-member solid-solution model and a surface complexation model accounting for the double layer binding of ions. Multi-species ingress simulations are used to compare the results from the two C-S-H models in terms of the predicted amount of solid phases formed or dissolved. The results are compared after 2 and 10 years simulated exposure, where the exposure solution is an average sea-water composition. The main differences in the solid phase composition, using the two models are found in the amount of ettringite and carbonate containing phases formed.

1. Introduction

of many cement based materials is the calcium silicate hydrate (C-S-H) phase and therefore one of the most studied parts. Chemical structural models are often used as a basis for the development of more phenomenological descriptive models. The term descriptive chemical model is used here for a chemical model that is described by a dissolution reaction and a solubility product. The descriptive chemical models are used in reactive mass transport models, where the mass transport is described at the macro level.

The structural complexity of the C-S-H phase has been debated in several papers over the last century and is to some extent still ongoing [1, 2]. Essentially, the discussions are about describing the calcium-to-silica ratio (C/S) in the C-S-H phase and to some extent incorporate other physical changes related to this. It is well known that the C/S ratio varies within the C-S-H phase for, e.g., ordinary Portland cement [3]. The variations have been measured by different techniques and the results have been interpreted differently in terms of natural analogs and structural formulas [4, 5, 6, 7]. The most used natural analogs for the C-S-H are properly tobermorite and jennite like structures [4, 6, 7]. Different structural models are summarized and compared to a model proposed by Richardson and Groves [8] in [5, 4]. It is to some extent concluded by Richardson [5, 4] that the basic formulation of the structural models proposed by different authors may not differ

significantly and the differences can be considered as special cases of one another.

Some descriptive thermodynamic models, used in reactive transport simulations of cement based materials, take into account the structural properties in order to keep the descriptive thermodynamic structurally consistent. A list of proposed thermodynamic C-S-H models is summarized by Soler [9], where the first models presented was empirical or semi-empirical and later evolved to solid-solution models. The thermodynamic solid-solution model proposed by Kulik and Kersten [10] and the later improvement by Kulik [11] takes into account structural considerations. Other thermodynamic models like Sugiyama and Fujita [12] and Carey and Lichtner [13] are based on dissolution data from different papers, where the structural consistency over the C/S range is only considered limited in these models.

Another type of thermodynamic C-S-H model is proposed in terms of surface complexations. This type of C-S-H model is, e.g., proposed by Nonat et al. [14] and later discussed by Nonat [6]. The complexation model proposed is in some sense directly related to the structural properties as the surface reactions are related to, e.g., bridging of elements and interlayer composition. The thermodynamic surface complexation model by Nonat [6] is, to the authors knowledge, the only model of this type for C-S-H suggested in the literature.

The use of thermodynamic chemical models in reactive mass transport models, for cement based materials, are relatively common see, e.g., Marchand and Samson [15], Hosokawa et al. [16], Carey and Lichtner [13], Le Bescop et al. [17]. The chemical C-S-H models used in these reactive mass transport models are often supported by a more

*Mads Mønster Jensen
Email address: mmoj@byg.dtu.dk (M. M. Jensen)

or less detailed list of thermodynamic reactions related to cement paste. A well known thermodynamic database for cement based materials is the Cemdata07 which contains data assembled from different papers and it is continuously updated [18, 19, 20, 21, 22].

This work will show two different thermodynamic C-S-H models, employed in a reactive mass transport model. The C-S-H models considered are, an ideal four end-member solid-solution model proposed by Kulik [11] and a slightly modified version of the surface complexation model proposed by Nonat [6] accounting for electrical double layer (EDL) binding of ions. The C-S-H models are combined with relevant solid phases from the Cemdata07 thermodynamic database in order to obtain a detailed description of a cement paste. The combination of the selected reactions from the Cemdata07 thermodynamic database with the two different C-S-H models and the use of this in a reactive mass transport model is new. A review of the mass transport model and the chemical equilibrium calculations are given. The C-S-H models are used in a multi-species ion ingress simulations. Results from the ingress simulations are shown in terms of the solid phase compositions. The solid phase compositions are compared after 2 and 10 years exposure simulations in order to evaluate any differences in the solid phase composition using the two different C-S-H models.

2. Numerical models and methods

The governing equations for the mass transport part of the model are shown together with a brief description of the finite element scheme used. An operator splitting approach is adopted for the numerical solution of the coupled mass transport and the chemical equilibrium. The operator splitting approach enables the use of an external chemical equilibrium solver, where the PHREEQC code is employed in this case. A review of the mass action laws used in PHREEQC to determine chemical equilibrium is given in order to present the complete mathematical structure of the adopted models.

2.1. Governing equations and solution method

The reactive mass transport is described by an extended Poisson–Nernst–Planck (PNP) system of equations, where a mass exchange term q_i is added to the classical representation of the PNP equation system. The exchange term q_i takes into account the chemical interactions between the species in the system and the supply from solid phases. A more generalized extended PNP version can, for instance, be obtained by hybrid mixture theory as described in Bennethum and Cushman [23, 24] which is essentially the PNP version presented here with the assumption of a fully saturated pore structure. An essential result from mixture theory is that $\sum_i q_i = 0$ must be satisfied to obtain mass balance in the system, see, e.g., Bowen [25], Bennethum and Cushman [23]. The extended Nernst-Planck part of the system is given as

$$\frac{\partial c_i}{\partial t} = \nabla \cdot (D_i \nabla c_i - A_i c_i z_i \nabla \Phi) + q_i; \quad i = 1, 2, \dots, m \quad (1)$$

where c_i is the concentration of specie i , t is time, D_i^l is the effective diffusion coefficient for constituent i , A_i^l is the ionic mobility. The relation $A_i^l = D_i^l F / (R_g T)$ is used see, e.g., Johannesson [26], where F is Faraday’s constant and R_g is the universal gas constant. The property z_i is the valence state of constituent i and Φ is the total electric potential or streaming potential. The relation $D_i^l = D_i^{l,0} \tau$ for the effective diffusion coefficient is used, where $D_i^{l,0}$ is the self diffusion coefficient and τ is the tortuosity factor. The diffusion coefficients $D_i^{l,0}$ are shown in Tab. B.6. The chemical equilibrium term q_i is solved by an operator splitting approach in the numerical solution scheme. Operator splitting is a common approach in reactive transport modeling, e.g., [27, 16, 28, 29]. The chemical reactions are assumed to take place instantaneously with respect to the mass transport, which facilitate the operator splitting method. The species concentrations determined by the mass transport are used as input values for the chemical equilibrium calculation and the species concentration determined from this are used as initial values for the mass transport calculation in the following discrete time step. The interface version of PHREEQC, the IPHREEQC library [30] is employed in this case, which use the mass action laws to solve chemical equilibrium. A review of the relevant parts of PHREEQC manual Parkhurst et al. [31] of the mass action laws is given in section 2.2.

The pore solution charge balance is considered by the Poisson part of the PNP system and coupled to Eq. (1) by the total electric intensity potential Φ . The Poisson equation is given as

$$\varepsilon_d \varepsilon_0 \nabla^2 \Phi = F \sum_{i=1}^M c_i z_i \quad (2)$$

where ε_d is the relative dielectricity coefficient, ε_0 is the dielectricity coefficient of vacuum and M is the total number of species considered.

The mass transport part of the PNP system is for this case solved by the finite element method using a single parameter time integration scheme. The finite element formulation is obtained by re-writing the strong forms of Eqs. (1) and (2) into weak forms. The system is multiplied with an arbitrary spatial weight function $w(x, y, z)$ and a arbitrary transient weight function $W(t)$, followed by integration over the spatial domain and the time domain of interest. The weak form is then obtained by using the Green-Gauss theorem [32, 33]. The state variables are approximated by the general expansion $\mathbf{N}\mathbf{a}$ where \mathbf{N} is the global shape function and \mathbf{a} contains the state variables at the nodal points. The Galerkin’s method is used for the approximation of the spatial weight function. The problem considered in Section 3 is one-dimensional using linear spatial elements, which yields the shape function as $\mathbf{N} =$

$[1 - x/l_e, x/l_e]$ where l_e is the element length. The global approximated equation system is: $\int_{t_1}^{t_2} W [\mathbf{C}\dot{\mathbf{a}} + \mathbf{K}\mathbf{a} - \mathbf{f}] dt$, where \mathbf{C} is the global mass matrix, \mathbf{K} is the global stiffness matrix, $\dot{\mathbf{a}}$ is the time derivatives of the state variables and \mathbf{f} is the load vector. A linear expansion in the time domain is employed to obtain a single parameter time integration scheme see, e.g., Zienkiewicz et al. [33]. The time integration scheme is

$$\mathbf{a}_{n+1} = (\mathbf{C} + \Delta t \theta \mathbf{K})^{-1} [\mathbf{C} + \Delta t (1 - \theta) \mathbf{K} \mathbf{a}_n + \mathbf{f}_n + \theta (\mathbf{f}_{n+1} - \mathbf{f}_n)] \quad (3)$$

where n is the discrete time step number and θ is the single weighting parameter between $0 \leq \theta \leq 1$ for the time domain. The initial value problem in Eq. (3) is solved for \mathbf{a}_{n+1} and the solution is improved by a modified Newton-Raphson scheme, see, e.g., Ottosen and Ristinmaa [34]. The modified Newton-Raphson scheme is employed to save computational time as the calculation of the true tangential stiffness is omitted. A system residual ψ is according to Ottosen and Ristinmaa [34] determined by

$$\psi^{l-1} = \mathbf{C}^{l-1} \frac{1}{\Delta t} (\mathbf{a}_{n+1}^{l-1} - \mathbf{a}_n) + \mathbf{K}^{l-1} \mathbf{a}_{n+1}^{l-1} - (\mathbf{f}_{n+1}^{l-1} - \mathbf{f}_n^l) \quad (4)$$

where l is the iteration number. The improved solution \mathbf{a}_{n+1}^l is determined from

$$\psi^{l-1} = \left[\mathbf{C}^{l-1} \frac{1}{\Delta t} + \mathbf{K}^{l-1} \right] (\mathbf{a}_{n+1}^l - \mathbf{a}_{n+1}^{l-1}) \quad (5)$$

The Newton-Raphson scheme iterates between Eqs. (4) and (5) until a defined criteria for the residual is reached. For this particular case it is observed that $\theta = 1$ is used in the modified Newton-Raphson scheme adopted.

2.2. Chemical equilibrium solution methods

The chemical interaction term q_i introduced in the mass transport Eq. 1 is decoupled from the differential equations in the finite element algorithm by an operator splitting approach. The decoupling facilitate the use of, e.g., mass action laws to obtain chemical equilibrium. The chemical equilibrium is considered between aqueous species and precipitation/dissolution reactions between solids and aqueous species in the liquid phase for this case.

As stated in Section 2.1, the geochemical code PHREEQC by Parkhurst et al. [31] is employed as solver and more specific the IPHREEQC interface is utilized [30]. The PHREEQC code has the capability of determine chemical equilibrium for aqueous reactions, pure phase reactions, solid-solution reactions and surface complexation reactions with explicit determination of the electrical double layer (EDL). All of the above listed features are used in this work. A review of the mass action laws as presented in Parkhurst et al. [31] is given in the following, the description of the equation system is supported by the descriptions in Bethke [35] and Appelo and Postma [36].

The description follows the terminology in [31] where master species are pure elements and elements at different valence state, e.g., Ca^{+2} , Fe^{+2} and Fe^{+3} . All other components in the chemical system considered is only allowed to contain these elements. This is a pure numerical separation of the components. The species activity a_i is obtained by defining the chemical potential μ_i as: $\mu_i \equiv \partial G_i / \partial n_i$ where G_i is the Gibb's free energy and n_i the mole number, see [35]. Equilibrium of a given reaction is found when the sum of all the species Gibb's free energies of the reaction G is at its minimum under the condition that the pressure and temperature are fixed. The chemical potential μ_i is defined as $\mu_i = \mu_i^0 + RT \ln a_i$, where μ_i^0 is the standard reference potential, R is the universal gas constant, T is the temperature and a_i is the activity of the species. The equilibrium constant K is defined in terms of the standard free energy G^0 as: $K = \Sigma \Delta G^0 / RT$, which leads to the general expression for aquas species equilibrium in PHREEQC. The mass action equation for the solution specie i , can be written as

$$K_i = a_i \prod_j a_j^{-b_{ij}} \quad (6)$$

where a_j is the activity of the master species j and b_{ij} denotes the stoichiometric coefficient of master species j in solution species i . The complete numerical system in PHREEQC includes a determination of the total moles of a solution specie n_i which in PHREEQC is derived from the mass action law Eq. (6), by re-writing the activity in terms of the activity coefficient γ_i , the molality m_i and the mass of water w_{aq} , so that $a_i = \gamma_i m_i$ and $n_i = m_i w_{aq}$. The relation for the total moles of the i 'th species in PHREEQC is

$$n_i = w_{aq} K_i \frac{\prod_j a_j^{-b_{ij}}}{\gamma_i} \quad (7)$$

The activity coefficient in PHREEQC is determined by either, the Davies equation, defined as

$$\log \gamma_i = -A z_i^2 \left(\frac{\sqrt{\mu_s}}{1 + \sqrt{\mu_s}} - 0.3 \mu_s \right) \quad (8)$$

or the extended WATEQ Debye-Hückel equation, defined as

$$\log \gamma_i = -\frac{A z_i^2 \sqrt{\mu_s}}{1 + B \alpha_i} + \beta_i \mu_s \quad (9)$$

where z_i is the valence, A and B are temperature depended parameters, α_i and β_i are ion-specific parameters and μ_s is the ionic strength given by Eq. (11). According to [31], the Eq. (9) is denoted extended Debye-Hückel if $\beta_i = 0$ and α_i is an ion size parameter. The use of either Eq. (8) or (9) is determined by the data available in the database.

In PHREEQC the activity of the water $a_{\text{H}_2\text{O}}$ is determined by an approximation based on Raoult's law in PHREEQC and is given as

$$a_{\text{H}_2\text{O}} = 1 - 0.017 \sum_i \frac{n_i}{w_{aq}} \quad (10)$$

The ionic strength μ_s of the pore solution is determined in PHREEQC, as

$$\mu_s = \frac{1}{2} \sum_i z_i^2 \frac{n_i}{w_{aq}} \quad (11)$$

The mass-action equation for the equilibrium solid phase equilibrium is similar to the mass action equation for the aqueous reactions Eq. (6). The activity of the equilibrium phase p is assumed to be 1.0, which results in the mass actions law, as

$$K_p = \prod_j a_j^{c_{pj}} \quad (12)$$

A saturation index SI is introduced in PHREEQC for the equilibrium phase calculation: $SI = \log \prod_j a_j^{c_{pj}}$. The saturation index is a numerical factor for the state of the phase in terms of supersaturated, equilibrium or under saturated, by $SI > 0$, $SI = 0$ and $SI < 0$, respectively.

Solid-solution equilibrium calculations are incorporated in PHREEQC and are of great importance in cement based material modeling. The mass action equation for solid-solutions in PHREEQC is based on the end-member activity, defined as: $a_{ss_p} = \lambda_{ss_p} x_{ss_p}$, where the notation ss_p refers to the p 'th equilibrium phase in solid-solution ss and x_{ss_p} is the mole fraction of the p 'th equilibrium phase in the solid-solution defined as: $x_{ss_p} = n_{ss_p} / \sum_p n_{ss_p}$. Solid-solution equilibrium can be difficult to solve numerically, as described in, e.g., Bethke [35] and is often restricted to ideal solid-solutions. For the ideal solid-solutions, it is assumed that $\lambda_{ss_p} = 1$ for all p , so the activity reduces to $a_{ss_p} = x_{ss_p}$. The general mass-action law for solid-solutions in PHREEQC is given as

$$K_{ss_p} = \frac{\prod_j a_j^{c_{sspj}}}{a_{ss_p}} = n_{ss_p} \frac{\prod_j a_j^{c_{sspj}}}{\sum_p n_{ss_p}} \quad (13)$$

A solubility quotient Q_{ss_p} for the solid-solution is introduced as: $Q_{ss_p} = \prod_j a_j^{c_{sspj}} / K_{ss_p} a_{ss_p}$ which is similar to the saturation index SI for the equilibrium phases.

Surface complexation modeling including electrical double layers is a feature included in PHREEQC. The surface complexation theory in PHREEQC is based on Dzombak and Morel [37] and the explicit calculation of the double layer composition is based on Borkovec and Westall [38]. The PHREEQC algorithm defines surface species separated from the aqueous species and surface master species are defined for the same matter. The presentation of the theory here is limited to a single surface site for simplicity. The mass action law for surface species is

$$K_{s_i} = \left(a_{s_i} \prod_m a_m^{-c_{m,s_i}} \right) e^{\frac{F\Psi_s}{RT} \Delta z_{s_i}} \quad (14)$$

where the subscript s_i denotes the i 'th surface species in the s surface, K_{s_i} is the equilibrium constant of the surface reaction, a_{s_i} is the activity for the surface species, a_m

is the activity for the master species m including the surface master species, c_{m,s_i} is the stoichiometric coefficient of master species m in the association reaction for surface species, Ψ_s denotes the surface potential and Δz_{s_i} is the net change in surface charge and F is Faraday's constant. The total moles of surface species n_{s_i} are determined by PHREEQC, as

$$n_{s_i} = K_{s_i} a_{\Psi_s}^{-2\Delta z_{s_i}} \prod_m a_m^{-c_{m,s_i}} \quad (15)$$

where the definition $\ln a_{\Psi_s} = \frac{F\Psi_s}{2RT}$ is used. Explicit calculation of the double layer composition, related to a specified surface is included in PHREEQC. The PHREEQC algorithm uses an explicit solution to the Poisson-Boltzmann equation obtained by Borkovec and Westall [38]. It is assumed in PHREEQC that the water density ρ_{aq} is constant $\rho_{aq} = 1000$ [kg/m³]. The excess of ions $\Gamma_{s,i}$ on surface s of species i is determined in PHREEQC by the relation

$$\Gamma_{s,i} = \int_{x_{d,s}}^{\infty} (c_{s,i}(x) - c_i) dx \quad (16)$$

where $c_{s,i}(x)$ is the ion concentration of species i as a function of the distance x from the surface s , c_i^0 is the bulk concentration of species i and $x_{d,s}$ is the location of the outer Helmholtz plane, d, s . Note that the total list of ion species i may be different from the species list considered in the bulk solution. The molality of the surface excess species $m_{s,i}$ is related to $\Gamma_{s,i}$ by the surface area A_s for 1.0 kg water, by $m_{s,i} = A_s \Gamma_{s,i}$ and the surface excess molality is related to the bulk molality m_i by $m_{s,i} = g_{s,i} m_i$. The $g_{s,i}$ function in PHREEQC is a function of the potential at the surface, the species concentrations and charges of all species in the bulk solution [31]. The $g_{s,i}$ in PHREEQC is given as

$$g_{s,i} = A_s \operatorname{sgn}(x_{s,d} - 1) \delta \int_1^{x_{s,d}} \frac{(X^{z_i} - 1)}{[X^2 \sum_i m_i (X^{z_i} - 1)]^{1/2}} dX \quad (17)$$

where the definition $X = e^{-\frac{F\Psi_s}{RT}}$ and $\delta = (\varepsilon_d \varepsilon_0 \frac{RT}{2})^{1/2}$ are used and where ε_d is the relative dielectricity coefficient and ε_0 is the dielectricity coefficient of vacuum. In the PHREEQC algorithm, a_{Ψ_s} is defined as unknown for the double layer calculation, this variable is related to the $g_{s,i}$ function in PHREEQC by $a_{\Psi_s} = X^{-2}$. With the $g_{s,i}$ function and the molality relation between the bulk and excess surface, PHREEQC is then able to determine the total moles of a species $n_{s,i}$ in the double layer. This is the sum of the amount from the double layer and the bulk amount. PHREEQC assumes that $W_{aq,bulk} \cong W_{aq}$ and the mass of water in the double layer $W_{aq,EDL}$ is known from $W_{aq,EDL} = t_{EDL} A_s$, where t_{EDL} is the thickness of the double layer. The total moles $n_{s,i}$ is determined by

$$\begin{aligned} n_{s,i} &= W_{aq,bulk} g_{s,i} \frac{n_i}{W_{aq}} + W_{aq,EDL} \frac{n_i}{W_{aq}} \\ &\cong g_{s,i} n_i + W_{aq,EDL} \frac{n_i}{W_{aq}} \end{aligned} \quad (18)$$

The surface species in PHREEQC is defined separately from the aqueous species as described earlier, in order to obtain charge balance for the surface, PHREEQC determines the charge balance between the surface and the double layer, as

$$f_{z,s} = \sum_{s_i} z_{s_i} n_{s_i} + \sum_i z_i n_{s,i} \quad (19)$$

where $f_{z,s}$ is the charge imbalance. Note that if several surface sites are considered, a summation over these should be considered. The total charge balance for the system with the reaction types considered is given in PHREEQC as

$$f_z = T_z - \sum_i z_i n_i + \sum_s f_{z,s} \quad (20)$$

where f_z is the charge imbalance and T_z is the total charge balance. A natural chemical solution is always in charge balance, so the imbalances described must be minimized to a sufficiently low level. The charge balance is particular important in the coupling to the mass transport system considered here.

The mass balance, or mole balance in this context, is obtained in PHREEQC by summarizing the total moles of all different chemical elements participating in the different chemical reactions described. The mole balance for all reaction types considered is given in PHREEQC as

$$\begin{aligned} f_j = T_j - \sum_p C_{j,p} n_p - \sum_{ss} \sum_p C_{j,ss,p} n_{ss,p} - \sum_i C_{j,i} n_i \\ - \sum_s \sum_i C_{j,s,i} n_{s,i} - \sum_s \sum_i C_{j,i,s} n_{i,s} \end{aligned} \quad (21)$$

where f_j is the mole imbalance of the system, T_j is the total moles of the elements and C_j is moles of element j per mole of each entity. C_j is usually, but not always, equal to the stoichiometric coefficient c in the mass action laws considered.

The PHREEQC code for forward modeling of chemical equilibrium uses a Newton-Raphson iteration scheme to find chemical equilibrium for a given system. A system with the components as described above is solved for the unknowns $\ln a_j$, $\ln m_{aq}$, $\ln a_{\text{H}_2\text{O}}$, $\ln W_{aq}$, μ_s , n_{ss} , n_p , $\ln a_{s_i}$ and $\ln a_{\Psi_s}$. Different numerical optimization techniques are applied by the PHREEQC algorithm to the solution procedure, e.g., to avoid singular matrices.

2.3. Extended EDL thickness iteration

The operator splitting approach used in the numerical solution to the coupled mass transport enables an extended determination of the double layer thickness which is an input parameter in PHREEQC. The approximated thickness of the diffuse layer is the Debye-length κ , given by

$$\kappa^{-1} = \left[\frac{2N_A e_c^2 \mu_s}{\epsilon \epsilon_0 k_B T} \right]^{-1/2} \quad (22)$$

where N_A is Avogadro's number, e_c is the electron charge and k_B is the Boltzmann's constant. Assuming constant temperature, yields that the Eq. (22) is a function of the ionic strength μ_s , which is determined by PHREEQC. The initial guess on the double layer thickness may not fit the calculated ionic strength and thereby change the chemical equilibrium. For this reason an extra chemical equilibrium calculation for each spatial location considered is introduced in this model. The double layer thickness is optimized by determining a double layer thickness from the initial chemical equilibrium calculation and use this in the additional chemical equilibrium calculation to improve the solution. The initial guess in the discrete time domain is the thickness determined from the ionic strength determined in the previous accepted time step.

2.4. Chemical models

Two thermodynamic C-S-H models are investigated in this paper; a solid-solution model by Kulik [11] and a slightly modified version of a surface complexation model proposed by Nonat [6]. Both models have undergone development and improvements since their initial publication, see Kulik and Kersten [10] and Nonat [6]. The models considered here are the state of the art within thermodynamic C-S-H models described by solid-solution and surface complexation.

The models considered are originated from chemical structural models of C-S-H and the reaction schemes are constructed based on these, in order to construct a sound predictive models that is valid in a broad C/S ratio range. The predictive solid-solution model proposed by Kulik [11] is based on a structural model proposed by Richardson [4] and experimental data from Chen et al. [39] and the model is valid in the range of $0.67 < \text{C/S} < 1.7$. The surface complexation model in Nonat [6] is based on a structural model proposed by Nonat and Lecoq [40], together with experimental data in Nonat et al. [14] and the model is valid in the range of $1 < \text{C/S} < 1.5$.

As described in the introduction several structural C-S-H models are proposed and discussions regarding their performance are ongoing. It is beyond the scope of this paper to contribute to this discussion but some conclusions regarding the structural background are emphasized. Such conclusions are relevant because results from the use of two different C-S-H models are compared in this work. According to Richardson [4], parts of the modeling work in Nonat and Lecoq [40] is similar to parts of the structural model in Richardson [4] and differs only regarding the presences of interlayer Ca^{2+} ions. It is emphasized in Nonat [6] that the elemental description of the C-S-H is chemically equivalent to that given by Richardson and Groves [41], but the formulation is directly related to the structural model Nonat and Lecoq [40]. From the above referred papers, it is concluded that the basic principals in the structural models are comparable and the thermodynamic models are comparable only to a certain extend.

2.4.1. C-S-H surface complexation model with diffuse double layer

The surface complexation model described in Nonat [6] has been implemented in a reactive mass transport model for cement paste by Hosokawa et al. [16]. The surface complexation model used in this work differs slightly from the original work, see Tab. 1 for the reactions considered. The diffuse double layer is taken into account, assuming that $t_{EDL}/\kappa^{-1} = 1.55$, which is based on data from Glasser et al. [42] and Hirao et al. [43]. The same assumption for the double layer thickness t_{EDL} will be used in Sec. 3.

Table 1: Reaction schemes for the surface complexation model and the C-S-H particle. The model differs slightly from the original work by Nonat [6].

External sites	
Reaction scheme	Solubility constant $\log K$
$-\text{SiOH} \leftrightarrow -\text{SiO}^- + \text{H}^+$	-11.8
$-\text{SiOH} + \text{Ca}^{2+} \leftrightarrow -\text{SiOCa}^+ + \text{H}^+$	-9.0
$-\text{SiOH} + \text{CaOH}^+ \leftrightarrow -\text{SiOCaOH} + \text{H}^+$	-12.0
$-\text{SiOH} + 0.5\text{H}_4\text{SiO}_4 \leftrightarrow -\text{SiOSi}_{0.5}\text{OH} + \text{H}_2\text{O}$	3.5
$-\text{SiOSi}_{0.5}\text{OH} + 0.5\text{Ca}^{2+} \leftrightarrow -\text{SiOSi}_{0.5}\text{Ca}_{0.5} + \text{H}^+$	-10.2
$-\text{SiOSi}_{0.5}\text{OH} \leftrightarrow -\text{SiOSi}_{0.5}\text{O}^- + \text{H}^+$	-11.8
$-\text{SiOSi}_{0.5}\text{OH} + \text{Ca}^{2+} \leftrightarrow -\text{SiOSi}_{0.5}\text{OCa}^+ + \text{H}^+$	-9.0
Internal sites	
Reaction scheme	Solubility constant $\log K$
$-\text{SiOH} + 0.5\text{Ca}^{2+} \leftrightarrow -\text{SiOCa}_{0.5} + \text{H}^+$	-10.2
$-\text{SiOH} + \text{CaOH}^+ \leftrightarrow -\text{SiOCaOH} + \text{H}^+$	-12.0
$-\text{SiOH} + 0.5\text{H}_4\text{SiO}_4 \leftrightarrow -\text{SiOSi}_{0.5}\text{OH} + \text{H}_2\text{O}$	3.5
$-\text{SiOSi}_{0.5}\text{OH} + 0.5\text{Ca}^{2+} \leftrightarrow -\text{SiOSi}_{0.5}\text{Ca}_{0.5} + \text{H}^+$	10.2
C-S-H particle	
Reaction scheme	Solubility constant $\log K$
$\text{Ca}_2\text{Si}_2\text{O}_5(\text{OH})_2 + 4\text{H}^+ + \text{H}_2\text{O} \leftrightarrow 2\text{Ca}^{2+} + 2\text{H}_4\text{SiO}_4$	29.6

The amount of the surface complexes is related to a equilibrium phase C-S-H particle, where 0.5 sites per moles is used for the internal sites and 1.5 sites per mole is used for the external sites. The internal and external sites have a specific surface area of $0 \text{ [m}^2/\text{mol}]$ and $83638.7 \text{ [m}^2/\text{mol}]$, respectively .

2.4.2. C-S-H solid-solution model Kulik [11]

The ideal solid-solution is adopted from Kulik [11] and has four end-members, each described by the reactions in Tab. 2. The solid-solution model is denoted CSHQ in Kulik [11]. The solid-solution coexist with SiO_2 at $\text{C/S} < 0.67$ and with $\text{Ca}(\text{OH})_2$ at $\text{C/S} > 1.7$.

3. Simulation setup

The simulations with the two different C-S-H models are considered as boundary value problems solved with a one-dimensional FE scheme with linear spatial elements as described in Sec. 2.1. Both simulations are using the same parameters and constants for the mass transport part in order to compare the results. The total time simulated is $t_{total} = 10$ years, with a time step length of $\Delta t = 30$ hours. The time step length and the associated error induced by the operator splitting approach for the chemical reactions

is not considered here. It is assumed that the boundary error due to the operator splitting approach is the same for the two simulations as the applied boundary values are the same. A summary of the input parameters and physical standard values used, is given in Tab. 4. The cement composition is shown in Tab. 3 and is used as input parameters for the chemical equilibrium model where it is assumed that the cement paste is fully hydrated.

Table 3: Oxide composition for the cement material used in the simulation

	CaO	SiO ₂	Al ₂ O ₃	Fe ₂ O ₃	SO ₃	K ₂ O	Na ₂ O
mass%	64.00	22.00	5.00	4.00	3.00	0.78	0.15

Table 4: Constants parameters for the numerical calculation and material parameters.

Simulation parameters	
w/c	0.45
Spatial elements	250
Total spatial distance [m]	0.05
Total Time t_{total} [years]	10
Time step, Δt [h]	30
Time parameter ¹ , θ	1
Tortuosity factor, τ	0.0039
Relative dielectricity ε_d [V/m]	78.54
Dielectricity in vacuum ε_0 [V/m]	$8.854 \cdot 10^{-12}$
Faraday's constant F [C/mol]	96490

¹ $\theta = 1$ due to the Newton-Raphson scheme adopted

4. Results

The solid phases that are formed or dissolved after a simulation of 10 years with the use of the C-S-H models in Tab. 1 and 2 are presented in Figs. 1 and 2, respectively. Only the phases that are present at the exact time are shown. Sub-sets of the transient solution are shown in terms of the phase compositions after 2 years exposure simulations in order to show the transient development. The simulation using the solid-solution C-S-H is denoted C-S-H(ss) and using the surface complexation model is denoted C-S-H(sc).

4.1. Solid-solution C-S-H

The calculated distribution of the equilibrium phases from the C-S-H(ss) simulation, are shown in Figs. 1a and 1b after 2 and 10 years simulation time, respectively. The portlandite is dissolved in two steps over the spatial domain after 2 years simulated exposure as shown in Fig. 1a. The dissolution front of portlandite at $\approx 0.02\text{[m]}$ is approximately equal to the spatial position of the Friedel's salt and ettringite formation fronts, which are a result of the external ion ingress. The portlandite has one dissolution front near the exposed boundary, after 10 years simulated

Table 2: C-S-H solid-solution model from Kulik [11].

solid-solution		
Name	Reaction scheme	Solubility constant
Tobermorite H	$(\text{CaO})_{0.66}(\text{SiO}_2)(\text{H}_2\text{O})_{1.5} + 1.32\text{H}^+ \leftrightarrow 0.66\text{Ca}^{2+} + \text{H}_4\text{SiO}_4 + 0.16\text{H}_2\text{O}$	8.272
Tobermorite D	$(\text{CaO})_{0.83}(\text{SiO}_2)_{0.66}(\text{H}_2\text{O})_{1.83} + 1.66\text{H}^+ \leftrightarrow 0.83\text{Ca}^{2+} + 0.66\text{H}_4\text{SiO}_4 + 1.34\text{H}_2\text{O}$	13.624
Jennite H	$(\text{CaO})_{1.33}(\text{SiO}_2)(\text{H}_2\text{O})_{2.16} + 2.66\text{H}^+ \leftrightarrow 1.33\text{Ca}^{2+} + \text{H}_4\text{SiO}_4 + 1.49\text{H}_2\text{O}$	22.173
Jennite D	$(\text{CaO})_{1.5}(\text{SiO}_2)_{0.66}(\text{H}_2\text{O})_{2.5} + 3.00\text{H}^+ \leftrightarrow 0.66\text{Ca}^{2+} + \text{H}_4\text{SiO}_4 + 0.16\text{H}_2\text{O}$	28.713

exposure and this is properly due to leaching. The base level amount of portlandite present after 10 years simulated exposure is equal to the bottom amount of the dissolution front at $\approx 0.02[\text{m}]$ after 2 years simulation.

A small amount of additional brucite is formed near the exposed boundary due to the simulated ingress of magnesium. The additional brucite amount and its formation front is only increased slightly from 2 to 10 years simulated exposure.

The C-S-H(ss) is shown in Figs. 1c and 1d. The internal composition of the end-members is only changed slightly from its initial values in the transient and spatial domains. The simulated exposure and its effects on the additional solid-solutions, given in Tab. A.5, are shown in Figs. 1e and 1f. The formation of Friedel's salt is very pronounced for the two exposure times presented. The Friedel's salt and ettringite formations substitutes the monosulfoaluminate and the C_4AH_{13} which is seen in Fig. 1e. The Friedel's salt and ettringite have completely substituted the monosulfoaluminate and C_4AH_{13} phases after 10 years simulated exposure. The total ettringite formation is the sum of the two end-members in the solid-solution AFt(1). The regular ettringite (or Al-ettringite) is initially formed and increases due to the ingress of external ions and its consequences in terms of changes in the pore solution composition. The Fe-ettringite is formed primarily near the exposed boundary where it substitutes the initially formed C_4FH_{13} . The amount of Fe-ettringite is increased in the spatial and transient domains. Fe-hemicarbonate is formed near the exposed surface after 2 years simulated exposure and increased into the spatial domain after 10 years simulated exposure. The carbonate containing phases are formed due to the ingress of dissolved carbonates from the exposure solution. Monocarboaluminate and hemicarboaluminate are formed parallel to the Fe-hemicarbonate in the order of $2 \cdot 10^{-6}[\text{mol}]$ and $2 \cdot 10^{-7}[\text{mol}]$, respectively. The C_4AH_{13} is present parallel with C_4FH_{13} after 10 years simulation in the order of $1 \cdot 10^{-5}[\text{mol}]$. Calcite is formed as an equilibrium phase at the first two nodes from the exposed boundary with a maximum of $4.24 \cdot 10^{-3}[\text{mol}]$. The calcite is only present in the case of the 10 years simulation, see Fig. 1b.

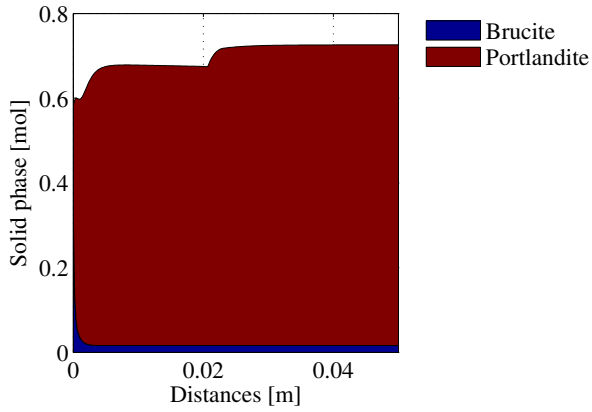
4.2. Surface complexation C-S-H

The Fig. 2 shows the solid phases formed and dissolved by using of the C-S-H(sc) model in Tab. 1 with EDL bind-

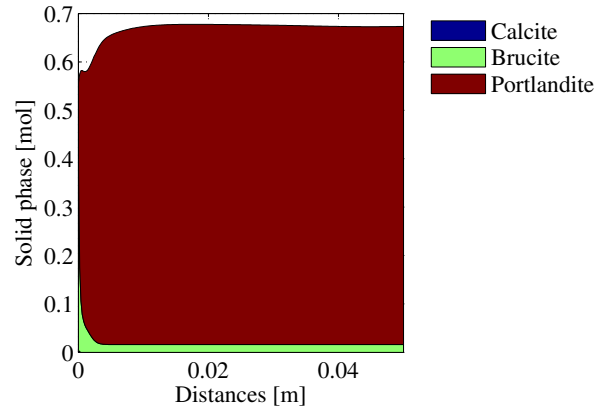
ing of ions included. The portlandite dissolution after 2 years exposure is comparable with the two step dissolution evolvment for the C-S-H(ss) simulation in Fig. 1a and the dissolution front at $\approx 0.02[\text{m}]$ is equivalent with the formation front of Friedel's salt and ettringite. The portlandite has a single dissolution front after 10 years simulated exposure which is similar to the C-S-H(ss) simulation results. Brucite is initially formed in the cement paste and an additional amount is formed near the exposed boundary. The additional amount of brucite formed is higher for both exposure times considered, compared to the corresponding calculated results using the C-S-H(ss) model. Calcite is formed to a larger extent using the C-S-H(sc) model at 2 and 10 years simulated exposure and penetrates further into the spatial domain compared to the results for the C-S-H(ss) model. The C-S-H(sc) reaction schemes as described in Tab. 1 are dependent on the actual amount of C-S-H particle and it is seen that the particle is only dissolved slightly near the exposed boundary after 10 years simulated exposure.

The amount of formed end-members from the included solid-solutions are shown in Figs. 2b and 2d. The formed amount of Friedel's salt and ettringite are comparable with the results obtained from the C-S-H(ss) model and their interchanging characteristics with respect to monosulfoaluminate and C_4AH_{13} are simulated in a similar way as the for the case of the C-S-H(ss) model. Both ettringite end-members considered are formed in a greater amount near the expose surface using the C-S-H(sc) model compared to the C-S-H(ss) model. The system is in favor of the ettringite end-members, so that none of the carbonate containing end-members are formed near the surface after 10 years simulated exposure as seen from the C-S-H(ss) modeling results. Fe-hemicarbonate is formed near the exposed boundary after 2 years, similar to the C-S-H(ss) simulation results, but in contrast, most of this is substituted by the ettringite end-members after 10 years simulation. The hemicarboaluminate and monocarboaluminate are formed in parallel with the Fe-hemicarbonate in the order of $2 \cdot 10^{-6}[\text{mol}]$ and $2 \cdot 10^{-7}[\text{mol}]$, respectively. The C_4AH_{13} is present in parallel with C_4FH_{13} after 10 years simulation in the order of $1 \cdot 10^{-5}[\text{mol}]$.

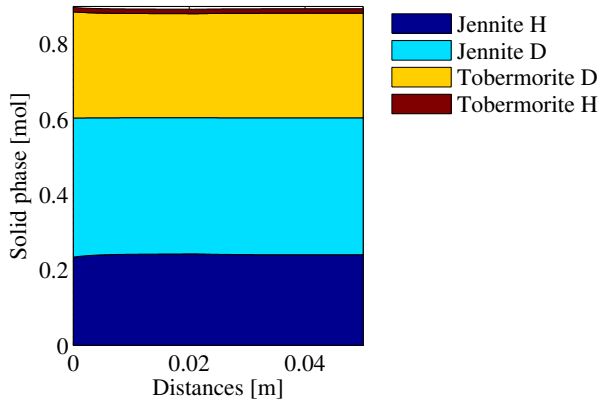
It is clear from the two presented simulations that the different C-S-H models considered yields different results for some of the phases considered in addition to the C-S-H. The most significant difference is seen for the amount



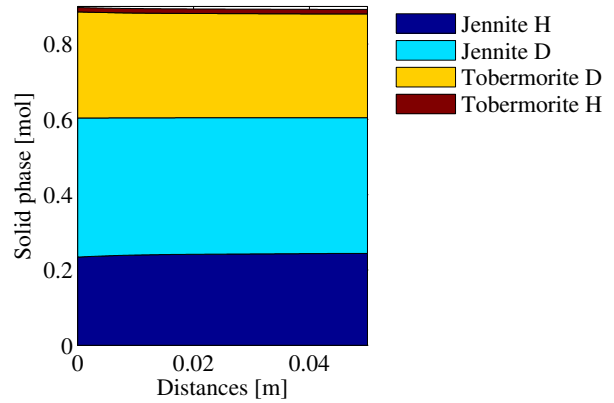
(a) Equilibrium phases after 2 years exposure simulation.



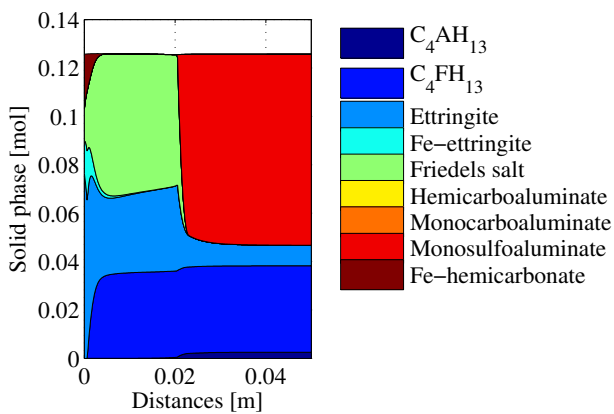
(b) Equilibrium phases after 10 years exposure simulation.



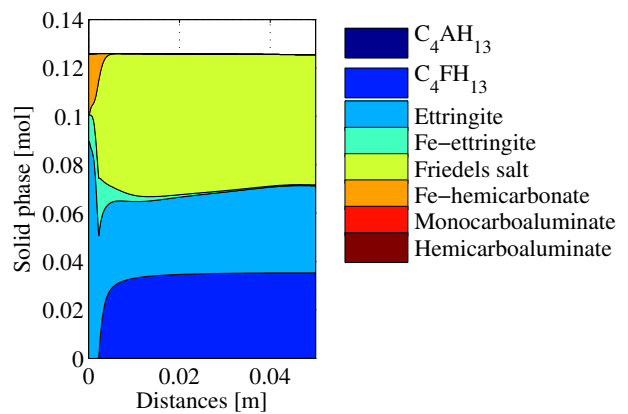
(c) C-S-H Solid-solution end-members after 2 years exposure simulation



(d) C-S-H Solid-solution end-members after 10 years exposure simulation

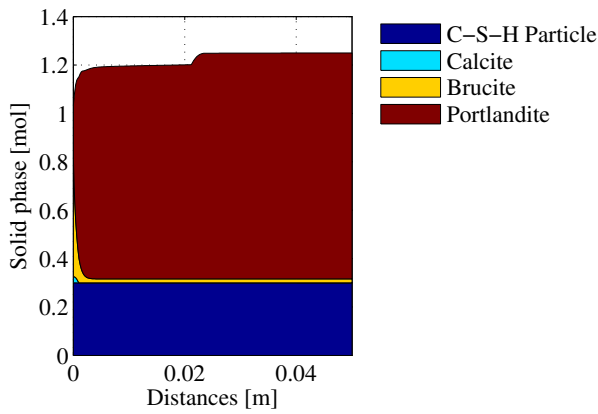


(e) Solid-solutions end-members after 2 years exposure simulation

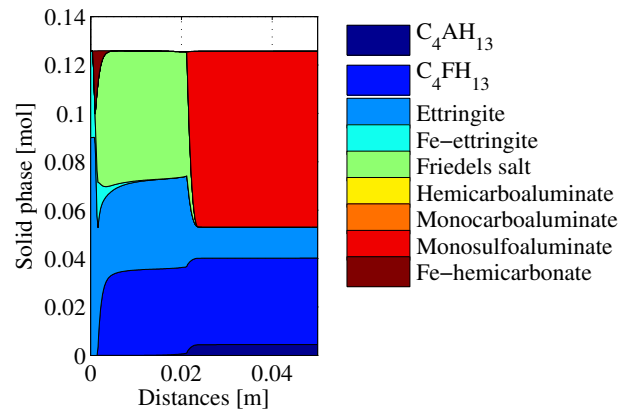


(f) Solid-solutions end-members after 10 years exposure simulation

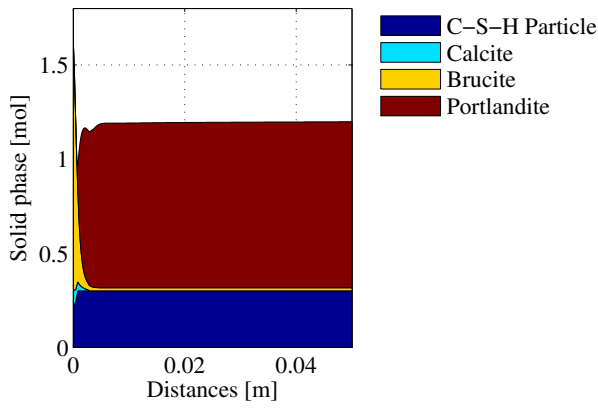
Figure 1: The composition of equilibrium phases and solid-solution end-members after 2 and 10 years simulated sea-water exposure, using the C-S-H(ss) model. The amount is given as moles in the element.



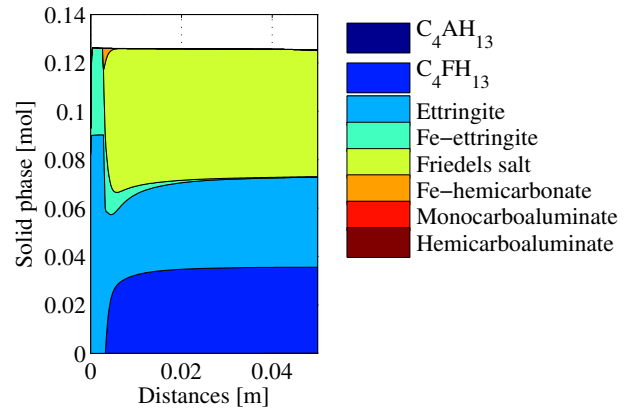
(a) Equilibrium phases after 2 years exposure simulation.



(b) Solid-solutions end-members after 2 years exposure simulation.



(c) Equilibrium phases after 10 years exposure simulation.



(d) Solid-solution end-members after 10 years exposure simulation.

Figure 2: The composition of equilibrium phases and solid-solution end-members after 2 and 10 years simulated exposure, using the C-S-H(*sc*) model. The amount is given as moles in the element.

of ettringite and hemiacarbonate formed. The exact reason for these kinds of different results are difficult to point out due to the coupled characteristics of the overall reactive transport model. It is beyond the scope of this work to indicate which of the models that will perform best in terms of reproducing experimental tests.

5. Discussion

It is important to emphasize that the results presented here are used to compare numerical calculations of two different chemical models. A significant assumption made in numerical modeling of reactive transport, used here, is that all constituents are available for reaction. However, in a natural system, the complex structure of the nano-scale porous matrix may limit the availability of some components to react because they are not in physical contact with each others.

The diffusion properties in the pore solution are also significantly affected by the changes in the solid phase composition. The tortuosity factor is for instance kept constant in time and spatial position which may be an unsound assumption compared to a real system.

6. Conclusion

Two different thermodynamic C-S-H models are used in a reactive transport model and the solid phase compositions are compared after 2 and 10 years simulated multi-species exposure. The chemical C-S-H models considered are a four end-member solid-solution model and a surface complexation model accounting for electrical double layer binding of ions. The numerical mass transport model is based on the Poisson–Nernst–Planck system of equations which are coupled to the thermodynamic chemical equilibrium code PHREEQC. The transport part of the model is solved by the finite element method and the chemical equilibrium problem is solved by the mass action laws by using an operator splitting approach. A review of the chemical equilibrium calculation using the mass action laws is presented in a fashion similar to what being described in the manual of PHREEQC.

Two simulations, with the same exposure conditions and with different C-S-H descriptions are conducted. The total simulation time is 10 years. The solid phase composition determined by the two different simulations are compared at a simulation time of 2 and 10 years in order to show the transient evolution. The simulations showed a significant difference, using the two different C-S-H models, in the amount of solid phases predicted besides the C-S-H phases. The differences are especially significant after 10 years simulated exposure. The most significant effect is observed for the ettringite formation, where the amount simulated with the C-S-H surface complexation model is significant higher near the exposed boundary, compared to the case using the C-S-H solid-solution model.

The amount of carbonate containing phases estimated are different using the two C-S-H models. These phases are formed to a greater extent using the solid-solution C-S-H model than compared to the case of the C-S-H surface complexation model.

The comparison of the two C-S-H models is purely numerical. The future work with the models should include some comparison with experimental data in order to evaluate the performance of predicting real cement based systems.

Bibliography

- [1] S. Soyer-Uzun, S. R. Chae, C. J. Benmore, H.-R. Wenk, P. J. Monteiro, Compositional Evolution of Calcium Silicate Hydrate (C-S-H) Structures by Total X-Ray Scattering, *Journal of the American Ceramic Society* 95 (2) (2012) 793–798.
- [2] S. Grangeon, F. Claret, C. Lerouge, F. Warmont, T. Sato, S. Anraku, C. Numako, Y. Linard, B. Lanson, On the nature of structural disorder in calcium silicate hydrates with a calcium/silicon ratio similar to tobermorite, *Cement and Concrete Research* 52 (2013) 31–37.
- [3] I. Richardson, The nature of CSH in hardened cements, *Cement and Concrete Research* 29 (8) (1999) 1131–1147.
- [4] I. Richardson, Tobermorite/jennite-and tobermorite/calcium hydroxide-based models for the structure of CSH: applicability to hardened pastes of tricalcium silicate, β -dicalcium silicate, Portland cement, and blends of Portland cement with blast-furnace slag, metakaolin, or silica fume, *Cement and Concrete Research* 34 (9) (2004) 1733–1777.
- [5] I. Richardson, The calcium silicate hydrates, *Cement and Concrete Research* 38 (2) (2008) 137–158.
- [6] A. Nonat, The structure and stoichiometry of CSH, *Cement and Concrete Research* 34 (9) (2004) 1521–1528.
- [7] H. M. Jennings, A model for the microstructure of calcium silicate hydrate in cement paste, *Cement and Concrete Research* 30 (1) (2000) 101–116.
- [8] I. Richardson, G. Groves, The incorporation of minor and trace elements into calcium silicate hydrate (C-S-H) gel in hardened cement pastes, *Cement and Concrete Research* 23 (1) (1993) 131–138.
- [9] J. M. Soler, Thermodynamic Description of the Solubility of C-S-H Gels in Hydrated Portland Cement Literature Review, Tech. Rep., Institut de Ciències de la Terra "Jaume Almera" (CSIC), 2007.
- [10] D. A. Kulik, M. Kersten, Articles - Microstructure and Phase Equilibria - Aqueous Solubility Diagrams for Cementitious Waste Stabilization Systems: II, End-Member Stoichiometries of Ideal Calcium Silicate Hydrate Solid Solutions, *Journal of the American Ceramic Society* 84 (12) (2001) 3017, ISSN 00027820, 15512916.
- [11] D. A. Kulik, Improving the structural consistency of C-S-H solid solution thermodynamic models, *Cement and Concrete Research* 41 (5) (2011) 477–495, ISSN 00088846, 18733948, doi: \bibinfo{doi}{10.1016/j.cemconres.2011.01.012}.
- [12] D. Sugiyama, T. Fujita, A thermodynamic model of dissolution and precipitation of calcium silicate hydrates, *Cement and Concrete Research* 36 (2) (2006) 227–237.
- [13] J. Carey, P. Lichtner, Calcium silicate hydrate (CSH) solid solution model applied to cement degradation using the continuum reactive transport model FLOTRAN, *Transport Properties and Concrete Quality: Materials Science of Concrete* (2007) 73–106.
- [14] A. Nonat, A.-C. Courault, D. Damidot, A new model describing the variation of C-S-H Ca/Si ratio with lime concentration in solution, *Cem., Wapno, Beton* 5 (2001) 184 – 191.
- [15] J. Marchand, E. Samson, Predicting the service-life of concrete structures—limitations of simplified models, *Cement and Concrete Composites* 31 (8) (2009) 515–521.

- [16] Y. Hosokawa, K. Yamada, B. Johannesson, L.-O. Nilsson, Development of a multi-species mass transport model for concrete with account to thermodynamic phase equilibria, *Materials and Structures* (2011) 1–16 ISSN 1359-5997, URL <http://dx.doi.org/10.1617/s11527-011-9720-2>, 10.1617/s11527-011-9720-2.
- [17] P. Le Bescop, B. Lothenbach, E. Samson, K. A. Snyder, Modeling Degradation of Cementitious Materials in Aggressive Aqueous Environments, in: *Performance of Cement-Based Materials in Aggressive Aqueous Environments*, Springer, 177–218, 2013.
- [18] G. Möschner, B. Lothenbach, F. Winnefeld, A. Ulrich, R. Figi, R. Kretzschmar, Solid solution between Al-ettringite and Fe-ettringite (Ca₆[Al_{1-x}Fe_x(OH)₆]₂(SO₄)₃·26H₂O), *Cement and Concrete Research* 39 (6) (2009) 482–489.
- [19] T. Schmidt, B. Lothenbach, M. Romer, K. Scrivener, D. Rentsch, R. Figi, A thermodynamic and experimental study of the conditions of thaumasite formation, *Cement and Concrete Research* 38 (3) (2008) 337–349.
- [20] G. Möschner, B. Lothenbach, J. Rose, A. Ulrich, R. Figi, R. Kretzschmar, Solubility of Fe-ettringite (Ca₆[Fe(OH)₆]₂(SO₄)₃·26H₂O), *Geochimica et Cosmochimica Acta* 72 (1) (2008) 1–18.
- [21] B. Lothenbach, T. Matschei, G. Möschner, F. P. Glasser, Thermodynamic modelling of the effect of temperature on the hydration and porosity of Portland cement, *Cement and Concrete Research* 38 (1) (2008) 1–18.
- [22] B. Lothenbach, F. Winnefeld, Thermodynamic modelling of the hydration of Portland cement, *Cement and Concrete Research* 36 (2) (2006) 209–226, ISSN 00088846, 18733948, doi: [10.1016/j.cemconres.2005.03.001](https://doi.org/10.1016/j.cemconres.2005.03.001).
- [23] L. Bennethum, J. Cushman, Multicomponent, multiphase thermodynamics of swelling porous media with electroquasistatics: I. Macroscale field equations, *Transport in Porous Media* 47 (3) (2002) 309–336.
- [24] L. Bennethum, J. Cushman, Multicomponent, multiphase thermodynamics of swelling porous media with electroquasistatics: II. Constitutive theory, *Transport in Porous Media* 47 (3) (2002) 337–362.
- [25] R. M. Bowen, Theory of mixtures, *Continuum physics* 3 (Pt I).
- [26] B. Johannesson, Development of a Generalized Version of the Poisson- Nernst-Planck Equations Using the Hybrid Mixture Theory: Presentation of 2D Numerical Examples, *Transport in Porous Media* 85 (2010) 565–592, ISSN 0169-3913, URL <http://dx.doi.org/10.1007/s11242-010-9578-8>, 10.1007/s11242-010-9578-8.
- [27] E. Samson, J. Marchand, Modeling the transport of ions in unsaturated cement-based materials, *Computers & Structures* 85 (23) (2007) 1740–1756.
- [28] V. Lagneau, J. Van Der Lee, Operator-splitting-based reactive transport models in strong feedback of porosity change: The contribution of analytical solutions for accuracy validation and estimator improvement, *Journal of contaminant hydrology* 112 (1) (2010) 118–129.
- [29] J. van der Lee, L. D. Windt, V. Lagneau, P. Goblet, Module-oriented modeling of reactive transport with {HYTEC}, *Computers & Geosciences* 29 (3) (2003) 265 – 275, ISSN 0098-3004, doi: [10.1016/S0098-3004\(03\)00004-9](https://doi.org/10.1016/S0098-3004(03)00004-9), URL <http://www.sciencedirect.com/science/article/pii/S0098300403000049>, reactive Transport Modeling in the Geosciences.
- [30] S. R. Charlton, D. L. Parkhurst, Modules based on the geochemical model {PHREEQC} for use in scripting and programming languages, *Computers & Geosciences* 37 (10) (2011) 1653 – 1663, ISSN 0098-3004, doi: [10.1016/j.cageo.2011.02.005](https://doi.org/10.1016/j.cageo.2011.02.005), URL <http://www.sciencedirect.com/science/article/pii/S0098300411000653>.
- [31] D. L. Parkhurst, C. Appelo, et al., User's guide to PHREEQC (Version 2): A computer program for speciation, batch-reaction, one-dimensional transport, and inverse geochemical calculations, *Water-Resources Investigations Report 99-4259*, U.S. DEPARTMENT OF THE INTERIOR .
- [32] N. Ottosen, H. Petersson, Introduction to the finite element method, Prentice-Hall, 1992.
- [33] O. Zienkiewicz, R. Taylor, J. Zhu, The finite element method: its basis and fundamentals, vol. 1, Butterworth-Heinemann, 2005.
- [34] N. Ottosen, M. Ristinmaa, *Mechanics of Constitutive Modeling*, Elsevier, 2005.
- [35] C. Bethke, *Geochemical reaction modeling: Concepts and applications*, Oxford University Press New York, 1996.
- [36] C. A. J. Appelo, D. Postma, *Geochemistry, groundwater and pollution*, CRC Press, 2005.
- [37] D. Dzombak, F. Morel, *Surface complexation modeling: Hydrous ferric oxide*, 1990.
- [38] M. Borkovec, J. Westall, Solution of the Poisson-Boltzmann equation for surface excesses of ions in the diffuse layer at the oxide-electrolyte interface, *Journal of Electroanalytical Chemistry and Interfacial Electrochemistry* 150 (1) (1983) 325–337.
- [39] J. Chen, J. Thomas, H. Taylor, H. Jennings, Solubility and structure of calcium silicate hydrate, *Cement and Concrete Research* 34 (9) (2004) 1499–1519.
- [40] A. Nonat, X. Lecoq, The structure, stoichiometry and properties of CSH prepared by C3S hydration under controlled conditions, Nuclear magnetic resonance spectroscopy of cement-based materials, Springer, Berlin (1998) 197–207.
- [41] I. Richardson, G. Groves, A reply to discussions by HFW Taylor of the papers "Models for the composition and structure of calcium silicate hydrate (C-S-H) gel in hardened tricalcium silicate pastes" and "the incorporation of minor and trace elements into calcium silicate hydrate (C-S-H) gel in hardened cement pastes", *Cement and Concrete Research* 23 (4) (1993) 999–1000.
- [42] F. Glasser, M. Tyrer, K. Quillin, D. Ross, J. Pedersen, K. Goldthorpe, D. Bennett, M. Atkins, The chemistry of blended cements and backfills intended for use in radioactive waste disposal, R and D Technical Report, P98 (1999) 333.
- [43] H. Hirao, K. Yamada, H. Takahashi, H. Zibara, Chloride binding of cement estimated by binding isotherms of hydrates, *Journal of Advanced Concrete Technology* 3 (1) (2005) 77–84.
- [44] M. Balonis, B. Lothenbach, G. Le Saout, F. Glasser, Impact of chloride on the mineralogy of hydrated Portland cement systems, *Cement and Concrete Research* 40 (7) (2010) 1009–1022.
- [45] D. Jacques, Benchmarking of the cement model and detrimental chemical reactions including temperature dependent parameters, Tech. Rep., ONDRAF/NIRAS, 2008.
- [46] T. Matschei, B. Lothenbach, F. P. Glasser, Thermodynamic properties of Portland cement hydrates in the system CaO-Al₂O₃-SiO₂-CaSO₄-CaCO₃-H₂O, *Cement and Concrete Research* 37 (10) (2007) 1379 – 1410, ISSN 0008-8846, doi: [10.1016/j.cemconres.2007.06.002](https://doi.org/10.1016/j.cemconres.2007.06.002), URL <http://www.sciencedirect.com/science/article/pii/S0008884607001299>.
- [47] J. A. Cotruvo, Desalination Processes and Associated Health and Environmental Issues, *Water Conditioning and Purification* 47 (1) (2005) 13–17.
- [48] D. R. e. Lide, W. M. e. Haynes, *CRC handbook of chemistry and physics: a ready-reference book of chemical and physical data*, CRC Press, 91. ed. edn., ISBN 1439820775, 9781439820773, gummibiblen., 2010.
- [49] J. Shen, P. Dangla, M. Thiery, Reactive Transport Modeling of CO₂ Through Cementitious Materials Under Supercritical Boundary Conditions, *Geomechanics in CO Storage Facilities* (2013) 181–208.

AppendixA. Thermodynamic database

AppendixB. Solution Species

Table A.5: Thermodynamic database for the chemical equilibrium model, describing solid phase reactions included in the chemical model.

Reactions		
Equilibrium phases		log K
Portlandite ^b	$\text{Ca}(\text{OH})_2 + 2\text{H}^+ \leftrightarrow \text{Ca}^{2+} + 2\text{H}_2\text{O}$	22.799
Silica(am) ^b	$\text{SiO}_2 + 2\text{H}_2\text{O} \leftrightarrow \text{H}_4\text{SiO}_4$	-2.714
Brucite ^b	$\text{Mg}(\text{OH})_2 + 2\text{H}^+ \leftrightarrow \text{Mg}^{2+} + \text{H}_2\text{O}$	16.839
Calcite ^b	$\text{CaCO}_3 \leftrightarrow \text{CO}_3^{2-} + \text{Ca}^{2+}$	1.849
Solid-solution		
AFm(1) (ss)		
C_4AH_{13} ^c	$\text{Ca}_4\text{Al}_2(\text{OH})_{14} : 6\text{H}_2\text{O} \leftrightarrow 4\text{Ca}^{2+} + 2\text{Al}(\text{OH})_4^- + 6\text{OH}^- + 6\text{H}_2\text{O}$	-25.403
C_4FH_{13} ^c	$\text{Ca}_4\text{Fe}_2(\text{OH})_{14} : 6\text{H}_2\text{O} \leftrightarrow 4\text{Ca}^{2+} + 2\text{Fe}(\text{OH})_4^- + 6\text{OH}^- + 6\text{H}_2\text{O}$	-29.403
AFt(1) (ss)		
Ettringite (Al-Ettringite) ^b	$\text{Ca}_6\text{Al}_2(\text{SO}_4)_3(\text{OH})_{12} : 26\text{H}_2\text{O} \leftrightarrow 6\text{Ca}^{2+} + 2\text{Al}(\text{OH})_4^- + 3\text{SO}_4^{2-} + 4\text{OH}^- + 26\text{H}_2\text{O}$	-44.909
Fe-Ettringite ^b	$\text{Ca}_6\text{Fe}_2(\text{SO}_4)_3(\text{OH})_{12} : 26\text{H}_2\text{O} \leftrightarrow 6\text{Ca}^{2+} + 2\text{Fe}(\text{OH})_4^- + 3\text{SO}_4^{2-} + 4\text{OH}^- + 26\text{H}_2\text{O}$	-44.008
AFm(2) (ss)		
Monosulfo-aluminate ^b	$\text{Ca}_4\text{Al}_2(\text{SO}_4)(\text{OH})_{12} : 6\text{H}_2\text{O} \leftrightarrow 4\text{Ca}^{2+} + 2\text{Al}(\text{OH})_4^- + \text{SO}_4^{2-} + 4\text{OH}^- + 6\text{H}_2\text{O}$	-29.263
C_4AH_{13} ^c	$\text{Ca}_4\text{Fe}_2(\text{OH})_{14} : 6\text{H}_2\text{O} \leftrightarrow 4\text{Ca}^{2+} + 2\text{Fe}(\text{OH})_4^- + 6\text{OH}^- + 6\text{H}_2\text{O}$	-29.403
Hemicarbonate		
Hemicarbo-aluminate ^b	$\text{Ca}_4\text{Al}_2(\text{CO}_3)_{0.5}(\text{OH})_{13} : 5.5\text{H}_2\text{O} \leftrightarrow 4\text{Ca}^{2+} + 2\text{Al}(\text{OH})_4^- + 0.5\text{CO}_3^{2-} + 5\text{OH}^- + 5.5\text{H}_2\text{O}$	-29.133
Fe-hemicarbo-nate ^b	$\text{Ca}_4\text{Fe}_2(\text{CO}_3)_{0.5}(\text{OH})_{13} : 5.5\text{H}_2\text{O} \leftrightarrow 4\text{Ca}^{2+} + 2\text{Fe}(\text{OH})_4^- + 0.5\text{CO}_3^{2-} + 5\text{OH}^- + 5.5\text{H}_2\text{O}$	-33.103
Monocarboaluminate + Friedel's salt (ss)		
Friedel's salt ^a	$\text{Ca}_4\text{Al}_2\text{Cl}_2(\text{OH})_{12} : 4\text{H}_2\text{O} \leftrightarrow 4\text{Ca}^{2+} + 2\text{Al}(\text{OH})_4^- + 4\text{OH}^- + 2\text{Cl}^- + 4\text{H}_2\text{O}$	-27.300
Monocarbo-aluminate ^b	$\text{Ca}_4\text{Al}_2(\text{CO}_3)(\text{OH})_{12} : 5\text{H}_2\text{O} \leftrightarrow 4\text{Ca}^{2+} + 2\text{Al}(\text{OH})_4^- + \text{CO}_3^{2-} + 4\text{OH}^- + 5\text{H}_2\text{O}$	-25.403

^aBalonis et al. [44]; ^bJacques [45]; ^cLothenbach et al. [21], Matschei et al. [46], Möschner et al. [20].

Table B.6: Diffusion properties for ionic components in the numerical examples. The boundary condition for seawater is found in Cotruvo [47].

	$D_i^{l,0} \cdot 10^{-8}$	$A_i^l \cdot 10^{-6}$	z_i	δ_i	Boundary condition mol/l
OH ⁻	0.5300 ^a	0.2253	-1	1	1.608e-07
H ⁺	0.9311 ^c	0.3958	1	1	1.324e-07
Al(OH) ₄ ⁻	0.5040 ^a	0.2142	-1	1	0.0
Al(OH) ₃	0.5040 ^f	-	-	1	0.0
Al(OH) ₂ ⁻	0.5040 ^f	0.2142	-1	1	0.0
Al ³⁺	0.0541 ^c	0.0229	3	1	0.0
AlSO ₄ ⁺	0.5040 ^f	0.0442	1	1	0.0
Al(SO ₄) ₂ ⁻	0.5040 ^f	0.0442	-1	1	0.0
AlOH ²⁺	0.5040 ^f	0.0442	1	1	0.0
CaOH ⁺	0.0792 ^a	0.0337	1	0.2	5.451e-09
CaSO ₄	0.0471 ^a	-	-	1	1.026e-03
CaHSO ₄ ⁺	0.0471 ^b	0.0200	1	1	9.384e-10
SO ₄ ²⁻	0.1070 ^a	0.0455	-2	1	1.406e-02
HSO ₄ ⁻	0.1385 ^c	0.0589	-2	1	3.869e-08
H ₂ SiO ₄ ²⁻	0.1100 ^a	0.0468	-2	0.02	9.587e-14
H ₃ SiO ₄ ⁻	0.107 ^e	0.0468	-1	0.02	4.682e-08
H ₄ SiO ₄	0.107 ^e	-	-	0.02	1.719e-05
Ca ²⁺	0.0792 ^a	0.0337	2	0.2	9.261e-03
CaHCO ₃ ⁺	0.107 ^e	0.0200	1	1	4.741e-05
CaCO ₃	0.0446 ^a	-	-	1	1.738e-06
Cl ⁻	0.203 ^a	0.0862	-1	1	5.544e-01
K ⁺	0.1957 ^a	0.0405	1	0.02	9.898e-03
KSO ₄ ⁻	0.1070 ^a	0.0454	-1	1	1.657e-04
Mg ²⁺	0.0705 ^a	0.0299	2	1	4.650e-02
MgSO ₄	0.0705 ^b	0.0299	-	1	6.971e-03
MgHCO ₃ ⁺	0.0705 ^b	0.0299	1	1	2.766e-04
MgCO ₃	0.0705 ^b	-	-	1	5.728e-06
MgOH ⁺	0.0705 ^a	0.0299	1	1	6.777e-07
Na ⁺	0.133 ^a	0.0565	1	0.02	4.690e-01
NaSO ₄ ⁻	0.618 ^a	0.0262	-1	1	6.332e-03
NaHCO ₃	0.133 ^g	-	-	1	1.777e-04
NaCO ₃ ⁻	0.0585 ^a	0.0405	-1	1	4.748e-06
CO ₂	0.191 ^e	-	-	1	2.186e-04
CO ₃ ²⁻	0.0955 ^a	0.0405	-2	1	2.487e-06
HCO ₃ ⁻	0.118 ^a	0.0501	-1	1	1.641e-03
FeCO ₃	0.0719 ^d	-	-	1	0.0
FeHCO ₃ ⁺	0.0719 ^d	0.0299	1	1	0.0
FeCl ⁺	0.0719 ^d	0.0299	1	1	0.0
FeSO ₄	0.0719 ^d	-	-	1	0.0
FeHSO ₄ ⁺	0.0719 ^d	0.0299	1	1	0.0
Fe(OH) ₄ ⁻	0.0719 ^d	0.0299	-1	1	0.0
Fe(OH) ₃	0.0719 ^d	-	-	1	0.0
Fe(OH) ₂ ⁺	0.0719 ^d	0.0299	1	1	0.0
FeOH ²⁺	0.0719 ^d	0.0299	2	1	0.0
FeOH ⁺	0.0719 ^d	0.0299	1	1	0.0
Fe ²⁺	0.0719 ^c	0.0299	2	1	0.0

(^a) Data from Hosokawa et al. [16]. (^b) Estimated value. (^c) Data from Lide and Haynes [48]. (^d) Estimated from Fe²⁺. (^e) Data from Shen et al. [49]. (^f) Estimates from Al(OH)₄⁻. (^g) Estimated from Na⁺

Paper IV

"Use of a multi-species reactive transport model to simulate chloride ingress in mortar exposed to NaCl solution or sea-water"

M. M. Jensen, K. De Weerd, M. R. Geiker, B. Johannesson

Submitted: *Computers and structures, Jul, 2014*

Use of a multi-species reactive transport model to simulate chloride ingress in mortar exposed to NaCl solution or sea-water

M. M. Jensen^{a,*}, K. De Weerd^b, M. R. Geiker^b, B. Johannesson^a

^aDepartment of Civil Engineering, Technical University of Denmark, Denmark

^bDepartment of Structural Engineering, Norwegian University of science and Technology, Norway

Abstract

A multi-species reactive transport model is in comparison with experimental test results of ion ingress in cement mortar. The model is an extended version of the Poisson–Nernst–Planck equations, accounting for chemical equilibrium. Saturated mortar samples were exposed to a NaCl-solution and sea-water for the experimental part. The samples were analyzed for the total chloride content after different exposure times and different depths. The usability of the model is shown by modeling of the experiments and compare the results. The model predicts the total chloride content fairly well. Improvements and further development of the model are discussed based on the comparison.

Keywords: Numerical modeling; Cement; Ion ingress

1. Introduction

goal is often to predict the long term behavior of the material exposed to natural environments. In the development state of numerical models, the first attempt to reproduce experimental observations should be simplified laboratory setups in order to, as far as possible, to limit chemical and physical processes that are not described in the numerical model. A simplification of a cement based system is difficult as the structure at nano-scale is complex and many chemical reactions have an influence on the system.

Chloride ingress into the cement paste is of special interest, especially for reinforced concrete as it plays an important role in initiation of rebar corrosion. Numerical models that predicts chloride ingress in concrete have been proposed over the last decades and only a limited number are referred to here. A common approach for modeling of chloride ingress in concrete is to use a time dependent diffusion coefficient together with different versions of Fick's law, see e.g., Conciatori et al. [4], Luping [14] and Sugiyama et al. [24]. The time dependent diffusion coefficient should account for all chemical and physical processes that change the system over time. Chloride binding isotherms are considered together with a time-dependent chloride diffusion coefficient [6]. Another approach is to directly describe the chemical interactions, together with the mass transport and solve the coupled model numerically. Reactive transport codes presented in e.g., Marchand [15] and Hosokawa et al. [7] solves multi-species ion transport coupled with chemical reactions. The chemical reactions

differs significantly for existing models and there is no detailed agreement on the chemical description of concrete. Solving chemical equilibrium direct from the chemical reactions enables investigation of the solid phases considered in a model. A change in the solid phase amount and composition will change the porosity which can be used as input data in a mass transport calculation.

The papers referred to above shows results of comparison between numerical modeling results and experimental data of different kinds. The work by Sugiyama et al. [24] shows modeling and experimental results of ion ingress in self-compacting concrete. Conciatori et al. [4] are using their model to predict ingress of ions from deicing salts. Concrete used in marine structures is often exposed to a harsh environment in terms of ion ingress. The chloride ingress from sea-water exposure is modeled and compared with experimental data in Luping [14]. The model proposed by Marchand [15] is used to model ingress of different species and results has been compared with experimental data where simple salt solutions were used as exposure solution. The same model is used in Marchand et al. [16] to reproduce field exposed concrete slabs. The model by Hosokawa et al. [7] is used to reproduce experimental data from sodium chloride exposed samples and show examples of long term prediction of sea-water exposed concrete.

The purpose of this paper is to compare numerical multi-species reactive transport modeling with laboratory controlled measurements of ion ingress in a mortar and thereby illustrate the applicability. The numerical model used is a durability model in a larger service life framework under development. The current status of the durability model is shown rather than a validation of the model. The numerical model is based on the Poisson–Nernst–Planck (PNP) system of equations coupled with the chemical equi-

*Mads Mønster Jensen Brovej 118, 2800 Kgs. Lyngby, Denmark
Email address: mmoj@byg.dtu.dk (M. M. Jensen)

librium code PHREEQC. The mortar samples were exposed to two different solutions, a NaCl solution and sea-water from Trondheim fjord in Norway. The total chloride content in the experimental samples was measured after 21, 90 and 180 days of exposure. The tortuosity factor in the transport model is used as adjustment parameter to obtain the best reproduction of the experimental data.

2. Numerical model and experimental setup

The governing equations for the numerical model and the solution method is briefly explained in this section. The PNP equations are employed and solved by the finite element method (FEM). The chemical equilibrium is solved by an operator splitting method in the transient finite element scheme.

2.1. Governing equations and numerical solution method

The governing equation for the mass transport of the ions in the pore solution is described by an extended version of the Nernst–Planck equation. The equation is extended from its original form by an mass exchange term q_i , accounting for chemical interactions between ions and the solid phases see e.g., Samson and Marchand [21], Hosokawa et al. [7] and Jensen et al. [9]. The Nernst–Planck equation is a mass balance equation describing the change in concentration of each constituent c_i , taking into account the total electrical potential of the solution Φ and its effect on the charged constituents. The change in constituent concentrations over time is determined by

$$\frac{\partial c_i}{\partial t} = \nabla \cdot (D_i \nabla c_i - A_i c_i z_i \nabla \Phi) + q_i; \quad (1)$$

$i = 1, 2, \dots, m$

where D_i is the effective diffusion coefficient for constituent i in a porous material, A_i is the ionic mobility and z_i the valence. The effective diffusion coefficient D_i is obtained from the self diffusion coefficient $D_{i,0}$, by the relation $D_i = D_{i,0} \delta_i / \tau^2$ where τ is the tortuosity factor of the material and δ_i is the constructivity of the pore structure [7]. The relation $A_i^l = D_i^l F / (RT)$ is used for the ionic mobility, where F is Faraday’s constant, R is the universal gas constant and T is the temperature. The chemical equilibrium term is solved by operator splitting, where the solution from the mass transport is used as initial values for the chemical equilibrium calculation. In order to use the operator splitting approach, instantaneous local chemical equilibrium with respect to the mass transport is assumed. The chemical equilibrium condition is determined by the geochemical code PHREEQC [20] where the interface module IPHREEQC [3] is utilized.

The Poisson equation, which enforces charge neutrality in the pore solution, is given as

$$\varepsilon_d \varepsilon_0 \nabla^2 \Phi = F \sum_{i=1}^m c_i z_i \quad (2)$$

where ε_d is the relative dielectricity coefficient and ε_0 is the dielectricity coefficient of vacuum.

The governing equation system for the mass transport Eqs. (1) and (2) are solved by the FEM. A weak form of Eqs. (1) and (2) are needed for discretization of the problem, see e.g., Samson et al. [22] and Johannesson [10]. The state variables in the weak formulations are approximated by the general expansion $\mathbf{N}\mathbf{a}$ where \mathbf{N} is the global shape function and \mathbf{a} contains the state variables at the nodal points of the domain. For the one dimensional case, which is used in this work, the local linear shape function is given as $\mathbf{N} = [1 - x/l_e, x/l_e]$ where l_e is the element length. The arbitrary spatial weight function w is approximated with the same general expansion following the Galerkin’s method. The discretization of the gradients of the state variables are approximated by the general expansion $\mathbf{B}\mathbf{a}$ where $\mathbf{B} = \nabla \mathbf{N}$. The global shape function and its gradient are assembled in the global stiffness matrix \mathbf{K} . The time derivative of the state variables are denote $\dot{\mathbf{a}}$ and their shape functions are arranged in the global mass matrix \mathbf{C} . Employing these matrices in single parameter time integration scheme, yields the discrete solution for time step $n + 1$, as

$$\mathbf{a}_{n+1} = (\mathbf{C} + \Delta t \theta \mathbf{K})^{-1} [\mathbf{C} + \Delta t (1 - \theta) \mathbf{K} \mathbf{a}_n + \mathbf{f}_n + \theta (\mathbf{f}_{n+1} - \mathbf{f}_n)] \quad (3)$$

where θ is the time integration parameter, which is a number between zero and one and \mathbf{f} is the force vector.

The non-linearity in the second term of Eq. (1) requires an improvement of the result obtained in Eq. (3). A modified Newton–Raphson scheme, which ignore the higher order terms in the Taylor expansion, is employed for this study, see e.g., Ottosen and Ristinmaa [19] and Johannesson [10]. The used Newton–Raphson scheme require a truly implicit time integration scheme, ($\theta = 1$), which reduces Eq. (3).

2.2. Chemical equilibrium

The chemical equilibrium state is calculated by using the mass actions laws where the geochemical code PHREEQC is used as solver algorithm. Mass action laws are defined for the aqueous reactions, the pure phase reactions and the solid-solution reactions in use. Common for these three types of reactions is the introduction of a solubility product K , which is related to the specific chemical reaction considered. The mass action law, as in Parkhurst et al. [20], for the aqueous reactions, is

$$K_i = a_i \prod_j a_j^{-c_{j_i}} \quad (4)$$

where K_i is the temperature dependent solubility product, a_i is the activity of the aqueous species i , a_j is the activity of the defined master species j , c_{j_i} is the stoichiometric coefficient for the master species j in the aqueous species

i. The heterogeneous mass-action equation for the pure phases is

$$K_p = \prod_j a_j^{c_{pj}} \quad (5)$$

where K_p is the solubility constant for the pure phase p described by a dissolution reaction and c_{pj} is the stoichiometric coefficient of the j 'th master species in the p 'th pure phase. The heterogeneous mass-action equation for the solid-solution reactions is

$$K_{ssp} = \frac{\prod_j a_j^{c_{sspj}}}{a_{ssp}} \quad (6)$$

where K_{ssp} is the solubility product for the p end-member in the solid-solution ss , c_{sspj} is the stoichiometric coefficient of the j 'th master species in the p end-member in the solid-solution, ss and a_{ssp} is the activity of the p end-member in the solid-solution ss . The activity a_{ssp} is, for ideal solid solutions, equal to the mole fraction $a_{ssp} = n_{ssp} / \sum_p n_{ssp}$ of the end-members.

The system of mass action laws is solved as a minimization problem in PHREEQC using a Newton-Raphson scheme. The complete equation system solved by PHREEQC takes into account, a.i., the total element balance and the total charge balance.

2.3. Experimental setup [5]

The experimental test samples used were cement mortar samples, using CEM I and Norm sand [1]. The water to cement (w/c) ratio was 0.4 and the sand to cement mass ratio was 2.5:1. The samples were casted in plastic containers with diameter 50[mm] and height 60[mm] and cured sealed for 3 days at 20[°C]. The casting containers were removed after 3 days of curing and the top of the samples were cut off. The samples were then epoxy impregnated, except at the top. The samples were left in a small amount of distilled water for 2 additional days prior to the exposure in order to saturate the samples.

The samples were exposed to the two different solutions by placing them in plastic boxes on small plastic grids, in order to have the whole non-epoxy coated surface exposed. The exposure solutions were filled in the plastic boxes, so the samples were submerged 3-5[mm] in the solution. The exposure solutions were changed every 3-4 day for the first 3 weeks and every week in the following period.

Three parallel mortar samples were analyzed for the chloride profiles. The mortar samples were profile ground in the following sections: 0-1, 1-3, 3-5, 5-7, 7-9, 9-13, 13-17 and 17-23[mm]. About 4[g] of the resulting concrete powder was weighed prior and after drying over night at 105[°C] in order to determine the moisture content. The dried powder was dissolved in 40[ml] 80[°C] HNO₃ (1:10). After 1 hour the suspension was filtrated. The chloride content of the filtrate was determined by potentiometric titration with a Titrand 905 titrator from Metrohm using 0.01[M] AgNO₃ solution.

2.4. Model parameters

The reactive transport model has an extensive list of input parameters for establishing a simulation, especially the specific choice of thermodynamic database for the chemical reactions is of great importance for the results. The diffusion coefficients used are based on standard values for the self-diffusion and adjusted by the tortuosity factor τ and the constituent parameter δ_i in order to describe the diffusion in specific material considered. The constituent parameters δ_i are dependent on both the pore structure and the type of species considered [7] but are assumed constant here for both exposure conditions. The values for δ_i are adopted from Hosokawa et al. [7]. The diffusion properties $D_{i,0}$ and δ_i used in this case are given in Tab. A.4.

The thermodynamic database used, is a modified version of the *wateq4f.dat* database, which comes with the geochemical software PHREEQC. The aqueous reactions are updated with additional reactions described in Jacques [8] and the majority of solid-phases from the Cemdata07 database is added. The solid-solution including Friedel's salt and the pure phase Kuzel's salt are adopted from Balonis et al. [2] for carbonate free systems. The pure solid-phases and solid-solutions considered in the numerical model are shown in Tab. B.5. The C-S-H phase in the model is an ideal solid-solution proposed in Kulik [11] denoted the CSHQ model. The C-S-H solid-solution has four end-members, described by the dissolution reactions and solubility constants shown in Tab. 1. The solid-solution coexist with SiO₂ at C/S < 0.67 and with Ca(OH)₂ at C/S > 1.7.

The experimental samples were assumed fully saturated and the temperature was kept constant for the whole exposure period. The same conditions are used for the numerical model. Chemical shrinkage and self-desiccation are not considered in the numerical model; i.e. the amount of water is calculated by the model as the initial water amount deducted the water bound in hydrates. The oxide composition of the cement used was determined by X-ray fluorescence (XRF), see Tab. 2. The oxide composition is used as a direct input in the model to determine the initial chemical composition of solid and liquid components using the proposed thermodynamic database.

The experimental test samples were analyzed at 21, 90 and 180 days after exposure initiation, where the total chloride content was determined. The total simulation time for numerical model is therefore 4320[h] (180 days) and simulation results for 504[h] (21 days) and 2160[h] (90 days) are sub results of the total simulation. Two time stepping intervals are considered, one time stepping scheme for the mass transport which is set to $\Delta t_{mt} = 2$ [h] and one the chemical equilibrium which is solved for every $\Delta t_{ce} = 4$ [h]. The experimental samples were analyzed to a depth of which is used as the total length for the spatial domain in the numerical model. The experimental samples are analyzed in up to eight points in the spatial domain and the spatial domain is discretized into 150 elements in the numerical model.

Table 1: End members in the C-S-H solid-solution model proposed by Kulik [11].

Solid solution		
Name	Reaction scheme	Solubility constant log K
Tobermorite H	$(\text{CaO})_{0.66}(\text{SiO}_2)(\text{H}_2\text{O})_{1.5} + 1.32\text{H}^+ \leftrightarrow 0.66\text{Ca}^{2+} + \text{H}_4\text{SiO}_4 + 0.16\text{H}_2\text{O}$	8.272
Tobermorite D	$(\text{CaO})_{0.83}(\text{SiO}_2)_{0.66}(\text{H}_2\text{O})_{1.83} + 1.66\text{H}^+ \leftrightarrow 0.83\text{Ca}^{2+} + 0.66\text{H}_4\text{SiO}_4 + 1.34\text{H}_2\text{O}$	13.624
Jennite H	$(\text{CaO})_{1.33}(\text{SiO}_2)(\text{H}_2\text{O})_{2.16} + 2.66\text{H}^+ \leftrightarrow 1.33\text{Ca}^{2+} + \text{H}_4\text{SiO}_4 + 1.49\text{H}_2\text{O}$	22.173
Jennite D	$(\text{CaO})_{1.5}(\text{SiO}_2)_{0.66}(\text{H}_2\text{O})_{2.5} + 3.00\text{H}^+ \leftrightarrow 0.66\text{Ca}^{2+} + \text{H}_4\text{SiO}_4 + 0.16\text{H}_2\text{O}$	28.713

Table 2: Oxide composition of a cement.

	CaO	SiO ₂	Al ₂ O ₃	Fe ₂ O ₃	SO ₃	K ₂ O	Na ₂ O	MgO*	LOI
mass%	61.6	19.62	4.51	3.45	3.36	1.00	0.45	2.43	2.41

* Note that MgO is inserted directly and is not a part of the hydration calculation.

Table 3: Boundary conditions for the exposure of the cement paste. Concentration of the different species.

	Sea-water [mol/l]	NaCl solution [mol/l]
Na	4.11e-1	5.45e-1
Cl	5.48e-1	5.45e-1
Ca	8.76e-3	
K	8.89e-3	
Mg	4.66e-2	
S	2.69e-2	
Si	2.25e-4	
Fe	7.84e-8	
Al	1.86e-6	

The experimental test samples were exposed to two different boundary solutions, a sodium chloride solution and sea-water from Trondheim fjord in Norway. The concentration of the boundary solutions are given in Tab. 3. The ion complexes in the sea-water are calculated by a standard equilibrium calculation in PHREEQC using the standard *wateq4f.dat* database in order to set boundary conditions for all considered ions in the exposure solution. Ions from the pore solution that are not present in the exposure solution are allowed to leach into the exposure solution, which is assumed to have an infinite buffer capacity. The experimental exposure solution were changed on regular basis which corresponds fairly well with the assumption of an infinite buffer capacity used in the numerical calculations. The calculated exposure concentrations of the ion complexes included are given in Tab. A.4. It should be noted that a small charge imbalance of 6% were found in the calculated boundary solution. The charge imbalance imposed in the domain by this is reduced by the Poisson equation (2).

3. Results

The results from the numerical calculation and its comparison with the experimental test results are presented in this section. The numerical simulations are adjusted by the tortuosity factor τ in order to obtain the best overall reproduction of the experimental test results.

3.1. NaCl exposure results

The results from the experimental test and modeling results for mortars exposed to a NaCl solution are presented. The best overall reproduction of the experimental results by the numerical model is found for the $1/\tau^2 = 2.12 \cdot 10^{-2}$. The results are presented in terms of total chloride contents as mass% of the dry cement paste, shown in Fig. 1a, where the experimental data and numerical modeling results are compared. The experimental results are shown with the standard deviations for two measurements at each spatial point. The results shown by the experimental data points are the average value of a certain distance which are much greater than the spatial elements in the numerical simulation, this should be taken into account in the evaluation of the comparison. The modeling results predicts the experimental results well in most parts of the spatial and time domains. The modeling and experimental results after 21 days of exposure show a good agreement in the whole domain. The modeling result show a thin peak value which is not shown directly by the experimental measurements, but the first measured value has a higher standard deviation compared to the other data points at the same exposure time. This may indicate that some deviations occurs in over the section 0-0.001[m] which are difficult to capture by the experimental resolution. The model prediction of the total chloride content after 90 and 180 days of exposure fits well from around 0.005[m] to the end of the spatial domain and to some extent at the first experimental data data points from the exposed boundary. The modeling results show an increasing peak value in both the spatial and time domain, starting from around

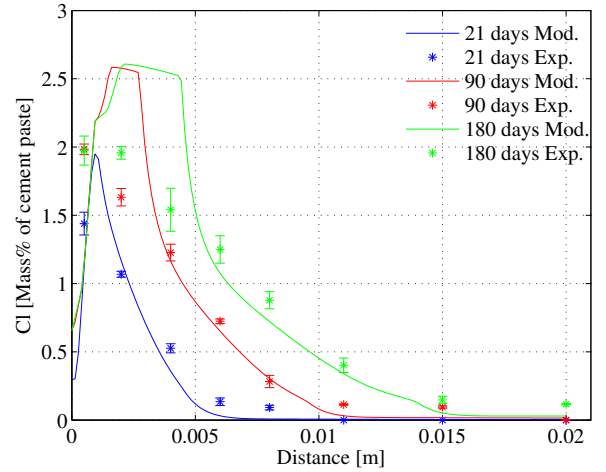
0.001[m]. The maximum mass% of chlorides estimated by the model is around 0.5 mass% higher than the maximum value determined by the experimental test.

The total amount of chloride is the sum of the amount in the pore solution, the chloride in the pure phase Kuzel's salt and the chloride present in the end-member Friedel's salt. The chloride molality in the pore solution for the different exposure times are shown in Fig. 3b, where peak values are seen near the exposed surface. The solid phases formed estimated by the numerical model after 180 days of exposure are shown in Fig. 2. The Kuzel's salt is formed in a small amount near the exposed surface see Fig 4a, in this domain the Friedel's salt is present at a low amount. According to the investigations performed by Balonis et al. [2] on designed systems, the Kuzel's salt should form prior to the Friedel's salt, this was not observed for any time steps in this calculation and the reason for this is unknown to the authors. The combination of the solid phases included in the model, which in some parts differ from Balonis et al. [2], may be one possible explanation to the above mentioned difference in results. The Friedel's salt is formed to a great extent in the spatial domain, which substitutes the monosulfoaluminate shown in Fig. 2a. The Friedel's salt contains the majority of the chlorides in the cement paste using this model and the calculated over estimation compared to the experimental test may originate from this fact. The C_4AH_{13} , C_4FH_{13} , C_2AH_8 and C_2FH_8 phases shown in Fig. 2a are present initially as predicted by the model. The C_4AH_{13} is reduced towards the exposed boundary, which may be caused by the chloride ingress. The C_2AH_8 and C_2FH_8 seems to dissolve and C_4FH_{13} is formed. Ettringite is calculated to be formed near the exposed surface, this end member phase binds a significant amount of water.

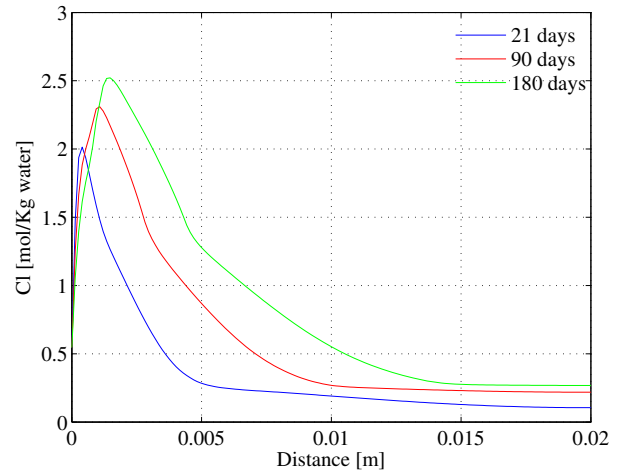
The amount of water in the pores calculated by the model is shown in Fig. 1c for the three different exposure times. The remaining water represents the total porosity, then it is seen that the porosity is predicted to decrease significantly near the boundary. The decreasing porosity will have an effect on the transport of ions both into and out of the domain, this is not taken into account in this model. The pure phases brucite and portlandite in Fig. 4a and the internal composition of the end members in the C-S-H are only changed slightly.

3.2. Sea-water exposure results

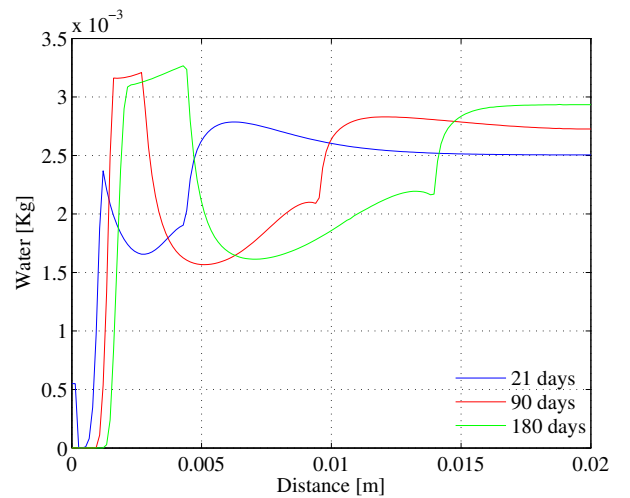
The results from the experimental test and modeling results for mortars exposed to natural sea-water are presented. The best overall reproduction of the experimental results by the model is found with $1/\tau^2 = 3.44 \cdot 10^{-2}$. The modeling results compared to the experimental data are shown in Fig. 3a and the modeling results are in good agreement with the experimental tests. The total modeled chloride contents for sea water exposure are similar to the modeled results for the NaCl exposure in Fig. 1a, so it seems that the additional ions considered at the boundary have a minor effect using this particular model. It is



(a) Comparison of modeled and measured total chloride content.

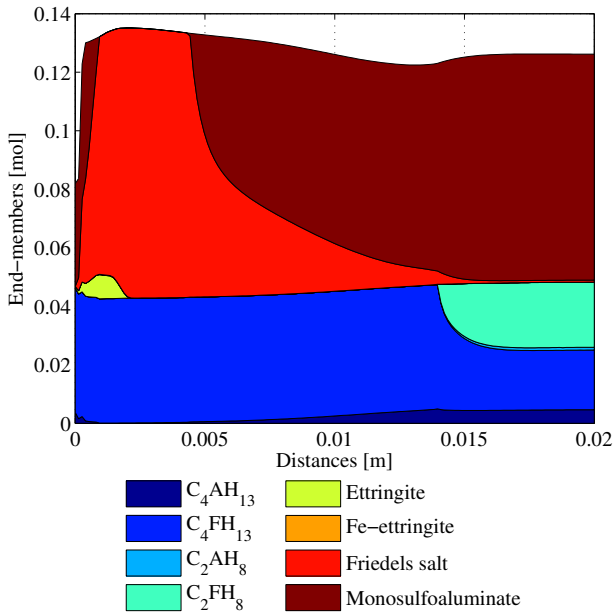


(b) Modeled chloride concentration in the pore solution.

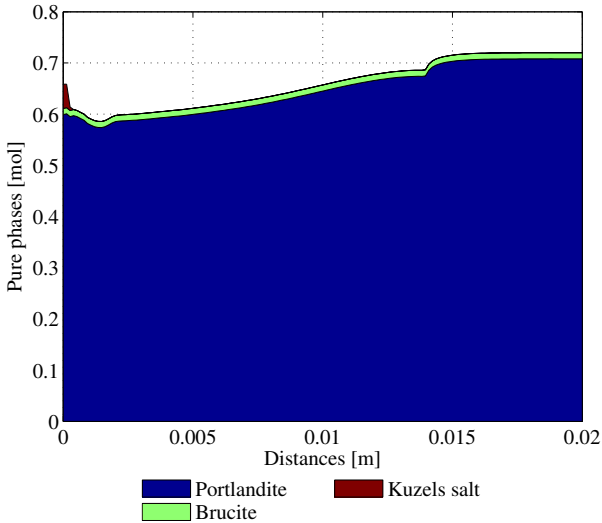


(c) Modeled amount of pore water in the discrete nodes.

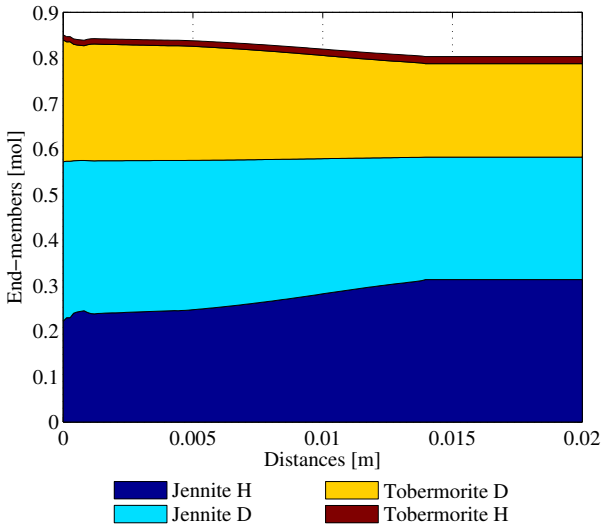
Figure 1: Results from modeling simulations and experimental tests of mortar exposed to a NaCl solution.



(a) Amount of formed end-members in solid solutions.



(b) Amount of formed pure phases.



(c) Amount of end-members in C-S-H model Tab. 1.

seen that the maximum chloride content predicted by the model and measured experimentally have the same magnitude, around 2.5 mass% of the dry cement paste. The modeled maximum values are found deeper in the domain compared to the maximum value from the experimental test.

The majority of the total chloride content is bound in the Friedel's salt and the remaining in the pore solution, see Figs. 4a and 3b respectively. The Kuzel's salt is not formed in any parts of the domain, which is different from the result for the NaCl exposure shown in Fig. 2a. Ettringite is formed near the exposed boundary and a minor peak of ettringite is seen further into the domain. The reason for the minor ettringite peak has not been determined. The end members C_4AH_{13} , C_4FH_{13} , C_2AH_8 and C_2FH_8 shown in Fig. 4a evolves over time similar to the results in Fig. 2a. The higher tortuosity factor used in this case compared to the NaCl exposure has increased the chemical composition changes further into the spatial domain. The end member composition of the C-S-H shown in Fig. 4c changes slightly over the spatial domain after 180 days exposure.

It is important to note that the modeling results in the comparison, Figs. 1a and 3a are not only dependent on the predicted chloride content as the amount of cement paste is also a modeling result. Leaching of ions is allowed which may change the amount of the solid phases which forms the cement paste and thereby have an influence on the modeled chloride mass% of the dry cement paste.

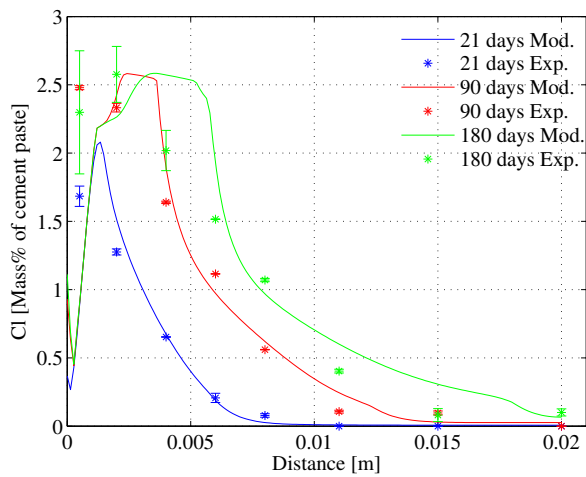
4. Discussion

The numerical model predicts the total amount of chlorides relative to the mass of dry cement paste fairly well in most part of the spatial domain. As it is described in the introduction, the comparison of the modeling results and the experimental results are to show current status of the model development. The discussion here is focused on the future development of the model in order to improve it in terms of accuracy and make it more general.

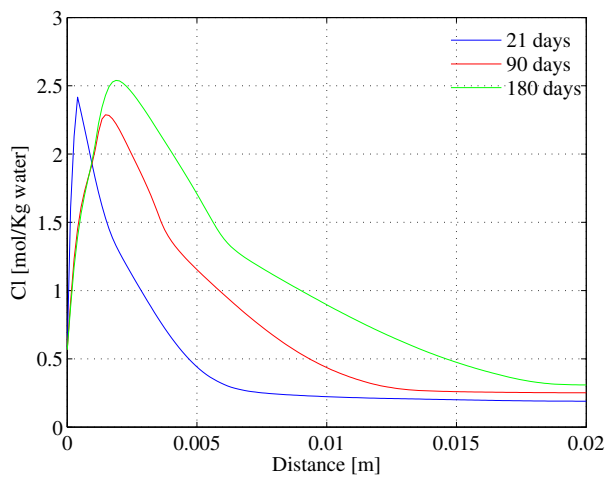
The first issue to address is the use τ as adjustment parameter which takes into account for all physical and chemical phenomena that are not included in the numerical model. This is beyond the classical definition of the tortuosity factor τ , which is purely a geometrical factor describing the complexity of the porous system.

The samples in the experimental test are exposed to the solutions at a relatively young age in terms of the hydration process, which means that the degree of hydration evolves simultaneously with the ingress of the external exposure solution. The ions may affect the hydration process near the exposed surface and change the equilibrium state. The development of the hydration is not taken into account in the model presented here, which may explain the deviations between model results and experimental data in the first part of the domain (0.0 – 0.005[m]). The numerical

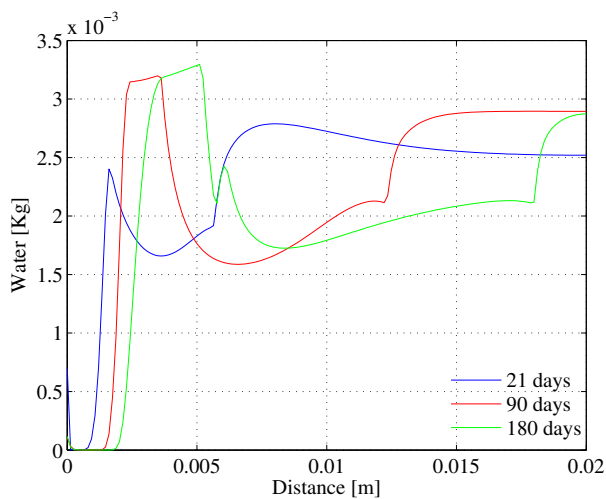
Figure 2: Modeled solid phases formed after 180 days of NaCl exposure. The amount is given as moles in the element.



(a) Comparison of modeled and measured total chloride content.

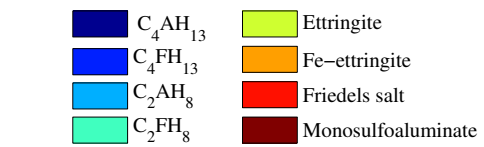
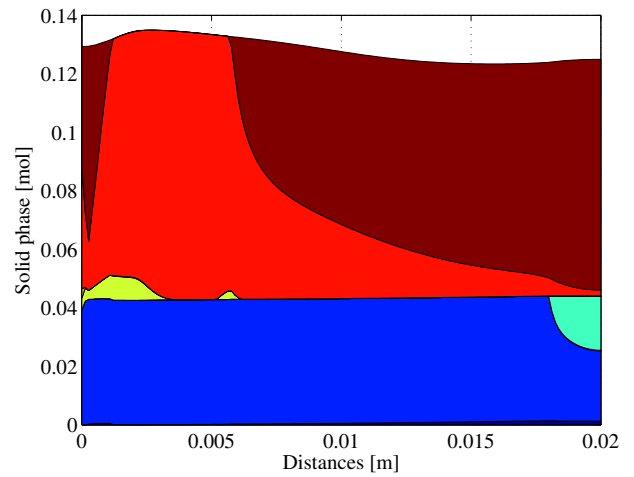


(b) Modeled chloride concentration in the pore solution.

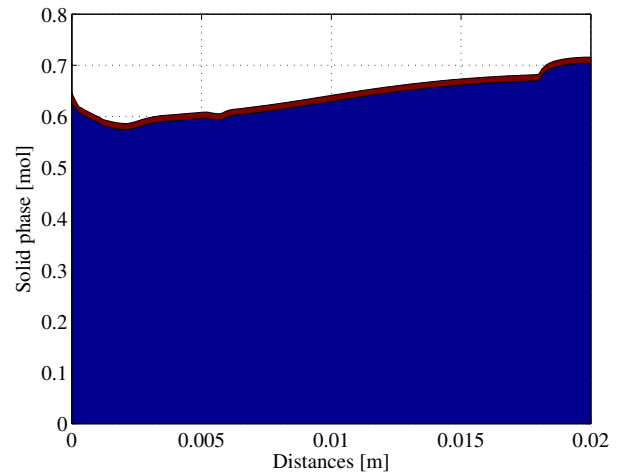


(c) Modeled amount of pore water in the discrete nodes.

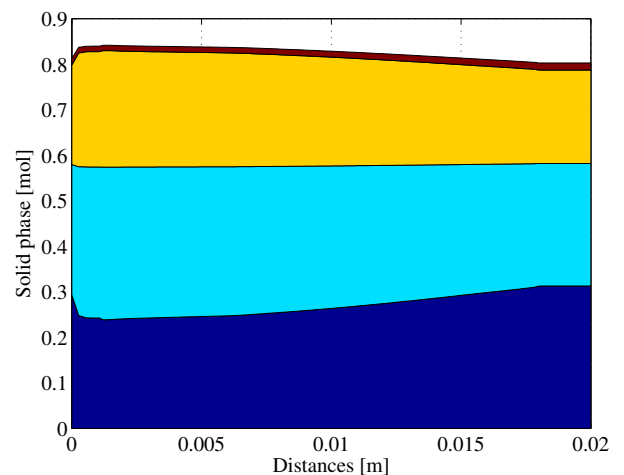
Figure 3: Results from modeling simulations and experimental tests of mortar exposed to sea-water from Trondheim fjord in Norway.



(a) Amount of formed end-members in solid solutions.



(b) Amount of formed pure phases.



(c) Amount of end-members in C-S-H model Tab. 1.

Figure 4: Modeled formed solid phases after 180 days of sea water exposure. The amount is given as moles in the element.

model is solved as an initial value problem, where any deviations introduced early in the time domain will influence the proceeding time steps.

The influence of the added silica fume in the samples is not taken into account in the model which may influence the results both in terms of the micro structure and the chemical interactions. The widespread use of supplementary cementitious materials in concrete urge a proper implementation of these in reactive transport models.

The phase diagrams Figure 2 and 4 do not fully agree with the experimental observations [5]. Brucite was observed at the surface of the sea water exposed sample; but not predicted by the model. On the other hand the predicted formation of monosulfoaluminate at the exposed surface was not been observed experimentally. In addition, the model only predicts a slight difference in the amount of ettringite between NaCl and sea water exposed samples; in the experimental study a sulphate enrichment– and an increase in the amount of ettringite - was observed near the surface for the sea water exposed samples, but not for the NaCl exposed samples. The reasons for this will be explored in future papers. The sea-water was taken from a natural source and may contained carbonates which were not accounted for. Including carbonates in the chemical model will introduce a list of new aqueous species and solid phases which may affect the results significantly. The level of detail of analyzing e.g., exposure solutions and cement composition is very important in order to validate models like the one presented here. The model should be validated against strictly controlled laboratory experiments, with designed multi species exposure solutions similar to natural analogs.

General issues for reactive transport models should also be taken into account, like the operator splitting method which introduce a numerical error at the boundary. For the same reason kinetics of the reactions should be considered in more details to make the model less sensitive to the choices of time step sizes in relation to the operator splitting approach. The assumption that all solid phases are available to the pore water and thereby available for reactions is another example of action that may change the overall results significantly.

5. Conclusion

The current development status of a numerical reactive mass transport model, aimed for durability simulations of cement based materials is described and simulation results are compared with experimental tests. The experimental results are simulated by a reactive transport model using the Poisson-Nernst-Planck equations and the geochemical code PHREEQC. The experimental tests are saturated mortar samples subjected to two different exposure solutions, a NaCl solution and natural sea-water from Trondheim fjord in Norway. The chloride content was measured after 21, 90 and 180 days of exposure. The tortuosity factor

in the model is adjusted in order to reproduce the experimental results. The model reproduced the experimental results well in the majority of the domain considered, but over estimated the chloride content relative to the cement paste in parts of the domain close to the exposed surface. Reasons for the observed deviations between the model results and the experimental data is discussed and areas for further development of the model are suggested.

References

- [1] EN196, 2005.
- [2] M. Balonis, B. Lothenbach, G. Le Saout, and F.P. Glasser. Impact of chloride on the mineralogy of hydrated portland cement systems. *Cement and Concrete Research*, 40(7):1009–1022, 2010.
- [3] Scott R. Charlton and David L. Parkhurst. Modules based on the geochemical model {PHREEQC} for use in scripting and programming languages. *Computers & Geosciences*, 37(10):1653 – 1663, 2011. ISSN 0098-3004. doi: <http://dx.doi.org/10.1016/j.cageo.2011.02.005>. URL <http://www.sciencedirect.com/science/article/pii/S0098300411000653>.
- [4] David Conciatori, Hamid Sadouki, and Eugen Brühwiler. Capillary suction and diffusion model for chloride ingress into concrete. *Cement and Concrete Research*, 38(12):1401–1408, 2008.
- [5] Klaartje De Weerd, Denisa Orsakova, and Mette Geiker. Phase changes in sea water and sodium chloride exposed mortars. *To be submitted*, 2014.
- [6] Fredrik P Glasser, Jacques Marchand, and Eric Samson. Durability of concrete – degradation phenomena involving detrimental chemical reactions. *Cement and Concrete Research*, 38(2):226–246, 2008.
- [7] Yoshifumi Hosokawa, Kazuo Yamada, Björn Johannesson, and Lars-Olof Nilsson. Development of a multi-species mass transport model for concrete with account to thermodynamic phase equilibriums. *Materials and Structures*, pages 1–16, 2011. ISSN 1359-5997. URL <http://dx.doi.org/10.1617/s11527-011-9720-2>.
- [8] D. Jacques. Benchmarking of the cement model and detrimental chemical reactions including temperature dependent parameters. Technical report, ONDRAF/NIRAS, 2008.
- [9] M.M. Jensen, B. Johannesson, and M.R. Geiker. Framework for reactive mass transport: Phase change modeling of concrete by a coupled mass transport and chemical equilibrium model. *Computational Materials Science*, 92(0):213 – 223, 2014. ISSN 0927-0256. doi: <http://dx.doi.org/10.1016/j.commatsci.2014.05.021>. URL <http://www.sciencedirect.com/science/article/pii/S0927025614003395>.
- [10] Björn Johannesson. Development of a generalized version of the poisson- nernst-planck equations using the hybrid mixture theory: Presentation of 2d numerical examples. *Transport in Porous Media*, 85:565–592, 2010. ISSN 0169-3913. URL <http://dx.doi.org/10.1007/s11242-010-9578-8>. 10.1007/s11242-010-9578-8.
- [11] Dmitrii A. Kulik. Improving the structural consistency of c-s-h solid solution thermodynamic models. *Cement and Concrete Research*, 41(5):477–495, 2011. ISSN 00088846, 18733948. doi: 10.1016/j.cemconres.2011.01.012.
- [12] David R. (ed.). Lide and William M. (ed.). Haynes. *CRC handbook of chemistry and physics: a ready-reference book of chemical and physical data*. CRC Press, 91. edition, 2010. ISBN 1439820775, 9781439820773. Gummibiblen.
- [13] Barbara Lothenbach, Thomas Matschei, Göril Möschner, and Fred P Glasser. Thermodynamic modelling of the effect of temperature on the hydration and porosity of portland cement. *Cement and Concrete Research*, 38(1):1–18, 2008.
- [14] Tang Luping. Engineering expression of the clinconc model for prediction of free and total chloride ingress in submerged ma-

- rine concrete. *Cement and Concrete Research*, 38(8):1092–1097, 2008.
- [15] J Marchand. Modeling the behavior of unsaturated cement systems exposed to aggressive chemical environments. *Materials and Structures*, 34(4):195–200, 2001.
- [16] J Marchand, E Samson, Y Maltais, RJ Lee, and S Sahu. Predicting the performance of concrete structures exposed to chemically aggressive environment—field validation. *Materials and Structures*, 35(10):623–631, 2002.
- [17] Thomas Matschei, Barbara Lothenbach, and Fredrik P. Glasser. Thermodynamic properties of portland cement hydrates in the system $\text{cao-al}_2\text{o}_3\text{-sio}_2\text{-caso}_4\text{-caco}_3\text{-h}_2\text{o}$. *Cement and Concrete Research*, 37(10):1379 – 1410, 2007. ISSN 0008-8846. doi: <http://dx.doi.org/10.1016/j.cemconres.2007.06.002>. URL <http://www.sciencedirect.com/science/article/pii/S0008884607001299>.
- [18] Göril Möschner, Barbara Lothenbach, Jerome Rose, Andrea Ulrich, Renato Figi, and Ruben Kretzschmar. Solubility of ferettringite ($\text{Ca}_6[\text{Fe}(\text{OH})_6]_2(\text{SO}_4)_3 \cdot 26\text{H}_2\text{O}$). *Geochimica et Cosmochimica Acta*, 72(1):1–18, 2008.
- [19] N. Ottosen and M. Ristinmaa. *Mechanics of Constitutive Modeling*. Elsevier, 2005.
- [20] David L. Parkhurst, C.A.J. Appelo, et al. User's guide to phreeqc (version 2): A computer program for speciation, batch-reaction, one-dimensional transport, and inverse geochemical calculations. *Water-Resources Investigations Report 99-4259*, U.S. DEPARTMENT OF THE INTERIOR, 1999.
- [21] E. Samson and J. Marchand. Modeling the transport of ions in unsaturated cement-based materials. *Computers & Structures*, 85(23):1740–1756, 2007.
- [22] E. Samson, J. Marchand, J.L. Robert, and J.P. Bournazel. Modelling ion diffusion mechanisms in porous media. *International Journal for Numerical Methods in Engineering*, 46(12):2043–2060, 1999.
- [23] Jitun Shen, Patrick Dangla, and Mickaël Thiery. Reactive transport modeling of CO_2 through cementitious materials under supercritical boundary conditions. *Geomechanics in CO Storage Facilities*, pages 181–208, 2013.
- [24] T Sugiyama, W Ritthichauy, and Y Tsuji. Experimental investigation and numerical modeling of chloride penetration and calcium dissolution in saturated concrete. *Cement and Concrete Research*, 38(1):49–67, 2008.

Appendix A. Diffusion properties

The diffusion parameters and boundary conditions for the sea-water exposure are shown in Tab. A.4.

Appendix B. Chemical reactions

The thermodynamic database used in the model is shown in Tab. B.5.

Table A.4: Diffusion properties for ionic components in the numerical examples.

	$D_i^{l,0} \cdot 10^{-8}$	$A_i^l \cdot 10^{-6}$	z_i	δ_i	Sea-water mol/l
OH ⁻	0.5300 ^a	0.2253	-1	1.0 ^a	1.600e-07
H ⁺	0.9311 ^c	0.3958	1	1.0 ^b	1.321e-07
Al(OH) ₄ ⁻	0.5040 ^a	0.2142	-1	1.0 ^a	1.793e-06
Al(OH) ₃	0.5040 ^f	-	-	1.0 ^b	6.223e-08
Al(OH) ₂ ⁺	0.5040 ^f	0.2142	-1	1.0 ^b	6.698e-08
Al ³⁺	0.0541 ^c	0.0229	3	1.0 ^b	8.125e-11
AlSO ₄ ⁺	0.5040 ^f	0.0442	1	1.0 ^b	7.694e-11
Al(SO ₄) ₂ ⁻	0.5040 ^f	0.0442	-1	1.0 ^b	6.632e-12
AlOH ²⁺	0.5040 ^f	0.0442	1	1.0 ^b	2.127e-09
CaOH ⁺	0.0792 ^a	0.0337	1	0.2 ^a	4.479e-09
CaSO ₄	0.0471 ^a	-	-	1.0 ^a	9.604e-04
CaHSO ₄ ⁺	0.0471 ^b	0.0200	1	1.0 ^b	8.759e-10
SO ₄ ²⁻	0.1070 ^a	0.0455	-2	1.0 ^a	1.457e-02
HSO ₄ ⁻	0.1385 ^c	0.0589	-2	1.0 ^b	3.569e-08
H ₂ SiO ₄ ²⁻	0.1100 ^a	0.0468	-2	0.02 ^a	8.856e-13
H ₃ SiO ₄ ⁻	0.107 ^e	0.0468	-1	0.02 ^b	5.328e-07
H ₄ SiO ₄	0.107 ^e	-	-	0.02 ^b	2.321e-04
Ca ²⁺	0.0792 ^a	0.0337	2	0.2 ^a	8.105e-03
Cl ⁻	0.203 ^a	0.0862	-1	1.0 ^a	5.666e-01
K ⁺	0.1957 ^a	0.0405	1	0.02 ^a	9.052e-03
KSO ₄ ⁻	0.1070 ^a	0.0454	-1	1.0 ^a	1.466e-04
KOH	0.196 ^a	-	-	1.0 ^a	1.674e-10
Mg ²⁺	0.0705 ^a	0.0299	2	1.0 ^a	4.160e-02
MgSO ₄	0.0705 ^b	0.0299	-	1.0 ^b	6.644e-03
MgOH ⁺	0.0705 ^a	0.0299	1	1.0 ^a	5.770e-07
Na ⁺	0.133 ^a	0.0565	1	0.02 ^a	4.200e-01
NaSO ₄ ⁻	0.618 ^a	0.0262	-1	1.0 ^a	5.459e-03
NaOH	0.133 ^g	-	-	1.0 ^b	1.665e-08
FeCl ⁺	0.0719 ^d	0.0299	1	1.0 ^b	0.0
FeSO ₄	0.0719 ^d	-	-	1.0 ^b	0.0
FeHSO ₄ ⁺	0.0719 ^d	0.0299	1	1.0 ^b	0.0
Fe(OH) ₄ ⁻	0.0719 ^d	0.0299	-1	1.0 ^b	0.0
Fe(OH) ₃	0.0719 ^d	-	-	1.0 ^b	0.0
Fe(OH) ₂ ⁺	0.0719 ^d	0.0299	1	1.0 ^b	0.0
FeOH ²⁺	0.0719 ^d	0.0299	2	1.0 ^b	0.0
FeOH ⁺	0.0719 ^d	0.0299	1	1.0 ^b	0.0
Fe ²⁺	0.0719 ^c	0.0299	2	1.0 ^b	0.0

(^a)Data from Hosokawa et al. [7], (^b)Estimated value in this work, (^c)Data from Lide and Haynes [12], (^d)Estimated from Fe²⁺, (^e)Data from Shen et al. [23], (^f)Estimates from Al(OH)₄⁻, (^g)Estimated from Na⁺.

Table B.5: Thermodynamic database for the chemical equilibrium model.

Reactions		log K
Pure phases		
Portlandite ^a	$\text{Ca(OH)}_2 + 2\text{H}^+ \leftrightarrow \text{Ca}^{2+} + 2\text{H}_2\text{O}$	22.799
Silica(am) ^a	$\text{SiO}_2 + 2\text{H}_2\text{O} \leftrightarrow \text{H}_4\text{SiO}_4$	-2.714
Brucite ^a	$\text{Mg(OH)}_2 + 2\text{H}^+ \leftrightarrow \text{Mg}^{2+} + \text{H}_2\text{O}$	16.839
Kuzel's salt ^b	$\text{Ca}_4\text{Al}_2(\text{SO}_4)_{0.5}\text{Cl(OH)}_{12} : 6\text{H}_2\text{O} \leftrightarrow 4\text{Ca}^{2+} + 2\text{Al(OH)}_4^- + 4\text{OH}^- + 0.5\text{SO}_4^{2-} + 6\text{H}_2\text{O}$	-28.53
Solid Solutions		
AFm(1) (ss)		
C_2AH_8 ^{a,c}	$\text{Ca}_2\text{Al}_2(\text{OH})_{10} : 3\text{H}_2\text{O} \leftrightarrow 2\text{Ca}^{2+} + 2\text{Al(OH)}_4^- + 2\text{OH}^- + 3\text{H}_2\text{O}$	-13.562
C_2FH_8 ^{a,c}	$\text{Ca}_2\text{Fe}_2(\text{OH})_{10} : 3\text{H}_2\text{O} \leftrightarrow 2\text{Ca}^{2+} + 2\text{Fe(OH)}_4^- + 2\text{OH}^- + 3\text{H}_2\text{O}$	-17.602
AFm(2) (ss)		
C_4AH_{13} ^{a,c}	$\text{Ca}_4\text{Al}_2(\text{OH})_{14} : 6\text{H}_2\text{O} \leftrightarrow 4\text{Ca}^{2+} + 2\text{Al(OH)}_4^- + 6\text{OH}^- + 6\text{H}_2\text{O}$	-25.403
C_4FH_{13} ^{a,c}	$\text{Ca}_4\text{Fe}_2(\text{OH})_{14} : 6\text{H}_2\text{O} \leftrightarrow 4\text{Ca}^{2+} + 2\text{Fe(OH)}_4^- + 6\text{OH}^- + 6\text{H}_2\text{O}$	-29.403
AFt(1) (ss)		
Ettringite ^{a,c}	$\text{Ca}_6\text{Al}_2(\text{SO}_4)_3(\text{OH})_{12} : 26\text{H}_2\text{O} \leftrightarrow 6\text{Ca}^{2+} + 2\text{Al(OH)}_4^- + 3\text{SO}_4^{2-} + 4\text{OH}^- + 26\text{H}_2\text{O}$	-44.909
Fe-Ettringite ^{a,c}	$\text{Ca}_6\text{Fe}_2(\text{SO}_4)_3(\text{OH})_{12} : 26\text{H}_2\text{O} \leftrightarrow 6\text{Ca}^{2+} + 2\text{Fe(OH)}_4^- + 3\text{SO}_4^{2-} + 4\text{OH}^- + 26\text{H}_2\text{O}$	-44.008
C_4AH_{13} + Friedel's salt (ss)		
Friedel's salt ^b	$\text{Ca}_4\text{Al}_2\text{Cl}_2(\text{OH})_{12} : 4\text{H}_2\text{O} \leftrightarrow 4\text{Ca}^{2+} + 2\text{Al(OH)}_4^- + 4\text{OH}^- + 2\text{Cl}^- + 4\text{H}_2\text{O}$	-27.300
C_4AH_{13} ^{a,c}	$\text{Ca}_4\text{Al}_2(\text{OH})_{14} : 6\text{H}_2\text{O} \leftrightarrow 4\text{Ca}^{2+} + 2\text{Al(OH)}_4^- + 6\text{OH}^- + 6\text{H}_2\text{O}$	-25.403
C_4AH_{13} + Monosulfoaluminate (ss)		
Monosulfoaluminate ^{a,c}	$\text{Ca}_4\text{Al}_2(\text{SO}_4)(\text{OH})_{12} : 6\text{H}_2\text{O} \leftrightarrow 4\text{Ca}^{2+} + 2\text{Al(OH)}_4^- + \text{SO}_4^{2-} + 4\text{OH}^- + 6\text{H}_2\text{O}$	-29.263
C_4AH_{13} ^{a,c}	$\text{Ca}_4\text{Al}_2(\text{OH})_{14} : 6\text{H}_2\text{O} \leftrightarrow 4\text{Ca}^{2+} + 2\text{Al(OH)}_4^- + 6\text{OH}^- + 6\text{H}_2\text{O}$	-25.403

^a is from Jacques [8], ^b is from Balonis et al. [2] and ^c is from Lothenbach et al. [13], Matschei et al. [17], Möschner et al. [18].

Part III
Appendix

Appendix A

Mixture Theory and Hybrid Mixture Theory

The governing equation system for coupled reactive mass transport is derived from the continuum theories, mixture theory and hybrid mixture theory. The mixture theory consider multiple species in a single phase and the hybrid mixture theory extend this concept to consider a mixture of multi-species in multi-phases. The presentation of the theories are relatively detailed in terms of showing all the essential mathematical steps for obtaining a result. The detailed derivation will facilitate the understanding, as these continuum approaches are not standard, especially within modeling of cement based materials. At the same time it is also important to show that the work conducted can be extended in terms of a general background theory.

The derivation presented is based on several published papers and non-published lecture notes where no direct references are given in the text. It is important to emphasize that this presentation of the theory do not extend the theory from the original papers but reproduce the mathematical derivation with explanations by the author of this thesis.

The theory for multi-species mixtures in a single phase is reproduced from Bowen (1976) and Johannesson (1998). The hybrid mixture theory is reproduced from Bennethum and Cushman (2002a,b) and lecture notes by Johannesson (2011b) from the course Introduction to Constitutive Theory and Continuum Physics with Numerical Applications using FEM at the Technical University of Denmark department of civil engineering. In addition to the main references Ristinmaa and Ottosen (2010); Tadmor et al. (2012); de Groot and Mazur (1984); Bear and Bachmat (1990); Griffiths and College (1999) has been used.

Thermodynamics is a funny subject. The first time you go through it, you don't understand it at all. The second time you go through it, you think you understand it, except for one or two small points. The third time you go through it, you know you don't understand it, but by that time you are so used to it, it doesn't bother you any more.

Arnold Johannes Wilhelm Sommerfeld

A.1 Mixture theory for multi-species in a single phase

The following section derive essential results within mixture theory for single phase and multi-species mixtures. The kinematic definitions, balance equations, the second axiom of thermodynamics and constitutive relations are presented in order to obtain a model for reactive mass transport problems.

A.1.1 Kinematics

For the kinematic definition of a single phase (mixture) with multi-species, consider a body \mathcal{B} in a three dimensional space. The body is build up by constituents labeled with the material coordinate \mathbf{X}_j in its reference configuration. It is assumed for the single phase that two constituents from the same body \mathbf{X}_1 and \mathbf{X}_2 cannot exist in the same spatial reference position in the three dimensional space considered.

The spatial position \mathbf{x}_j of a species in a body is described by a function χ_j , which is the deformation function or motion function for the species. The motion is defined as

$$\mathbf{x} = \chi_j(\mathbf{X}_j, t) \quad (\text{A.1.1})$$

where t is the time. The constituent can overlap i.e., occupy the same x but not in the reference configuration \mathbf{X}_j . The inverse of the deformation function χ_a^{-1} is assumed to exist and given as

$$\mathbf{X}_j = \chi_j^{-1}(\mathbf{x}, t) \quad (\text{A.1.2})$$

The velocity and acceleration of the species are defined as

$$\mathbf{x}'_j = \partial \chi_j(\mathbf{X}_j, t) / \partial t \quad (\text{A.1.3})$$

$$\mathbf{x}''_j = \partial^2 \chi_j(\mathbf{X}_j, t) / \partial t^2 \quad (\text{A.1.4})$$

The definitions in (A.1.3) and (A.1.4) are material derivatives following the motion of the j 'th species. From the inverse function of the motion Eq. (A.1.2) it is seen that material coordinate \mathbf{X}_j are given as a function of (\mathbf{x}, t) , i.e.

$$\mathbf{x}'_j = \mathbf{x}'_j(\mathbf{x}, t) \quad (\text{A.1.5})$$

$$\mathbf{x}''_j = \mathbf{x}''_j(\mathbf{x}, t) \quad (\text{A.1.6})$$

The deformation gradient \mathbf{F}_j for the j 'th species is defined in terms of the deformation function χ_j as

$$\mathbf{F}_j = \text{GRAD}\chi_j(\mathbf{X}_j, t); \quad F_{(j)ik} = \frac{\partial x_i}{\partial X_{(j)k}} \quad (\text{A.1.7})$$

where the gradient notation 'GRAD' refer to the derivative with respect to the material coordinates. It was assumed in (A.1.2) that the inverse of the deformation function exist, which give the following result for the determinant of the deformation gradient

$$\det \mathbf{F}_j \neq 0 \quad (\text{A.1.8})$$

and the inverse of deformation gradient \mathbf{F}_j is thereby given as

$$\mathbf{F}_j^{-1} = \text{grad}\chi_j^{-1}(\mathbf{x}, t); \quad F_{(j)kj}^{-1} = \frac{\partial X_{(j)k}}{\partial x_j} \quad (\text{A.1.9})$$

where the notation 'grad' is the derivative with respect to the spatial position. From the definition of the deformation gradient and its inverse, it is concluded that

$$\mathbf{F}_j \mathbf{F}_j^{-1} = \mathbf{F}_j^{-1} \mathbf{F}_j = \mathbf{I}; \quad \frac{\partial x_i \partial X_{(j)k}}{\partial X_{(j)k} \partial x_j} = \delta_{ij} \quad (\text{A.1.10})$$

A velocity gradient \mathbf{L}_j for the j 'th specie is defined in a similar matter, by use of the velocity \mathbf{x}'_j defined in (A.1.5), as

$$\mathbf{L}_j = \text{grad} \mathbf{x}'_j(\mathbf{x}, t); \quad L_{(j)ij} = \frac{\partial x'_{(j)i}}{\partial x_i} \quad (\text{A.1.11})$$

The velocity gradient can be decomposed in two parts, a symmetric part \mathbf{D}_j and a skew-symmetric part \mathbf{W}_j , as

$$\mathbf{L}_j = \mathbf{D}_j + \mathbf{W}_j \quad (\text{A.1.12})$$

The symmetric part \mathbf{D}_j is referred to as the strain or stretching tensor and the skew-symmetric part \mathbf{W}_j is the spin tensor. The two parts are defined as

$$\mathbf{D}_j = \frac{1}{2} (\mathbf{L}_j + \mathbf{L}_j^T) \quad (\text{A.1.13})$$

$$\mathbf{W}_j = \frac{1}{2} (\mathbf{L}_j - \mathbf{L}_j^T) \quad (\text{A.1.14})$$

A relation between the deformation gradient \mathbf{F}_j and the velocity gradient \mathbf{L}_j can be found, by using the chain rule with the definition of \mathbf{L}_j in A.1.7, that is

$$L_{(j)ij} = \frac{\partial x'_{(j)i}}{\partial x_i} = \frac{\partial x'_{(j)i} \partial X_{(j)k}}{\partial X_{(j)k} \partial x_i} \quad (\text{A.1.15})$$

and the fact that \mathbf{X}_j is independent of the time t , is

$$L_{(j)ij} = \left(\frac{\partial x_{(j)i}}{\partial X_{(j)k}} \right)' \frac{\partial X_{(j)k}}{\partial x_i} = F'_{(j)ik} F_{(j)kj}^{-1} \quad (\text{A.1.16})$$

and written in matrix notation as

$$\mathbf{L}_j = \mathbf{F}'_j \mathbf{F}_j^{-1} \quad (\text{A.1.17})$$

Each of the j species considered have a density ρ_j which is a function of the current spatial position and time, as

$$\rho_j = \rho_j(\mathbf{x}, t) \quad (\text{A.1.18})$$

The density of the mixture ρ is defined as the sum of the constituents building up the mixture, that is

$$\rho = \rho(\mathbf{x}, t) = \sum_{j=1}^N \rho_j(\mathbf{x}, t) \quad (\text{A.1.19})$$

By using A.1.18 and A.1.19, the mass concentration c_j of the j 'th species is defined as

$$c_j = c_j(\mathbf{x}, t) = \frac{\rho_j}{\rho} \quad (\text{A.1.20})$$

where the summation of A.1.20 over the species yields

$$\sum_{j=1}^N c_j = 1 \quad (\text{A.1.21})$$

The velocity of the mixture or the mean velocity \mathbf{x}' , is defined as a mass averaged velocity, based on the density and the velocity of each individual species, that is

$$\mathbf{x}' = \mathbf{x}'(\mathbf{x}, t) = \frac{1}{\rho} \sum_{j=1}^N \rho_j \mathbf{x}'_j(\mathbf{x}, t) \quad (\text{A.1.22})$$

The diffusion velocity \mathbf{u}_j of the j 'th species in the mixture is defined in terms of (A.1.22) and (A.1.3), as

$$\mathbf{u}_j = \mathbf{u}_j(\mathbf{x}, t) = \mathbf{x}'_j(\mathbf{x}, t) - \mathbf{x}'(\mathbf{x}, t) \quad (\text{A.1.23})$$

where it directly follows from (A.1.19), (A.1.22) and (A.1.23) that

$$\sum_{j=1}^N \rho_j \mathbf{u}_j = 0 \quad (\text{A.1.24})$$

Similar to the velocity gradient \mathbf{L}_j of the j 'th species in (A.1.11) the velocity gradient of the mixture \mathbf{L} is defined as

$$\mathbf{L} = \text{grad } \mathbf{x}'(\mathbf{x}, t); \quad L_{mn} = \frac{\partial x'_m}{\partial x_n} \quad (\text{A.1.25})$$

A relation between \mathbf{L} and \mathbf{L}_j can be established by examine the identity

$$\text{grad } (\rho_j \mathbf{u}_j) = \mathbf{u}_j \otimes \text{grad } \rho_j + \rho_j \text{grad } \mathbf{u}_j \quad (\text{A.1.26})$$

where \otimes is the dyad product. From (A.1.24) it is seen that the left-hand side of (A.1.26) is

$$\text{grad } \sum_{j=1}^N \rho_j \mathbf{u}_j = 0 \quad (\text{A.1.27})$$

which reduces (A.1.26) to

$$-\sum_{j=1}^N \mathbf{u}_j \otimes \text{grad } \rho_j = \sum_{j=1}^N \rho_j \text{grad } \mathbf{u}_j \quad (\text{A.1.28})$$

The relation for $\rho \mathbf{L}$ is obtained by

$$\rho \mathbf{L} = \sum_{j=1}^N \rho_j \mathbf{L} = \sum_{j=1}^N \rho_j \text{grad } \mathbf{x}' = \sum_{j=1}^N \rho_j \text{grad } (\mathbf{x}'_j - \mathbf{u}_j) \quad (\text{A.1.29})$$

where (A.1.19) and (A.1.23) are used. Finally the definition in (A.1.11) and the relations in (A.1.28) and (A.1.29) are combined to give

$$\rho \mathbf{L} = \sum_{j=1}^N (\rho_j \mathbf{L}_j + \mathbf{u}_j \otimes \text{grad } \rho_j) \quad (\text{A.1.30})$$

General definition 1:

Consider the arbitrary function Γ represented as

$$\Gamma [\chi (\mathbf{X}, t), t] = \Gamma (\mathbf{x}, t) \quad (\text{A.1.31})$$

The relation between the spatial derivative and the material derivative following the j 'th phase is defined as

$$\frac{D_j \Gamma}{Dt} = \frac{\partial \Gamma (\mathbf{x}, t)}{\partial t} + \text{grad } \Gamma (\mathbf{x}, t) \mathbf{x}'_j (\mathbf{x}, t) \quad (\text{A.1.32})$$

A similar relation is defined between the material derivative and the spatial derivative for the whole mixture, this is

$$\frac{D \Gamma}{Dt} = \frac{\partial \Gamma (\mathbf{x}, t)}{\partial t} + \text{grad } \Gamma (\mathbf{x}, t) \mathbf{x}' (\mathbf{x}, t) \quad (\text{A.1.33})$$

by expressing $\partial \Gamma (\mathbf{x}, t) / \partial t$ in (A.1.32) and (A.1.33) and further use (A.1.23) it is concluded that

$$\frac{D_j \Gamma}{Dt} - \frac{D \Gamma}{Dt} = (\text{grad } \Gamma) \mathbf{u}_j \quad (\text{A.1.34})$$

As an example of the use of the relation (A.1.32), the mass concentration c_j is inserted as Γ to get

$$\frac{D_j c_j}{Dt} = \frac{\partial c_j}{\partial t} + \text{grad } (c_j) \cdot \mathbf{x}'_j \quad (\text{A.1.35})$$

A.1.2 Mass balance

The mass balance for a mixture with N species is considered in the following section. The overall purpose is to demonstrate that the mass balance is established for each of the species and the summation of these is the whole mixture. It is important to note the mass exchange term introduced for the mass balance of the species, as an essential result for mixtures is derived involving this term.

The postulate for the mass balance for the j 'th species is

$$\frac{\partial}{\partial t} \int_{\Omega} \rho_j dv = - \oint_{\partial \Omega} \rho_j \mathbf{x}'_j \cdot d\mathbf{s} + \int_{\Omega} \hat{c}_j dv \quad (\text{A.1.36})$$

where Ω is a fixed volume, $\partial \Omega$ is the surface of the volume and \hat{c}_j is the mass exchange of the j 'th species. The mass exchange represent the internal exchange of species, this could be a chemical reaction where reactions exchange

species to established an equilibrium state. The first term on the left-hand side is the integration of the flux of mass over the surface $\partial\Omega$, where $\mathbf{x}'_j \cdot d\mathbf{s}$ is the outward drawn normal to the same surface.

The postulate for the mass balance of the whole mixture is

$$\frac{\partial}{\partial t} \int_{\Omega} \rho \, dv = - \oint_{\partial\Omega} \rho \mathbf{x}' \cdot d\mathbf{s} \quad (\text{A.1.37})$$

which is similar in its form with (A.1.36) but without the mass exchange term. In order to compare the species in the mixture with the whole mixture, summation of Eq. (A.1.36) over the j 'th species is used as

$$\sum_{j=1}^N \frac{\partial}{\partial t} \int_{\Omega} \rho_j \, dv = \sum_{j=1}^N \oint_{\partial\Omega} \rho_j \mathbf{x}'_j \cdot d\mathbf{s} + \sum_{j=1}^N \int_{\Omega} \hat{c}_j \, dv \quad (\text{A.1.38})$$

where the definitions (A.1.19), (A.1.22) are used to obtain a relation between (A.1.36) and (A.1.37). It follows directly from the comparison that the summation of the mass exchange term must be zero in order to obtain mass balance, that is

$$\sum_{j=1}^N \int_{\Omega} \hat{c}_j \, dv = 0 \quad (\text{A.1.39})$$

This is a fundamental result that states that the net production/exchange of mass should be zero in order to make (A.1.36) and (A.1.37) to be comparable.

It is convenient to write the mass balance postulate for the j 'th species (A.1.36) in a local form. By the use of the divergence theorem on the surface integral of (A.1.36), one obtain

$$\int_{\Omega} \left[\frac{\partial \rho_j}{\partial t} + \text{div} (\rho_j \mathbf{x}'_j) - \hat{c}_j \right] \, dv = 0 \quad (\text{A.1.40})$$

assuming that (A.1.40) is valid in the whole volume Ω , the local form of (A.1.40) is

$$\frac{\partial \rho_j}{\partial t} + \text{div} (\rho_j \mathbf{x}'_j) = \hat{c}_j \quad (\text{A.1.41})$$

The local form for the whole mixture (A.1.37), that is

$$\frac{\partial \rho}{\partial t} + \text{div} (\rho \mathbf{x}') = 0 \quad (\text{A.1.42})$$

which results in the local version of (A.1.39) as

$$\sum_{j=1}^N \hat{c}_j = 0 \quad (\text{A.1.43})$$

It is convenient for diffusion problems to express the mass balance in terms of the mass concentration c_j defined in (A.1.20) and the diffusion velocity \mathbf{u}_j . The velocity \mathbf{x}'_j in (A.1.41) is rewritten in terms of the diffusion velocity (A.1.23), as

$$\frac{\partial \rho_j}{\partial t} + \operatorname{div}(\rho_j \mathbf{x}') = -\operatorname{div}(\rho_j \mathbf{u}_j) + \hat{c}_j \quad (\text{A.1.44})$$

Using the product rule for the divergence operator and the definition (A.1.20), the second term on the left-hand side of (A.1.44) can be expressed as

$$\operatorname{div}(\rho_j \mathbf{x}') = \operatorname{div}(c_j \rho \mathbf{x}') = c_j \operatorname{div}(\rho \mathbf{x}') + \rho \mathbf{x}' \cdot \operatorname{grad}(c_j) \quad (\text{A.1.45})$$

Using the definition (A.1.20) for the first term of the left-hand side of (A.1.44) and applying the product rule for this term, combined with (A.1.45) to yields

$$c_j \left[\frac{\partial \rho}{\partial t} + \operatorname{div}(\rho \mathbf{x}') \right] + \rho \left[\frac{\partial c_j}{\partial t} + \mathbf{x}' \cdot \operatorname{grad}(c_j) \right] = -\operatorname{div}(\rho_j \mathbf{u}_j) + \hat{c}_j \quad (\text{A.1.46})$$

The first term in the square brackets cancels due to (A.1.42) and the general definition (A.1.33) used for the second term in square brackets of the left-hand side of (A.1.46), reduces (A.1.46) to

$$\rho \frac{Dc_j}{Dt} = -\operatorname{div}(\rho_j \mathbf{u}_j) + \hat{c}_j \quad (\text{A.1.47})$$

A.1.3 Momentum balance

Momentum balance is considered for the j 'th species and the whole mixture, the equations are analyzed in a similar fashion as the mass balance postulates. Both linear and angular momentum balance needs to be considered.

Linear momentum balance

The postulate for linear momentum for the j 'th species integrated over the volume Ω and the surface $\partial\Omega$ of interest is given as

$$\begin{aligned} \frac{\partial}{\partial t} \int_{\Omega} \rho_j \mathbf{x}'_j dv &= - \oint_{\partial\Omega} \rho_j \mathbf{x}'_j (\mathbf{x}'_j \cdot d\mathbf{s}) + \oint_{\partial\Omega} \mathbf{T}_j d\mathbf{s} \\ &+ \int_{\Omega} (\rho_j \mathbf{b}_j + \hat{\mathbf{p}}_j + \hat{c}_j \mathbf{x}'_j) dv \end{aligned} \quad (\text{A.1.48})$$

where \mathbf{T}_j is the partial stress tensor for the j 'th species, $\hat{\mathbf{p}}_j$ is the momentum supply from other species in the mixture and \mathbf{b}_j is the external body force density. The presence of different species and mass supply of the j 'th species

in the mixture will cause interactions and create local forces. These local forces are described by $\int_{\Omega} (\hat{\mathbf{p}}_j + \hat{c}_j \mathbf{x}'_j) dv$, in which $\hat{\mathbf{p}}_j$ is the momentum from the surrounding species and $\hat{c}_j \mathbf{x}'_j$ is momentum caused by the mass supply of the j 'th species, due to e.g., chemical reactions.

The surface integrals in (A.1.48) is rewritten by the divergence theorem, as

$$\oint_{\partial\Omega} \rho_j \mathbf{x}'_j (\mathbf{x}'_j \cdot d\mathbf{s}) = \int_{\Omega} \operatorname{div} (\rho_j \mathbf{x}'_j \otimes \mathbf{x}'_j) dv \quad (\text{A.1.49})$$

$$\oint_{\partial\Omega} \mathbf{T}_j d\mathbf{s} = \int_{\Omega} \operatorname{div} \mathbf{T}_j dv \quad (\text{A.1.50})$$

which give the postulate for the linear momentum for the j 'th species in terms of volume integrals only, as

$$\begin{aligned} \frac{\partial}{\partial t} \int_{\Omega} \rho_j \mathbf{x}'_j dv &= \int_{\Omega} (-\operatorname{div} (\rho_j \mathbf{x}'_j \otimes \mathbf{x}'_j) + \operatorname{div} \mathbf{T}_j + \rho_j \mathbf{b}_j \\ &\quad + \hat{\mathbf{p}}_j + \hat{c}_j \mathbf{x}'_j) dv \end{aligned} \quad (\text{A.1.51})$$

By assuming that (A.1.51) is valid for the whole volume Ω , the local form is obtained as

$$\frac{\partial \rho_j \mathbf{x}'_j}{\partial t} = -\operatorname{div} (\rho_j \mathbf{x}'_j \otimes \mathbf{x}'_j) + \operatorname{div} \mathbf{T}_j + \rho_j \mathbf{b}_j + \hat{\mathbf{p}}_j + \hat{c}_j \mathbf{x}'_j \quad (\text{A.1.52})$$

Using the product rule and (A.1.32) on the left-hand side of (A.1.52) yields

$$\frac{\partial \rho_j \mathbf{x}'_j}{\partial t} = \mathbf{x}'_j \frac{\partial \rho_j}{\partial t} + \rho_j \frac{\partial \mathbf{x}'_j}{\partial t} = \mathbf{x}'_j \frac{\partial \rho_j}{\partial t} + \rho_j \frac{D_j \mathbf{x}'_j}{Dt} + \rho_j (\operatorname{grad} \mathbf{x}'_j) \mathbf{x}'_j \quad (\text{A.1.53})$$

Consider the first term on the right-hand side of (A.1.51) with the product rule to obtain

$$\operatorname{div} (\rho_j \mathbf{x}'_j \otimes \mathbf{x}'_j) = \mathbf{x}'_j \operatorname{div} (\rho_j \mathbf{x}'_j) + \rho_j (\operatorname{grad} \mathbf{x}'_j) \mathbf{x}'_j \quad (\text{A.1.54})$$

The linear momentum balance (A.1.52) is rewritten by using (A.1.53) and (A.1.54) to obtain

$$\rho_j \frac{D_j \mathbf{x}'_j}{Dt} + \mathbf{x}'_j \left[\frac{\partial \rho_j}{\partial t} + \operatorname{div} (\rho_j \mathbf{x}'_j) - \hat{c}_j \right] = \operatorname{div} \mathbf{T}_j + \rho_j \mathbf{b}_j + \hat{\mathbf{p}}_j \quad (\text{A.1.55})$$

where the terms in the square brackets cancels due to the mass balance (A.1.41), which reduce the local form of the linear momentum balance for the j 'th species to

$$\rho_j \frac{D_j \mathbf{x}'_j}{Dt} = \operatorname{div} \mathbf{T}_j + \rho_j \mathbf{b}_j + \hat{\mathbf{p}}_j \quad (\text{A.1.56})$$

The postulate for the local form of the momentum balance of the whole mixture is

$$\rho \frac{D\mathbf{x}'}{Dt} = \operatorname{div} \mathbf{T} + \rho \mathbf{b} \quad (\text{A.1.57})$$

In order to compare the two postulates, angular momentum is examined where an important property in relation to the linear momentum is derived. The comparison of the linear momentum is continued at page 148.

Angular momentum balance

The global postulate for the angular momentum of the whole mixture is

$$\begin{aligned} \frac{\partial}{\partial t} \int_{\Omega} \mathbf{x} \times \rho \mathbf{x}' dv &= - \oint_{\partial\Omega} \mathbf{x} \times \rho \mathbf{x}' (\mathbf{x}' \cdot d\mathbf{s}) + \oint_{\partial\Omega} \mathbf{x} \times \mathbf{T} ds \\ &+ \int_{\Omega} \mathbf{x} \times \rho \mathbf{b} dv \end{aligned} \quad (\text{A.1.58})$$

and the local form of (A.1.58) is obtained by the divergence theorem and by assuming that it is valid for the whole volume Ω , that is

$$\frac{\partial}{\partial t} (\mathbf{x} \times \rho \mathbf{x}') = -\operatorname{div} (\rho (\mathbf{x} \times \mathbf{x}') \otimes \mathbf{x}') + \operatorname{div} (\mathbf{x} \times \mathbf{T}) + \rho \mathbf{x} \times \mathbf{b} \quad (\text{A.1.59})$$

The equation (A.1.59) is reduced further by expanding the left-hand side by the product rule and using (A.1.33) with $\Gamma = \mathbf{x} \times \mathbf{x}'$ which yields

$$\begin{aligned} \frac{\partial}{\partial t} (\mathbf{x} \times \rho \mathbf{x}') &= \rho \frac{\partial}{\partial t} (\mathbf{x} \times \mathbf{x}') + (\mathbf{x} \times \mathbf{x}') \frac{\partial \rho}{\partial t} \\ &= (\mathbf{x} \times \mathbf{x}') \frac{\partial \rho}{\partial t} + \rho \frac{D}{Dt} (\mathbf{x} \times \mathbf{x}') \\ &+ \rho \operatorname{grad} (\mathbf{x} \times \mathbf{x}') \mathbf{x}' \end{aligned} \quad (\text{A.1.60})$$

The first divergence term on the right-hand side in (A.1.59) is expanded by the product rule, that is

$$\operatorname{div} (\rho (\mathbf{x} \times \mathbf{x}') \otimes \mathbf{x}') = (\mathbf{x} \times \mathbf{x}') \operatorname{div} (\rho \mathbf{x}') + \rho \operatorname{grad} (\mathbf{x} \times \mathbf{x}') \mathbf{x}' \quad (\text{A.1.61})$$

Using (A.1.61) and (A.1.60) together with (A.1.59) eliminates the gradient term and one obtains

$$(\mathbf{x} \times \mathbf{x}') \left(\operatorname{div} (\rho \mathbf{x}') + \frac{\partial \rho}{\partial t} \right) + \rho \frac{D}{Dt} (\mathbf{x} \times \mathbf{x}') = \operatorname{div} (\mathbf{x} \times \mathbf{T}) + \rho \mathbf{x} \times \mathbf{b} \quad (\text{A.1.62})$$

where re-arranging shows that the mass balance for the whole mixture is identified and the angular momentum balance reduces to

$$\rho \frac{D}{Dt} (\mathbf{x} \times \mathbf{x}') = \operatorname{div} (\mathbf{x} \times \mathbf{T}) + \rho \mathbf{x} \times \mathbf{b} \quad (\text{A.1.63})$$

Consider the left-hand side of (A.1.63) written as

$$\rho \frac{D}{Dt} (\mathbf{x} \times \mathbf{x}') = \mathbf{x} \times \rho \frac{D\mathbf{x}'}{Dt} \quad (\text{A.1.64})$$

where it is used that $\mathbf{x}' \times \mathbf{x}' = 0$. The divergence term in (A.1.63) can be written as

$$\begin{aligned} \operatorname{div} (\mathbf{x} \times \mathbf{T}) &= \mathbf{x} \times \operatorname{div} (\mathbf{T}) + \mathbf{T} \times \operatorname{div} (\mathbf{x}) \\ &= \mathbf{x} \times \operatorname{div} (\mathbf{T}) + (T_{32} - T_{23}) \mathbf{i}_1 + (T_{12} - T_{21}) \mathbf{i}_2 \\ &\quad + (T_{31} - T_{13}) \mathbf{i}_3 \end{aligned} \quad (\text{A.1.65})$$

inserting (A.1.64) and (A.1.65) in (A.1.63) yields

$$\begin{aligned} \mathbf{x} \times \left(\rho \frac{D\mathbf{x}'}{Dt} - \operatorname{div} (\mathbf{T}) - \rho \mathbf{b} \right) &= (T_{32} - T_{23}) \mathbf{i}_1 + (T_{12} - T_{21}) \mathbf{i}_2 \\ &\quad + (T_{31} - T_{13}) \mathbf{i}_3 \end{aligned} \quad (\text{A.1.66})$$

The equation of linear momentum is identified in (A.1.66) so the left-hand side cancels out and as a result

$$\mathbf{T} = \mathbf{T}^T \quad (\text{A.1.67})$$

need to be fulfilled.

Linear momentum balance (continued)

Consider the linear momentum balances (A.1.56) and (A.1.57), where the summation over the j 'th constituent for the postulate (A.1.56), must be equal to the postulate of the whole mixture (A.1.57).

Some definitions for the summation over j are stated in the following. The summation of the body force \mathbf{b}_j to yield the whole mixture is

$$\mathbf{b} = \frac{1}{\rho} \sum_{j=1}^N \rho_j \mathbf{b}_j \quad (\text{A.1.68})$$

which is the weighted average of the body force of each species with respect to the mass density. The inner part of the stress tensor is defined as

$$\mathbf{T}_I = \sum_{j=1}^N \mathbf{T}_j \quad (\text{A.1.69})$$

and the stress tensor for the whole mixture is defined as

$$\mathbf{T} = \mathbf{T}_I + \sum_{j=1}^N \rho_j \mathbf{u}_j \otimes \mathbf{u}_j \quad (\text{A.1.70})$$

the second term on the right-hand side is known as the Reynolds stress tensor, which is observed to be symmetric. It is observed that the inner part of the stress tensor must be symmetric, i.e. $\mathbf{T}_I = \mathbf{T}_I^T$, which is a consequence of the angular momentum balance. Symmetry of \mathbf{T}_j is not imposed in this case and therefore the property $\hat{\mathbf{M}}_j$ is introduced as

$$\hat{\mathbf{M}}_j = \mathbf{T}_j - \mathbf{T}_j^T \quad (\text{A.1.71})$$

where $\hat{\mathbf{M}}_j$ is the skew-symmetric linear transformation, which lead to the important result

$$\sum_{j=1}^N \hat{\mathbf{M}}_j = 0 \quad (\text{A.1.72})$$

The summation of the momentum balance for the j 'th species (A.1.56) is

$$\sum_{j=1}^N \rho_j \frac{D_j \mathbf{x}'_j}{Dt} = \text{div} \mathbf{T}_I + \rho \mathbf{b} + \sum_{j=1}^N \hat{\mathbf{p}}_j \quad (\text{A.1.73})$$

where the definitions (A.1.68) and (A.1.69) are used.

General relation 1:

A relation between the general property $\Gamma_j(\mathbf{x}, t)$ for the j 'th species and the material time derivative $\frac{D}{Dt} \Gamma(\mathbf{x}, t)$ of the whole mixture is established. The general relation between $\Gamma_j(\mathbf{x}, t)$ and $\Gamma(\mathbf{x}, t)$ is used, together with (A.1.20) to give

$$\Gamma(\mathbf{x}, t) = \frac{1}{\rho} \sum_{j=1}^N \rho_j \Gamma_j(\mathbf{x}, t) = \sum_{j=1}^N c_j \Gamma_j(\mathbf{x}, t) \quad (\text{A.1.74})$$

Differentiation and using of the product rule, one obtain

$$\frac{D\Gamma(\mathbf{x}, t)}{Dt} = \sum_{j=1}^N \left(c_j \frac{D\Gamma_j}{Dt} + \frac{Dc_j}{Dt} \Gamma_j \right) \quad (\text{A.1.75})$$

Multiplying (A.1.75) with ρ , using (A.1.34) with $\frac{D}{Dt}\Gamma_j$ and using (A.1.47) with the product $\rho\frac{D}{Dt}c_a$, yields

$$\rho\frac{D\Gamma(\mathbf{x}, t)}{Dt} = \sum_{j=1}^N \left(\rho_j \frac{D_j\Gamma_j}{Dt} - \rho_j (\text{grad } \Gamma_j) \mathbf{u}_j - \Gamma_j \text{div}(\rho_j \mathbf{u}_j) + \hat{c}_j \Gamma_j \right) \quad (\text{A.1.76})$$

The divergence and gradient term in (A.1.76) is the divergence of the product $(\rho_j \Gamma_j \mathbf{u}_j)$, that is

$$\text{div}(\rho_j \Gamma_j \mathbf{u}_j) = \rho_j (\text{grad } \Gamma_j) \mathbf{u}_j + \Gamma_j \text{div}(\rho_j \mathbf{u}_j) \quad (\text{A.1.77})$$

The relation (A.1.77) inserted into (A.1.76) show the sought general relation, that is

$$\rho\frac{D\Gamma(\mathbf{x}, t)}{Dt} = \sum_{j=1}^N \left(\rho_j \frac{D_j\Gamma_j}{Dt} - \text{div}(\rho_j \Gamma_j \mathbf{u}_j) + \hat{c}_j \Gamma_j \right) \quad (\text{A.1.78})$$

Using (A.1.78) with $\Gamma = \mathbf{x}'$ yields

$$\rho\frac{D\mathbf{x}'}{Dt} = \sum_{j=1}^N \left(\rho_j \frac{D_j\mathbf{x}'_j}{Dt} - \text{div}(\rho_j \mathbf{x}'_j \otimes \mathbf{u}_j) + \hat{c}_j \mathbf{x}'_j \right) \quad (\text{A.1.79})$$

and re-writing the divergence term with (A.1.23) results in

$$\begin{aligned} \rho\frac{D\mathbf{x}'}{Dt} &= \sum_{j=1}^N \left(\rho_j \frac{D_j\mathbf{x}'_j}{Dt} \right) - \text{div} \sum_{j=1}^N (\rho_j \mathbf{u}_j \otimes \mathbf{u}_j) - \text{div} \sum_{j=1}^N (\rho_j \mathbf{u}_j) \otimes \mathbf{x}' \\ &\quad + \sum_{j=1}^N (\hat{c}_j \mathbf{u}_j) + \sum_{j=1}^N \hat{c}_j \mathbf{x}' \end{aligned} \quad (\text{A.1.80})$$

Equation (A.1.80) can be reduced, by using (A.1.24) and (A.1.43), to give

$$\rho\frac{D\mathbf{x}'}{Dt} = \sum_{j=1}^N \left(\rho_j \frac{D_j\mathbf{x}'_j}{Dt} + \rho_j \mathbf{u}_j \otimes \mathbf{u}_j + \hat{c}_j \mathbf{u}_j \right) \quad (\text{A.1.81})$$

Re-arrange (A.1.81) in terms of $\sum_{j=1}^N \left(\rho_j \frac{D_j}{Dt} \mathbf{x}'_j \right)$ and inserting into (A.1.73), yields

$$\rho\frac{D\mathbf{x}'}{Dt} = \text{div} \left(\mathbf{T}_I - \sum_{j=1}^N (\rho_j \mathbf{u}_j \otimes \mathbf{u}_j) \right) + \rho \mathbf{b} + \sum_{j=1}^N (\hat{c}_j \mathbf{u}_j + \hat{\mathbf{p}}_j) \quad (\text{A.1.82})$$

and with the definition (A.1.70), (A.1.82) can be written as

$$\rho \frac{D\mathbf{x}'}{Dt} = \operatorname{div}\mathbf{T} + \rho\mathbf{b} + \sum_{j=1}^N (\hat{c}_j \mathbf{u}_j + \hat{\mathbf{p}}_j) \quad (\text{A.1.83})$$

Comparing (A.1.57) and (A.1.83), yields the following result for the supply terms in the momentum balance for the j species

$$\sum_{j=1}^N (\hat{c}_j \mathbf{u}_j + \hat{\mathbf{p}}_j) = \mathbf{0} \quad (\text{A.1.84})$$

which is the requirement for (A.1.48) in order to represent the whole mixture.

A.1.4 Balance of energy

The balance of energy is presented in a similar format as to the balance postulates considered in the previous sections. That is, to introducing balance equations of energy for j 'th species and for the whole mixture. Some important results are determined in order to show that the mixture can be represented by the sum of species, building up the mixture. The global balance of energy is the first axiom of thermodynamics and is for the j 'th species given as,

$$\begin{aligned} \frac{\partial}{\partial t} \int_{\Omega} \rho_j \left(e_j + \frac{1}{2} (x'_j)^2 \right) dv &= - \oint_{\partial\Omega} \rho_j \left(e_j + \frac{1}{2} (x'_j)^2 \right) \mathbf{x}'_j \cdot d\mathbf{s} \\ &+ \oint_{\partial\Omega} (\mathbf{T}_j^T \mathbf{x}'_j - \mathbf{q}_j) \cdot d\mathbf{s} \\ &+ \int_{\Omega} (\rho_j r_j + \rho_j \mathbf{x}'_j \cdot \mathbf{b}_j + \mathbf{x}'_j \cdot \mathbf{x}'_j \hat{\mathbf{p}} + \hat{e}_j) dv \\ &+ \int_{\Omega} \hat{c}_j \left(e_j + \frac{1}{2} (x'_j)^2 \right) dv \end{aligned} \quad (\text{A.1.85})$$

where $x'_j{}^2 = \mathbf{x}'_j \cdot \mathbf{x}'_j$, e_j is the internal energy density of the j 'th species, \mathbf{q}_j is the heat flux for the j 'th species, r_j is the external heat supply to the j 'th species and \hat{e}_j is interaction energy (energy supply) to the j 'th species from all other species present in the mixture. The term $\rho_j \frac{1}{2} (x'_j)^2$ is the kinetic energy supply.

The surface integrals in (A.1.85) is written in terms of volume integrals by using the divergence theorem, as

$$\oint_{\partial\Omega} \rho_j \left(e_j + \frac{1}{2} (x'_j)^2 \right) \mathbf{x}'_j \cdot d\mathbf{s} = \int_{\Omega} \operatorname{div} \left(\rho_j \left(e_j + \frac{1}{2} (x'_j)^2 \right) \mathbf{x}'_j \right) dv \quad (\text{A.1.86})$$

$$\oint_{\partial\Omega} (\mathbf{T}_j^T \mathbf{x}'_j - \mathbf{q}_j) \cdot d\mathbf{s} = \int_{\Omega} \operatorname{div} (\mathbf{T}_j^T \mathbf{x}'_j - \mathbf{q}_j) dv \quad (\text{A.1.87})$$

Inserting (A.1.86) and (A.1.87) in (A.1.85) together with the assumption that (A.1.85) is valid for all parts of the volume Ω , gives the local form of the balance of energy expressed as

$$\begin{aligned} \frac{\partial}{\partial t} \rho_j (e_j + \frac{1}{2} (x'_j)^2) \\ + \operatorname{div} (\rho_j (e_j + \frac{1}{2} (x'_j)^2) \mathbf{x}'_j) = \operatorname{div} (\mathbf{T}_j^T \mathbf{x}'_j - \mathbf{q}_j) + \rho_j r_j + \rho_j \mathbf{x}'_j \cdot \mathbf{b}_j + \mathbf{x}'_j \\ + \mathbf{x}'_j \cdot \hat{\mathbf{p}} + \hat{e}_j + \hat{c}_j (e_j + \frac{1}{2} (x'_j)^2) \end{aligned} \quad (\text{A.1.88})$$

The terms on the left-hand side of (A.1.88) is rewritten in terms of the product rules for differentiation and divergence, to yield

$$\begin{aligned} \frac{\partial}{\partial t} \rho_j (e_j + \frac{1}{2} (x'_j)^2) &= \rho_j \frac{\partial}{\partial t} (e_j + \frac{1}{2} (x'_j)^2) \\ &+ (e_j + \frac{1}{2} (x'_j)^2) \frac{\partial}{\partial t} \rho_j \end{aligned} \quad (\text{A.1.89})$$

$$\begin{aligned} \operatorname{div} (\rho_j (e_j + \frac{1}{2} (x'_j)^2) \mathbf{x}'_j) &= (e_j + \frac{1}{2} (x'_j)^2) \cdot \operatorname{div} (\rho_j \mathbf{x}'_j) \\ &+ \operatorname{grad} (e_j + \frac{1}{2} (x'_j)^2) \cdot \rho_j \mathbf{x}'_j \end{aligned} \quad (\text{A.1.90})$$

The general definition (A.1.32) with the property $\Gamma = (e_j + \frac{1}{2} (x'_j)^2)$ is

$$\frac{D_j}{Dt} (e_j + \frac{1}{2} (x'_j)^2) = \frac{\partial}{\partial t} (e_j + \frac{1}{2} (x'_j)^2) + \operatorname{grad} (e_j + \frac{1}{2} (x'_j)^2) \mathbf{x}'_j \quad (\text{A.1.91})$$

Multiplying (A.1.91) by ρ_j and combined with (A.1.90), yields

$$\begin{aligned} \operatorname{div} (\rho_j (e_j + \frac{1}{2} (x'_j)^2) \mathbf{x}'_j) &= (e_j + \frac{1}{2} (x'_j)^2) \cdot \operatorname{div} (\rho_j \mathbf{x}'_j) \\ &+ \rho_j \frac{D_j}{Dt} (e_j + \frac{1}{2} (x'_j)^2) \\ &- \rho_j \frac{\partial}{\partial t} (e_j + \frac{1}{2} (x'_j)^2) \end{aligned} \quad (\text{A.1.92})$$

Consider the mass balance equation (A.1.41), multiplied with $(e_j + \frac{1}{2} (x'_j)^2)$, to obtain

$$(e_j + \frac{1}{2} (x'_j)^2) \cdot \operatorname{div} (\rho_j \mathbf{x}'_j) = \hat{c}_j (e_j + \frac{1}{2} (x'_j)^2) - (e_j + \frac{1}{2} (x'_j)^2) \frac{\partial \rho_j}{\partial t} \quad (\text{A.1.93})$$

which is the first term in (A.1.92). Combining (A.1.93) and (A.1.92) yields

$$\begin{aligned} 0 &= \operatorname{div} (\rho_j (e_j + \frac{1}{2} (x'_j)^2) \mathbf{x}'_j) - \hat{c}_j (e_j + \frac{1}{2} (x'_j)^2) + (e_j + \frac{1}{2} (x'_j)^2) \frac{\partial \rho_j}{\partial t} \\ &- \rho_j \frac{D_j}{Dt} (e_j + \frac{1}{2} (x'_j)^2) + \rho_j \frac{\partial}{\partial t} (e_j + \frac{1}{2} (x'_j)^2) \end{aligned} \quad (\text{A.1.94})$$

It is seen from (A.1.94) that the two terms involving the spatial time derivatives is equal to (A.1.89) and (A.1.94) reduces to

$$\begin{aligned} \frac{\partial}{\partial t} \rho_j (e_j + \frac{1}{2} (x'_j)^2) &= -\text{div} (\rho_j (e_j + \frac{1}{2} (x'_j)^2) \mathbf{x}') + \hat{c}_j (e_j + \frac{1}{2} (x'_j)^2) \\ &\quad + \rho_j \frac{D_j}{Dt} (e_j + \frac{1}{2} (x'_j)^2) \end{aligned} \quad (\text{A.1.95})$$

Using (A.1.95) together with (A.1.88) is

$$\begin{aligned} \rho_j \frac{D_j}{Dt} (e_j + \frac{1}{2} (x'_j)^2) &= \text{div} (\mathbf{T}_j^T \mathbf{x}'_j - \mathbf{q}_j) + \rho_j r_j + \rho_j \mathbf{x}'_j \cdot \mathbf{b}_j \\ &\quad + \mathbf{x}'_j + \mathbf{x}'_j \cdot \hat{\mathbf{p}}_j + \hat{e}_j \end{aligned} \quad (\text{A.1.96})$$

Consider the identities

$$\frac{D_j}{Dt} \frac{1}{2} (x'_j)^2 = \mathbf{x}'_j \cdot \frac{D_j \mathbf{x}'_j}{Dt} \quad (\text{A.1.97})$$

and

$$\text{div} (\mathbf{T}_j^T \mathbf{x}'_j) = \mathbf{x}'_j \cdot \text{div} \mathbf{T}_j^T + \mathbf{T}_j^T \cdot \text{grad} \mathbf{x}'_j = \mathbf{x}'_j \cdot \text{div} \mathbf{T}_j^T + \text{tr} \mathbf{T}_j^T \mathbf{L}_j \quad (\text{A.1.98})$$

where the definition (A.1.11) is used in (A.1.98). Using the identities (A.1.97) and A.1.98 in (A.1.96) yields the energy balance as

$$\begin{aligned} \rho_j \frac{D_j e_j}{Dt} &= \text{tr} \mathbf{T}_j^T \mathbf{L}_j - \text{div} \mathbf{q}_j + \rho_j r_j + \hat{e}_j \\ &\quad + \mathbf{x}'_j \cdot \left(\rho_j \frac{D_j \mathbf{x}'_j}{Dt} - \text{div} \mathbf{T}_j - \rho_j \mathbf{b}_j - \hat{\mathbf{p}}_j \right) \end{aligned} \quad (\text{A.1.99})$$

where the term in brackets cancels due to (A.1.56) and the final expression is obtained as

$$\rho_j \frac{D_j e_j}{Dt} = \text{tr} \mathbf{T}_j^T \mathbf{L}_j - \text{div} \mathbf{q}_j + \rho_j r_j + \hat{e}_j \quad (\text{A.1.100})$$

Consider now the energy balance for the whole mixture, which is the postulate

$$\rho \frac{D}{Dt} (e + \frac{1}{2} \dot{x}^2) = \text{div} (\mathbf{T} \mathbf{x}' - \mathbf{q}) + \rho r + \sum_{j=1}^N (\rho_j \mathbf{x}'_j \cdot \mathbf{b}_j) \quad (\text{A.1.101})$$

Some relations between the constituent description (A.1.85) and the whole mixture is defined directly by weighted summation. The external heat supply r in (A.1.101) is defined in terms of the heat supply from each specie r_j as

$$r = \frac{1}{\rho} \sum_{j=1}^N \rho_j r_j \quad (\text{A.1.102})$$

The inner part of the internal energy density $e_{\mathbf{I}}$ is defined as

$$e_{\mathbf{I}} = \frac{1}{\rho} \sum_{j=1}^N \rho_j e_j \quad (\text{A.1.103})$$

and the internal energy e for the whole mixture is defined as

$$e = e_{\mathbf{I}} + \frac{1}{2\rho} \sum_{j=1}^N \rho_j u_j^2 \quad (\text{A.1.104})$$

where $u_j^2 = \mathbf{u}_j \cdot \mathbf{u}_j$. The inner part of the heat flux $\mathbf{q}_{\mathbf{I}}$ is defined as

$$\mathbf{q}_{\mathbf{I}} = \sum_{j=1}^N (\mathbf{q}_j - \mathbf{T}_j^{\mathbf{T}} \mathbf{u}_j + \rho_j e_j \mathbf{u}_j) \quad (\text{A.1.105})$$

and the heat flux for the whole mixture \mathbf{q} is defined as

$$\mathbf{q} = \mathbf{q}_{\mathbf{I}} + \frac{1}{2} \sum_{j=1}^N \rho_j u_j^2 \mathbf{u}_j \quad (\text{A.1.106})$$

A quantity \mathbf{k} is introduced and defined from (A.1.105) and (A.1.106) as

$$\begin{aligned} \mathbf{k} &= \sum_{j=1}^N (\mathbf{q}_j + \rho_j e_j \mathbf{u}_j) = \mathbf{q}_{\mathbf{I}} + \sum_{j=1}^N (\mathbf{T}_j^{\mathbf{T}} \mathbf{u}_j) \quad (\text{A.1.107}) \\ &= \mathbf{q} - \sum_{j=1}^N \rho_j \left(-\mathbf{T}_j^{\mathbf{T}} / \rho_j + \frac{1}{2} u_j^2 \mathbf{I} \right) \mathbf{u}_j \end{aligned}$$

Three terms from the energy postulate (A.1.101) is rewritten in order to express the momentum balance in the energy balance. Consider the left-hand side of energy postulate for the mixture (A.1.101) written in terms of the mixture velocity \mathbf{x}' , as

$$\rho \frac{D}{Dt} \left(e + \frac{1}{2} x'^2 \right) = \rho \frac{De}{Dt} + \rho \frac{D}{Dt} \left(\frac{1}{2} \mathbf{x}' \cdot \mathbf{x}' \right) = \rho \frac{De}{Dt} + \rho \mathbf{x}' \cdot \mathbf{x}' \quad (\text{A.1.108})$$

Furthermore, consider the last term on the right-hand side of (A.1.101) together with the diffusion velocity \mathbf{u}_j (A.1.23), which is

$$\begin{aligned} \sum_{j=1}^N (\rho_j \mathbf{x}'_j + \mathbf{b}_j) &= \sum_{j=1}^N (\rho_j (\mathbf{x}' + \mathbf{u}_j) + \mathbf{b}_j) \\ &= \sum_{j=1}^N (\rho_j \mathbf{b}_j) \cdot \mathbf{x}' + \sum_{j=1}^N \rho_j \mathbf{u}_j \cdot \mathbf{b}_j \quad (\text{A.1.109}) \end{aligned}$$

It is seen from the momentum balance (A.1.68), that (A.1.109) can be written as

$$\sum_{j=1}^N (\rho_j \mathbf{x}'_j + \mathbf{b}_j) = \rho \mathbf{b} \cdot \mathbf{x}' + \sum_{j=1}^N \rho_j \mathbf{u}_j \cdot \mathbf{b}_j \quad (\text{A.1.110})$$

The divergence term $\text{div}(\mathbf{T}\mathbf{x}')$ in (A.1.101) written in terms of (A.1.25) is

$$\text{div}(\mathbf{T}\mathbf{x}') = \mathbf{x}' \cdot \text{div}\mathbf{T} + \text{tr}\mathbf{T}\mathbf{L} \quad (\text{A.1.111})$$

Inserting the three rewritten terms (A.1.108), (A.1.110) and (A.1.111) into (A.1.101) yields

$$\rho \frac{De}{Dt} = \text{tr}\mathbf{T}\mathbf{L} - \text{div}\mathbf{q} + \rho r + \sum_{j=1}^N \rho_j \mathbf{u}_j \cdot \mathbf{b}_j - \mathbf{x}' \cdot \left(\rho \frac{D\mathbf{x}'}{Dt} - \text{div}\mathbf{T} - \rho \mathbf{b} \right) \quad (\text{A.1.112})$$

where the momentum balance of the mixture (A.1.57) is obtained in the brackets and cancels out. The energy postulate (A.1.112) is thereby reduced to

$$\rho \frac{De}{Dt} = \text{tr}\mathbf{T}\mathbf{L} - \text{div}\mathbf{q} + \rho r + \sum_{j=1}^N \rho_j \mathbf{u}_j \cdot \mathbf{b}_j \quad (\text{A.1.113})$$

Consider the left-hand side of (A.1.113) where the material derivative of the internal energy for the mixture e is extended by the definition (A.1.104). The relation $u_j^2 = \mathbf{u}_j \cdot \mathbf{u}_j$ is used to obtain the form presented here, as

$$\rho \frac{De}{Dt} = \rho \frac{De_{\mathbf{I}}}{Dt} + \rho \sum_{j=1}^N \frac{1}{2} (c_j u_j^2) \quad (\text{A.1.114})$$

The summation term in (A.1.114) expressed by the general relation (A.1.78) using $\Gamma = \sum_{j=1}^N c_j \frac{1}{2} u_j^2$ and $\Gamma_j = \frac{1}{2} u_j^2$ as

$$\rho \sum_{j=1}^N \frac{1}{2} \frac{D}{Dt} (c_j u_j^2) = \sum_{j=1}^N \left(\rho_j \frac{1}{2} \frac{D_j}{Dt} (u_j^2) - \text{div}(\rho_j \frac{1}{2} u_j^2 \mathbf{u}_j) + \hat{c}_j \frac{1}{2} u_j^2 \right) \quad (\text{A.1.115})$$

Examine the first summation term on the right-hand side of (A.1.115) and expand it with $u_j^2 = \mathbf{u}_j \cdot \mathbf{u}_j$ to obtain

$$\sum_{j=1}^N \rho_j \frac{1}{2} \frac{D_j}{Dt} (u_j^2) = \sum_{j=1}^N \rho_j \frac{1}{2} \frac{D_j}{Dt} (\mathbf{u}_a \cdot \mathbf{u}_a) = \sum_{j=1}^N \rho_j \mathbf{u}_j \cdot \frac{D_j \mathbf{u}_j}{Dt} \quad (\text{A.1.116})$$

where the diffusion velocity \mathbf{u}'_j in (A.1.116) written in terms of its definition (A.1.23), is

$$\sum_{j=1}^N \rho_j \mathbf{u}_j \cdot \frac{D_j \mathbf{u}_j}{Dt} = \sum_{j=1}^N \rho_j \mathbf{u}_j \cdot \left(\frac{D_j \mathbf{x}'_j}{Dt} - \frac{D_j \mathbf{x}'}{Dt} \right) \quad (\text{A.1.117})$$

Furthermore, the last term in the brackets of (A.1.117) written in terms of (A.1.34) with $\Gamma = \mathbf{x}'$ and the definition (A.1.25), is

$$\sum_{j=1}^N \rho_j \mathbf{u}_j \cdot \left(\frac{D_j \mathbf{x}'_j}{Dt} - \frac{D_j \mathbf{x}'}{Dt} \right) = \sum_{j=1}^N \rho_j \mathbf{u}_j \cdot \left(\frac{D_j \mathbf{x}'_j}{Dt} - \frac{D \mathbf{x}'}{Dt} - \mathbf{L} \mathbf{u}_j \right) \quad (\text{A.1.118})$$

The term $\sum_{j=1}^N \rho_j \mathbf{u}_j \cdot (\mathbf{L} \mathbf{u}_j)$ in (A.1.118) can be formulated as

$$\sum_{j=1}^N \rho_j \mathbf{u}_j \cdot (\mathbf{L} \mathbf{u}_j) = \text{tr} \sum_{j=1}^N \rho_j \mathbf{L} (\mathbf{u}_j \otimes \mathbf{u}_j) \quad (\text{A.1.119})$$

Combining (A.1.116) and (A.1.118) with (A.1.115), yields the energy balance equation as

$$\begin{aligned} \rho \sum_{j=1}^N \frac{1}{2} \frac{D}{Dt} (c_j u_j^2) &= \sum_{j=1}^N \rho_j \mathbf{u}_j \cdot \frac{D_j \mathbf{x}'_j}{Dt} - \sum_{j=1}^N (\rho_j \mathbf{u}_j) \cdot \frac{D \mathbf{x}'}{Dt} \\ &\quad - \text{tr} \sum_{j=1}^N \rho_j \mathbf{L} (\mathbf{u}_j \otimes \mathbf{u}_j) \\ &\quad - \sum_{j=1}^N (\text{div} (\rho_j \frac{1}{2} u_j^2 \mathbf{u}_j) + \hat{c}_j \frac{1}{2} u_j^2) \end{aligned} \quad (\text{A.1.120})$$

where the second term on the right-hand side cancels out due to the summation of the diffusion velocities (A.1.24).

Consider (A.1.113) written in terms of (A.1.70), (A.1.106) and (A.1.114), which is

$$\begin{aligned} \rho \frac{D e_{\mathbf{I}}}{Dt} + \rho \sum_{j=1}^N \frac{1}{2} \frac{D}{Dt} (c_a u_a^2) &= \text{tr} \left(\mathbf{T}_{\mathbf{I}} - \sum_{j=1}^N \rho_j \mathbf{u}_j \otimes \mathbf{u}_j \right) \mathbf{L} \\ &\quad - \text{div} \left(\mathbf{q}_{\mathbf{I}} + \frac{1}{2} \sum_{j=1}^N \rho_j u_j^2 \mathbf{u}_j \right) \\ &\quad + \rho r + \sum_{j=1}^N \rho_j \mathbf{u}_j \cdot \mathbf{b}_j \end{aligned} \quad (\text{A.1.121})$$

Solving for the second term on the left-hand side of (A.1.121), show that this equals (A.1.120). Combining (A.1.121) and (A.1.120) gives

$$\rho \frac{De_{\mathbf{I}}}{Dt} = \text{tr} \mathbf{T}_{\mathbf{I}} \mathbf{L} - \text{div} \mathbf{q}_{\mathbf{I}} + \rho r - \sum_{j=1}^N \mathbf{u}_j \cdot \left(\rho_j \frac{D_j \mathbf{x}'_j}{Dt} - \rho_j \mathbf{b}_j \right) - \sum_{j=1}^N \hat{c}_j \frac{1}{2} u_j^2 \quad (\text{A.1.122})$$

A reformulation of the term $\text{tr} \mathbf{T}_{\mathbf{I}} \mathbf{L}$ in (A.1.122) is needed. First consider the term $\text{tr} \sum_{j=1}^N \mathbf{T}_j^T \mathbf{L}_j$, combined with (A.1.11) and (A.1.23), that is

$$\text{tr} \sum_{j=1}^N \mathbf{T}_j^T \mathbf{L}_j = \text{tr} \sum_{j=1}^N \mathbf{T}_j^T \text{grad} (\mathbf{u}_j + \mathbf{x}') \quad (\text{A.1.123})$$

The equation (A.1.123) combined with (A.1.25) and (A.1.69), is

$$\text{tr} \sum_{j=1}^N \mathbf{T}_j^T \mathbf{L}_j = \text{tr} \sum_{j=1}^N \mathbf{T}_j^T \text{grad} \mathbf{u}_j + \text{tr} \mathbf{T}_{\mathbf{I}} \mathbf{L} \quad (\text{A.1.124})$$

where the first term on the right-hand side can be written in terms of a divergence product as

$$\text{tr} \sum_{j=1}^N \mathbf{T}_j^T \text{grad} \mathbf{u}_j = \text{div} \sum_{j=1}^N \mathbf{T}_j^T \mathbf{u}_j - \sum_{j=1}^N \mathbf{u}_j \cdot \text{div} \mathbf{T}_j \quad (\text{A.1.125})$$

Combining (A.1.125) and (A.1.124) yields

$$\text{tr} \sum_{j=1}^N \mathbf{T}_j^T \mathbf{L}_j = \text{div} \sum_{j=1}^N \mathbf{T}_j^T \mathbf{u}_j - \sum_{j=1}^N \mathbf{u}_j \cdot \text{div} \mathbf{T}_j + \text{tr} \mathbf{T}_{\mathbf{I}} \mathbf{L} \quad (\text{A.1.126})$$

Solving (A.1.126) for $\text{tr} \mathbf{T}_{\mathbf{I}} \mathbf{L}$ and insert the result in (A.1.122) yields

$$\begin{aligned} \rho \frac{De_{\mathbf{I}}}{Dt} &= \text{tr} \sum_{j=1}^N \mathbf{T}_j^T \mathbf{L}_j - \text{div} \left(\mathbf{q}_{\mathbf{I}} - \sum_{j=1}^N \mathbf{T}_j^T \mathbf{u}_j \right) + \rho r \\ &\quad - \sum_{j=1}^N \mathbf{u}_j \cdot \left(\rho_j \frac{D_j \mathbf{x}'_j}{Dt} - \rho_j \mathbf{b}_j - \text{div} \mathbf{T}_j \right) \\ &\quad - \sum_{j=1}^N \hat{c}_j \frac{1}{2} u_j^2 \end{aligned} \quad (\text{A.1.127})$$

where the terms in the first bracket equals the definition of \mathbf{k} shown in (A.1.107) and the terms in the second bracket are reduced by the momentum balance (A.1.56), so the internal energy balance for the whole mixture is

$$\rho \frac{De_{\mathbf{I}}}{Dt} = \text{tr} \sum_{j=1}^N \mathbf{T}_j^T \mathbf{L}_j - \text{div} \mathbf{k} + \rho r - \sum_{j=1}^N \mathbf{u}_j \cdot \hat{\mathbf{p}}_j - \sum_{j=1}^N \hat{c}_j \frac{1}{2} u_j^2 \quad (\text{A.1.128})$$

As for the mass balance and momentum balance, mixture theory require that the sum of j species for the postulate (A.1.85) corresponds to the energy postulate for the whole mixture. The sum of (A.1.100) with direct use of (A.1.102) gives

$$\sum_{j=1}^N \rho_j \frac{D_j e_j}{Dt} = \sum_{j=1}^N \text{tr} \mathbf{T}_j^T \mathbf{L}_j - \sum_{j=1}^N \text{div} \mathbf{q}_j + \rho r + \sum_{j=1}^N \hat{e}_j \quad (\text{A.1.129})$$

The general relations (A.1.78) and (A.1.74) together with the definition (A.1.103) is used to express the left-hand side of (A.1.129) as

$$\sum_{j=1}^N \rho_j \frac{D_j e_j}{Dt} = \rho \frac{De_{\mathbf{I}}}{Dt} + \sum_{j=1}^N \text{div} (\rho_j e_j \mathbf{u}_j) - \sum_{j=1}^N \hat{c}_j e_j \quad (\text{A.1.130})$$

Inserting (A.1.130) in (A.1.129) and arrange the terms to obtain \mathbf{k} , from the definition (A.1.107), yields

$$\rho \frac{De_{\mathbf{I}}}{Dt} = \text{tr} \sum_{j=1}^N \mathbf{T}_j^T \mathbf{L}_j - \text{div} \mathbf{k} + \rho r + \sum_{j=1}^N \hat{e}_j + \sum_{j=1}^N \hat{c}_a e_j \quad (\text{A.1.131})$$

The summed species energy balance equations (A.1.131) and the energy balance for the mixture (A.1.127) equals the left-hand side and the requirement for the postulate of the j specie is therefore,

$$\sum_{j=1}^N (\hat{c}_j (\frac{1}{2} u_j^2 + e_j) + \mathbf{u}_j \cdot \hat{\mathbf{p}}_j + \hat{e}_j) = 0 \quad (\text{A.1.132})$$

A.1.5 Second axiom of thermodynamics

The second axiom of thermodynamics has been postulated in different forms. The general postulate is an inequality where each j species have individual temperatures θ_j . However, a postulate for the whole mixture is considered and rewritten to a form where all species have the same temperature.

The entropy density of the mixture η is defined as a weighted sum as

$$\eta = \eta(\mathbf{x}, t) = \frac{1}{\rho} \sum_{j=1}^{\mathcal{R}} \rho_j \eta_j(\mathbf{x}, t) \quad (\text{A.1.133})$$

The temperature θ_j for each species is assumed by a positive value function

$$\theta_j = \Theta_j(\mathbf{x}, t) \quad (\text{A.1.134})$$

The second axiom of thermodynamics for the mixture, valid in the volume Ω is the postulate

$$\begin{aligned} \frac{\partial}{\partial t} \int_{\Omega} \rho \eta \, dv &\geq - \oint_{\partial\Omega} \rho \eta \mathbf{x}' \cdot d\mathbf{s} - \oint_{\partial\Omega} \sum_{j=1}^{\mathcal{R}} (\mathbf{h}_j / \theta_j) \cdot d\mathbf{s} \\ &+ \oint_{\Omega} \sum_{j=1}^{\mathcal{R}} (\rho_j r_j / \theta_j) \, dv \end{aligned} \quad (\text{A.1.135})$$

where \mathbf{h}_j is an entropy influx vector the j 'th species. To obtain the local form of (A.1.135), the surface integrals are rewritten by the divergence theorem, that is

$$\oint_{\partial\Omega} \rho \eta \mathbf{x}' \cdot d\mathbf{s} = \int_{\Omega} \text{div}(\rho \eta \mathbf{x}') \, dv \quad (\text{A.1.136})$$

and

$$\oint_{\partial\Omega} \sum_{j=1}^{\mathcal{R}} (\mathbf{h}_j / \theta_j) \cdot d\mathbf{s} = \int_{\Omega} \text{div} \sum_{j=1}^{\mathcal{R}} (\mathbf{h}_j / \theta_j) \, dv \quad (\text{A.1.137})$$

Combining (A.1.136), (A.1.138) with (A.1.135) yields the local form of the second axiom of thermodynamics as

$$\frac{\partial(\rho\eta)}{\partial t} \geq -\text{div}(\rho\eta\mathbf{x}') - \text{div} \sum_{j=1}^{\mathcal{R}} (\mathbf{h}_j / \theta_j) + \sum_{j=1}^{\mathcal{R}} (\rho_j r_j / \theta_j) \quad (\text{A.1.138})$$

Using the product rule for the first term on the right-hand side and first term on the left-hand side of (A.1.138) is

$$\text{div}(\rho\eta\mathbf{x}') = \eta \text{div}(\rho\mathbf{x}') + \rho\mathbf{x}' \cdot \text{grad}(\eta) \quad (\text{A.1.139})$$

and

$$\frac{\partial(\rho\eta)}{\partial t} = \eta \frac{\partial\rho}{\partial t} + \rho \frac{\partial\eta}{\partial t} \quad (\text{A.1.140})$$

Inserting (A.1.139) and (A.1.140) in (A.1.138) yields the following inequality

$$\begin{aligned} \eta \left(\frac{\partial \rho}{\partial t} + \operatorname{div}(\rho \mathbf{x}') \right) + \rho \frac{\partial \eta}{\partial t} &\geq -\rho \mathbf{x}' \cdot \operatorname{grad}(\eta) - \operatorname{div} \sum_{j=1}^N (\mathbf{h}_j / \theta_j) \\ &\quad + \sum_{j=1}^{\mathcal{R}} (\rho_j r_j / \theta_j) \end{aligned} \quad (\text{A.1.141})$$

It is seen that the first term on the left-hand side cancels due to the mass balance (A.1.42) and the second term can be expressed by (A.1.33) with $\Gamma = \eta$, which reduce (A.1.141) to

$$\rho \frac{D\eta}{Dt} \geq -\operatorname{div} \sum_{j=1}^N (\mathbf{h}_j / \theta_j) + \sum_{j=1}^N (\rho_j r_j / \theta_j) \quad (\text{A.1.142})$$

It is convenient to introduce another form of the inequality, in order to examine the definition of \mathbf{h}_j , with the postulate

$$\begin{aligned} \frac{\partial}{\partial t} \int_{\Omega} \rho \eta \, dv &\geq - \oint_{\partial\Omega} \sum_{j=1}^N \rho_j \eta_j \mathbf{x}'_j \cdot d\mathbf{s} - \oint_{\partial\Omega} \sum_{j=1}^N (\mathbf{q}_j / \theta_j) \cdot d\mathbf{s} \\ &\quad + \oint_{\Omega} \sum_{j=1}^N (\rho_j r_j / \theta_j) \, dv \end{aligned} \quad (\text{A.1.143})$$

Following the same mathematical steps as performed from (A.1.136) to (A.1.142) leads to a reduced local form of (A.1.143), that is

$$\rho \frac{D\eta}{Dt} \geq -\operatorname{div} \sum_{j=1}^N (\mathbf{q}_j / \theta_j + \rho_j \eta_j \mathbf{u}_j) + \sum_{j=1}^N (\rho_j r_j / \theta_j) \quad (\text{A.1.144})$$

Comparing (A.1.142) and (A.1.144) shows that the form of the entropy influx vector \mathbf{h}_j must be identified as

$$\mathbf{h}_j = \mathbf{q}_j + \rho_j \theta_j \eta_j \mathbf{u}_j \quad (\text{A.1.145})$$

Further rewriting of (A.1.144), using (A.1.78) with $\Gamma_j = \eta_j$, gives an alternative form of the inequality, as

$$\sum_{j=1}^N \left(\rho_j \frac{D_j \eta_j}{Dt} + \operatorname{div}(\mathbf{q}_j / \theta_j) - \rho_j r_j / \theta_j + \hat{c}_j \eta_j \right) \geq 0 \quad (\text{A.1.146})$$

which also can be written as

$$\sum_{j=1}^N \frac{1}{\theta_j} \left(\theta_j \rho_j \frac{D_j \eta_j}{Dt} + \theta_j \operatorname{div}(\mathbf{q}_j / \theta_j) - \rho_j r_j + \theta_j \hat{c}_j \eta_j \right) \geq 0 \quad (\text{A.1.147})$$

The second term in (A.1.147) is written in terms of the divergence product rule is

$$\operatorname{div} \mathbf{q}_j = \operatorname{div}(\theta_j \mathbf{q}_j / \theta_j) = \theta_j \operatorname{div}(\mathbf{q}_j / \theta_j) + \operatorname{grad}(\theta_j) \cdot \mathbf{q}_j / \theta_j \quad (\text{A.1.148})$$

and substitution of (A.1.148) into (A.1.147), yields

$$\sum_{j=1}^N \frac{1}{\theta_j} \left(\theta_j \rho_j \frac{D_j \eta_j}{Dt} + \operatorname{div} \mathbf{q}_j - \operatorname{grad}(\theta_j) \cdot \mathbf{q}_j / \theta_j - \rho_j r_j + \theta_j \hat{c}_j \eta_j \right) \geq 0 \quad (\text{A.1.149})$$

The energy equation (A.1.100) is solved for the term $\rho_j r_j$ and inserted into (A.1.149), in order to obtain

$$\begin{aligned} \sum_{j=1}^N \frac{1}{\theta_j} \left(\rho_j \left(\theta_j \frac{D_j \eta_j}{Dt} - \frac{D_j e_j}{Dt} \right) \right) &\geq \sum_{j=1}^N \frac{1}{\theta_j} \left(-\operatorname{tr} \mathbf{T}_j^T \mathbf{L}_j + \operatorname{grad}(\theta_j) \cdot \mathbf{q}_j / \theta_j \right. \\ &\quad \left. + \sum_{j=1}^N \left(\frac{1}{\theta_j} \mathbf{u}_j \cdot \hat{\mathbf{p}}_j - \tilde{e}_j \right) \right. \\ &\quad \left. + \hat{c}_j \left(e_j - \theta_j \eta_j + \frac{1}{2} u_j^2 \right) \right) \end{aligned} \quad (\text{A.1.150})$$

where

$$\tilde{e}_j = \hat{e}_j + \mathbf{u}_j \cdot \hat{\mathbf{p}}_j + \hat{c}_j \left(e_j + \frac{1}{2} u_j^2 \right) \quad (\text{A.1.151})$$

The Helmholtz free energy density ψ_j is defined as

$$\psi_j = e_j - \eta_j \theta_j \quad (\text{A.1.152})$$

which implies that the material derivative is

$$\frac{D_j \psi_j}{Dt} = \frac{D_j e_j}{Dt} - \frac{D_j \eta_j}{Dt} \theta_j - \eta_j \frac{D_j \theta_j}{Dt} \quad (\text{A.1.153})$$

Using (A.1.152) and (A.1.153) with (A.1.150), yields

$$\begin{aligned} \sum_{j=1}^N \frac{1}{\theta_j} \left(-\rho_j \left(\frac{D_j \psi_j}{Dt} + \eta_j \frac{D_j \theta_j}{Dt} \right) \right) &\geq \sum_{j=1}^N \frac{1}{\theta_j} \left(-\text{tr} \mathbf{T}_j^T \mathbf{L}_j + \text{grad}(\theta_j) \cdot \mathbf{q}_j / \theta_j \right) \\ &+ \sum_{j=1}^N \left(\frac{1}{\theta_j} \mathbf{u}_j \cdot \hat{\mathbf{p}}_j - \tilde{e}_j \right. \\ &\left. + \hat{c}_j \left(\psi_j + \frac{1}{2} u_j^2 \right) \right) \end{aligned} \quad (\text{A.1.154})$$

The inequality for the case of the same temperature for the whole mixture is considered in the following. The temperature constraint is given as

$$\theta = \Theta(\mathbf{x}, t) \quad (\text{A.1.155})$$

so that

$$\Theta_1 = \Theta_2 \dots \Theta_N \quad (\text{A.1.156})$$

Consider the term $\sum_{j=1}^N \rho_j \eta_j \frac{D_j \theta_j}{Dt}$ written in terms of (A.1.34) with $\Gamma_j = \theta$ which results in

$$\sum_{j=1}^N \rho_j \eta_j \frac{D_j \theta_j}{Dt} = \rho \eta \frac{D\theta}{Dt} + \sum_{j=1}^N \rho_j \eta_j \text{grad}(\theta) \cdot \mathbf{u}_j \quad (\text{A.1.157})$$

where $\sum_{j=1}^N \rho_j \eta_j = \rho \eta$. Furthermore, consider the equation (A.1.145) with the constraint (A.1.155) and $\mathbf{h} = \sum_{j=1}^N \mathbf{h}_j$, that is

$$\sum_{j=1}^N \mathbf{q}_j = \mathbf{h} - \sum_{j=1}^N \rho_j \eta_j \theta \mathbf{u}_j \quad (\text{A.1.158})$$

multiplying (A.1.158) with $\text{grad}(\theta) / \theta$ yields

$$\sum_{j=1}^N \mathbf{q}_j \cdot \text{grad}(\theta) / \theta = \mathbf{h} \cdot \text{grad}(\theta) / \theta - \sum_{j=1}^N \rho_j \eta_j \text{grad}(\theta) \cdot \mathbf{u}_j \quad (\text{A.1.159})$$

It is seen that the second term on the left-hand side of (A.1.154) is equal to (A.1.157) and the second term on the right-hand side is equal to (A.1.159), where inserting cancels out the term $\sum_{j=1}^N \rho_j \eta_j \text{grad}(\theta) \cdot \mathbf{u}_j$ in (A.1.154) and consequently (A.1.154) can be written as

$$\begin{aligned} 0 &\leq - \sum_{j=1}^N \rho_j \frac{D_j \psi_j}{Dt} - \rho \eta \frac{D\theta}{Dt} + \sum_{j=1}^N \frac{1}{\theta_j} \left(\text{tr} \mathbf{T}_j^T \mathbf{L}_j - \mathbf{h} \cdot \text{grad}(\theta) / \theta \right) \\ &- \sum_{j=1}^N \left(\mathbf{u}_j \cdot \hat{\mathbf{p}}_j - \hat{c}_j \left(\psi_j + \frac{1}{2} u_j^2 \right) \right) \end{aligned} \quad (\text{A.1.160})$$

where $\sum_{j=1}^N \tilde{e}_a = 0$ due to (A.1.132) and (A.1.155).

Internal free energy inequality

The inequality presented in (A.1.160) can be written in different formats, in the following case in terms of the internal free energy $\psi_{\mathbf{I}}$ of the mixture as

$$0 \leq -\rho \left(\frac{D\psi_{\mathbf{I}}}{Dt} + \eta \frac{D\theta}{Dt} \right) + \text{tr} \mathbf{T}_j^T \mathbf{L}_j - \sum_{j=1}^N (\mathbf{u}_j \cdot \hat{\mathbf{p}}_j + \hat{c}_j \frac{1}{2} u_j^2) - \mathbf{h} \cdot \text{grad}(\theta) / \theta_j - \text{div} \left(\sum_{j=1}^N \rho_j \psi_j \mathbf{u}_j \right) \quad (\text{A.1.161})$$

which is (A.1.160) combined with (A.1.78), the contracted term

$$\sum_{j=1}^N \left(\rho_j \frac{D_j \psi_j}{Dt} + \hat{c}_j \psi_j \right) = \rho \frac{D\psi_{\mathbf{I}}}{Dt} + \text{div} \left(\sum_{j=1}^N \rho_j \psi_j \mathbf{u}_j \right) \quad (\text{A.1.162})$$

and the internal free energy $\psi_{\mathbf{I}}$ for the mixture defined as

$$\psi_{\mathbf{I}} = \frac{1}{\rho} \sum_{j=1}^N \rho_j \psi_j = e_{\mathbf{I}} - \eta \theta \quad (\text{A.1.163})$$

Chemical potential inequality

Another form of (A.1.160) introduces the chemical potential \mathbf{K}_j for the general mixtures as

$$0 \leq - \sum_{j=1}^N \frac{D_j}{Dt} (\rho_j \psi_j) - \rho \eta \frac{D\theta}{Dt} - \text{tr} \sum_{j=1}^N \rho_j \mathbf{K}_j \mathbf{L}_j - \mathbf{h} \cdot \text{grad}(\theta) \frac{1}{\theta} - \sum_{j=1}^N (\mathbf{u}_j \cdot \hat{\mathbf{p}}_j + \hat{c}_j \frac{1}{2} u_j^2) \quad (\text{A.1.164})$$

where \mathbf{K}_j is defined as

$$\mathbf{K}_j = \psi_j \mathbf{I} - \mathbf{T}_j^T \frac{1}{\rho_a} \quad (\text{A.1.165})$$

note that only if $\mathbf{T}_j = -\pi_j \mathbf{I}$, with π being the hydrostatic pressure, then the chemical potential for general mixtures reduces to $\mathbf{K}_j = \mu_j \mathbf{I}$, where μ_j is the classical scalar chemical potential.

Energy balance in terms of chemical potential and Helmholtz free energy

As a supplement to the different forms of the entropy inequality, the energy balance (A.1.131) can be expressed in terms of the Helmholtz free energy ψ_j and the chemical potential \mathbf{K}_j . The material derivative of (A.1.152) is

$$\frac{D\psi_j}{Dt} = \frac{De_j}{Dt} - \frac{D\eta_j}{Dt}\theta_j - \eta_j \frac{D\theta_j}{Dt} \quad (\text{A.1.166})$$

The term $\text{div} \mathbf{k}$ in (A.1.131) can be rewritten in terms of the definitions (A.1.145) and (A.1.107) as

$$\mathbf{k} = \mathbf{h} - \sum_{j=1}^N \rho_j \eta_j \theta \mathbf{u}_j + \sum_{j=1}^N \rho_j \varepsilon_j \mathbf{u}_j \quad (\text{A.1.167})$$

Using the entropy η_j expressed in terms of the Helmholtz free energy ψ_j and inserting in (A.1.167), yields

$$\mathbf{k} = \mathbf{h} + \sum_{j=1}^N \rho_j \psi_j \mathbf{u}_j \quad (\text{A.1.168})$$

Combining (A.1.131), (A.1.166) and (A.1.168), one obtains

$$\begin{aligned} \rho \frac{D\eta_j}{Dt} \theta_j + \rho \eta_j \frac{D\theta_j}{Dt} - \rho r \\ + \sum_{j=1}^N \mathbf{u}_j \cdot \hat{\mathbf{p}}_j + \sum_{j=1}^N \hat{c}_j \frac{1}{2} u_j^2 = -\rho \frac{D\psi_j}{Dt} + \text{tr} \sum_{j=1}^N \mathbf{T}_j^T \mathbf{L}_j \\ - \text{div} \mathbf{h} - \text{div} \sum_{j=1}^N \rho_j \psi_j \mathbf{u}_j \end{aligned} \quad (\text{A.1.169})$$

Using (A.1.78) with $\Gamma = \psi$ and combining with (A.1.169) yields the following format of the energy equation

$$\begin{aligned} \rho \frac{D\eta_j}{Dt} \theta_j + \rho \eta_j \frac{D\theta_j}{Dt} - \rho r \\ + \sum_{j=1}^N \mathbf{u}_j \cdot \hat{\mathbf{p}}_j + \sum_{j=1}^N \hat{c}_j \frac{1}{2} u_j^2 = \sum_{j=1}^N (\rho_j \psi'_j + \hat{c}_j \psi_j) \\ + \text{tr} \sum_{j=1}^N \mathbf{T}_j^T \mathbf{L}_j - \text{div} \mathbf{h} \end{aligned} \quad (\text{A.1.170})$$

A.1.5.1 Entropy inequality for the whole system

The use of the entropy inequality to obtain governing equations is demonstrated in the following. It is shown how Fick's law can be derived from the classical definition of chemical potential μ , with a specific choice of Helmholtz free energy ψ . Consider the entropy inequality for the case with a single temperature for the whole system, as

$$\rho \frac{D\eta}{Dt} \geq -\operatorname{div}(\mathbf{h}/\theta) + \rho r/\theta \quad (\text{A.1.171})$$

where the entropy influx vector \mathbf{h} can be expressed as (A.1.168) and (A.1.107) to yield the form

$$\rho \frac{D\eta}{Dt} \geq -\operatorname{div} \left(\mathbf{q}/\theta - \sum_{j=1}^N \frac{\rho_j}{\theta} \left(-\mathbf{T}_j^T/\rho_j + \psi_j + \frac{1}{2}u_j^2 \mathbf{I} \right) \mathbf{u}_j \right) + \rho r/\theta \quad (\text{A.1.172})$$

Using the definition of the chemical potential \mathbf{K}_j in (A.1.165) reduce (A.1.172) to

$$\rho \frac{D\eta}{Dt} \geq -\operatorname{div} \left(\mathbf{q}/\theta - \sum_{j=1}^N \frac{\rho_j}{\theta} \left(\mathbf{K}_j + \frac{1}{2}u_j^2 \mathbf{I} \right) \mathbf{u}_j \right) + \rho r/\theta \quad (\text{A.1.173})$$

The chemical potential \mathbf{K}_j is assumed simplified as $\mathbf{K}_j = \mu_j \mathbf{I}$, using this in (A.1.173) and rewrite (A.1.173) in terms of the temperature θ , for further use, yields

$$\theta \rho \frac{D\eta}{Dt} \geq -\theta \operatorname{div} \left(\frac{1}{\theta} \left(\mathbf{q} - \sum_{j=1}^N \rho_j \left(\mu_j + \frac{1}{2}u_j^2 \right) \mathbf{u}_j \right) \right) + \rho r \quad (\text{A.1.174})$$

The last term in (A.1.174) is found in the energy balance for the system (A.1.113) and inserting this yields

$$\begin{aligned} \theta \rho \frac{D\eta}{Dt} - \rho \frac{De}{Dt} &\geq -\theta \operatorname{div} \left(\frac{1}{\theta} \left(\mathbf{q} - \sum_{j=1}^N \rho_j \left(\mu_j + \frac{1}{2}u_j^2 \right) \mathbf{u}_j \right) \right) - \operatorname{tr} \mathbf{TL} \\ &\quad + \operatorname{div} \mathbf{q} - \sum_{j=1}^N \rho_j \mathbf{u}_j \cdot \mathbf{b}_j \end{aligned} \quad (\text{A.1.175})$$

The terms $\operatorname{div} \mathbf{q}$ and $\theta \operatorname{div} \left(\frac{\mathbf{q}}{\theta} \right)$ in (A.1.175) can be rewritten as

$$\theta \operatorname{div} \left(\frac{\mathbf{q}}{\theta} \right) = -\frac{\mathbf{q}}{\theta} \cdot \operatorname{grad}(\theta) + \operatorname{div} \mathbf{q} \quad (\text{A.1.176})$$

Inserting (A.1.176) in (A.1.175), yields

$$\begin{aligned} \theta \rho \frac{D\eta}{Dt} - \rho \frac{De}{Dt} &\geq \theta \operatorname{div} \left(\frac{1}{\theta} \left(\sum_{j=1}^N \rho_j (\mu_j + \frac{1}{2} u_j^2) \mathbf{u}_j \right) \right) - \operatorname{tr} \mathbf{T} \mathbf{L} \\ &\quad + \frac{\mathbf{q}}{\theta} \cdot \operatorname{grad}(\theta) - \sum_{j=1}^N \rho_j \mathbf{u}_j \cdot \mathbf{b}_j \end{aligned} \quad (\text{A.1.177})$$

For the further rewriting of (A.1.177) consider the following relation

$$\begin{aligned} \theta \operatorname{div} \left(\frac{1}{\theta} \left(\sum_{j=1}^N \rho_j (\mu_j + \frac{1}{2} u_j^2) \mathbf{u}_j \right) \right) &= \theta \sum_{j=1}^N \rho_j \mathbf{u}_j \cdot \operatorname{grad} \left(\frac{1}{\theta} (\mu_j + \frac{1}{2} u_j^2) \right) \\ &\quad + \sum_{j=1}^N (\mu_j + \frac{1}{2} u_j^2) \operatorname{div}(\rho_j \mathbf{u}_j) \end{aligned} \quad (\text{A.1.178})$$

and the mass balance (A.1.47) multiplied by $(\mu_j + \frac{1}{2} u_j^2)$, which is

$$\begin{aligned} \rho \sum_{j=1}^N \frac{Dc_j}{Dt} (\mu_j + \frac{1}{2} u_j^2) &= - \sum_{j=1}^N (\mu_j + \frac{1}{2} u_j^2) \operatorname{div}(\rho_j \mathbf{u}_j) \\ &\quad + \sum_{j=1}^N (\mu_j + \frac{1}{2} u_j^2) \hat{c}_j \end{aligned} \quad (\text{A.1.179})$$

Substituting the first term on the right-hand side of (A.1.177) in (A.1.178) and substituting the last term on the right-hand side of (A.1.178) in (A.1.179), yields the inequality

$$\begin{aligned} \theta \rho \frac{D\eta}{Dt} - \rho \frac{De}{Dt} \\ + \rho \sum_{j=1}^N \frac{Dc_j}{Dt} (\mu_j + \frac{1}{2} u_j^2) &\geq \sum_{j=1}^N \rho_j \mathbf{u}_j \cdot \left[\theta \operatorname{grad} \left(\frac{1}{\theta} (\mu_j + \frac{1}{2} u_j^2) \right) - \mathbf{b}_j \right] \\ &\quad + \sum_{j=1}^N (\mu_j + \frac{1}{2} u_j^2) \hat{c}_j - \operatorname{tr} \mathbf{T} \mathbf{L} + \frac{\mathbf{q}}{\theta} \cdot \operatorname{grad}(\theta) \end{aligned} \quad (\text{A.1.180})$$

For future use consider the relation between the internal energy e and the inner internal energy $e_{\mathbf{I}}$, as shown in (A.1.104), with the expansion $u_j^2 = \mathbf{u}_j \cdot \mathbf{u}_j$. The material derivative of the internal energy $\frac{De}{Dt}$ in (A.1.180) is

$$\frac{De}{Dt} = \frac{De_{\mathbf{I}}}{Dt} + \frac{1}{2} \sum_{j=1}^N \frac{Dc_j}{Dt} u_j^2 + \sum_{j=1}^N c_j \frac{D\mathbf{u}_j}{Dt} \cdot \mathbf{u}_j \quad (\text{A.1.181})$$

Substituting (A.1.181) into (A.1.180) and using the derivative of (A.1.163) for the inner internal energy $e_{\mathbf{I}}$ yields the sought entropy inequality form

$$\begin{aligned}
0 \leq \rho \left(-\eta \frac{D\theta}{Dt} - \frac{D\psi_{\mathbf{I}}}{Dt} + \sum_{j=1}^N \frac{Dc_j}{Dt} \mu_j \right) \\
- \sum_{j=1}^N \rho_j \mathbf{u}_j \cdot \left[\theta \text{grad} \left(\frac{1}{\theta} \left(\mu_j + \frac{1}{2} u_j^2 \right) \right) - \mathbf{b}_j + \frac{D\mathbf{u}_j}{Dt} \right] \\
- \sum_{j=1}^N \left(\mu_j + \frac{1}{2} u_j^2 \right) \hat{c}_j + \text{tr} \mathbf{T} \mathbf{L} - \frac{\mathbf{q}}{\theta} \cdot \text{grad}(\theta) \quad (\text{A.1.182})
\end{aligned}$$

A.2 Mixture theory for multi-species in multi-phases

The following section will show a detailed review of the derivation of multi-phase and multi-constituent mixture theory also referred to as hybrid mixture theory (HMT). Consider a mixture of \mathcal{R} continuous bodies $\mathcal{B}_1, \dots, \mathcal{B}_{\mathcal{R}}$ in a three dimensional physical space, with the possibility of the different bodies to occupy common physical space. As a result of this \mathbf{X}_{a_j} and \mathbf{X}_{b_j} are allowed to occupy the the same spatial position in the space.

The notation of the derivatives is extended compared to the single phase mixture in order to include multiple phases. The velocity of the constituents, the phases and the whole mixture are defined as

$$\mathbf{x}'_{\alpha_j} = \frac{\partial \chi_{\alpha_j}(\mathbf{X}_{\alpha_j}, t)}{\partial t}; \quad \mathbf{x}'_{\alpha} = \frac{\partial \chi_{\alpha}(\mathbf{X}_{\alpha}, t)}{\partial t}; \quad \mathbf{x}' = \frac{\partial \chi(\mathbf{X}, t)}{\partial t} \quad (\text{A.2.1})$$

The material time derivatives are also extended to include multiple phases where Γ is an arbitrary property. The material time derivative following the j constituent in the α phase is

$$\frac{D_{\alpha_j}(\Gamma)}{Dt} = \frac{\partial \Gamma}{\partial t} + \text{grad}(\Gamma) \mathbf{x}'_{\alpha_j} \quad (\text{A.2.2})$$

The material time derivative following the α phase is

$$\frac{D_{\alpha}(\Gamma)}{Dt} = \frac{\partial \Gamma}{\partial t} + \text{grad}(\Gamma) \mathbf{x}'_{\alpha} \quad (\text{A.2.3})$$

The material time derivative for the whole mixture is given as

$$\frac{D(\Gamma)}{Dt} = \frac{\partial \Gamma}{\partial t} + \text{grad}(\Gamma) \mathbf{x}' \quad (\text{A.2.4})$$

The diffusion velocity is defined in two levels, one for the constituents with respect to a phase and one for the phases with respect to the whole mixture, these are defined as

$$\mathbf{u}_{\alpha_j} = \mathbf{x}'_{\alpha_j} - \mathbf{x}'_{\alpha}; \quad \mathbf{u}_{\alpha} = \mathbf{x}'_{\alpha} - \mathbf{x}' \quad (\text{A.2.5})$$

The definitions of the material derivatives and the diffusion velocities, leads to the following relations between the material derivatives

$$\begin{aligned} (a) : \quad \frac{D_{\alpha_j}(\Gamma)}{Dt} - \frac{D_{\alpha}(\Gamma)}{Dt} &= \text{grad}(\Gamma)\mathbf{u}_{\alpha_j} \\ (b) : \quad \frac{D_{\alpha}(\Gamma)}{Dt} - \frac{D(\Gamma)}{Dt} &= \text{grad}(\Gamma)\mathbf{u}_{\alpha} \end{aligned} \quad (\text{A.2.6})$$

which is used in the the following derivations.

The difference between describing multiple-phases and multiple-species is that a clear boundary exist between phases, whereas the species do not have clear physical boundaries. In HMT a volume ratio ε_{α} of the phases α in a body \mathcal{B} is defined as

$$\varepsilon_{\alpha} = \frac{dv_{\alpha}}{dv} \quad (\text{A.2.7})$$

where v_{α} is the volume of the phase α and v is the volume of the whole mixture. The definition (A.2.7) implies that

$$\sum_{\alpha=1}^N \varepsilon_{\alpha} = 1 \quad (\text{A.2.8})$$

must be satisfied. The density of the whole mixture determined from the summation of the phase masses $dm = \sum_{\alpha=1}^N \rho_{\alpha} dv_{\alpha}$ is the mass of the total mixture, determines as

$$dm = \rho dv = \sum_{\alpha=1}^M \rho_{\alpha} dv_{\alpha} \quad (\text{A.2.9})$$

which yields the density of the whole mixture as

$$\rho = \sum_{\alpha=1}^M \varepsilon_{\alpha} \rho_{\alpha} \quad (\text{A.2.10})$$

The density of the whole mixture is described by summation of the densities of the phases, recall from Sec. A.1.1 that the density of a phase is described by the summation of densities of the species, see equation (A.1.19)

and repeated here with the phase index α and $j = 1 \dots N$ as the total number of species in the phase

$$\rho_\alpha = \sum_{j=1}^N \rho_{\alpha_j} \quad (\text{A.2.11})$$

The equations (A.2.10) and (A.2.11) relates the phases and species to the mixture.

A.2.1 Mass balance

The mass balance postulate for an M - phase and N - species mixture is given as

$$\frac{\partial}{\partial t} \int_{\Omega} \varepsilon_\alpha \rho_{\alpha_j} dv = - \oint_{\partial\Omega} \varepsilon_\alpha \rho_{\alpha_j} \mathbf{x}'_{\alpha_j} \cdot d\mathbf{s} + \int_{\Omega} (\hat{r}_{\alpha_j} + \hat{c}_{\alpha_j}) dv \quad (\text{A.2.12})$$

where \hat{r}_{α_j} is the mass exchange term between the phases. Using the divergence theorem for the first term on the right hand side of (A.2.12), yields the local form of mass balance as

$$\frac{\partial \varepsilon_\alpha \rho_{\alpha_j}}{\partial t} + \text{div} \left(\varepsilon_\alpha \rho_{\alpha_j} \mathbf{x}'_{\alpha_j} \right) = \hat{r}_{\alpha_j} + \hat{c}_{\alpha_j} \quad \alpha = 1, \dots, M \quad j = 1, \dots, N \quad (\text{A.2.13})$$

The local form of the mass balance for the phase α given as

$$\frac{\partial \varepsilon_\alpha \rho_\alpha}{\partial t} + \text{div} (\varepsilon_\alpha \rho_\alpha \mathbf{x}'_\alpha) = \hat{r}_\alpha \quad (\text{A.2.14})$$

where the summation of the mass exchange term \hat{r}_{α_j} yields the left-hand side of (A.2.14)

$$\hat{r}_\alpha = \sum_{j=1}^N \hat{r}_{\alpha_j} \quad (\text{A.2.15})$$

Summation of the constituents in (A.2.13), together with (A.1.19) and (A.1.22) enables the comparison of (A.2.13) and (A.2.14), Using (A.2.15) yields the summation of the chemical interactions in the α phase as

$$\sum_{j=1}^N \hat{c}_{\alpha_j} = 0 \quad (\text{A.2.16})$$

which is equal to the result obtained in (A.1.43) for the single phase system. The further derivation to include multiple phases in the mixture is similar to

the constituent derivation. The postulate for the mass balance of the mixture is

$$\frac{\partial \rho}{\partial t} + \operatorname{div}(\rho \mathbf{x}') = 0 \quad (\text{A.2.17})$$

summation of (A.2.14), over the phases and use

$$\mathbf{x}' = \frac{1}{\rho} \sum_{\alpha=1}^{\mathcal{R}} \rho_{\alpha} \mathbf{x}'_{\alpha}(\mathbf{x}, t) \quad (\text{A.2.18})$$

with (A.2.8), (A.2.10) and finally compare with (A.2.17), yields

$$\sum_{\alpha=1}^N \hat{r}_{\alpha} = 0 \quad (\text{A.2.19})$$

With the results in (A.2.16) and (A.2.19), it is shown that a summation over the constituents and the phases yields the result for the mixture as a whole.

As described earlier, it is convenient to work with the concentrations of the species due to the fact no direct boundary exist between the species. The mass balance for a single phase written in terms of species concentrations is given in (A.1.47) and extended in the following to include multiple-phases.

The equation (A.2.13) written in terms of the diffusion velocity (A.1.23), yields

$$\frac{\partial \varepsilon_{\alpha} \rho_{\alpha_j}}{\partial t} + \operatorname{div}(\varepsilon_{\alpha} \rho_{\alpha_j} \mathbf{u}_{\alpha_j}) + \operatorname{div}(\varepsilon_{\alpha} \rho_{\alpha_j} \mathbf{x}'_{\alpha}) = \hat{r}_{\alpha_j} + \hat{c}_{\alpha_j} \quad (\text{A.2.20})$$

The first term on the left-hand side of (A.2.20) written in terms of the species concentration, c_{α_j} , is

$$\frac{\partial \varepsilon_{\alpha} \rho_{\alpha_j}}{\partial t} = \frac{\partial \varepsilon_{\alpha} c_{\alpha_j} \rho_{\alpha}}{\partial t} = c_{\alpha_j} \frac{\partial \varepsilon_{\alpha} \rho_{\alpha}}{\partial t} + \varepsilon_{\alpha} \rho_{\alpha} \frac{\partial c_{\alpha_j}}{\partial t} \quad (\text{A.2.21})$$

The divergence product rule used on the third term in (A.2.20) together with (A.1.20) gives the result

$$\operatorname{div}(c_{\alpha_j} \varepsilon_{\alpha} \rho_{\alpha} \mathbf{x}'_{\alpha}) = c_{\alpha_j} \operatorname{div}(\varepsilon_{\alpha} \rho_{\alpha} \mathbf{x}'_{\alpha}) + \varepsilon_{\alpha} \rho_{\alpha} \mathbf{x}'_{\alpha} \operatorname{grad} c_{\alpha_j} \quad (\text{A.2.22})$$

Inserting (A.2.21) and (A.2.22) into (A.2.20) and collect the terms including c_{α_j} , yields

$$\begin{aligned} \hat{r}_{\alpha_j} + \hat{c}_{\alpha_j} &= c_{\alpha_j} \left[\frac{\partial \varepsilon_{\alpha} \rho_{\alpha}}{\partial t} + \operatorname{div}(\varepsilon_{\alpha} \rho_{\alpha} \dot{\mathbf{x}}_{\alpha}) \right] + \varepsilon_{\alpha} \rho_{\alpha} \frac{\partial c_{\alpha_j}}{\partial t} \\ &\quad + \operatorname{div}(\varepsilon_{\alpha} \rho_{\alpha_j} \mathbf{u}_{\alpha_j}) + \varepsilon_{\alpha} \rho_{\alpha} \dot{\mathbf{x}}_{\alpha} \operatorname{grad} c_{\alpha_j} \end{aligned} \quad (\text{A.2.23})$$

where the mass balance for the phase (A.2.14) is identified in the square bracket. Using (A.1.33) with $\Gamma = c_{\alpha_j}$ simplifies (A.2.24) to

$$\varepsilon_{\alpha}\rho_{\alpha}\frac{D_{\alpha}c_{\alpha_j}}{Dt} + \operatorname{div}(\varepsilon_{\alpha}\rho_{\alpha_j}\mathbf{u}_{\alpha_j}) = \hat{r}_{\alpha_j} + \hat{c}_{\alpha_j} - c_{\alpha_j}\hat{r}_{\alpha} \quad (\text{A.2.24})$$

which is the material derivative of the mass balance for the species, expressed in terms of the diffusion velocity and the concentration of the species.

The mass balance for the phase can be rewritten in terms of the diffusion velocity of the phase, using $\Gamma = \varepsilon_{\alpha}\rho_{\alpha}$ in (A.2.3) to obtain

$$\frac{D_{\alpha}(\varepsilon_{\alpha}\rho_{\alpha})}{Dt} = \frac{\partial\varepsilon_{\alpha}\rho_{\alpha}}{\partial t} + \operatorname{grad}(\varepsilon_{\alpha}\rho_{\alpha})\mathbf{x}'_{\alpha} \quad (\text{A.2.25})$$

and the identity

$$\operatorname{div}(\varepsilon_{\alpha}\rho_{\alpha}\mathbf{x}'_{\alpha}) = \varepsilon_{\alpha}\rho_{\alpha}\operatorname{div}(\mathbf{x}'_{\alpha}) + \operatorname{grad}(\varepsilon_{\alpha}\rho_{\alpha})\mathbf{x}'_{\alpha} \quad (\text{A.2.26})$$

Combining (A.2.25) and (A.2.26) with (A.2.14), yields

$$\frac{D_{\alpha}(\varepsilon_{\alpha}\rho_{\alpha})}{Dt} + \varepsilon_{\alpha}\rho_{\alpha}\operatorname{div}(\mathbf{x}'_{\alpha}) = \hat{r}_{\alpha} \quad (\text{A.2.27})$$

The equation (A.2.27) written in terms of the diffusion velocity, with respect to the whole mixture is

$$\frac{D(\varepsilon_{\alpha}\rho_{\alpha})}{Dt} + \operatorname{div}(\varepsilon_{\alpha}\rho_{\alpha}\mathbf{u}_{\alpha}) + \varepsilon_{\alpha}\rho_{\alpha}\operatorname{div}(\mathbf{x}') = \hat{r}_{\alpha} \quad (\text{A.2.28})$$

The mass balance for the whole mixture is obtained by using ρ in (A.2.4) to get

$$\frac{D(\rho)}{Dt} = \frac{\partial\rho}{\partial t} + \operatorname{grad}(\rho)\mathbf{x}' \quad (\text{A.2.29})$$

and using the identity

$$\operatorname{div}(\rho\mathbf{x}') = \rho\operatorname{div}(\mathbf{x}') + \operatorname{grad}(\rho)\mathbf{x}' \quad (\text{A.2.30})$$

Combining (A.2.29) and (A.2.30) yields the mass balance of the whole mixture, that is

$$\frac{D(\rho)}{Dt} + \rho\operatorname{div}(\mathbf{x}') = 0 \quad (\text{A.2.31})$$

A.2.2 Momentum balance

The momentum balance for a mixture, with α phases and j species is derived. Consider a system of α phases and j species which expands the postulate of momentum balance (A.1.48) to include momentum gain for the j species from other phases in the mixture by $\hat{\mathbf{t}}_{\alpha_j}$. The local form of the momentum balance is

$$\begin{aligned} \frac{\partial \left(\varepsilon_{\alpha_j} \rho_{\alpha_j} \mathbf{x}'_{\alpha_j} \right)}{\partial t} &= -\operatorname{div} \left(\varepsilon_{\alpha_j} \rho_{\alpha_j} \mathbf{x}'_{\alpha_j} \otimes \mathbf{x}'_{\alpha_j} \right) + \operatorname{div} \left(\varepsilon_{\alpha_j} \mathbf{T}_{\alpha_j} \right) + \varepsilon_{\alpha_j} \rho_{\alpha_j} \mathbf{b}_{\alpha_j} \\ &\quad + \hat{\mathbf{t}}_{\alpha_j} + \hat{\mathbf{p}}_{\alpha_j} + \hat{\mathbf{c}}_{\alpha_j} \mathbf{x}'_{\alpha_j} + \hat{\mathbf{r}}_{\alpha_j} \mathbf{x}'_{\alpha_j} \end{aligned} \quad (\text{A.2.32})$$

where the mass balance (A.2.13) can be identified by similar mathematical steps as shown from (A.1.53) to (A.1.55) and therefore (A.2.25) reduces to

$$\varepsilon_{\alpha} \rho_{\alpha} \frac{D_{\alpha} \mathbf{x}'_{\alpha}}{Dt} = \operatorname{div} \left(\varepsilon_{\alpha} \mathbf{T}_{\alpha} \right) + \varepsilon_{\alpha} \rho_{\alpha} \mathbf{b}_{\alpha} + \hat{\mathbf{t}}_{\alpha} + \hat{\mathbf{p}}_{\alpha} \quad (\text{A.2.33})$$

The local postulate for the momentum balance of the phases is defined as

$$\varepsilon_{\alpha} \rho_{\alpha} \frac{D_{\alpha} \mathbf{x}'_{\alpha}}{Dt} = \operatorname{div} \left(\varepsilon_{\alpha} \mathbf{T}_{\alpha} \right) + \varepsilon_{\alpha} \rho_{\alpha} \mathbf{b}_{\alpha} + \hat{\mathbf{t}}_{\alpha} \quad (\text{A.2.34})$$

Summation over the species of (A.2.33) yields

$$\sum_{j=1}^N \varepsilon_{\alpha} \rho_{\alpha_j} \frac{D_{\alpha_j} \mathbf{x}'_{\alpha_j}}{Dt} = \sum_{j=1}^N \left(\operatorname{div} \left(\varepsilon_{\alpha} \mathbf{T}_{\alpha_j} \right) + \varepsilon_{\alpha} \rho_{\alpha_j} \mathbf{b}_{\alpha_j} + \hat{\mathbf{t}}_{\alpha_j} + \hat{\mathbf{p}}_{\alpha_j} \right) \quad (\text{A.2.35})$$

where the inner stress tensor $\mathbf{T}_{\mathbf{I},\alpha}$ of the α phase is defined as

$$\mathbf{T}_{\mathbf{I},\alpha} = \sum_{j=1}^N \mathbf{T}_{\alpha_j} \quad (\text{A.2.36})$$

and the body force for the phase is defined as

$$\mathbf{b}_{\alpha} = \frac{1}{\rho_{\alpha}} \sum_{j=1}^N \rho_{\alpha_j} \mathbf{b}_{\alpha_j} \quad (\text{A.2.37})$$

Inserting (A.2.36) and (A.2.37) into (A.2.35), yields

$$\sum_{j=1}^N \varepsilon_{\alpha} \rho_{\alpha_j} \frac{D_{\alpha_j} \mathbf{x}'_{\alpha_j}}{Dt} = \operatorname{div} \left(\varepsilon_{\alpha} \mathbf{T}_{\mathbf{I},\alpha} \right) + \varepsilon_{\alpha} \rho_{\alpha} \mathbf{b}_{\alpha} + \sum_{j=1}^N \hat{\mathbf{t}}_{\alpha_j} + \sum_{j=1}^N \hat{\mathbf{p}}_{\alpha_j} \quad (\text{A.2.38})$$

General relation 2:

A general relation for a arbitrary property $\Gamma(\mathbf{x}, t)$ is shown in order to compare the summation of the species (A.2.38) to the postulate of the phase (A.2.34). Consider the property $\Gamma(\mathbf{x}, t)$ and assume that the relation between the species level and the phase level is described by

$$\Gamma_\alpha = \frac{1}{\rho_\alpha} \sum_{j=1}^N \rho_{\alpha_j} \Gamma_{\alpha_j} = \sum_{j=1}^N c_{\alpha_j} \Gamma_{\alpha_j} \quad (\text{A.2.39})$$

The material time derivative of the general property is

$$\frac{D_\alpha \Gamma_\alpha}{Dt} = \sum_{j=1}^N \frac{D_\alpha (c_{\alpha_j} \Gamma_{\alpha_j})}{Dt} = \sum_{j=1}^N \left[\Gamma_{\alpha_j} \frac{D_\alpha (c_{\alpha_j})}{Dt} + c_{\alpha_j} \frac{D_\alpha (\Gamma_{\alpha_j})}{Dt} \right] \quad (\text{A.2.40})$$

For the further derivation, consider (A.2.6)-(a) with $\Gamma = \Gamma_{\alpha_j}$ which yields the time derivative of the last term in the square brackets in (A.2.40). Multiplying (A.2.40) by $\varepsilon_\alpha \rho_\alpha$, shows that a part of the first term in the square brackets is equal to the mass balance shown in (A.2.24). Inserting these relation into (A.2.40) yields the form

$$\begin{aligned} \varepsilon_\alpha \rho_\alpha \frac{D_\alpha \Gamma_\alpha}{Dt} &= \varepsilon_\alpha \rho_\alpha \sum_{j=1}^N \left[\Gamma_{\alpha_j} \frac{D_\alpha (c_{\alpha_j})}{Dt} + c_{\alpha_j} \frac{D_\alpha (\Gamma_{\alpha_j})}{Dt} \right] \\ &= \sum_{j=1}^N \left[\Gamma_{\alpha_j} \varepsilon_\alpha \rho_\alpha \frac{D_\alpha (c_{\alpha_j})}{Dt} + \varepsilon_\alpha \rho_\alpha c_{\alpha_j} \left(\frac{D_{\alpha_j} (\Gamma_{\alpha_j})}{Dt} - \text{grad}(\Gamma_{\alpha_j}) \mathbf{u}_{\alpha_j} \right) \right] \\ &= \sum_{j=1}^N \left[\varepsilon_\alpha \rho_\alpha c_{\alpha_j} \frac{D_{\alpha_j} (\Gamma_{\alpha_j})}{Dt} - \varepsilon_\alpha \rho_\alpha c_{\alpha_j} \text{grad}(\Gamma_{\alpha_j}) \mathbf{u}_{\alpha_j} \right. \\ &\quad \left. - \Gamma_{\alpha_j} \text{div} (\varepsilon_\alpha \rho_{\alpha_j} \mathbf{u}_{\alpha_j}) + \Gamma_{\alpha_j} (\hat{r}_{\alpha_j} + \hat{c}_{\alpha_j} - c_{\alpha_j} \hat{r}_\alpha) \right] \quad (\text{A.2.41}) \end{aligned}$$

The divergence term in (A.2.41) is rewritten by the identity

$$\text{div} (\varepsilon_\alpha \rho_{\alpha_j} \Gamma_{\alpha_j} \mathbf{u}_{\alpha_j}) = \varepsilon_\alpha \rho_{\alpha_j} \text{grad} (\Gamma_{\alpha_j}) \mathbf{u}_{\alpha_j} + \Gamma_{\alpha_j} \text{div} (\varepsilon_\alpha \rho_{\alpha_j} \mathbf{u}_{\alpha_j}) \quad (\text{A.2.42})$$

Combining (A.2.41) and (A.2.42) yields the desired final relation as

$$\begin{aligned} \varepsilon_\alpha \rho_\alpha \frac{D_\alpha \Gamma_\alpha}{Dt} &= \sum_{j=1}^N \left[\varepsilon_\alpha \rho_\alpha c_{\alpha_j} \frac{D_{\alpha_j} (\Gamma_{\alpha_j})}{Dt} - \text{div} (\varepsilon_\alpha \rho_{\alpha_j} \Gamma_{\alpha_j} \mathbf{u}_{\alpha_j}) \right. \\ &\quad \left. + \Gamma_{\alpha_j} (\hat{r}_{\alpha_j} + \hat{c}_{\alpha_j} - c_{\alpha_j} \hat{r}_\alpha) \right] \quad (\text{A.2.43}) \end{aligned}$$

Using the general relation (A.2.43), with $\Gamma = \mathbf{x}'$, yields

$$\begin{aligned} \varepsilon_\alpha \rho_\alpha \frac{D_\alpha \mathbf{x}'_\alpha}{Dt} &= \sum_{j=1}^N \left[\varepsilon_\alpha \rho_\alpha c_{\alpha_j} \frac{D_{\alpha_j}(\mathbf{x}'_{\alpha_j})}{Dt} - \operatorname{div} (\varepsilon_\alpha \rho_{\alpha_j} \mathbf{x}'_{\alpha_j} \otimes \mathbf{u}_{\alpha_j}) \right. \\ &\quad \left. + \mathbf{x}'_{\alpha_j} (\hat{r}_{\alpha_j} + \hat{c}_{\alpha_j} - c_{\alpha_j} \hat{r}_\alpha) \right] \end{aligned} \quad (\text{A.2.44})$$

Applying the diffusion velocity for the j 'th species, $\mathbf{x}'_{\alpha_j} = \mathbf{u}_{\alpha_j} + \mathbf{x}'_\alpha$ in the divergence term of (A.2.44) yields

$$\begin{aligned} \varepsilon_\alpha \rho_\alpha \frac{D_\alpha \mathbf{x}'_\alpha}{Dt} &= \sum_{j=1}^N \varepsilon_\alpha \rho_\alpha c_{\alpha_j} \frac{D_{\alpha_j}(\mathbf{x}'_{\alpha_j})}{Dt} - \operatorname{div} \sum_{j=1}^N (\varepsilon_\alpha \rho_{\alpha_j} \mathbf{u}'_{\alpha_j} \otimes \mathbf{u}_{\alpha_j}) \\ &\quad - \operatorname{div} \sum_{j=1}^N (\varepsilon_\alpha \rho_{\alpha_j} \mathbf{u}_{\alpha_j}) \otimes \mathbf{x}'_\alpha + \sum_{j=1}^N (\hat{r}_{\alpha_j} + \hat{c}_{\alpha_j} - c_{\alpha_j} \hat{r}_\alpha) \mathbf{x}'_\alpha \\ &\quad + \sum_{j=1}^N (\hat{r}_{\alpha_j} + \hat{c}_{\alpha_j} - c_{\alpha_j} \hat{r}_\alpha) \mathbf{u}_{\alpha_j} \end{aligned} \quad (\text{A.2.45})$$

The fact that $\sum_{j=1}^N (\rho_{\alpha_j} \mathbf{u}_{\alpha_j}) = 0$ is used to reduce (A.2.45) further, which eliminates the second divergence term in (A.2.45). Furthermore, it is noted that $\sum_{j=1}^N (\hat{r}_{\alpha_j} + \hat{c}_{\alpha_j} - c_{\alpha_j} \hat{r}_\alpha) = 0$ is obtained for the mass balance and the fact that $\sum_{j=1}^N c_{\alpha_j} = 1$, which yields a reduced form of (A.2.45), as

$$\begin{aligned} \varepsilon_\alpha \rho_\alpha \frac{D_\alpha \mathbf{x}'_\alpha}{Dt} &= \sum_{j=1}^N \varepsilon_\alpha \rho_\alpha c_{\alpha_j} \frac{D_{\alpha_j}(\mathbf{x}'_{\alpha_j})}{Dt} - \operatorname{div} \sum_{j=1}^N (\varepsilon_\alpha \rho_{\alpha_j} \mathbf{u}_{\alpha_j} \otimes \mathbf{u}_{\alpha_j}) \\ &\quad + \sum_{j=1}^N (\hat{r}_{\alpha_j} + \hat{c}_{\alpha_j} - c_{\alpha_j} \hat{r}_\alpha) \mathbf{u}_{\alpha_j} \end{aligned} \quad (\text{A.2.46})$$

by substituting the first term on right-hand side of (A.2.46) with (A.2.38), to get

$$\begin{aligned} \varepsilon_\alpha \rho_\alpha \frac{D_\alpha \mathbf{x}'_\alpha}{Dt} &= \operatorname{div} \left(\varepsilon_\alpha \mathbf{T}_{\mathbf{I},\alpha} - \sum_{j=1}^N (\varepsilon_\alpha \rho_{\alpha_j} \mathbf{u}'_{\alpha_j} \otimes \mathbf{u}_{\alpha_j}) \right) + \varepsilon_\alpha \rho_\alpha \mathbf{b}_\alpha \\ &\quad + \sum_{j=1}^N \hat{\mathbf{t}}_{\alpha_j} + \sum_{j=1}^N \hat{\mathbf{p}}_{\alpha_j} + \sum_{j=1}^N \hat{r}_{\alpha_j} \mathbf{u}'_{\alpha_j} + \sum_{j=1}^N \hat{c}_{\alpha_j} \mathbf{u}'_{\alpha_j} \\ &\quad - \frac{\hat{r}_\alpha}{\rho_\alpha} \sum_{j=1}^N \rho_{\alpha_j} \mathbf{u}'_{\alpha_j} \end{aligned} \quad (\text{A.2.47})$$

where the last term is eliminated by $\sum_{j=1}^N (\rho_{\alpha_j} \mathbf{u}_{\alpha_j}) = 0$ with the use of the expansion of c_{α_j} .

The momentum balance for the species (A.2.47) and the phase (A.2.34) are compatible which yields the criteria

$$\varepsilon_{\alpha} \mathbf{T}_{\alpha} = \varepsilon_{\alpha} \mathbf{T}_{\mathbf{I},\alpha} - \sum_{j=1}^N (\varepsilon_{\alpha} \rho_{\alpha_j} \mathbf{u}_{\alpha_j} \otimes \mathbf{u}_{\alpha_j}) \quad (\text{A.2.48})$$

$$\hat{\mathbf{t}}_{\alpha} = \sum_{j=1}^N \hat{\mathbf{t}}_{\alpha_j} + \sum_{j=1}^N \hat{r}_{\alpha_j} \mathbf{u}_{\alpha_j} \quad (\text{A.2.49})$$

and

$$\sum_{j=1}^N \hat{\mathbf{p}}_{\alpha_j} + \sum_{j=1}^N \hat{c}_{\alpha_j} \mathbf{u}_{\alpha_j} = 0 \quad (\text{A.2.50})$$

where the second order tensor $\rho_{\alpha_j} \mathbf{u}'_{\alpha_j} \otimes \mathbf{u}'_{\alpha_j}$ is the so-called Reinholds stress tensor.

A similar approach is used to show that the summation of the phases is compatible with the postulate for the whole mixture. The local postulate for the momentum balance of the whole mixture is

$$\rho \frac{D\mathbf{x}'}{Dt} = \text{div} \mathbf{T} + \rho \mathbf{b} \quad (\text{A.2.51})$$

Direct definition for summations over the phases are given for the stress tensor and the body force as

$$\mathbf{T}_{\mathbf{I}} = \sum_{\alpha=1}^N \varepsilon_{\alpha} \mathbf{T}_{\alpha} \quad (\text{A.2.52})$$

and

$$\mathbf{b} = \frac{1}{\rho} \sum_{\alpha=1}^N \varepsilon_{\alpha} \rho_{\alpha} \mathbf{b}_{\alpha} \quad (\text{A.2.53})$$

where (A.2.8) is used. By use of the definitions (A.2.52) and (A.2.53) in (A.2.34) yields

$$\sum_{\alpha=1}^N \varepsilon_{\alpha} \rho_{\alpha} \frac{D_{\alpha} \mathbf{x}'_{\alpha}}{Dt} = \text{div} \mathbf{T}_{\mathbf{I}} + \rho \mathbf{b} + \sum_{\alpha=1}^N \hat{\mathbf{t}}_{\alpha} \quad (\text{A.2.54})$$

General relation 3:

A relation similar to (A.2.43), is established between the phase description and the whole mixture description. First consider the arbitrary variable Γ , with the definition

$$\rho\Gamma = \sum_{\alpha=1}^N \varepsilon_{\alpha}\rho_{\alpha}\Gamma_{\alpha} \quad (\text{A.2.55})$$

The material derivative of (A.2.55) with respect to the mixture is

$$\frac{D(\rho\Gamma)}{Dt} = \sum_{\alpha=1}^N \left(\Gamma_{\alpha} \frac{D(\varepsilon_{\alpha}\rho_{\alpha})}{Dt} + \varepsilon_{\alpha}\rho_{\alpha} \frac{D(\Gamma_{\alpha})}{Dt} \right) \quad (\text{A.2.56})$$

The first term on the left-hand side of (A.2.56) is (A.2.28), substituting this and using (A.2.6)-(b) with $\Gamma = \Gamma_{\alpha}$, yields

$$\begin{aligned} \frac{D(\rho\Gamma)}{Dt} &= \sum_{\alpha=1}^N \left(\Gamma_{\alpha} \left(-\text{div}(\varepsilon_{\alpha}\rho_{\alpha}\mathbf{u}_{\alpha}) - \varepsilon_{\alpha}\rho_{\alpha}\text{div}(\mathbf{x}') + \hat{r}_{\alpha} \right) \right. \\ &\quad \left. + \varepsilon_{\alpha}\rho_{\alpha} \left(\frac{D_{\alpha}(\Gamma_{\alpha})}{Dt} - \text{grad}(\Gamma_{\alpha})\mathbf{u}_{\alpha} \right) \right) \end{aligned} \quad (\text{A.2.57})$$

The first divergence term and the gradient term on the left-hand side, is equivalent to the divergence of the product of the variables

$$\text{div}(\varepsilon_{\alpha}\rho_{\alpha}\Gamma_{\alpha}\mathbf{u}_{\alpha}) = \varepsilon_{\alpha}\rho_{\alpha}\text{grad}(\Gamma_{\alpha})\mathbf{u}_{\alpha} + \Gamma_{\alpha}\text{div}(\varepsilon_{\alpha}\rho_{\alpha}\mathbf{u}_{\alpha}) \quad (\text{A.2.58})$$

Substituting (A.2.58) into (A.2.57), yields

$$\begin{aligned} \frac{D(\rho\Gamma)}{Dt} &= \sum_{\alpha=1}^N \left(-\text{div}(\varepsilon_{\alpha}\rho_{\alpha}\Gamma_{\alpha}\mathbf{u}_{\alpha}) - \varepsilon_{\alpha}\rho_{\alpha}\Gamma_{\alpha}\text{div}(\mathbf{x}') \right. \\ &\quad \left. + \Gamma_{\alpha}\hat{r}_{\alpha} + \varepsilon_{\alpha}\rho_{\alpha} \frac{D_{\alpha}(\Gamma_{\alpha})}{Dt} \right) \end{aligned} \quad (\text{A.2.59})$$

Applying the product rule to the right-hand side of (A.2.59) and by using $\sum_{\alpha=1}^N \varepsilon_{\alpha}\rho_{\alpha}\Gamma_{\alpha}\text{div}(\mathbf{x}') = \rho\Gamma\text{div}(\mathbf{x}')$, show that the mass balance for the whole mixture (A.2.31) is identified in the below square brackets, that is

$$\begin{aligned} \Gamma \left[\frac{D(\rho)}{Dt} + \rho\text{div}(\mathbf{x}') \right] + \rho \frac{D(\Gamma)}{Dt} &= \sum_{\alpha=1}^N \left(-\text{div}(\varepsilon_{\alpha}\rho_{\alpha}\Gamma_{\alpha}\mathbf{u}_{\alpha}) \right. \\ &\quad \left. + \Gamma_{\alpha}\hat{r}_{\alpha} + \varepsilon_{\alpha}\rho_{\alpha} \frac{D_{\alpha}(\Gamma_{\alpha})}{Dt} \right) \end{aligned} \quad (\text{A.2.60})$$

which reduce (A.2.60) to

$$\rho \frac{D(\Gamma)}{Dt} = -\operatorname{div} \sum_{\alpha=1}^N (\varepsilon_{\alpha} \rho_{\alpha} \Gamma_{\alpha} \mathbf{u}_{\alpha}) + \sum_{\alpha=1}^N \Gamma_{\alpha} \hat{r}_{\alpha} + \sum_{\alpha=1}^N \varepsilon_{\alpha} \rho_{\alpha} \frac{D_{\alpha}(\Gamma_{\alpha})}{Dt} \quad (\text{A.2.61})$$

Using the general relation (A.2.61) with $\Gamma = \mathbf{x}'$ and the definition of the diffusion velocity for the phase $\mathbf{x}'_{\alpha} = \mathbf{u}_{\alpha} + \mathbf{x}'$, yields

$$\begin{aligned} \rho \frac{D(\mathbf{x}')}{Dt} &= -\operatorname{div} \sum_{\alpha=1}^N (\varepsilon_{\alpha} \rho_{\alpha} \mathbf{u}_{\alpha} \otimes \mathbf{u}_{\alpha}) - \operatorname{div} \sum_{\alpha=1}^N (\varepsilon_{\alpha} \rho_{\alpha} \mathbf{u}_{\alpha}) \otimes \mathbf{x}' \\ &\quad + \sum_{\alpha=1}^N \hat{r}_{\alpha} \mathbf{u}_{\alpha} + \sum_{\alpha=1}^N \hat{r}_{\alpha} \mathbf{x}' + \sum_{\alpha=1}^N \varepsilon_{\alpha} \rho_{\alpha} \frac{D_{\alpha}(\mathbf{x}'_{\alpha})}{Dt} \end{aligned} \quad (\text{A.2.62})$$

The relation between the momentum for the whole mixture and the summation of the momentum of the phases is established in (A.2.62). The second divergence term in (A.2.62) is eliminated by the definition $\sum_{\alpha=1}^N (\varepsilon_{\alpha} \rho_{\alpha} \mathbf{u}_{\alpha}) = 0$ and it is shown by the compatible mass balance terms that $\sum_{\alpha=1}^N \hat{r}_{\alpha} = 0$. Furthermore, combining (A.2.62) and (A.2.54) reduces (A.2.62) to

$$\rho \frac{D(\mathbf{x}')}{Dt} = \operatorname{div} \sum_{\alpha=1}^N (\mathbf{T}_{\alpha} - \varepsilon_{\alpha} \rho_{\alpha} \mathbf{u}_{\alpha} \otimes \mathbf{u}_{\alpha}) + \rho \mathbf{b} + \sum_{\alpha=1}^N \hat{\mathbf{t}}_{\alpha} + \sum_{\alpha=1}^N \hat{r}_{\alpha} \mathbf{u}_{\alpha} \quad (\text{A.2.63})$$

Comparing (A.2.63) with (A.2.51) show that

$$\mathbf{T} = \sum_{\alpha=1}^N (\mathbf{T}_{\alpha} - \varepsilon_{\alpha} \rho_{\alpha} \mathbf{u}_{\alpha} \otimes \mathbf{u}_{\alpha}) \quad (\text{A.2.64})$$

and

$$\sum_{\alpha=1}^N \hat{\mathbf{t}}_{\alpha} + \sum_{\alpha=1}^N \hat{r}_{\alpha} \mathbf{u}_{\alpha} = 0 \quad (\text{A.2.65})$$

A.2.3 Angular momentum balance

The angular momentum is derived for the whole mixture in Sec. A.1.3, where it is shown that the stress tensor must be symmetric $\mathbf{T} = \mathbf{T}^T$ and also that the inner stress tensor must be symmetric $\mathbf{T}_{\mathbf{I}} = \mathbf{T}_{\mathbf{I}}^T$. Since the symmetry condition is deduced from the whole mixture, then it is directly transferable to the multi-phase and multi-species approach. The summation over the species yields

$$\sum_{j=1}^N \mathbf{M}_{\alpha_j} = \sum_{j=1}^N (\mathbf{T}_{\alpha_j} - \mathbf{T}_{\alpha_j}^T) = 0 \quad (\text{A.2.66})$$

and with summation over the phases yields

$$\sum_{\alpha=1}^N \sum_{j=1}^N \mathbf{M}_{\alpha_j} = \sum_{\alpha=1}^N \sum_{j=1}^N \left(\mathbf{T}_{\alpha_j} - \mathbf{T}_{\alpha_j}^T \right) = 0 \quad (\text{A.2.67})$$

A.2.4 Energy balance

Energy balance postulates are given in Sec. A.2.4.2 where compatible versions of the postulates between the whole mixture, the phases and the species are obtained. The compatible versions is deduced with help from, among other things, relations given in Sec. A.2.4.1.

A.2.4.1 Definitions for energy balances

The relation for summation of the external heat r_α and the inner internal energy $e_{\mathbf{I},\alpha}$ for the α phase is

$$r_\alpha = \frac{1}{\rho_\alpha} \sum_{j=1}^N \rho_{\alpha_j} r_{\alpha_j}; \quad e_{\mathbf{I},\alpha} = \frac{1}{\rho_\alpha} \sum_{j=1}^N \rho_{\alpha_j} e_{\alpha_j} \quad (\text{A.2.68})$$

The internal energy of the phase is related to the energy density e_α for the phase, as

$$e_\alpha = e_{\mathbf{I},\alpha} - \frac{1}{2\rho_\alpha} \sum_{j=1}^N \rho_{\alpha_j} (u_{\alpha_j})^2 \quad (\text{A.2.69})$$

where $(u_{\alpha_j})^2 = \mathbf{u}_{\alpha_j} \cdot \mathbf{u}_{\alpha_j}$.

The inner heat flux $\mathbf{q}_{\mathbf{I},\alpha}$ for the α phase is defined as

$$\mathbf{q}_{\mathbf{I},\alpha} = \sum_{j=1}^N \left(\mathbf{q}_{\alpha_j} - \mathbf{T}_{\alpha_j}^T \mathbf{u}_{\alpha_j} + \rho_{\alpha_j} e_{\alpha_j} \mathbf{u}_{\alpha_j} \right) \quad (\text{A.2.70})$$

which is related to the heat flux \mathbf{q}_α for the phase as

$$\mathbf{q}_\alpha = \mathbf{q}_{\mathbf{I},\alpha} + \frac{1}{2} \sum_{j=1}^N \rho_{\alpha_j} (u_{\alpha_j})^2 \mathbf{u}_{\alpha_j} \quad (\text{A.2.71})$$

A quantity \mathbf{k}_α related to the heat flux is introduced as

$$\begin{aligned}
\mathbf{k}_\alpha &= \sum_{j=1}^N (\mathbf{q}_{\alpha_j} + \rho_{\alpha_j} e_{\alpha_j} \mathbf{u}_{\alpha_j}) \\
&= \mathbf{q}_{\mathbf{I},\alpha} + \sum_{j=1}^N \mathbf{T}_{\alpha_j}^T \mathbf{u}_{\alpha_j} \\
&= \mathbf{q}_\alpha - \sum_{j=1}^N \rho_{\alpha_j} \left(-\frac{1}{\rho_{\alpha_j}} \mathbf{T}_{\alpha_j}^T + \frac{1}{2} (u_{\alpha_j})^2 \mathbf{I} \right) \mathbf{u}_{\alpha_j} \quad (\text{A.2.72})
\end{aligned}$$

Similar definitions is given for the whole mixture, The definition for the external heat r_α and the inner internal energy $e_{\mathbf{I},\alpha}$ for the whole mixture is given as

$$r = \frac{1}{\rho} \sum_{\alpha=1}^N \varepsilon_\alpha \rho_\alpha r_\alpha; \quad e_{\mathbf{I}} = \frac{1}{\rho} \sum_{\alpha=1}^N \varepsilon_\alpha \rho_\alpha e_\alpha \quad (\text{A.2.73})$$

The internal energy $e_{\mathbf{I}}$ is related to the energy density e the whole mixture as

$$e = e_{\mathbf{I}} - \frac{1}{2\rho} \sum_{\alpha=1}^N \varepsilon_\alpha \rho_\alpha (u_\alpha)^2 \quad (\text{A.2.74})$$

where $(u_\alpha)^2 = \mathbf{u}_\alpha \cdot \mathbf{u}_\alpha$.

The inner heat flux for the mixture is defined as

$$\mathbf{q}_{\mathbf{I}} = \sum_{\alpha=1}^N (\mathbf{q}_\alpha - \mathbf{T}_\alpha^T \mathbf{u}_\alpha + \varepsilon_\alpha \rho_\alpha e_\alpha \mathbf{u}_\alpha) \quad (\text{A.2.75})$$

which is related to the heat flux \mathbf{q} for the whole mixture as

$$\mathbf{q} = \mathbf{q}_{\mathbf{I}} + \frac{1}{2} \sum_{\alpha=1}^N \varepsilon_\alpha \rho_\alpha (u_\alpha)^2 \mathbf{u}_\alpha \quad (\text{A.2.76})$$

A quantity \mathbf{k} related to the heat flux \mathbf{q} is introduced as

$$\begin{aligned}
\mathbf{k} &= \sum_{\alpha=1}^N (\varepsilon_\alpha \mathbf{q}_\alpha + \varepsilon_\alpha \rho_\alpha e_\alpha \mathbf{u}_\alpha) \\
&= \mathbf{q}_{\mathbf{I}} + \sum_{\alpha=1}^N \mathbf{T}_\alpha^T \mathbf{u}_\alpha \\
&= \mathbf{q} - \sum_{j=1}^N \left(-\mathbf{T}_\alpha^T + \varepsilon_\alpha \rho_\alpha \frac{1}{2} (u_\alpha)^2 \mathbf{I} \right) \mathbf{u}_\alpha \quad (\text{A.2.77})
\end{aligned}$$

A.2.4.2 Energy balance for constituents

The energy balance postulate for the j 'th specie in the α phase is

$$\begin{aligned}
\frac{\partial}{\partial t} \int_{\Omega} \varepsilon_{\alpha} \rho_{\alpha_j} \left(e_{\alpha_j} + \frac{1}{2} \left(x'_{\alpha_j} \right)^2 \right) dv = & \\
& - \oint_{\partial\Omega} \varepsilon_{\alpha} \rho_{\alpha_j} \left(e_{\alpha_j} + \frac{1}{2} \left(x'_{\alpha_j} \right)^2 \right) \mathbf{x}'_{\alpha_j} \cdot d\mathbf{s} \\
& + \oint_{\partial\Omega} \varepsilon_{\alpha} \left(\mathbf{T}_{\alpha_j} \mathbf{x}'_{\alpha_j} - \mathbf{q}_{\alpha_j} \right) \cdot d\mathbf{s} \\
& + \int_{\Omega} \left[\varepsilon_{\alpha} \rho_{\alpha_j} r_{\alpha_j} + \varepsilon_{\alpha} \rho_{\alpha_j} \mathbf{x}'_{\alpha_j} \cdot \mathbf{b}_{\alpha_j} \right. \\
& \left. + \mathbf{x}'_{\alpha_j} \cdot \left(\hat{\mathbf{p}}_{\alpha_j} + \hat{\mathbf{t}}_{\alpha_j} \right) + \hat{e}_{\alpha_j} + \hat{Q}_{\alpha_j} \right] dv \\
& + \int_{\Omega} \hat{c}_{\alpha_j} \left(e_{\alpha_j} + \frac{1}{2} \left(x'_{\alpha_j} \right)^2 \right) dv \\
& + \int_{\Omega} \hat{r}_{\alpha_j} \left(e_{\alpha_j} + \frac{1}{2} \left(x'_{\alpha_j} \right)^2 \right) dv \quad (\text{A.2.78})
\end{aligned}$$

Using the mathematical operations similar to (A.1.86)-(A.1.98) yields the local form of the energy balance for the species, that is

$$\begin{aligned}
\varepsilon_{\alpha} \rho_{\alpha_j} \frac{D_{\alpha_j} e_{\alpha_j}}{Dt} = & \text{tr} \left(\varepsilon_{\alpha} \mathbf{T}_{\alpha_j} \mathbf{L}_{\alpha_j} \right) - \text{div} \left(\varepsilon_{\alpha} \mathbf{q}_{\alpha_j} \right) + \\
& + \mathbf{x}'_{\alpha_j} \cdot \left[\text{div} \left(\varepsilon_j \mathbf{T}_{\alpha_j} \right) + \varepsilon_{\alpha} \rho_{\alpha_j} \mathbf{b}_{\alpha_j} + \left(\hat{\mathbf{p}}_{\alpha_j} + \hat{\mathbf{t}}_{\alpha_j} \right) \right. \\
& \left. - \varepsilon_{\alpha} \rho_{\alpha_j} \frac{D_{\alpha_j} \mathbf{x}'_{\alpha_j}}{Dt} \right] + \varepsilon_{\alpha} \rho_{\alpha_j} r_{\alpha_j} + \hat{e}_{\alpha_j} + \hat{Q}_{\alpha_j} \quad (\text{A.2.79})
\end{aligned}$$

The momentum balance for the species is identified in the square brackets in (A.2.79) and cancels out. The reduced form of (A.2.79) is

$$\begin{aligned}
\varepsilon_{\alpha} \rho_{\alpha_j} \frac{D_{\alpha_j} e_{\alpha_j}}{Dt} = & \text{tr} \left(\varepsilon_{\alpha} \mathbf{T}_{\alpha_j} \mathbf{L}_{\alpha_j} \right) - \text{div} \left(\varepsilon_{\alpha} \mathbf{q}_{\alpha_j} \right) + \varepsilon_{\alpha} \rho_{\alpha_j} r_{\alpha_j} \\
& + \hat{e}_{\alpha_j} + \hat{Q}_{\alpha_j} \quad (\text{A.2.80})
\end{aligned}$$

The summation over the species of (A.2.80) where the definition (A.2.68)-(b) is used, is

$$\begin{aligned}
\varepsilon_{\alpha} \sum_{j=1}^N \rho_{\alpha_j} \frac{D_{\alpha_j} e_{\alpha_j}}{Dt} = & \text{tr} \sum_{j=1}^N \left(\varepsilon_{\alpha} \mathbf{T}_{\alpha_j} \mathbf{L}_{\alpha_j} \right) - \text{div} \sum_{j=1}^N \left(\varepsilon_{\alpha} \mathbf{q}_{\alpha_j} \right) + \varepsilon_{\alpha} \rho_{\alpha} r_{\alpha} \\
& + \sum_{j=1}^N \hat{e}_{\alpha_j} + \sum_{j=1}^N \hat{Q}_{\alpha_j} \quad (\text{A.2.81})
\end{aligned}$$

The left-hand side of (A.2.81) is the first term of the right-hand side of (A.2.43) with $\Gamma = e$. The summation of e_{α_j} over the species is (A.2.68) which is the internal energy of the phase $e_{\mathbf{I},\alpha}$, which change the notation of the left-hand side of (A.2.39) to $\Gamma_{\mathbf{I},\alpha}$ with $\Gamma = e$ and further into (A.2.43), which is

$$\begin{aligned} \varepsilon_\alpha \sum_{j=1}^N \rho_{\alpha_j} \frac{D_{\alpha_j} e_{\alpha_j}}{Dt} &= \varepsilon_\alpha \rho_\alpha \frac{D_\alpha e_{\mathbf{I},\alpha}}{Dt} + \operatorname{div} \sum_{j=1}^N (\varepsilon_\alpha \rho_{\alpha_j} e_{\alpha_j} \mathbf{u}_{\alpha_j}) \\ &\quad - \sum_{j=1}^N (\hat{r}_{\alpha_j} + \hat{c}_{\alpha_j} - c_{\alpha_j} \hat{r}_\alpha) e_{\alpha_j} \end{aligned} \quad (\text{A.2.82})$$

Combining (A.2.81) and (A.2.82) yields

$$\begin{aligned} \varepsilon_\alpha \rho_\alpha \frac{D_\alpha e_{\mathbf{I},\alpha}}{Dt} &= \operatorname{tr} \sum_{j=1}^N (\varepsilon_\alpha \mathbf{T}_{\alpha_j} \mathbf{L}_{\alpha_j}) - \operatorname{div} \sum_{j=1}^N (\varepsilon_\alpha \mathbf{q}_{\alpha_j}) + \varepsilon_\alpha \rho_\alpha r_\alpha \\ &\quad + \sum_{j=1}^N \hat{e}_{\alpha_j} + \sum_{j=1}^N \hat{Q}_{\alpha_j} - \operatorname{div} \sum_{j=1}^N (\varepsilon_\alpha \rho_{\alpha_j} e_{\alpha_j} \mathbf{u}_{\alpha_j}) \\ &\quad + \sum_{j=1}^N (\hat{r}_{\alpha_j} + \hat{c}_{\alpha_j} - c_{\alpha_j} \hat{r}_\alpha) e_{\alpha_j} \end{aligned} \quad (\text{A.2.83})$$

where \mathbf{k}_α is identified by combining the divergence terms and (A.2.83) reduces to

$$\begin{aligned} \varepsilon_\alpha \rho_\alpha \frac{D_\alpha e_{\mathbf{I},\alpha}}{Dt} &= \operatorname{tr} \sum_{j=1}^N (\varepsilon_\alpha \mathbf{T}_{\alpha_j} \mathbf{L}_{\alpha_j}) - \operatorname{div} (\varepsilon_\alpha \mathbf{k}_\alpha) + \varepsilon_\alpha \rho_\alpha r_\alpha + \sum_{j=1}^N \hat{e}_{\alpha_j} + \sum_{j=1}^N \hat{Q}_{\alpha_j} \\ &\quad + \sum_{j=1}^N (\hat{r}_{\alpha_j} + \hat{c}_{\alpha_j} - c_{\alpha_j} \hat{r}_\alpha) e_{\alpha_j} \end{aligned} \quad (\text{A.2.84})$$

In the following, the energy balance postulate for the α phase is brought to a form, which is compatible with (A.2.84). The postulate for the energy

balance for the α phase is

$$\begin{aligned}
\frac{\partial}{\partial t} \int_{\Omega} \varepsilon_{\alpha} \rho_{\alpha} (e_{\alpha} + \frac{1}{2} (x'_{\alpha})^2) dv &= - \oint_{\partial\Omega} \varepsilon_{\alpha} \rho_{\alpha} (e_{\alpha} + \frac{1}{2} (x'_{\alpha})^2) \mathbf{x}'_{\alpha} \cdot d\mathbf{s} + \\
&+ \oint_{\partial\Omega} \varepsilon_{\alpha} (\mathbf{T}_{\alpha} \mathbf{x}'_{\alpha} - \mathbf{q}_{\alpha}) \cdot d\mathbf{s} + \\
&+ \int_{\Omega} [\varepsilon_{\alpha} \rho_{\alpha} r_{\alpha} + \varepsilon_{\alpha} \rho_{\alpha} \mathbf{x}'_{\alpha} \cdot \mathbf{b}_{\alpha} + \\
&+ \mathbf{x}'_{\alpha} \cdot \hat{\mathbf{t}}_{\alpha} + \hat{Q}_{\alpha}] dv + \\
&+ \int_{\Omega} \hat{r}_{\alpha} (e_{\alpha} + \frac{1}{2} (x'_{\alpha})^2) dv \quad (\text{A.2.85})
\end{aligned}$$

Using the divergence theorem on the first and second term on the right-hand side and rewrite the left-hand side by mathematical steps similar to (A.1.86)-(A.1.96), yields a reduced local form of (A.2.81) as

$$\begin{aligned}
\varepsilon_{\alpha} \rho_{\alpha} \frac{D_{\alpha}}{Dt} (e_{\alpha} + \frac{1}{2} (x'_{\alpha})^2) &= \operatorname{div} (\varepsilon_{\alpha} (\mathbf{T}_{\alpha} \mathbf{x}'_{\alpha} - \mathbf{q}_{\alpha})) + \varepsilon_{\alpha} \rho_{\alpha} r_{\alpha} \\
&+ \varepsilon_{\alpha} \rho_{\alpha} \mathbf{x}'_{\alpha} \cdot \mathbf{b}_{\alpha} + \mathbf{x}'_{\alpha} \cdot \hat{\mathbf{t}}_{\alpha} + \hat{Q}_{\alpha} \quad (\text{A.2.86})
\end{aligned}$$

Note that the momentum balance for the α phase has not been identified in (A.2.86). The left-hand side of (A.2.86), where the velocity term is written by its definition $(x'_{\alpha})^2 = \mathbf{x}'_{\alpha} \cdot \mathbf{x}'_{\alpha}$ and expanded by the product rule is

$$\varepsilon_{\alpha} \rho_{\alpha} \frac{D_{\alpha} e_{\alpha}}{Dt} + \varepsilon_{\alpha} \rho_{\alpha} \frac{D_{\alpha}}{Dt} (\frac{1}{2} \mathbf{x}'_{\alpha} \cdot \mathbf{x}'_{\alpha}) = \varepsilon_{\alpha} \rho_{\alpha} \frac{D_{\alpha}}{Dt} e_{\alpha} + \varepsilon_{\alpha} \rho_{\alpha} \mathbf{x}'_{\alpha} \cdot \frac{D_{\alpha} \mathbf{x}'_{\alpha}}{Dt} \quad (\text{A.2.87})$$

The first part of divergence term on the right-hand side of (A.2.86), expanded by the product rule and using the definition of the velocity gradient, $\mathbf{L}_{\alpha} = \operatorname{grad}(\mathbf{x}'_{\alpha})$, is

$$\operatorname{div} (\varepsilon_{\alpha} \mathbf{T}_{\alpha} \mathbf{x}'_{\alpha}) = \mathbf{x}'_{\alpha} \cdot \operatorname{div} (\varepsilon_{\alpha} \mathbf{T}_{\alpha}) + \varepsilon_{\alpha} \operatorname{tr} (\mathbf{T}_{\alpha} \mathbf{L}_{\alpha}) \quad (\text{A.2.88})$$

The third term in (A.2.86), expressed in terms of the phase velocity and the diffusion velocity (A.2.5)-(a), is

$$\sum_{j=1}^N \varepsilon_{\alpha} \rho_{\alpha_j} \mathbf{x}'_{\alpha_j} \cdot \mathbf{b}_{\alpha_j} = \sum_{j=1}^N \varepsilon_{\alpha} \rho_{\alpha_j} (\mathbf{u}_{\alpha_j} + \mathbf{x}'_{\alpha}) \cdot \mathbf{b}_{\alpha_j} \quad (\text{A.2.89})$$

It is shown in (A.2.37) that summation over the species of the body force \mathbf{b}_{α_j} yields the body force of the phase \mathbf{b}_{α} . Using this condition with (A.2.89) results in

$$\sum_{j=1}^N \varepsilon_{\alpha} \rho_{\alpha_j} (\mathbf{u}_{\alpha_j} + \mathbf{x}'_{\alpha}) \cdot \mathbf{b}_{\alpha_j} = \varepsilon_{\alpha} \rho_{\alpha} \mathbf{b}_{\alpha} \cdot \mathbf{x}'_{\alpha} + \varepsilon_{\alpha} \sum_{j=1}^N \rho_{\alpha_j} \mathbf{u}_{\alpha_j} \cdot \mathbf{b}_{\alpha_j} \quad (\text{A.2.90})$$

The three rewritten terms (A.2.87), (A.2.88) and (A.2.90) substituted into (A.2.86), yields

$$\begin{aligned} \varepsilon_\alpha \rho_\alpha \frac{D_\alpha}{Dt} e_\alpha &= -\mathbf{x}'_\alpha \cdot \left[\varepsilon_\alpha \rho_\alpha \frac{D_\alpha \mathbf{x}'_\alpha}{Dt} + \operatorname{div} (\varepsilon_\alpha \mathbf{T}_\alpha) + \varepsilon_\alpha \rho_\alpha \mathbf{b}_\alpha + \hat{\mathbf{t}}_\alpha \right] \\ &\quad + \varepsilon_\alpha \operatorname{tr} (\mathbf{T}_\alpha \mathbf{L}_\alpha) - \operatorname{div} (\varepsilon_\alpha \mathbf{q}_\alpha) + \varepsilon_\alpha \rho_\alpha r_\alpha \\ &\quad + \varepsilon_\alpha \sum_{j=1}^N \rho_{\alpha_j} \mathbf{u}_{\alpha_j} \cdot \mathbf{b}_{\alpha_j} + \hat{Q}_\alpha \end{aligned} \quad (\text{A.2.91})$$

where the momentum balance for the α phase is identified in the square brackets which reduces (A.2.91) to

$$\begin{aligned} \varepsilon_\alpha \rho_\alpha \frac{D_\alpha e_\alpha}{Dt} &= \varepsilon_\alpha \operatorname{tr} (\mathbf{T}_\alpha \mathbf{L}_\alpha) - \operatorname{div} (\varepsilon_\alpha \mathbf{q}_\alpha) + \varepsilon_\alpha \rho_\alpha r_\alpha \\ &\quad + \varepsilon_\alpha \sum_{j=1}^N \rho_{\alpha_j} \mathbf{u}_{\alpha_j} \cdot \mathbf{b}_{\alpha_j} + \hat{Q}_\alpha \end{aligned} \quad (\text{A.2.92})$$

The reduced energy balance written in terms of the definitions (A.2.48), (A.2.69) and (A.2.71), is

$$\begin{aligned} \frac{\varepsilon_\alpha \rho_\alpha}{2} \sum_{j=1}^N \frac{D_\alpha}{Dt} \left(c_{\alpha_j} (u_{\alpha_j})^2 \right) &= \varepsilon_\alpha \operatorname{tr} \left(\left(\mathbf{T}_{\mathbf{I},\alpha} - \sum_{j=1}^N (\rho_{\alpha_j} \mathbf{u}'_{\alpha_j} \otimes \mathbf{u}_{\alpha_j}) \right) \mathbf{L}_\alpha \right) \\ &\quad - \operatorname{div} \left(\varepsilon_\alpha \left(\mathbf{q}_{\mathbf{I},\alpha} + \frac{1}{2} \sum_{j=1}^N \rho_{\alpha_j} (u_{\alpha_j})^2 \mathbf{u}_{\alpha_j} \right) \right) \\ &\quad + \varepsilon_\alpha \rho_\alpha r_\alpha + \varepsilon_\alpha \sum_{j=1}^N \rho_{\alpha_j} \mathbf{u}_{\alpha_j} \cdot \mathbf{b}_{\alpha_j} + \hat{Q}_\alpha \end{aligned} \quad (\text{A.2.93})$$

It is convenient to rewrite the left-hand side by considering (A.2.43) with $\Gamma = \frac{1}{2} (u)^2$, which results in

$$\begin{aligned} \frac{\varepsilon_\alpha \rho_\alpha}{2} \sum_{j=1}^N \frac{D_\alpha}{Dt} \left(c_{\alpha_j} (u_{\alpha_j})^2 \right) &= \sum_{j=1}^N \left[\varepsilon_\alpha \rho_{\alpha_j} \frac{D_{\alpha_j} \frac{1}{2} (u_{\alpha_j})^2}{Dt} \right. \\ &\quad \left. - \operatorname{div} \left(\varepsilon_\alpha \rho_{\alpha_j} \frac{1}{2} (u_{\alpha_j})^2 \mathbf{u}_{\alpha_j} \right) \right. \\ &\quad \left. + \frac{1}{2} (u_{\alpha_j})^2 (\hat{r}_{\alpha_j} + \hat{c}_{\alpha_j} - c_{\alpha_j} \hat{r}_\alpha) \right] \end{aligned} \quad (\text{A.2.94})$$

where the left-hand side of (A.2.133) is written as a summation, according to (A.2.39). The first term in the square brackets, expanded by the definitions $u_{\alpha_j} = \mathbf{u}_{\alpha_j} \cdot \mathbf{u}_{\alpha_j}$ and $\mathbf{u}_{\alpha_j} = \mathbf{x}'_{\alpha_j} - \mathbf{x}'_{\alpha}$ are

$$\varepsilon_{\alpha} \rho_{\alpha_j} \frac{D_{\alpha_j} \frac{1}{2} (u_{\alpha_j})^2}{Dt} = \varepsilon_{\alpha} \rho_{\alpha_j} \mathbf{u}_{\alpha_j} \cdot \frac{D_{\alpha_j} \mathbf{u}_{\alpha_j}}{Dt} \quad (\text{A.2.95})$$

$$= \varepsilon_{\alpha} \rho_{\alpha_j} \mathbf{u}_{\alpha_j} \cdot \frac{D_{\alpha_j}}{Dt} (\mathbf{x}'_{\alpha_j} - \mathbf{x}'_{\alpha}) \quad (\text{A.2.96})$$

Consider now (A.2.6)-(a) with $\Gamma = \mathbf{x}'$, where the last differential term in (A.2.96) and the definition $\mathbf{L}_{\alpha} = \text{grad}(\mathbf{x}'_{\alpha})$ is used, this yields

$$\begin{aligned} \varepsilon_{\alpha} \rho_{\alpha_j} \mathbf{u}_{\alpha_j} \cdot \frac{D_{\alpha_j}}{Dt} (\mathbf{x}'_{\alpha_j} - \mathbf{x}'_{\alpha}) &= \varepsilon_{\alpha} \rho_{\alpha_j} \mathbf{u}_{\alpha_j} \cdot \left(\frac{D_{\alpha_j} \mathbf{x}'_{\alpha_j}}{Dt} - \frac{D_{\alpha} \mathbf{x}'_{\alpha}}{Dt} - \text{grad}(\mathbf{x}'_{\alpha}) \mathbf{u}_{\alpha_j} \right) \\ &= \varepsilon_{\alpha} \rho_{\alpha_j} \mathbf{u}_{\alpha_j} \cdot \left(\frac{D_{\alpha_j} \mathbf{x}'_{\alpha_j}}{Dt} - \frac{D_{\alpha} \mathbf{x}'_{\alpha}}{Dt} - \mathbf{L}_{\alpha} \mathbf{u}_{\alpha_j} \right) \end{aligned} \quad (\text{A.2.97})$$

The last term in (A.2.97) is rewritten to obtain

$$\varepsilon_{\alpha} \rho_{\alpha_j} \mathbf{u}_{\alpha_j} \cdot \mathbf{L}_{\alpha} \mathbf{u}_{\alpha_j} = \varepsilon_{\alpha} \text{tr}(\rho_{\alpha_j} \mathbf{L}_{\alpha} (\mathbf{u}_{\alpha_j} \otimes \mathbf{u}_{\alpha_j})) \quad (\text{A.2.98})$$

Combining (A.2.98) and (A.2.97) and inserting (A.2.97) into (A.2.133), yields

$$\begin{aligned} \varepsilon_{\alpha} \rho_{\alpha} \sum_{j=1}^N \frac{1}{2} \frac{D_{\alpha}}{Dt} (c_{\alpha_j} (u_{\alpha_j})^2) &= \sum_{j=1}^N \left[\varepsilon_{\alpha} \rho_{\alpha_j} \mathbf{u}_{\alpha_j} \cdot \frac{D_{\alpha_j} \mathbf{x}'_{\alpha_j}}{Dt} - \varepsilon_{\alpha} \rho_{\alpha_j} \mathbf{u}_{\alpha_j} \cdot \frac{D_{\alpha} \mathbf{x}'_{\alpha}}{Dt} \right. \\ &\quad - \varepsilon_{\alpha} \text{tr}(\rho_{\alpha_j} \mathbf{L}_{\alpha} (\mathbf{u}_{\alpha_j} \otimes \mathbf{u}_{\alpha_j})) \\ &\quad - \text{div} \left(\varepsilon_{\alpha} \rho_{\alpha_j} \frac{1}{2} (u_{\alpha_j})^2 \mathbf{u}_{\alpha_j} \right) \\ &\quad \left. + \frac{1}{2} (u_{\alpha_j})^2 (\hat{r}_{\alpha_j} + \hat{c}_{\alpha_j} - c_{\alpha_j} \hat{r}_{\alpha}) \right] \end{aligned} \quad (\text{A.2.99})$$

The second term in the square brackets in (A.2.99) cancels due to the condition $\sum_{j=1}^N \rho_{\alpha_j} \mathbf{u}_{\alpha_j} = 0$.

The second term of the left-hand side of (A.2.93) is (A.2.99) and combining these yields

$$\begin{aligned} \varepsilon_{\alpha} \rho_{\alpha} \frac{D_{\alpha} e_{\mathbf{I},\alpha}}{Dt} &= \varepsilon_{\alpha} \text{tr}(\mathbf{T}_{\mathbf{I},\alpha} \mathbf{L}_{\alpha}) - \text{div}(\varepsilon_{\alpha} \mathbf{q}_{\mathbf{I},\alpha}) + \varepsilon_{\alpha} \rho_{\alpha} r_{\alpha} + \hat{Q}_{\alpha} \\ &\quad - \sum_{j=1}^N \frac{1}{2} (u_{\alpha_j})^2 (\hat{r}_{\alpha_j} + \hat{c}_{\alpha_j} - c_{\alpha_j} \hat{r}_{\alpha}) \\ &\quad - \sum_{j=1}^N \varepsilon_{\alpha} \mathbf{u}_{\alpha_j} \cdot \left(\rho_{\alpha_j} \frac{D_{\alpha_j} \mathbf{x}'_{\alpha_j}}{Dt} - \rho_{\alpha_j} \mathbf{b}_{\alpha_j} \right) \end{aligned} \quad (\text{A.2.100})$$

Consider the term $\text{tr} \left(\mathbf{T}_{\alpha_j}^T \mathbf{L}_{\alpha_j} \right)$ in (A.2.100) written by the definition $\mathbf{L}_{\alpha_j} = \text{grad}(\mathbf{x}'_\alpha)$ and the diffusion velocity \mathbf{u}_{α_j} , as

$$\begin{aligned} \text{tr} \sum_{j=1}^N \left(\mathbf{T}_{\alpha_j}^T \mathbf{L}_{\alpha_j} \right) &= \text{tr} \sum_{j=1}^N \left(\mathbf{T}_{\alpha_j}^T \text{grad}(\mathbf{u}_{\alpha_j} + \mathbf{x}'_\alpha) \right) \\ &= \text{tr} \sum_{j=1}^N \left(\mathbf{T}_{\alpha_j}^T \text{grad} \mathbf{u}_{\alpha_j} \right) + \text{tr} \sum_{j=1}^N \left(\mathbf{T}_{\alpha_j}^T \text{grad} \mathbf{x}'_\alpha \right) \\ &= \text{tr} \sum_{j=1}^N \left(\mathbf{T}_{\alpha_j}^T \text{grad} \mathbf{u}_{\alpha_j} \right) + \text{tr} \sum_{j=1}^N \left(\mathbf{T}_{\alpha_j} \mathbf{L}_\alpha \right) \quad (\text{A.2.101}) \end{aligned}$$

Furthermore, the first term on the right-hand side is

$$\text{tr} \sum_{j=1}^N \left(\mathbf{T}_{\alpha_j}^T \text{grad} \mathbf{u}_{\alpha_j} \right) = \text{div} \sum_{j=1}^N \left(\mathbf{T}_{\alpha_j}^T \mathbf{u}_{\alpha_j} \right) - \sum_{j=1}^N \mathbf{u}_{\alpha_j} \cdot \text{div} \mathbf{T}_{\alpha_j} \quad (\text{A.2.102})$$

Combining (A.2.102) and (A.2.101) and inserting into (A.2.100), yields

$$\begin{aligned} \varepsilon_\alpha \rho_\alpha \frac{D_\alpha e_{\mathbf{I},\alpha}}{Dt} &= \varepsilon_\alpha \left(\text{div} \sum_{j=1}^N \left(\mathbf{T}_{\alpha_j}^T \mathbf{u}_{\alpha_j} \right) - \text{div} \sum_{j=1}^N \left(\mathbf{T}_{\alpha_j} \mathbf{u}_{\alpha_j} \right) \right) - \text{div}(\varepsilon_\alpha \mathbf{q}_{\mathbf{I},\alpha}) \\ &\quad - \sum_{j=1}^N \varepsilon_\alpha \mathbf{u}_{\alpha_j} \cdot \left(\rho_{\alpha_j} \frac{D_{\alpha_j} \mathbf{x}'_{\alpha_j}}{Dt} - \rho_{\alpha_j} \mathbf{b}_{\alpha_j} - \text{div} \mathbf{T}_{\alpha_j} \right) \\ &\quad - \sum_{j=1}^N \frac{1}{2} (u_{\alpha_j})^2 (\hat{r}_{\alpha_j} + \hat{c}_{\alpha_j} - c_{\alpha_j} \hat{r}_\alpha) \\ &\quad + \varepsilon_\alpha \rho_\alpha r_\alpha + \hat{Q}_\alpha \quad (\text{A.2.103}) \end{aligned}$$

where the momentum balance for the constituent is identified and using, further, (A.2.72) in (A.2.103) in order to obtain

$$\begin{aligned} \varepsilon_\alpha \rho_\alpha \frac{D_\alpha e_{\mathbf{I},\alpha}}{Dt} &= \varepsilon_\alpha \text{div} \sum_{j=1}^N \left(\mathbf{T}_{\alpha_j}^T \mathbf{u}_{\alpha_j} \right) - \text{div}(\varepsilon_\alpha \mathbf{k}_\alpha) + \varepsilon_\alpha \rho_\alpha r_\alpha + \hat{Q}_\alpha \\ &\quad - \sum_{j=1}^N \frac{1}{2} (u_{\alpha_j})^2 (\hat{r}_{\alpha_j} + \hat{c}_{\alpha_j} - c_{\alpha_j} \hat{r}_\alpha) \\ &\quad - \sum_{j=1}^N \mathbf{u}_{\alpha_j} \cdot (\hat{\mathbf{t}}_{\alpha_j} + \hat{\mathbf{p}}_{\alpha_j}) \quad (\text{A.2.104}) \end{aligned}$$

Compatible versions of the energy balance are obtained in (A.2.104) and (A.2.84), where a comparison show that

$$\begin{aligned} \hat{Q}_\alpha &= \sum_{j=1}^N \left(\hat{e}_{\alpha_j} + \hat{Q}_{\alpha_j} + \mathbf{u}_{\alpha_j} \cdot (\hat{\mathbf{t}}_{\alpha_j} + \hat{\mathbf{p}}_{\alpha_j}) \right. \\ &\quad \left. + \left(e_\alpha + (u_{\alpha_j})^2 \right) (\hat{r}_{\alpha_j} + \hat{c}_{\alpha_j} - c_{\alpha_j} \hat{r}_\alpha) \right) \end{aligned} \quad (\text{A.2.105})$$

Similar to the derived mass balance and momentum balance equations, one can compare a summation of the phases with the whole mixture to reach a restriction for $\sum_{j=1}^N \hat{Q}_\alpha$. The comparison is established by similar mathematical steps as for the species. Here the calculation steps are shown in less detailed fashion compared to the species level.

Consider the energy balance postulate for phases (A.2.86), with (A.1.97) and (A.1.98), where the j is substituted by α , written as

$$\begin{aligned} \varepsilon_\alpha \rho_\alpha \frac{D_\alpha e_\alpha}{Dt} &= \text{tr} \left(\varepsilon_\alpha \mathbf{T}_\alpha^T \mathbf{L}_\alpha \right) - \text{div} (\varepsilon_\alpha \mathbf{q}_\alpha) + \varepsilon_\alpha \rho_\alpha r_\alpha + \hat{Q}_\alpha \\ &\quad + \mathbf{x}'_\alpha \cdot \left[\text{div} (\varepsilon_\alpha \mathbf{T}_\alpha) + \varepsilon_\alpha \rho_\alpha \mathbf{b}_\alpha + \hat{\mathbf{t}}_\alpha - \varepsilon_\alpha \rho_\alpha \frac{D_\alpha \mathbf{x}'_\alpha}{Dt} \right] \end{aligned} \quad (\text{A.2.106})$$

The momentum balance for the phases is identified and reduces (A.2.106) to

$$\varepsilon_\alpha \rho_\alpha \frac{D_\alpha e_\alpha}{Dt} = \text{tr} \left(\varepsilon_\alpha \mathbf{T}_\alpha^T \mathbf{L}_\alpha \right) - \text{div} (\varepsilon_\alpha \mathbf{q}_\alpha) + \varepsilon_\alpha \rho_\alpha r_\alpha + \hat{Q}_\alpha \quad (\text{A.2.107})$$

Summation over the phases of (A.2.107), together with (A.2.77) and (A.2.61) using $\Gamma = e$ (note for this case that the left-hand side of (A.2.61) is $e_{\mathbf{I}}$ due to (A.2.73)-(b)), yields

$$\begin{aligned} \rho \frac{D e_{\mathbf{I}}}{Dt} &= -\text{div} (\mathbf{k}) + \text{tr} \sum_{\alpha=1}^N \left(\varepsilon_\alpha \mathbf{T}_\alpha^T \mathbf{L}_\alpha \right) + \sum_{\alpha=1}^N (\varepsilon_\alpha \rho_\alpha r_\alpha + e_\alpha \hat{r}_\alpha) \\ &\quad + \sum_{\alpha=1}^N \hat{Q}_\alpha \end{aligned} \quad (\text{A.2.108})$$

Consider now the energy balance postulate for the whole mixture

$$\begin{aligned} \frac{\partial}{\partial t} \int_\Omega \left(e + \frac{1}{2} (x')^2 \right) dv &= - \oint_{\partial\Omega} \left(e + \frac{1}{2} (x')^2 \right) \mathbf{x}' \cdot d\mathbf{s} + \oint_{\partial\Omega} (\mathbf{T} \mathbf{x}' - \mathbf{q}) \cdot d\mathbf{s} \\ &\quad + \int_\Omega \left[\rho r + \sum_{\alpha=1}^N (\varepsilon_\alpha \rho_\alpha \mathbf{x}'_\alpha \cdot \mathbf{b}_\alpha) \right] dv \end{aligned} \quad (\text{A.2.109})$$

where the body force \mathbf{b}_α is written as the sum of phases which is used later. Using the divergence theorem, together with similar mathematical steps as shown in (A.1.89) to (A.1.96), yields the local energy balance postulate for the whole mixture, as

$$\rho \frac{D}{Dt} \left(e + \frac{1}{2} (x')^2 \right) = \operatorname{div} (\mathbf{T}\mathbf{x}' - \mathbf{q}) + \rho r + \sum_{\alpha=1}^N (\varepsilon_\alpha \rho_\alpha \mathbf{x}'_\alpha \cdot \mathbf{b}_\alpha) \quad (\text{A.2.110})$$

The left-hand side of (A.2.110) is rewritten with the definition $(x')^2 = \mathbf{x}' \cdot \mathbf{x}'$ as

$$\rho \frac{D}{Dt} \left(e + \frac{1}{2} (x')^2 \right) = \rho \frac{De}{Dt} + \rho \mathbf{x}' \cdot \frac{D\mathbf{x}'}{Dt} \quad (\text{A.2.111})$$

The first divergence term on right-hand side of (A.2.110) with the definition $\mathbf{L} = \operatorname{grad}(\mathbf{x}')$, is

$$\operatorname{div} (\mathbf{T}\mathbf{x}') = \mathbf{x}' \cdot \operatorname{div} (\mathbf{T}) + \operatorname{tr} (\mathbf{T}\mathbf{L}) \quad (\text{A.2.112})$$

The last term on right-hand side of (A.2.110) using the diffusion velocity of the phases (A.2.5) and summation over the phases of the body force (A.2.53), is

$$\sum_{\alpha=1}^N (\varepsilon_\alpha \rho_\alpha \mathbf{x}'_\alpha \cdot \mathbf{b}_\alpha) = \rho \mathbf{b} + \sum_{\alpha=1}^N (\varepsilon_\alpha \rho_\alpha \mathbf{u}_\alpha \cdot \mathbf{b}_\alpha) \quad (\text{A.2.113})$$

Combining (A.2.111), (A.2.112) and (A.2.113) with (A.2.110) show that the momentum balance for the mixture (A.2.51) is identified and reduces (A.2.110) to the following expression

$$\rho \frac{De}{Dt} = \operatorname{tr} (\mathbf{T}\mathbf{L}) + \rho r - \operatorname{div} (\mathbf{q}) + \sum_{\alpha=1}^N (\varepsilon_\alpha \rho_\alpha \mathbf{u}_\alpha \cdot \mathbf{b}_\alpha) \quad (\text{A.2.114})$$

The equation (A.2.114) written in terms of the definitions (A.2.74), (A.2.76) and the results from the momentum balance (A.2.64) is

$$\begin{aligned} \rho \frac{De_{\mathbf{I}}}{Dt} - \frac{1}{2} \frac{D}{Dt} \left(\sum_{\alpha=1}^N \varepsilon_\alpha \rho_\alpha (u_\alpha)^2 \right) &= \operatorname{tr} \left(\left(\mathbf{T}_{\mathbf{I}} - \sum_{\alpha=1}^N \varepsilon_\alpha \rho_\alpha \mathbf{u}_\alpha \otimes \mathbf{u}_\alpha \right) \mathbf{L} \right) \\ &+ \rho r - \operatorname{div} \left(\mathbf{q}_{\mathbf{I}} + \frac{1}{2} \sum_{\alpha=1}^N \varepsilon_\alpha \rho_\alpha (u_\alpha)^2 \mathbf{u}_\alpha \right) \\ &+ \sum_{\alpha=1}^N (\varepsilon_\alpha \rho_\alpha \mathbf{u}_\alpha \cdot \mathbf{b}_\alpha) \end{aligned} \quad (\text{A.2.115})$$

It is convenient to rewrite the second term on the left-hand side of (A.2.115). The approach is similar to the mathematical steps taken from (A.2.133) to

(A.2.99), using the diffusion velocity and the property definitions for the phases and mixture. The left-hand side of (A.2.115) is

$$\begin{aligned} \frac{1}{2} \frac{D}{Dt} \left(\sum_{\alpha=1}^N \varepsilon_{\alpha} \rho_{\alpha} (u_{\alpha})^2 \right) &= -\text{tr} \sum_{\alpha=1}^N (\varepsilon_{\alpha} \rho_{\alpha} \mathbf{L} \mathbf{u}_{\alpha} \otimes \mathbf{u}_{\alpha}) + \frac{1}{2} \sum_{\alpha=1}^N \hat{r}_{\alpha} (u_{\alpha})^2 \\ &+ \sum_{\alpha=1}^N \varepsilon_{\alpha} \rho_{\alpha} \mathbf{u}_{\alpha} \cdot \frac{D_{\alpha} \mathbf{x}'_{\alpha}}{Dt} - \sum_{\alpha=1}^N \varepsilon_{\alpha} \rho_{\alpha} \mathbf{u}_{\alpha} \cdot \frac{D \mathbf{x}'}{Dt} \\ &- \text{div} \left(\frac{1}{2} \sum_{\alpha=1}^N \varepsilon_{\alpha} \rho_{\alpha} (u_{\alpha})^2 \mathbf{u}_{\alpha} \right) \end{aligned} \quad (\text{A.2.116})$$

Inserting (A.2.116) into (A.2.115) and using that $\sum_{\alpha=1}^N \varepsilon_{\alpha} \rho_{\alpha} \mathbf{u}_{\alpha} = 0$, yields

$$\begin{aligned} \rho \frac{D e_{\mathbf{I}}}{Dt} &= \text{tr}(\mathbf{T}_{\mathbf{I}} \mathbf{L}) + \rho r - \text{div}(\mathbf{q}_{\mathbf{I}}) + \sum_{\alpha=1}^N (\varepsilon_{\alpha} \rho_{\alpha} \mathbf{u}_{\alpha} \cdot \mathbf{b}_{\alpha}) \\ &+ \sum_{\alpha=1}^N \varepsilon_{\alpha} \rho_{\alpha} \mathbf{u}_{\alpha} \cdot \frac{D_{\alpha} \mathbf{x}'_{\alpha}}{Dt} + \frac{1}{2} \sum_{\alpha=1}^N \hat{r}_{\alpha} (u_{\alpha})^2 \end{aligned} \quad (\text{A.2.117})$$

The first term on the right-hand side written by an expression similar to (A.2.101) and (A.2.102) summed over the phases. Inserting this into (A.2.117) show that the momentum balance (A.2.54) for the phases is identified and (A.2.117) reduces to

$$\begin{aligned} \rho \frac{D e_{\mathbf{I}}}{Dt} &= \text{tr} \sum_{\alpha=1}^N (\varepsilon_{\alpha} \mathbf{T}_{\alpha}^{\text{T}} \mathbf{L}_{\alpha}) + \rho r - \text{div}(\mathbf{k}) + \sum_{\alpha=1}^N (\varepsilon_{\alpha} \rho_{\alpha} \mathbf{u}_{\alpha} \cdot \mathbf{b}_{\alpha}) \\ &+ \sum_{\alpha=1}^N \mathbf{u}_{\alpha} \cdot \hat{\mathbf{t}}_{\alpha} + \frac{1}{2} \sum_{\alpha=1}^N \hat{r}_{\alpha} (u_{\alpha})^2 \end{aligned} \quad (\text{A.2.118})$$

where also the definition (A.2.77) is used.

It is now possible to compare (A.2.118) which is the re-written version of the energy balance for the whole mixture and the energy balance for the phases (A.2.108). The comparison yields the restriction for the phases to be

$$\sum_{\alpha=1}^N \left(\hat{Q}_{\alpha} + \mathbf{u}_{\alpha} \cdot \hat{\mathbf{t}}_{\alpha} + \hat{r}_{\alpha} \left(e_{\alpha} + \frac{1}{2} (u_{\alpha})^2 \right) \right) = 0 \quad (\text{A.2.119})$$

A.2.5 Entropy inequality

Different versions of the entropy inequality are considered in Sec. A.2.5. One postulate is considered for the case with multiple phases and species. The

second axiom postulate used in HMT, is

$$\begin{aligned} \frac{\partial}{\partial t} \int_{\Omega} \varepsilon_{\alpha} \rho_{\alpha} \eta_{\alpha} dv &\geq - \oint_{\partial\Omega} \varepsilon_{\alpha} \sum_{j=1}^{\mathcal{R}} \rho_{\alpha_j} \eta_{\alpha_j} \mathbf{x}'_{\alpha_j} \cdot d\mathbf{s} - \oint_{\partial\Omega} \varepsilon_{\alpha} \sum_{j=1}^{\mathcal{R}} \left(\frac{1}{\theta} \mathbf{q}_{\alpha_j} \right) \cdot d\mathbf{s} \\ &+ \oint_{\Omega} \varepsilon_{\alpha} \sum_{j=1}^{\mathcal{R}} \left(\frac{1}{\theta} \rho_{\alpha_j} r_{\alpha_j} \right) dv \end{aligned} \quad (\text{A.2.120})$$

which is an extended version of (A.1.143). The entropy for multiple phases is the summation given as

$$\eta_{\alpha} = \frac{1}{\rho} \sum_{j=1}^N \rho_{\alpha_j} \eta_{\alpha_j} = \sum_{j=1}^N c_{\alpha_j} \eta_{\alpha_j}$$

The local form of (A.2.120), obtained by using the divergence theorem, is

$$\begin{aligned} \frac{\partial}{\partial t} (\varepsilon_{\alpha} \rho_{\alpha} \eta_{\alpha}) &\geq -\text{div} \left(\sum_{j=1}^N \varepsilon_{\alpha} \rho_{\alpha_j} \eta_{\alpha_j} \mathbf{x}'_{\alpha_j} \right) - \text{div} \left(\varepsilon_{\alpha} \sum_{j=1}^N \frac{1}{\theta} \mathbf{q}_{\alpha_j} \right) \\ &+ \varepsilon_{\alpha} \sum_{j=1}^N \left(\frac{1}{\theta} \rho_{\alpha_j} r_{\alpha_j} \right) \end{aligned} \quad (\text{A.2.121})$$

Using the product rule for first divergence term on the right-hand side of (A.2.121), yields

$$\text{div} (\varepsilon_{\alpha} \rho_{\alpha} \eta_{\alpha} \mathbf{x}'_{\alpha}) = \eta_{\alpha} \text{div} (\varepsilon_{\alpha} \rho_{\alpha} \mathbf{x}'_{\alpha}) + \varepsilon_{\alpha} \rho_{\alpha} \mathbf{x}'_{\alpha} \text{grad} (\eta_{\alpha}) \quad (\text{A.2.122})$$

The product rule on the left-hand side of (A.2.121) and (A.2.120) for $\Gamma = \eta$, yields

$$\frac{\partial}{\partial t} (\varepsilon_{\alpha} \rho_{\alpha} \eta_{\alpha}) = \varepsilon_{\alpha} \rho_{\alpha} \frac{\partial \eta_{\alpha}}{\partial t} + \eta_{\alpha} \frac{\partial}{\partial t} (\varepsilon_{\alpha} \rho_{\alpha}) \quad (\text{A.2.123})$$

$$\begin{aligned} &= \varepsilon_{\alpha} \rho_{\alpha} \frac{D_{\alpha} \eta_{\alpha}}{Dt} - \varepsilon_{\alpha} \rho_{\alpha} \mathbf{x}'_{\alpha} \text{grad} (\eta_{\alpha}) \\ &+ \eta_{\alpha} \frac{\partial}{\partial t} (\varepsilon_{\alpha} \rho_{\alpha}) \end{aligned} \quad (\text{A.2.124})$$

The species velocity \mathbf{x}'_{α_j} written in terms of the diffusion velocity by (A.2.5)-(a), combined with the rewritings in (A.2.122) and (A.2.123) inserted into

(A.2.121), yields

$$\begin{aligned} \varepsilon_\alpha \rho_\alpha \frac{D_\alpha \eta_\alpha}{Dt} &\geq -\eta_\alpha \left[\frac{\partial}{\partial t} (\varepsilon_\alpha \rho_\alpha) + \operatorname{div} (\varepsilon_\alpha \rho_\alpha \mathbf{x}'_\alpha) \right] \\ &\quad - \operatorname{div} \left(\sum_{j=1}^N \varepsilon_\alpha \rho_{\alpha_j} \eta_{\alpha_j} \mathbf{u}_{\alpha_j} \right) - \operatorname{div} \left(\varepsilon_\alpha \sum_{j=1}^N \frac{1}{\theta} \mathbf{q}_{\alpha_j} \right) \\ &\quad + \varepsilon_\alpha \sum_{j=1}^N \left(\frac{1}{\theta} \rho_{\alpha_j} r_{\alpha_j} \right) \end{aligned} \quad (\text{A.2.125})$$

where the grad terms in (A.2.122) and (A.2.123) cancels. The mass balance for the α -phase is identified in the square brackets of (A.2.125). Inserting (A.2.14) into, reduces (A.2.125) into the expression

$$\begin{aligned} \varepsilon_\alpha \rho_\alpha \frac{D_\alpha \eta_\alpha}{Dt} &\geq -\operatorname{div} \left(\varepsilon_\alpha \sum_{j=1}^N \left(\rho_{\alpha_j} \eta_{\alpha_j} \mathbf{u}_{\alpha_j} + \frac{1}{\theta} \mathbf{q}_{\alpha_j} \right) \right) \\ &\quad + \varepsilon_\alpha \sum_{j=1}^N \left(\frac{1}{\theta} \rho_{\alpha_j} r_{\alpha_j} \right) - \eta_\alpha \hat{r}_\alpha \end{aligned} \quad (\text{A.2.126})$$

The inequality (A.2.126) is rewritten into a form, which involves the energy balance equation. This form have a more physical intuitive formulation. First consider the general relation (A.2.43) with $\Gamma = \eta$, which is

$$\begin{aligned} \varepsilon_\alpha \rho_\alpha \frac{D_\alpha \eta_\alpha}{Dt} &= \sum_{j=1}^N \left[\varepsilon_\alpha \rho_{\alpha_j} \frac{D_{\alpha_j} (\eta_{\alpha_j})}{Dt} - \operatorname{div} (\varepsilon_\alpha \rho_{\alpha_j} \eta_{\alpha_j} \mathbf{u}_{\alpha_j}) \right. \\ &\quad \left. + \eta_{\alpha_j} (\hat{r}_{\alpha_j} + \hat{c}_{\alpha_j} - c_{\alpha_j} \hat{r}_\alpha) \right] \end{aligned} \quad (\text{A.2.127})$$

Substituting (A.2.127) into (A.2.126) and multiply by the temperature θ yields

$$\begin{aligned} 0 &\leq \theta \varepsilon_\alpha \sum_{j=1}^N \rho_{\alpha_j} \frac{D_{\alpha_j} (\eta_{\alpha_j})}{Dt} + \operatorname{div} \sum_{j=1}^N (\varepsilon_\alpha \mathbf{q}_{\alpha_j}) - \varepsilon_\alpha \sum_{j=1}^N (\rho_{\alpha_j} r_{\alpha_j}) \\ &\quad + \theta \eta_\alpha \hat{r}_\alpha + \theta \sum_{j=1}^N \eta_{\alpha_j} (\hat{r}_{\alpha_j} + \hat{c}_{\alpha_j} - c_{\alpha_j} \hat{r}_\alpha) \end{aligned} \quad (\text{A.2.128})$$

Expanding the divergence term in (A.2.128) and re-writing, by use of the product rule, yields

$$\operatorname{div} (\varepsilon_\alpha \mathbf{q}_{\alpha_j}) = \operatorname{div} \left(\theta \varepsilon_\alpha \frac{\mathbf{q}_{\alpha_j}}{\theta} \right) = \theta \operatorname{div} \left(\varepsilon_\alpha \frac{\mathbf{q}_{\alpha_j}}{\theta} \right) + \varepsilon_\alpha \frac{\mathbf{q}_{\alpha_j}}{\theta} \operatorname{grad} \theta \quad (\text{A.2.129})$$

Inserting (A.2.129) into (A.2.128) and by dividing by the temperature θ for the mixture, yields

$$0 \leq \varepsilon_\alpha \sum_{j=1}^N \rho_{\alpha_j} \frac{D_{\alpha_j}(\eta_{\alpha_j})}{Dt} + \operatorname{div} \left(\varepsilon_\alpha \frac{\mathbf{q}_{\alpha_j}}{\theta} \right) + \varepsilon_\alpha \frac{\mathbf{q}_{\alpha_j}}{\theta^2} \operatorname{grad} \theta - \varepsilon_\alpha \frac{1}{\theta} \sum_{j=1}^N (\rho_{\alpha_j} r_{\alpha_j}) \\ + \eta_\alpha \hat{r}_\alpha + \sum_{j=1}^N \eta_{\alpha_j} (\hat{r}_{\alpha_j} + \hat{c}_{\alpha_j} - c_{\alpha_j} \hat{r}_\alpha) \quad (\text{A.2.130})$$

The energy balance for the constituents (A.2.81) divided by the temperature θ , give the result

$$\frac{\varepsilon_\alpha}{\theta} \sum_{j=1}^N \rho_{\alpha_j} \frac{D_{\alpha_j} e_{\alpha_j}}{Dt} = \frac{1}{\theta} \operatorname{tr} \sum_{j=1}^N (\varepsilon_\alpha \mathbf{T}_{\alpha_j} \mathbf{L}_{\alpha_j}) - \operatorname{div} \sum_{j=1}^N \left(\varepsilon_\alpha \frac{\mathbf{q}_{\alpha_j}}{\theta} \right) \\ + \frac{1}{\theta} \sum_{j=1}^N \left(\varepsilon_\alpha \rho_{\alpha_j} r_{\alpha_j} + \hat{e}_{\alpha_j} + \hat{Q}_{\alpha_j} \right) \quad (\text{A.2.131})$$

Combining the presented versions of the energy balance and the inequality gives

$$\varepsilon_\alpha \sum_{j=1}^N \rho_{\alpha_j} \left(\frac{D_{\alpha_j}(\eta_{\alpha_j})}{Dt} - \frac{1}{\theta} \frac{D_{\alpha_j} e_{\alpha_j}}{Dt} \right) \geq \varepsilon_\alpha \frac{\mathbf{q}_{\alpha_j}}{\theta^2} \operatorname{grad} \theta - \frac{1}{\theta} \operatorname{tr} \sum_{j=1}^N (\varepsilon_\alpha \mathbf{T}_{\alpha_j} \mathbf{L}_{\alpha_j}) \\ - \eta_\alpha \hat{r}_\alpha - \sum_{j=1}^N \eta_{\alpha_j} (\hat{r}_{\alpha_j} + \hat{c}_{\alpha_j} - c_{\alpha_j} \hat{r}_\alpha) \\ - \frac{1}{\theta} \sum_{j=1}^N (\hat{e}_{\alpha_j} + \hat{Q}_{\alpha_j}) \quad (\text{A.2.132})$$

The last summation term in (A.2.132) is evaluated. The term is identified in the results from the energy balance of the constituents and phases, (A.2.105) and (A.2.119), respectively,

$$- \sum_{\alpha=1}^N \sum_{j=1}^N (\hat{e}_{\alpha_j} + \hat{Q}_{\alpha_j}) = \sum_{\alpha=1}^N \sum_{j=1}^N \left[\mathbf{u}_{\alpha_j} \cdot (\hat{\mathbf{t}}_{\alpha_j} + \hat{\mathbf{p}}_{\alpha_j}) \right. \\ \left. + \left(e_\alpha + (u_{\alpha_j})^2 \right) (\hat{r}_{\alpha_j} + \hat{c}_{\alpha_j} - c_{\alpha_j} \hat{r}_\alpha) \right. \\ \left. + \mathbf{u}_\alpha \cdot \hat{\mathbf{t}}_\alpha + \hat{r}_\alpha \left(e_\alpha + \frac{1}{2} (u_\alpha)^2 \right) \right] \quad (\text{A.2.133})$$

Summation of (A.2.132) over the phases and inserting into (A.2.133), yields

$$\begin{aligned}
& \sum_{\alpha=1}^N \sum_{j=1}^N \varepsilon_{\alpha} \rho_{\alpha_j} \left(\frac{D_{\alpha_j}(\eta_{\alpha_j})}{Dt} - \frac{1}{\theta} \frac{D_{\alpha_j} e_{\alpha_j}}{Dt} \right) \geq \\
& \quad \sum_{\alpha=1}^N \varepsilon_{\alpha} \frac{\mathbf{q}_{\alpha_j}}{\theta^2} \text{grad} \theta - \frac{1}{\theta} \text{tr} \sum_{\alpha=1}^N \sum_{j=1}^N (\varepsilon_{\alpha} \mathbf{T}_{\alpha_j} \mathbf{L}_{\alpha_j}) \\
& \quad - \sum_{\alpha=1}^N \eta_{\alpha} \hat{r}_{\alpha} - \sum_{\alpha=1}^N \sum_{j=1}^N \eta_{\alpha_j} (\hat{r}_{\alpha_j} + \hat{c}_{\alpha_j} - c_{\alpha_j} \hat{r}_{\alpha}) \\
& \quad + \sum_{\alpha=1}^N \sum_{j=1}^N \frac{1}{\theta} \left[\mathbf{u}_{\alpha_j} \cdot (\hat{\mathbf{t}}_{\alpha_j} + \hat{\mathbf{p}}_{\alpha_j}) + \left(e_{\alpha} + (u_{\alpha_j})^2 \right) \right. \\
& \quad \left. (\hat{r}_{\alpha_j} + \hat{c}_{\alpha_j} - c_{\alpha_j} \hat{r}_{\alpha}) + \mathbf{u}_{\alpha} \cdot \hat{\mathbf{t}}_{\alpha} + \hat{r}_{\alpha} \left(e_{\alpha} + \frac{1}{2} (u_{\alpha})^2 \right) \right] \quad (\text{A.2.134})
\end{aligned}$$

It is convenient to write the inequality (A.2.134) in terms of the Helmholtz free energy, that is

$$\psi_{\alpha_j} = e_{\alpha_j} - \theta \eta_{\alpha_j} \quad (\text{A.2.135})$$

The free energy for the species is related to the phase, by the species density and concentration, as

$$\psi_{\alpha} = \frac{1}{\rho_{\alpha}} \sum_{j=1}^N \rho_{\alpha_j} \psi_{\alpha_j} = \sum_{j=1}^N c_{\alpha_j} \psi_{\alpha_j} \quad (\text{A.2.136})$$

The material time derivative of (A.2.135), is

$$\frac{D_{\alpha_j} \psi_{\alpha_j}}{Dt} = \frac{D_{\alpha_j} e_{\alpha_j}}{Dt} - \theta \frac{D_{\alpha_j} \eta_{\alpha_j}}{Dt} - \eta_{\alpha_j} \frac{D_{\alpha_j} \theta}{Dt} \quad (\text{A.2.137})$$

The inequality (A.2.134) multiplied by the temperature θ and using the

Helmholtz energy definition (A.2.135) and (A.2.137), yields

$$\begin{aligned}
& - \sum_{\alpha=1}^N \sum_{j=1}^N \varepsilon_{\alpha} \rho_{\alpha_j} \left(\frac{D_{\alpha_j}(\psi_{\alpha_j})}{Dt} + \eta_{\alpha_j} \frac{D_{\alpha_j} \theta}{Dt} \right) \geq \\
& \quad \sum_{\alpha=1}^N \varepsilon_{\alpha} \frac{\mathbf{q}_{\alpha_j}}{\theta} \text{grad} \theta - \text{tr} \sum_{\alpha=1}^N \sum_{j=1}^N (\varepsilon_{\alpha} \mathbf{T}_{\alpha_j} \mathbf{L}_{\alpha_j}) \\
& \quad - \sum_{\alpha=1}^N \psi_{\alpha} \hat{r}_{\alpha} + \sum_{\alpha=1}^N \sum_{j=1}^N \psi_{\alpha_j} (\hat{r}_{\alpha_j} + \hat{c}_{\alpha_j} - c_{\alpha_j} \hat{r}_{\alpha}) \\
& \quad + \sum_{\alpha=1}^N \sum_{j=1}^N \left[\mathbf{u}_{\alpha_j} \cdot (\hat{\mathbf{t}}_{\alpha_j} + \hat{\mathbf{p}}_{\alpha_j}) + (u_{\alpha_j})^2 \right. \\
& \quad \quad \left. (\hat{r}_{\alpha_j} + \hat{c}_{\alpha_j} - c_{\alpha_j} \hat{r}_{\alpha}) + \mathbf{u}_{\alpha} \cdot \hat{\mathbf{t}}_{\alpha} + \hat{r}_{\alpha} \frac{1}{2} (u_{\alpha})^2 \right] \quad (\text{A.2.138})
\end{aligned}$$

The equation (A.2.138) is the second axiom of thermodynamics following the material time derivative of the species. This expression is further rewritten to follow the α phase. Consider the (A.2.6)-(a) with $\Gamma = \theta$ and multiplied by $\rho_{\alpha_j} \eta_{\alpha_j}$, that is

$$\sum_{j=1}^N \rho_{\alpha_j} \eta_{\alpha_j} \frac{D_{\alpha_j} \theta}{Dt} - \rho_{\alpha} \eta_{\alpha} \frac{D_{\alpha} \theta}{Dt} = \sum_{j=1}^N \rho_{\alpha_j} \eta_{\alpha_j} \text{grad}(\theta) \mathbf{u}_{\alpha_j} \quad (\text{A.2.139})$$

The entropy flux (A.1.145) for the species using the definition $\sum_{\alpha=1}^N \mathbf{h}_{\alpha_j} = \mathbf{h}_{\alpha}$, is

$$\sum_{\alpha=1}^N \mathbf{q}_{\alpha_j} = \mathbf{h}_{\alpha} - \sum_{\alpha=1}^N (\rho_{\alpha_j} \theta \eta_{\alpha_j} \mathbf{u}_{\alpha_j}) \quad (\text{A.2.140})$$

Multiplying (A.2.140) by $\text{grad}(\theta)/\theta$, yields

$$\sum_{\alpha=1}^N \mathbf{q}_{\alpha_j} \cdot \text{grad}(\theta) \frac{1}{\theta} = \mathbf{h}_{\alpha} \cdot \text{grad}(\theta) \frac{1}{\theta} - \sum_{\alpha=1}^N (\rho_{\alpha_j} \eta_{\alpha_j} \mathbf{u}_{\alpha_j} \cdot \text{grad}(\theta)) \quad (\text{A.2.141})$$

Substituting (A.2.141) and (A.2.139) into (A.2.138), yields

$$\begin{aligned}
\sum_{\alpha=1}^N \left(- \sum_{j=1}^N \left(\varepsilon_{\alpha} \rho_{\alpha_j} \frac{D_{\alpha_j}(\psi_{\alpha_j})}{Dt} \right) - \rho_{\alpha} \eta_{\alpha} \frac{D_{\alpha} \theta}{Dt} \right) \geq \\
\sum_{\alpha=1}^N \frac{\varepsilon_{\alpha}}{\theta} \mathbf{h}_{\alpha} \cdot \text{grad}(\theta) - \text{tr} \sum_{\alpha=1}^N \sum_{j=1}^N (\varepsilon_{\alpha} \mathbf{T}_{\alpha_j} \mathbf{L}_{\alpha_j}) \\
- \sum_{\alpha=1}^N \psi_{\alpha} \hat{r}_{\alpha} + \sum_{\alpha=1}^N \sum_{j=1}^N \psi_{\alpha_j} (\hat{r}_{\alpha_j} + \hat{c}_{\alpha_j} - c_{\alpha_j} \hat{r}_{\alpha}) \\
+ \sum_{\alpha=1}^N \sum_{j=1}^N \left[\mathbf{u}_{\alpha_j} \cdot (\hat{\mathbf{t}}_{\alpha_j} + \hat{\mathbf{p}}_{\alpha_j}) + (u_{\alpha_j})^2 \right. \\
\left. (\hat{r}_{\alpha_j} + \hat{c}_{\alpha_j} - c_{\alpha_j} \hat{r}_{\alpha}) + \mathbf{u}_{\alpha} \cdot \hat{\mathbf{t}}_{\alpha} + \hat{r}_{\alpha} \frac{1}{2} (u_{\alpha})^2 \right] \quad (\text{A.2.142})
\end{aligned}$$

The material derivative of the Helmholtz free energy on the left-hand side of (A.2.142) written by the relation (A.2.43), with $\Gamma = \psi$ and summarizing over the phase, is

$$\begin{aligned}
\sum_{\alpha=1}^N \varepsilon_{\alpha} \rho_{\alpha} \frac{D_{\alpha} \psi_{\alpha}}{Dt} = \sum_{\alpha=1}^N \sum_{j=1}^N \left[\varepsilon_{\alpha} \rho_{\alpha} c_{\alpha_j} \frac{D_{\alpha_j}(\psi_{\alpha_j})}{Dt} - \text{div} (\varepsilon_{\alpha} \rho_{\alpha_j} \psi_{\alpha_j} \mathbf{u}_{\alpha_j}) \right. \\
\left. + \psi_{\alpha_j} (\hat{r}_{\alpha_j} + \hat{c}_{\alpha_j} - c_{\alpha_j} \hat{r}_{\alpha}) \right] \quad (\text{A.2.143})
\end{aligned}$$

Substituting (A.2.143) into (A.2.142), which yields the desired form of the entropy inequality, is

$$\begin{aligned}
- \sum_{\alpha=1}^N \left(\varepsilon_{\alpha} \rho_{\alpha} \frac{D_{\alpha} \psi_{\alpha}}{Dt} + \rho_{\alpha} \eta_{\alpha} \frac{D_{\alpha} \theta}{Dt} \right) \geq \\
\sum_{\alpha=1}^N \frac{\varepsilon_{\alpha}}{\theta} \mathbf{h}_{\alpha} \cdot \text{grad}(\theta) - \text{tr} \sum_{\alpha=1}^N \sum_{j=1}^N (\varepsilon_{\alpha} \mathbf{T}_{\alpha_j} \mathbf{L}_{\alpha_j}) \\
- \sum_{\alpha=1}^N \psi_{\alpha} \hat{r}_{\alpha} + \text{div} (\varepsilon_{\alpha} \rho_{\alpha_j} \psi_{\alpha_j} \mathbf{u}_{\alpha_j}) \\
+ \sum_{\alpha=1}^N \sum_{j=1}^N \left[\mathbf{u}_{\alpha_j} \cdot (\hat{\mathbf{t}}_{\alpha_j} + \hat{\mathbf{p}}_{\alpha_j}) + (u_{\alpha_j})^2 \right. \\
\left. (\hat{r}_{\alpha_j} + \hat{c}_{\alpha_j} - c_{\alpha_j} \hat{r}_{\alpha}) + \mathbf{u}_{\alpha} \cdot \hat{\mathbf{t}}_{\alpha} + \hat{r}_{\alpha} \frac{1}{2} (u_{\alpha})^2 \right] \quad (\text{A.2.144})
\end{aligned}$$

Note that the entropy flux \mathbf{h}_α is identified as

$$\mathbf{h}_\alpha = \mathbf{q}_\alpha + \sum_{j=1}^N \left(\mathbf{T}_{\alpha_j}^T \mathbf{u}_{\alpha_j} - \rho_{\alpha_j} \psi_{\alpha_j} \mathbf{u}_{\alpha_j} + \frac{1}{2} \rho_{\alpha_j} (u_{\alpha_j})^2 \mathbf{u}_{\alpha_j} \right) \quad (\text{A.2.145})$$

where the heat flux \mathbf{q}_α is identified as

$$\mathbf{q}_\alpha = \sum_{j=1}^N \left(\mathbf{q}_{\alpha_j} - \mathbf{T}_{\alpha_j}^T \mathbf{u}_{\alpha_j} - \rho_{\alpha_j} e_{\alpha_j} \mathbf{u}_{\alpha_j} + \frac{1}{2} \rho_{\alpha_j} (u_{\alpha_j})^2 \mathbf{u}_{\alpha_j} \right) \quad (\text{A.2.146})$$

A.3 Multi-species, multi-phase balance laws with electroquasistatics

The following chapter introduces the quasi-static versions of Maxwell's equations into the hybrid mixture theory framework as described by Bennethum and Cushman (2002a).

Maxwell's equations are introduced for each species, but the momentum and energy balance for the species are based on the total electrical field. The electrical field for each species is well described by Gauss law. It is assumed for all balance laws in this section that the interface between the phases are massless and holds no thermodynamic properties. A superscript β indicates the gain of a physical quantity of the j specie in the α phase from the β phase, where $\alpha \neq \beta$.

A.3.1 Mass balance with massless interface.

The material time derivative of the mass balance for the j specie in the α phase is

$$\frac{D_{\alpha_j} \varepsilon_\alpha \rho_{\alpha_j}}{Dt} = -\varepsilon_\alpha \rho_{\alpha_j} \operatorname{div}(\mathbf{x}'_{\alpha_j}) + \varepsilon_\alpha \rho_{\alpha_j} \hat{c}_{\alpha_j} + \sum_{\alpha \neq \beta} \varepsilon_\alpha \rho_{\alpha_j} \hat{r}_{\alpha_j}^\beta \quad (\text{A.3.1})$$

where $\hat{r}_{\alpha_j}^\beta$ is net rate of mass of the f 'th species the from β phase to the α phase. The mass balance for the phase is

$$\frac{D_\alpha \varepsilon_\alpha \rho_\alpha}{Dt} = -\varepsilon_\alpha \rho_\alpha \operatorname{div}(\mathbf{x}'_\alpha) + \sum_{\alpha \neq \beta} \varepsilon_\alpha \rho_\alpha \hat{c}_{\alpha_j} \quad (\text{A.3.2})$$

The restriction for the chemical reaction in the α phase is

$$\sum_{j=1}^N \varepsilon_\alpha \rho_{\alpha_j} \hat{c}_{\alpha_j} = 0 \quad (\text{A.3.3})$$

The assumption of the massless interface between phases yields the restriction

$$\varepsilon_\alpha \rho_{\alpha_j} \hat{r}_{\alpha_j}^\beta + \varepsilon_\beta \rho_{\beta_j} \hat{r}_{\beta_j}^\alpha = 0 \quad (\text{A.3.4})$$

which differs from what is presented in Sec. A.2.1.

A.3.2 Macroscopic form of Gauss' Law

The macroscopic form of Gauss' Law for the species is

$$\text{div}(\varepsilon_\alpha \mathbf{D}_{\alpha_j}) = \varepsilon_\alpha q_{\alpha_j}^e + \varepsilon_\alpha \hat{d}_{\alpha_j} + \sum_{\alpha \neq \beta} \varepsilon_\alpha \hat{d}_{\alpha_j}^\beta \quad (\text{A.3.5})$$

where \mathbf{D}_{α_j} is the volume averaged electric displacement, defined as

$$\mathbf{D}_{\alpha_j} = \varepsilon_0 \mathbf{E}_{\alpha_j} + \mathbf{P}_{\alpha_j} \quad (\text{A.3.6})$$

where ε_0 is the permittivity in vacuum, \mathbf{E}_{α_j} is the electrical field density for the j 'th species in the α phase and \mathbf{P}_{α_j} is the polarization density of the j 'th species. Moreover in (A.3.5) where $q_{\alpha_j}^e$ is the charge density of the j 'th species, \hat{d}_{α_j} is the excess charge density from other species and $\hat{d}_{\alpha_j}^\beta$ is the excess charge effect, from the j 'th species in phase β , on the same constituent in phase α . The electrical field is defined so that $\sum_{j=1}^N \mathbf{E}_{\alpha_j} = \mathbf{E}_T$, where \mathbf{E}_T is the total electrical field.

Summation of (A.3.5) over the species yields Gauss law for the α phase, as

$$\text{div}(\varepsilon_\alpha \mathbf{D}_\alpha) = \varepsilon_\alpha q_\alpha^e + \sum_{\alpha \neq \beta} \varepsilon_\alpha \hat{d}_\alpha^\beta \quad (\text{A.3.7})$$

A restriction for the sum of the excess charge density of the species is identified directly by comparing (A.3.5) and (A.3.7), which yields

$$\sum_{j=1}^N \hat{d}_{\alpha_j} = 0 \quad (\text{A.3.8})$$

The net effect from the the species in the α phase must be zero in order to fulfill the assumption that the interface holds no physical properties, that is, a second restriction is invoked by

$$\varepsilon_\alpha \hat{d}_{\alpha_j}^\beta + \varepsilon_\alpha \hat{d}_{\beta_j}^\alpha = 0 \quad (\text{A.3.9})$$

A.3.3 Macroscopic form of Faraday's law

The macroscopic form of Faraday's law for the j 'th species in the α phase is

$$\text{curl}(\varepsilon_\alpha \mathbf{E}_{\alpha_j}) = \varepsilon_\alpha \widehat{\boldsymbol{\sigma}}_{\alpha_j} + \sum_{\alpha \neq \beta} \varepsilon_\alpha \widehat{\boldsymbol{\sigma}}_{\alpha_j}^\beta \quad (\text{A.3.10})$$

where $\widehat{\boldsymbol{\sigma}}_{\alpha_j}$ is the effect of the electrical field from species in the α phase and $\widehat{\boldsymbol{\sigma}}_{\alpha_j}^\beta$ incorporates the effects from the β phases. Summation of (A.3.10) yields

$$\text{curl}(\varepsilon_\alpha \mathbf{E}_\alpha) = \sum_{\alpha \neq \beta} \varepsilon_\alpha \widehat{\boldsymbol{\sigma}}_\alpha^\beta \quad (\text{A.3.11})$$

By comparing (A.3.10) and (A.3.11), a restriction for summing $\widehat{\boldsymbol{\sigma}}_{\alpha_j}$ over the species, is

$$\sum_{j=1}^N \varepsilon_\alpha \widehat{\boldsymbol{\sigma}}_{\alpha_j} = 0 \quad (\text{A.3.12})$$

No net effects from the electrical fields between the surface phases is allowed, which is the restriction

$$\varepsilon_\alpha \widehat{\boldsymbol{\sigma}}_{\alpha_j}^\beta + \varepsilon_\alpha \widehat{\boldsymbol{\sigma}}_{\beta_j}^\alpha = 0 \quad (\text{A.3.13})$$

A.3.4 Macroscopic form of Ampère's law

The quasi-static macroscopic form of Ampère's law for the j 'th species is

$$\begin{aligned} \varepsilon_\alpha \mathbf{J}_{\alpha_j} = & -\frac{\partial(\varepsilon_\alpha \mathbf{D}_{\alpha_j})}{\partial t} + \text{curl}(\varepsilon_\alpha \mathbf{H}_{\alpha_j}) - \text{curl}(\varepsilon_\alpha \mathbf{P}_{\alpha_j} \times \mathbf{x}'_{\alpha_j}) \\ & + \varepsilon_\alpha \widehat{\mathbf{h}}_{\alpha_j} - \sum_{\alpha \neq \beta} \varepsilon_\alpha \widehat{\mathbf{h}}_{\alpha_j}^\beta \end{aligned} \quad (\text{A.3.14})$$

where \mathbf{H}_{α_j} is the magnetic field intensity, \mathbf{J}_{α_j} is the free current density of the j 'th species in a fixed frame, $\widehat{\mathbf{h}}_{\alpha_j}$ is the free current density supply from other species in the same phase and $\widehat{\mathbf{h}}_{\alpha_j}^\beta$ is the free current density supply from the j 'th species in the β phase.

Summation of (A.3.14) over the j 'th species yields the macroscopic form of Ampère's law for the α phase, that is

$$\varepsilon_\alpha \mathbf{J}_\alpha = -\frac{\partial(\varepsilon_\alpha \mathbf{D}_\alpha)}{\partial t} + \text{curl}(\varepsilon_\alpha \mathbf{H}_\alpha) - \text{curl}(\varepsilon_\alpha \mathbf{P}_\alpha \times \mathbf{x}'_\alpha) - \sum_{\alpha \neq \beta} \varepsilon_\alpha \widehat{\mathbf{h}}_\alpha^\beta \quad (\text{A.3.15})$$

By comparing (A.3.14) and (A.3.15) gives the restriction for $\widehat{\mathbf{h}}_{\alpha_j}$ as

$$\sum_{j=1}^N \widehat{\mathbf{h}}_{\alpha_j} = 0 \quad (\text{A.3.16})$$

and the assumption of a mass less phase interface yields

$$\varepsilon_\alpha \widehat{\mathbf{h}}_{\alpha_j}^\beta + \varepsilon_\alpha \widehat{\mathbf{h}}_{\beta_j}^\alpha = 0 \quad (\text{A.3.17})$$

A.3.5 Macroscopic form of conservation of electrical charge

The conservation of charge is derived from the divergence of Ampère's law together with the time derivative of Gauss' law, which is

$$\begin{aligned} \operatorname{div} \left(\varepsilon_\alpha \mathcal{J}_{\alpha_j} + \varepsilon_\alpha q_{\alpha_j}^e \mathbf{x}'_{\alpha_j} \right) + \frac{\partial}{\partial t} \left(\varepsilon_\alpha q_{\alpha_j}^e \right) &= \varepsilon_\alpha \widehat{q}_{\alpha_j}^e + \varepsilon_\alpha \rho_{\alpha_j} z_{\alpha_j} \widehat{c}_{\alpha_j} \\ &+ \sum_{\alpha \neq \beta} \varepsilon_\alpha \rho_{\alpha_j} \left(\widehat{Z}_{\alpha_j}^\beta + z_{\alpha_j} \widehat{r}_{\alpha_j}^\beta \right) \end{aligned} \quad (\text{A.3.18})$$

where z_{α_j} is the charge per unit mass, $\widehat{q}_{\alpha_j}^e$ is the rate of charge gain from the j 'th species, due to interactions with other species in the α phase and $\widehat{Z}_{\alpha_j}^\beta$ is the rate of charge from other phases than α . The free current density relative to the species \mathcal{J}_{α_j} , is related to \mathbf{J}_{α_j} by the relation

$$\mathcal{J}_{\alpha_j} = \mathbf{J}_{\alpha_j} - q_{\alpha_j}^e \mathbf{x}'_{\alpha_j} \quad (\text{A.3.19})$$

Using the mass balance equation (A.3.1) together with (A.3.18) yields the form

$$\varepsilon_\alpha \rho_{\alpha_j} \frac{D_{\alpha_j} z_{\alpha_j}}{Dt} + \operatorname{div} \left(\varepsilon_\alpha \mathcal{J}_{\alpha_j} \right) = \varepsilon_\alpha \widehat{q}_{\alpha_j}^e + \sum_{\alpha \neq \beta} \varepsilon_\alpha \rho_{\alpha_j} \widehat{Z}_{\alpha_j}^\beta \quad (\text{A.3.20})$$

Summation of (A.3.18) over the species yields

$$\operatorname{div} \left(\varepsilon_\alpha \mathcal{J}_\alpha + \varepsilon_\alpha q_\alpha^e \mathbf{x}'_\alpha \right) + \frac{\partial}{\partial t} \left(\varepsilon_\alpha q_\alpha^e \right) = \sum_{\alpha \neq \beta} \varepsilon_\alpha \rho_\alpha \left(\widehat{Z}_\alpha^\beta + z_\alpha \widehat{r}_\alpha^\beta \right) \quad (\text{A.3.21})$$

where a comparison between (A.3.18) and (A.3.21) yields the restriction

$$\sum_{j=1}^N \left(\widehat{q}_{\alpha_j}^e + \rho_{\alpha_j} z_{\alpha_j} \widehat{c}_{\alpha_j} \right) = 0 \quad (\text{A.3.22})$$

and

$$\varepsilon_\alpha \rho_{\alpha_j} \left(\widehat{Z}_{\alpha_j}^\beta + z_{\alpha_j} \widehat{r}_{\alpha_j}^\beta \right) + \varepsilon_\beta \rho_{\beta_j} \left(\widehat{Z}_{\beta_j}^\alpha + z_{\beta_j} \widehat{r}_{\beta_j}^\alpha \right) = 0 \quad (\text{A.3.23})$$

The combination of Ampère's law and Gauss' law implies more restrictions for the exchange terms. It can be shown that

$$\begin{aligned} \operatorname{div} \left(\varepsilon_\alpha \widehat{\mathbf{h}}_{\alpha_j} + \sum_{\alpha \neq \beta} \varepsilon_\alpha \widehat{\mathbf{h}}_{\alpha_j}^\beta \right) - \frac{\partial \left(\varepsilon_\alpha \widehat{d}_{\alpha_j} \right)}{\partial t} \\ - \sum_{\alpha \neq \beta} \frac{\partial \left(\varepsilon_\alpha \widehat{d}_{\alpha_j} \right)}{\partial t} = \varepsilon_\alpha \widehat{q}_{\alpha_j}^e + \varepsilon_\alpha \widehat{q}_{\alpha_j}^e \widehat{c}_{\alpha_j} \\ + \sum_{\alpha \neq \beta} \varepsilon_\alpha \rho_{\alpha_j} \left(\widehat{Z}_{\alpha_j}^\beta + z_{\alpha_j} \widehat{r}_{\alpha_j}^\beta \right) \end{aligned} \quad (\text{A.3.24})$$

A.3.6 Linear momentum with electromagnetic forces

The linear momentum in (A.2.32) is expanded when electromagnetic forces are introduced. The macroscopic form of linear momentum for the species, introduced in HMT, is defined as

$$\begin{aligned} \varepsilon_\alpha \rho_{\alpha_j} \widehat{\mathbf{i}}_{\alpha_j} + \sum_{\alpha \neq \beta} \varepsilon_\alpha \rho_{\alpha_j} \widehat{\mathbf{T}}_{\alpha_j}^\beta = \varepsilon_\alpha \rho_{\alpha_j} \frac{D_{\alpha_j} \mathbf{x}'_{\alpha_j}}{Dt} - \operatorname{div} \left(\varepsilon_\alpha \mathbf{T}_{\alpha_j} \right) - \varepsilon_\alpha q_{\alpha_j}^e \mathbf{E}_T \\ + \frac{1}{2} \varepsilon_0 \mathbf{E}_T \cdot \mathbf{E}_{\alpha_j} \operatorname{grad} \left(\varepsilon_\alpha \right) - \varepsilon_\alpha \rho_{\alpha_j} \left(\mathbf{b}_{\alpha_j} + \mathbf{b}_{\mathbf{I}, \alpha_j} \right) \\ - \varepsilon_\alpha \mathbf{P}_{\alpha_j} \operatorname{grad} \left(\mathbf{E}_T \right) \end{aligned} \quad (\text{A.3.25})$$

where $\widehat{\mathbf{i}}_{\alpha_j}$ is the gain of linear momentum from other species, except chemical reaction, \mathbf{T}_{α_j} is the partial Cauchy stress tensor, \mathbf{b}_{α_j} is the external body force acting on j 'th species in the α phase, $\mathbf{b}_{\mathbf{I}, \alpha_j}$ is an additional inner body force, due to differences in the electromagnetic fields and $\widehat{\mathbf{T}}_{\alpha_j}^\beta$ is the rate of mechanical momentum from the j 'th species in the β phase to the same constituent in the α phase.

Summation of (A.3.25) over the phases yields

$$\begin{aligned} \sum_{\alpha \neq \beta} \varepsilon_\alpha \rho_\alpha \widehat{\mathbf{T}}_\alpha^\beta = \frac{D_\alpha \mathbf{x}'_\alpha}{Dt} - \operatorname{div} \left(\varepsilon_\alpha \mathbf{T}_\alpha \right) - \frac{1}{2} \varepsilon_0 \mathbf{E}_T \cdot \mathbf{E}_\alpha \operatorname{grad} \left(\varepsilon_\alpha \right) \\ - \varepsilon_\alpha \rho_\alpha \left(\mathbf{b}_\alpha + \mathbf{b}_{\mathbf{I}, \alpha} \right) - \varepsilon_\alpha q_\alpha^e \mathbf{E}_T - \varepsilon_\alpha \mathbf{P}_\alpha \operatorname{grad} \left(\mathbf{E}_T \right) \end{aligned} \quad (\text{A.3.26})$$

Comparing (A.3.25) and (A.3.26) yields the restriction

$$\sum_{j=1}^N \rho_{\alpha_j} \left(\hat{\mathbf{i}}_{\alpha_j} + \hat{c}_{\alpha_j} \mathbf{x}'_{\alpha_j} \right) = 0 \quad (\text{A.3.27})$$

and for the interface between the phases, the following condition is obtained

$$\varepsilon_{\alpha} \rho_{\alpha_j} \left(\hat{\mathbf{T}}_{\alpha_j}^{\beta} + \hat{r}_{\alpha_j}^{\beta} \mathbf{x}'_{\alpha_j} \right) + \varepsilon_{\beta} \rho_{\beta_j} \left(\hat{\mathbf{T}}_{\beta_j}^{\alpha} + \hat{r}_{\beta_j}^{\alpha} \mathbf{x}'_{\beta_j} \right) = 0 \quad (\text{A.3.28})$$

A.3.7 Angular momentum with electromagnetic forces

The balance postulate for the macroscale form of angular momentum, written with index notation using the permutation tensor ϵ_{klm} , is

$$\begin{aligned} -\varepsilon_{\alpha} \epsilon_{klm} T_{(\alpha_j)kl} - \varepsilon_{\alpha} \epsilon_{klm} P_{(\alpha_j)k} (E_T)_l &= \varepsilon_{\alpha} \rho_{\alpha_j} \hat{m}_{(\alpha_j)m} + M_{(\alpha_j)m} \\ &+ \sum_{\alpha \neq \beta} \varepsilon_{\alpha} \rho_{\alpha_j} \hat{m}_{(\alpha_j)m}^{\beta} \end{aligned} \quad (\text{A.3.29})$$

where $\hat{m}_{(\alpha_j)m}$ is the exchange of momentum from the j 'th species in the α phase, $\hat{m}_{(\alpha_j)m}^{\beta}$ is the exchange of momentum in from the j 'th species in the β phase to the α phase and $M_{(\alpha_j)m}$ rate of angular momentum gain due to the microscale angular momentum terms.

Summation of (A.3.29) over the phases is

$$-\varepsilon_{\alpha} \epsilon_{klm} T_{(\alpha)kl} - \varepsilon_{\alpha} \epsilon_{klm} P_{(\alpha)k} (E_T)_l = M_{(\alpha)m} + \sum_{\alpha \neq \beta} \varepsilon_{\alpha} \rho_{\alpha} \hat{m}_{(\alpha)m}^{\beta} \quad (\text{A.3.30})$$

The following restriction in the bulk phase must hold in order to ensure momentum transfer in the phase

$$\sum_{j=1}^N \rho_{\alpha_j} \hat{\mathbf{m}}_{\alpha_j} = 0 \quad (\text{A.3.31})$$

and the interface restriction between the phases is

$$\varepsilon_{\alpha} \rho_{\alpha_j} \hat{\mathbf{m}}_{\alpha_j}^{\beta} + \varepsilon_{\alpha} \rho_{\alpha_j} \hat{\mathbf{m}}_{\alpha_j}^{\beta} = 0 \quad (\text{A.3.32})$$

A.3.8 Energy balance with electromagnetic forces

The energy balance for the species accounting for the electromagnetic forces is an further extension of the form presented in Sec. A.2.4. The macroscopic

form of the HMT quasi-static energy balance, is given by

$$\begin{aligned}
\varepsilon_\alpha \rho_{\alpha_j} \frac{D_{\alpha_j} e_{\alpha_j}}{Dt} &= \text{tr}(\varepsilon_\alpha \mathbf{T}_{\alpha_j} \mathbf{L}_{\alpha_j}) + \text{div}(\varepsilon_\alpha \mathbf{q}_{\alpha_j}) + \frac{1}{2} \varepsilon_0 \mathbf{E}_T \cdot \mathbf{E}_{\alpha_j} \frac{D_{\alpha_j} \varepsilon_\alpha}{Dt} \\
&\quad + \varepsilon_\alpha \mathcal{J}_{\alpha_j} \cdot \mathbf{E}_T + \frac{\partial(\varepsilon_\alpha \mathbf{P}_{\alpha_j})}{\partial t} \cdot \mathbf{E}_T + \text{div}(\varepsilon_\alpha \mathbf{x}'_{\alpha_j} \mathbf{P}_{\alpha_j}) \cdot \mathbf{E}_T \\
&\quad + \varepsilon_{\alpha_j} \rho_{\alpha_j} r_{\alpha_j} + \varepsilon_\alpha \rho_{\alpha_j} \widehat{Q}_{\alpha_j} + \sum_{\alpha \neq \beta} \varepsilon_\alpha \rho_{\alpha_j} \widehat{Q}_{\alpha_j}^\beta \quad (\text{A.3.33})
\end{aligned}$$

where r_{α_j} is the external energy supply, \widehat{Q}_{α_j} is the rate of energy gain from other species in the same phase, $\widehat{Q}_{\alpha_j}^\beta$ is the rate of energy gain from constituent j in the β phase on the same constituent in the α phase. Additional terms are added to \mathbf{q}_{α_j} and \widehat{Q}_{α_j} compared to A.2.4.2, due to the electromagnetic field and that the third term on the right-hand is to account for electro quasi-static effects for swelling materials (Bennethum and Cushman, 2002a). The sum of the three terms in the second row of (A.3.33) is the electrical induced energy source.

Summation of (A.3.33) over the species yields

$$\begin{aligned}
\varepsilon_\alpha \rho_\alpha \frac{D_\alpha e_\alpha}{Dt} &= \text{tr}(\varepsilon_\alpha \mathbf{T}_\alpha \mathbf{L}_\alpha) + \text{div}(\varepsilon_\alpha \mathbf{q}_\alpha) + \frac{1}{2} \varepsilon_0 \mathbf{E}_T \cdot \mathbf{E}_\alpha \frac{D_\alpha \varepsilon_\alpha}{Dt} \\
&\quad + \varepsilon_\alpha \mathcal{J}_\alpha \cdot \mathbf{E}_T + \frac{\partial(\varepsilon_\alpha \mathbf{P}_\alpha)}{\partial t} \cdot \mathbf{E}_T + \text{div}(\varepsilon_\alpha \mathbf{x}'_\alpha \mathbf{P}_\alpha) \cdot \mathbf{E}_T \\
&\quad + \varepsilon_{\alpha_j} \rho_{\alpha_j} r_\alpha + \sum_{\alpha \neq \beta} \varepsilon_\alpha \rho_\alpha \widehat{Q}_\alpha^\beta \quad (\text{A.3.34})
\end{aligned}$$

Comparing (A.3.33) with (A.3.34) one obtain the restriction

$$\sum_{j=1}^N \left(\rho_{\alpha_j} \widehat{Q}_{\alpha_j} + \rho_{\alpha_j} \widehat{\mathbf{i}}_{\alpha_j} \cdot \mathbf{x}'_{\alpha_j} + \rho_{\alpha_j} \widehat{c}_{\alpha_j} \left(e_{\alpha_j} + \frac{1}{2} (x'_{\alpha_j})^2 \right) \right) = 0 \quad (\text{A.3.35})$$

The energy is assumed to be transferred to other species in the bulk and the phase interface restriction is

$$\begin{aligned}
&\left[\varepsilon_\alpha \rho_{\alpha_j} \widehat{Q}_{\alpha_j}^\beta + \varepsilon_\alpha \rho_{\alpha_j} \widehat{\mathbf{T}}_{\alpha_j}^\beta \cdot \mathbf{x}'_{\alpha_j} + \varepsilon_\alpha \rho_{\alpha_j} \widehat{r}_{\alpha_j} \left(e_{\alpha_j} + \frac{1}{2} (x_{\alpha_j})^2 \right) \right] \\
&+ \left[\varepsilon_\alpha \rho_{\alpha_j} \widehat{Q}_{\beta_j}^\alpha + \varepsilon_\beta \rho_{\beta_j} \widehat{\mathbf{T}}_{\beta_j}^\alpha \cdot \mathbf{x}'_{\beta_j} + \varepsilon_\beta \rho_{\beta_j} \widehat{r}_{\beta_j} \left(e_{\beta_j} + \frac{1}{2} (x_{\beta_j})^2 \right) \right] = 0 \quad (\text{A.3.36})
\end{aligned}$$

which is the condition describing that no energy is accumulated at the interfaces.

A.3.9 Entropy balance with electromagnetic forces

The entropy balance for the j 'th species is

$$\varepsilon_\alpha \rho_{\alpha_j} \frac{D_{\alpha_j} \eta_{\alpha_j}}{Dt} - \operatorname{div}(\varepsilon_\alpha \mathbf{h}_{\alpha_j}) - \varepsilon_\alpha \rho_{\alpha_j} g_{\alpha_j} = \sum_{\alpha \neq \beta} \varepsilon_\alpha \rho_{\alpha_j} \widehat{\mathbf{h}}_{\alpha_j}^\beta + \varepsilon_\alpha \rho_{\alpha_j} \widehat{\eta}_{\alpha_j} + \varepsilon_\alpha \rho_{\alpha_j} \widehat{\Lambda}_{\alpha_j} \quad (\text{A.3.37})$$

where \mathbf{h}_{α_j} is the entropy flux, $\widehat{\mathbf{h}}_{\alpha_j}^\beta$ is the entropy transfer from mechanical interactions between phases, g_{α_j} is an external entropy source, $\widehat{\eta}_{\alpha_j}$ is the entropy gain from other species in the same phase and $\widehat{\Lambda}_{\alpha_j}$ is the energy production per unit mass.

Summation of (A.3.37) over the species yields

$$\varepsilon_\alpha \rho_\alpha \frac{D_\alpha \eta_\alpha}{Dt} - \operatorname{div}(\varepsilon_\alpha \mathbf{h}_\alpha) - \varepsilon_\alpha \rho_\alpha g_\alpha = \sum_{\alpha \neq \beta} \varepsilon_\alpha \rho_\alpha \widehat{\mathbf{h}}_\alpha^\beta + \varepsilon_\alpha \rho_\alpha \widehat{\Lambda}_\alpha \quad (\text{A.3.38})$$

Comparing (A.3.37) and (A.3.38) yields the restriction for the entropy gain, as

$$\sum_{j=1}^N \rho_{\alpha_j} (\widehat{\eta}_{\alpha_j} + \widehat{c}_{\alpha_j} \eta_{\alpha_j}) = 0 \quad (\text{A.3.39})$$

and the restriction for the interface between phases, as

$$\varepsilon_\alpha \rho_{\alpha_j} \left(\widehat{\mathbf{h}}_{\alpha_j}^\beta + \widehat{e}_{\alpha_j}^\beta \eta_{\alpha_j} \right) + \varepsilon_\beta \rho_{\beta_j} \left(\widehat{\mathbf{h}}_{\beta_j}^\alpha + \widehat{e}_{\beta_j}^\alpha \eta_{\beta_j} \right) = 0 \quad (\text{A.3.40})$$

In order to obtain an entropy inequality for a system with a solid part ($\alpha = s$) and a liquid part ($\alpha = l$), one should consider the assumption for the entropy generation for the whole mixture, given as

$$\rho \widehat{\Lambda} = \sum_{\alpha=1}^N \sum_{j=1}^N \varepsilon_\alpha \rho_{\alpha_j} \widehat{\Lambda}_{\alpha_j} \geq 0 \quad (\text{A.3.41})$$

It is further assumed that the whole mixture have the same temperature θ , which results in the following conditions

$$\mathbf{h}_{\alpha_j} = \frac{\mathbf{q}_{\alpha_j}}{\theta}; \quad g_{\alpha_j} = \frac{r_{\alpha_j}}{\theta}; \quad \mathbf{h}_\alpha = \frac{\mathbf{q}_\alpha}{\theta}; \quad g_\alpha = \frac{r_\alpha}{\theta} \quad (\text{A.3.42})$$

where it follows that

$$\sum_{\alpha=1}^N \varepsilon_\alpha \mathbf{h}_\alpha = \sum_{\alpha=1}^N \frac{\varepsilon_\alpha \mathbf{q}_\alpha}{\theta}; \quad \sum_{\alpha=1}^N \varepsilon_\alpha g_\alpha = \sum_{\alpha=1}^N \frac{\varepsilon_\alpha r_\alpha}{\theta} \quad (\text{A.3.43})$$

As shown in Sec. A.2.5, it is convenient to introduce and write the inequality in terms of the Helmholtz free energy, which is defined as

$$\psi_{\alpha_j} = e_{\alpha_j} - \theta \eta_{\alpha_j}; \quad \psi_{\alpha} = \sum_{j=1}^N c_{\alpha_j} \psi_{\alpha_j} \quad (\text{A.3.44})$$

An extended definition of the Helmholtz free energy is introduced due to the inclusion of electrical fields and polarization effects, which is

$$\tilde{\psi}_{\alpha_j} = e_{\alpha_j} - \theta \eta_{\alpha_j} - \frac{1}{\rho_{\alpha_j}} \mathbf{E}_T \cdot \mathbf{P}_{\alpha_j}; \quad \tilde{\psi}_{\alpha} = \sum_{j=1}^N c_{\alpha_j} \tilde{\psi}_{\alpha_j} \quad (\text{A.3.45})$$

A useful form of the entropy inequality, including the Helmholtz free energy, is obtained by the same procedure as shown in Sec. A.2.5, where the energy balance is introduced in the inequality together with the definition of Helmholtz free energy. For the case with electromagnetic forces considered here, the entropy balance (A.3.37) together with (A.3.41), (A.3.33), in which the definitions (A.3.42) are used, together with the restrictions (A.3.35), (A.3.36), (A.3.39) and (A.3.40), are used to establish the following

$$\begin{aligned} \sum_{\alpha} \varepsilon_{\alpha} \rho_{\alpha} \theta \hat{\Lambda}_{\alpha} = & \sum_{\alpha=l,s} \sum_{j=1}^N \left[-\varepsilon_{\alpha} \rho_{\alpha_j} \frac{D_{\alpha_j} \tilde{\psi}_{\alpha_j}}{Dt} - \varepsilon_{\alpha} \rho_{\alpha_j} \frac{D_{\alpha_j} \theta}{Dt} \right. \\ & + \frac{\varepsilon_{\alpha}}{\theta} \mathbf{E}_T \cdot \mathbf{P}_{\alpha_j} \frac{D_{\alpha_j} \rho_{\alpha_j}}{Dt} - \varepsilon_{\alpha} \mathbf{P}_{\alpha_j} \cdot \frac{D_{\alpha_j} \mathbf{E}_T}{Dt} - \varepsilon_{\alpha} \mathbf{E}_T \cdot \frac{D_{\alpha_j} \mathbf{P}_{\alpha_j}}{Dt} \\ & + \frac{\varepsilon_{\alpha}}{\theta} \text{grad}(\theta) \cdot \mathbf{q}_{\alpha_j} + \text{tr} \left(\varepsilon_{\alpha} \mathbf{T}_{\alpha_j}^T \mathbf{L}_{\alpha_j} \right) + \varepsilon_{\alpha} \mathcal{J}_{\alpha} \cdot \mathbf{E}_T \\ & + \frac{\partial (\varepsilon_{\alpha} \mathbf{P}_{\alpha_j})}{\partial t} \cdot \mathbf{E}_T + \frac{\partial (\varepsilon_{\alpha} \mathbf{P}_{\alpha_j})}{\partial t} \cdot \mathbf{E}_T + \text{div} \left(\varepsilon_{\alpha} \mathbf{x}'_{\alpha_j} \mathbf{P}_{\alpha_j} \right) \cdot \mathbf{E}_T \\ & + \varepsilon_{\alpha} \rho_{\alpha_j} \theta \left(\sum_{\alpha \neq \beta} \tilde{e}_{\alpha_j}^{\beta} \eta_{\alpha_j} + \hat{c}_{\alpha_j} \eta_{\alpha_j} \right) - \varepsilon_{\alpha} \rho_{\alpha_j} \left(\sum_{\alpha \neq \beta} \hat{\mathbf{T}}_{\alpha_j}^{\beta} \cdot \mathbf{x}'_{\alpha_j} \right. \\ & + \tilde{e}_{\alpha_j}^{\beta} \left(\tilde{\psi}_{\alpha_j} + \theta \eta_{\alpha_j} \frac{1}{\rho_{\alpha_j}} \mathbf{E}_T \cdot \mathbf{P}_{\alpha_j} + \frac{1}{2} (x_{\alpha_j})^2 \right) \left. \right) - \varepsilon_{\alpha} \rho_{\alpha_j} \hat{\mathbf{i}}_{\alpha_j} \cdot \mathbf{x}'_{\alpha_j} \\ & \left. - \varepsilon_{\alpha_j} \rho_{\alpha_j} c_{\alpha_j} \left(\tilde{\psi}_{\alpha_j} + \theta \eta_{\alpha_j} \frac{1}{\rho_{\alpha_j}} \mathbf{E}_T \cdot \mathbf{P}_{\alpha_j} + \frac{1}{2} (x_{\alpha_j})^2 \right) \right] \geq 0 \quad (\text{A.3.46}) \end{aligned}$$

Additional relations are used to obtain the desired inequality, where the

following is used

$$\begin{aligned} \mathbf{q}_\alpha \cdot \text{grad}(\theta) &= \sum_{j=1}^N \mathbf{q}_{\alpha_j} \cdot \text{grad}(\theta); & \eta_\alpha \frac{D_\alpha \theta}{Dt} &= \eta_{\alpha_j} \sum_{j=1}^N \frac{D_{\alpha_j} \theta}{Dt}; \\ \mathbf{T}_\alpha \mathbf{L}_\alpha &= \sum_{j=1}^N \mathbf{T}_{\alpha_j} \mathbf{L}_{\alpha_j} \end{aligned} \quad (\text{A.3.47})$$

Another relation of importance to reach a useful form of the entropy inequality, is

$$\begin{aligned} - \sum_{j=1}^N \varepsilon_\alpha \rho_{\alpha_j} \frac{D_{\alpha_j} \tilde{\psi}_{\alpha_j}}{Dt} &= -\varepsilon_\alpha \rho_{\alpha_j} \frac{D_\alpha \tilde{\psi}_{\alpha_j}}{Dt} - \tilde{\psi}_{\alpha_j} \frac{D_\alpha \varepsilon_\alpha \rho_{\alpha_j}}{Dt} + \sum_{j=1}^N \left[\tilde{\psi}_{\alpha_j} \frac{D_s \varepsilon_\alpha \rho_{\alpha_j}}{Dt} \right. \\ &\quad + \tilde{\psi}_{\alpha_j} \mathbf{x}'_{\alpha_j, \alpha} \cdot \text{grad}(\varepsilon_\alpha \rho_{\alpha_j}) + \tilde{\psi}_{\alpha_j} \mathbf{x}'_{\alpha, s} \cdot \text{grad}(\varepsilon_\alpha \rho_{\alpha_j}) \\ &\quad \left. - \mathbf{x}'_{\alpha_j, \alpha} \cdot \text{grad}(\varepsilon_\alpha \rho_{\alpha_j} \tilde{\psi}_{\alpha_j}) \right] \quad (\text{A.3.48}) \\ &= -\varepsilon_\alpha \rho_{\alpha_j} \frac{D_\alpha \tilde{\psi}_{\alpha_j}}{Dt} + \sum_{j=1}^N \left[\tilde{\psi}_{\alpha_j} \frac{D_s \varepsilon_\alpha \rho_{\alpha_j}}{Dt} \right. \\ &\quad + \varepsilon_\alpha \rho_{\alpha_j} \tilde{\psi}_{\alpha_j} \text{div}(\mathbf{x}'_\alpha) + \tilde{\psi}_{\alpha_j} \mathbf{x}'_{\alpha, s} \cdot \text{grad}(\varepsilon_\alpha \rho_{\alpha_j}) \\ &\quad + \varepsilon_\alpha \rho_{\alpha_j} \text{div}(\tilde{\psi}_{\alpha_j}) \cdot \mathbf{x}'_{\alpha_j, \alpha} \\ &\quad \left. - \sum_{\alpha \neq \beta} (\varepsilon_\alpha \rho_{\alpha_j} \tilde{\psi}_\alpha \tilde{\varepsilon}_{\alpha_j}^\beta) \right] \quad (\text{A.3.49}) \end{aligned}$$

where the notation α, s refers to a relative velocity of the α -phase with respect to the solid s , ($\mathbf{x}'_{\alpha, s} = \mathbf{x}'_\alpha - \mathbf{x}'_s$).

Summation of (A.3.46) and using (A.3.47) and (A.3.49) yields the desired inequality, as

$$\begin{aligned}
\sum_{\alpha} \varepsilon_{\alpha} \rho_{\alpha} \theta \widehat{\Lambda}_{\alpha} &= - \sum_{\alpha} \varepsilon_{\alpha} \rho_{\alpha} \left(\frac{D_{\alpha} \widetilde{\psi}_{\alpha}}{Dt} + \eta_{\alpha} \frac{D_{\alpha} \theta}{Dt} \right) + \sum_{\alpha} \mathcal{J}_{\alpha} \cdot \mathbf{E}_T \\
&+ \sum_{\alpha} \left[\varepsilon_{\alpha} \mathbf{T}_{\alpha} + \varepsilon_{\alpha} \mathbf{P}_{\alpha} \cdot \mathbf{E}_T \mathbf{I} + \sum_{j=1}^N \varepsilon_{\alpha} \rho_{\alpha_j} \left(\widetilde{\psi}_{\alpha_j} \mathbf{I} \right) \right] : \mathbf{L}_{\alpha} \\
&+ \sum_{\alpha} \sum_{j=1}^N \left[\varepsilon_{\alpha} \mathbf{T}_{\alpha_j} + \varepsilon_{\alpha} \mathbf{P}_{\alpha_j} \cdot \mathbf{E}_T \mathbf{I} \right] : \mathbf{L}_{\alpha_j, \alpha} \\
&+ \sum_{\alpha} \frac{D_s \varepsilon_{\alpha}}{Dt} \left[\frac{1}{2} \varepsilon_0 \mathbf{E}_T \cdot \mathbf{E}_{\alpha} + \mathbf{E}_T \cdot \mathbf{P}_{\alpha} + \rho_{\alpha} \psi_{\alpha} \right] + \sum_{\alpha} \frac{\varepsilon_{\alpha}}{\theta} \text{grad} \theta \\
&\times \left[\mathbf{q}_{\alpha} + \sum_{j=1}^N \left[\rho_{\alpha_j} \mathbf{x}'_{\alpha_j, \alpha} \left(\widetilde{\psi}_{\alpha_j} + \frac{1}{2} \mathbf{x}'_{\alpha_j, \alpha} \cdot \mathbf{x}'_{\alpha_j, \alpha} \right) - \mathbf{T}_{\alpha_j} \cdot \mathbf{x}'_{\alpha_j, \alpha} \right] \right] \\
&+ \sum_{\alpha} \sum_{j=1}^N \frac{D_s \rho_{\alpha_j}}{Dt} \left[\frac{1}{\rho_{\alpha_j}} \mathbf{E}_T \cdot \mathbf{P}_{\alpha_j} + \psi_{\alpha_j} \right] - \sum_{\alpha} \varepsilon_{\alpha} \frac{D_s \mathbf{E}_T}{Dt} \cdot \mathbf{P}_{\alpha_j} \\
&+ \mathbf{x}'_{l, s} \cdot \left[-\varepsilon_l \rho_l \widehat{\mathbf{T}}_s^l + \sum_{j=1}^N \left(\psi_{l_j} \text{grad} (\varepsilon_l \rho_{l_j}) + \frac{1}{\rho_{l_j}} \mathbf{E}_T \cdot \mathbf{P}_{l_j} \text{grad} (\varepsilon_l \rho_{l_j}) \right) \right. \\
&\quad \left. - \varepsilon_l \text{grad} (\mathbf{E}_T) \cdot \mathbf{P}_{l_j} + \frac{1}{2} \varepsilon_0 \mathbf{E}_T \cdot \mathbf{E}_{l_j} \text{grad} (\varepsilon_l) \right] + \sum_{\alpha} \sum_{j=1}^N \mathbf{x}'_{\alpha_j, \alpha} \\
&\times \left[-\varepsilon_{\alpha} \rho_{\alpha_j} \left(\widehat{\mathbf{i}}_{\alpha_j} + \sum_{\alpha \neq \beta} \widehat{\mathbf{T}}_{\alpha_j}^{\beta} \right) - \varepsilon_{\alpha} \rho_{\alpha_j} \text{grad} (\widetilde{\psi}_{\alpha_j}) - \varepsilon_{\alpha} q_{\alpha_j}^e \mathbf{E}_T - \right. \\
&\quad \left. - \varepsilon_{\alpha} \mathbf{P}_{\alpha_j} \text{grad} (\mathbf{E}_T) + \frac{1}{2} \varepsilon_0 \mathbf{E}_T \cdot \mathbf{E}_{\alpha_j} \text{grad} (\varepsilon_{\alpha}) + \frac{1}{\rho_{\alpha_j}} \mathbf{E}_T \cdot \mathbf{P}_{\alpha_j} \text{grad} (\varepsilon_{\alpha} \rho_{\alpha_j}) \right] \\
&- \sum_{\alpha} \sum_{j=1}^N \sum_{\beta \neq \alpha} \varepsilon_{\alpha} \rho_{\alpha_j} \widehat{e}_{\alpha_j}^{\beta} \left[\widetilde{\psi}_{\alpha_j} + \theta \eta_{\alpha_j} \frac{1}{\rho_{\alpha_j}} \mathbf{E}_T \cdot \mathbf{P}_{\alpha_j} + \frac{1}{2} (x'_{\alpha_j, \alpha})^2 \right. \\
&\quad \left. + \widetilde{\psi}_{\alpha} + \frac{1}{2} (x'_{\alpha, s})^2 \right] + \sum_{\alpha} \sum_{j=1}^N \varepsilon_{\alpha} \rho_{\alpha_j} \widehat{c}_{\alpha_j} \left[-\frac{1}{2} (x'_{\alpha_j, \alpha})^2 - \widetilde{\psi}_{\alpha_j} \right. \\
&\quad \left. - \frac{1}{\rho_{\alpha_j}} \mathbf{E}_T \cdot \mathbf{P}_{\alpha_j} \right] \quad (\text{A.3.50})
\end{aligned}$$

The final form can be used to define constitutive relations and to define definitions of physical properties such as the hydrostatic pressure and the

entropy, to form governing equation systems.

A.3.10 Constitutive theory with electroquasistatic effects

A short review of parts of the constitutive theory used in Bennethum and Cushman (2002b), where the inequality (A.3.50) is used to derive thermodynamic definitions and constitutive assumptions is presented in the following. The mathematical steps for evaluating the inequality (A.3.50) is similar to the more simple cases described in Sec. 2.1.2. A two phase system, including a solid and liquid phase is considered by Bennethum and Cushman (2002b), where the choice of Helmholtz free energy $\tilde{\psi}_\alpha$, are

$$\tilde{\psi}_l = \tilde{\psi}_l \left(\varepsilon_l, \theta, \rho_{l_j}, \mathbf{x}'_{l,s}, \mathbf{x}'_{l_j,l}, \mathcal{E}_s, \mathbf{E}_T, z_{l_j}, \nabla\theta, \nabla\rho_{l_j}, \mathbf{d}_l, \boldsymbol{\omega}_l, \nabla\mathbf{x}'_{l_j,l} \right) \quad (\text{A.3.51})$$

and

$$\tilde{\psi}_s = \tilde{\psi}_s \left(\varepsilon_l, \theta, \rho_{s_j}, \mathbf{x}'_{s_j,s}, \mathcal{E}_s, \mathbf{E}_T, z_{s_j}, \nabla\theta, \nabla\rho_{s_j}, \boldsymbol{\omega}_s \right) \quad (\text{A.3.52})$$

where \mathcal{E}_s is the Green-Lagrange strain tensor of the solid, z_{l_j} is the charge per unit mass density of the j 'th species in the α phase, \mathbf{d}_l is the rate of deformation tensor of the liquid and $\boldsymbol{\omega}$ is the vorticity tensor. The material time derivative of (A.3.51) and (A.3.52) are used to evaluate the terms in (A.3.50) in order to satisfy the inequality.

A Lagrange multiplier Λ is introduced by Bennethum and Cushman (2002b) from which the streaming (or electrical) potential is defined. The total charge balance is introduced as

$$\frac{D_s}{Dt} (\varepsilon_l q_l^e + \varepsilon_s q_s^e) = 0 \quad (\text{A.3.53})$$

where q_l^e and q_s^e is the charge density of the liquid and solid phases, respectively.

The Lagrange multiplier Λ is multiplied with (A.3.53) and added to the inequality (A.3.50). The specific choice of the Helmholtz free energy yields the definition of the Lagrange multiplier, as

$$\Lambda = \frac{\rho_\alpha}{\rho_{\alpha_j}} \frac{\partial \tilde{\psi}_\alpha}{\partial z_{\alpha_j}} \quad (\text{A.3.54})$$

It is noted that the Lagrange multiplier, in this case, is identified to be of reference character, since one reference species (in this case the j 'th species) needs to be chosen for the definition of Λ .

The Fick's law for diffusion using the entropy inequality with electroquasistatics, the specific choice of the Helmholtz free energy and the definition of the Lagrange multiplier, is

$$\begin{aligned}
\sum_{k=1}^N \mathbf{r}_{l_{jk}} \cdot \mathbf{x}'_{k,l} &= -\varepsilon_l \rho_{l_j} \nabla \mu_{l_j} + \varepsilon_l \rho_{l_j} (\mathbf{b}_{l_j} - \mathbf{b}_{\mathbf{I},l_j}) + \varepsilon_l \rho_l \frac{\partial \tilde{\psi}_l}{\partial z_{l_j}} \nabla z_{l_j} \\
&+ \varepsilon_l q_l^e \nabla \Lambda + \varepsilon_l \rho_{l_j} z_l \mathbf{E}_T + \varepsilon_l \rho_{l_j} \frac{\partial \tilde{\psi}_l}{\partial \theta} \nabla \theta \\
&- (\mathbf{r}_{l_j})^\theta \cdot \mathbf{x}'_{l,s}
\end{aligned} \tag{A.3.55}$$

where $\mathbf{r}_{l_{jk}}$ is the material coefficient tensor for the coupled diffusion. The first term on the right hand side of (A.3.56) is similar to that derived for the more simple case in Sec. 2.1.2. The fourth term on the right hand side is the electrical potential gradient, which is a part of the Poisson-Nernst-Planck system. If the total electrical field is constituted as $\mathbf{E}_T = \text{grad} \Lambda$ then the Gauss law can be used to calculate Λ which is the Poisson part of the Poisson-Nernst-Planck system.

The liquid flow, following a generalized Darcy's law, is derived as

$$\begin{aligned}
\mathbf{R} \cdot \mathbf{x}'_{l,s} &= -\varepsilon_l \nabla p_l + \varepsilon_l \rho_l (\mathbf{b}_{l_j} - \mathbf{b}_{\mathbf{I},l_j}) + \pi^l \nabla \varepsilon_l + \varepsilon_l q_l^e \mathbf{E}_T \\
&+ \varepsilon_l q_l^e \nabla \Lambda + \varepsilon_l \rho_l \frac{\partial \tilde{\psi}_l}{\partial \mathcal{E}_s} : (\nabla \mathcal{E}_s)^\theta - \varepsilon_l \rho_l \frac{\partial \tilde{\psi}_l}{\partial \mathbf{E}_T} \cdot (\nabla \mathbf{E}_T)^\theta \\
&- \varepsilon_l \rho_l \frac{\partial \tilde{\psi}_l}{\partial \theta} \cdot (\nabla^2 \theta) - \sum_{j=1}^N \mathbf{r}_{l_{jk}} \cdot \mathbf{x}'_{k,l}
\end{aligned} \tag{A.3.56}$$

where \mathbf{R} is a second-order material coefficient tensor, p_l is the thermodynamic pressure and π^l is the swelling pressure. This constitutive relation for the liquid flow is much more involved than compared to the relation used in the papers of this thesis in which only the third term on the right hand side is used. It should be mentioned that even though the HMT results shown here is very general, it does not account for history dependent sorption hysteresis effects. Attempts to check the thermodynamic relevance of using different history dependent sorption hysteresis laws within continuum mixture theories is rare and no consensus in this matter has been reached, e.g., see Ristinmaa et al. (2011).

References for App. A

Jacob Bear and Yehuda Bachmat. *Introduction to modeling of transport phenomena in porous media*, volume 4. Springer, 1990.

- L.S. Bennethum and J.H. Cushman. Multicomponent, multiphase thermodynamics of swelling porous media with electroquasistatics: I. macroscale field equations. *Transport in Porous Media*, 47(3):309–336, 2002a.
- L.S. Bennethum and J.H. Cushman. Multicomponent, multiphase thermodynamics of swelling porous media with electroquasistatics: II. constitutive theory. *Transport in Porous Media*, 47(3):337–362, 2002b.
- Ray M Bowen. Theory of mixtures. *Continuum physics*, 3(Pt I), 1976.
- Sybren Ruurds de Groot and Peter Mazur. *Non-equilibrium Thermodynamics*. Courier Dover Publications, 1984.
- David Jeffrey Griffiths and Reed College. *Introduction to electrodynamics*, volume 3. prentice Hall Upper Saddle River, NJ, 1999.
- B. Johannesson. *Modelling of transport processes involved in service life prediction of concrete: important principles*, volume Licentiate thesis, 3083. Div of Building Materials LTH, Lund university, 1998.
- Björn Johannesson. *Introduction to Engineering Continuum Mixture Theory with Numerical Application using FEM*. 2011b. Lecture notes.
- M. Ristinmaa, N.S. Ottosen, and B. Johannesson. Mixture theory for a thermoelasto-plastic porous solid considering fluid flow and internal mass exchange. *International Journal of Engineering Science*, 49(11):1185–1203, 2011.
- Matti Ristinmaa and Niels Saabye Ottosen. *Mixture theory - A Framework for Paper Mechanics*. 2010.
- Ellad B. Tadmor, Ronald E. Miller, and Ryan S. Elliott. *Continuum mechanics and thermodynamics: from fundamental concepts to governing equations*. Cambridge University Press, 2012.